ARGESIM REPORT

MATHMOD 2022

Discussion Contribution Volume

Discussion Contributions 10th Vienna Conference on Mathematical Modelling

Vienna, Austria, July 27-29, 2022, TU Wien

Edited by Felix Breitenecker,
Wolfgang Kemmetmüller,
Andreas Körner, Andreas Kugi,
and Inge Troch
TU Wien

ARGESIM Report no. 17 – ISBN 978-3-901608-95-7 (ebook)
ARGESIM Publisher – Vienna – www.argesim.org
DOI: 10.11128/arep.17

MATHMOD 2022

Discussion Contribution Volume

Discussion Contributions of 10th Vienna Conference on Mathematical Modelling

Vienna, Austria, July 27 – 29, 2022, TU Wien

Edited by
Felix Breitenecker, Wolfgang Kemmetmüller,
Andreas Körner, Andreas Kugi, and Inge Troch
TU Wien

ARGESIM Report no. 17 – ISBN 978-3-901608-95-7 (ebook)
ARGESIM Publisher – Vienna – www.argesim.org
DOI: 10.11128/arep.17

Bibliographic Data:

Publisher: ARGESIM Publisher, Vienna
Title: MATHMOD 2022 Discussion Contribution Volume
Subtitle: Discussion Contribution of 10th Vienna Conference on Mathematical Modelling, Vienna, Austria, July 27-29, 2022, TU Wien
Author(s):
Editor(s): Felix Breitenecker, Wolfgang Kemmetmüller, Andreas Körner, Andreas Kugi, Inge Troch
Series: ARGESIM Reports
Series Editors: Felix Breitenecker, Thorsten Pawletta, ASIM
Volume: ARGESIM Report no. 17
ISBN: 978-3-901608-95-7 (ebook)
DOI: 10.11128/arep.17
Publication Date: July 15, 2022
Number of Pages: 102 +viii pages
Cover: 2 reproductions of algorithmic art graphic series 'Amulet' by Vlatko Ceric, www.vceric.net, with permission of the artist

Copyright Information / Regulations ARGESIM

ARGESIM is a non-profit scientific society generally aiming for dissemination of information on system simulation - from research via development to applications of system simulation. ARGESIM's primary publication is the journal SNE – Simulation Notes Europe with open access to all contributions; generally, the authors retain the copyright of their SNE contributions. This copyright regulation holds also for *ARGESIM Reports* and *ARGESIM Advances in Simulation* publishing conference volumes for ASIM, MTHMOD, and EUROSIM (in consideration of copyright regulations for related conference publications) and monographs on system simulation (mainly PhD theses).

About ARGESIM

ARGESIM is a non-profit society generally aiming for dissemination of information on system simulation from research via development to applications of system simulation. ARGESIM is closely co-operating with EUROSIM, the Federation of European Simulation Societies, and with ASIM, the German Simulation Society. ARGESIM is an 'outsourced' activity from the Mathematical Modelling and Simulation Group of TU Wien, there is also close co-operation with TU Wien (organisationally and personally). *ARGESIM Publisher* organizes publishing activities, with ISBN root 978-3-901608-xx-y and DOI root 10.11128/xx…x.

ARGESIM's activities are:

- Publication of the scientific journal SNE - Simulation Notes Europe (Membership Journal of EUROSIM, the Federation of European Simulation Societies) → *www.sne-journal.org*
- Organisation and Publication of the ARGESIM Benchmarks for Modelling Approaches and Simulation Implementations → *www.argesim.org/benchmarks/*
- Publication of the series ARGESIM Reports (for monographs in system simulation, and proceedings of simulation conferences and workshops) → *www.argesim.org/publications/*
- Publication of the special series FBS Simulation - Advances in Simulation / Fortschrittsberichte Simulation (monographs in co-operation with ASIM, the German Simulation Society
- Organisation of the Conference Series MATHMOD Vienna (triennial, in co-operation with EUROSIM, ASIM, and TU Wien) → *www.mathmod.at*
- Administration and support of ASIM (German Simulation Society → *www.asim-gi.org*) and of EUROSIM (Federation of European Simulation Societies → *www.eurosim.info*)

ARGESIM – Arbeitsgemeinschaft Simulation News – Working Committee Simulation News – SNE Publication
Mommsengasse 19/8, 1040 Vienna, Austria; Tel +43-1-58801-10111, -10115; Fax +43-1-58801-910111
Email: office@argesim.org, office@sne-journal.org; WWW: www.argesim.org, www.sne-journal.org
Incorporated Austrian Society ZVR No 213056164 – EU VAT ID No ATU 72054279
Bank Account: ARGESIM, IBAN AT07 2011 1828 9115 0800, BIC GIBAATWWXXX, ERSTE BANK VIENNA

FOREWORD

Welcome to **MATHMOD 2022**, the *10th Vienna Conference on Mathematical Modelling – a conference as it used to be*. 'A conference as it used to be' was our guideline for the **MATHMOD Conference Series** during Corona times. We had to postpone the **10th MATHMOD** twice – from February 2021 to February 2022, and then to July 2022, an unusual date for **MATHMOD** conference – but we definitely wanted to run the **10th MATHMOD** Conference as a face-to-face event, not running the conference as virtual conference, or as hybrid conference - *a conference as it used to be*.

Since 1994, the **MATHMOD Conference Series** invites scientists, engineers, and experts to present their ideas, methods, applications, and results in the field of mathematical modelling and share their experiences in different application domains.

Like a mathematical model, **MATHMOD** has constants, parameters, and variables. Constants are the frequency – triennial – and the date – February; only the Corona pandemics forced this constant to become a parameter for **10th MATHMOD**, organized exceptionally after four years in July 2022; aim and scope are parameters to be tuned with respect to the recent developments in mathematical modelling. Parameters reflect the organisation: the first **MATHMODs** were organised under the flag of *IMACS* (International Association for Mathematics and Computers in Simulation), recent **MATHMOD**s are *IFAC* (International Federation of Automatic Control) co-sponsored conferences with all advantages of *IFAC* online publications for the **MATHMOD** Proceedings (full contributions). The local organisation team at *TU Wien* has been extended: the *Institute of Analysis and Scientific Computing* (*ASC*) has won the *Automation and Control Institute* (*ACIN*) as partner in the organisation of the conference. In addition, *ARGESIM*, a scientific society 'outsourced' from the institutes, developed from local supporter to international publication partner *ARGESIM Publisher* for the **MATHMOD** *Discussion Contributions* or *Short Contributions*. New constants are other co-sponsorships, as for instance **MATHMOD** is also a *EUROSIM (Federation of European Simulation Societies) Conference.*

MATHMOD variables are the participants and the contributions. Successful models have output variables, and these are the contributions to the **MATHMOD** conferences. A classification of the contributions in model attribute parameters *Full Contributions*, *Discussion Contributions*, and *Student Contributions* has proven most appropriate. The success variables are the **MATHMOD** participants, spread over twenty-five countries, some concentrated in specific submodels, the very successful **MATHMOD Minisymposia**, some providing contributions to the classic submodels **MATHMOD Thematic Sessions** and **MATHMOD Poster Session**, and crowned by the **MATHMOD Plenary Lectures**.

MATHMOD 2022, the *10th Vienna International Conference on Mathematical Modelling*, implements all these developments in a successful conference with about 220 participants and about 150 contributions at TU Vienna from July 27 to July 29 – with a tutorial pre-programme on July 26, 2022.

This **MATHMOD 2022 Discussion Volume** publishes the two-page papers of all accepted *Discussion Contributions* in the online *ARGESIM Report* 17, ISBN 978-3-901608-95-7, DOI 10.11128/arep.17, available with open access at the website *www.argesim.org/mathmod-vienna/.* The review by an associate editor and by an IPC reviewer resulted in 51 accepted *Discussion Contributions* – a third of all accepted contributions.
ARGESIM Publisher already took care on publication of short papers, abstract papers, student papers, and discussion contributions for previous **MATHMOD** conferences, but for **MATHMOD 2018** and **MATHMOD 2022** each contribution is assigned an individual DOI number for

quick web access and reliable documentation. Thus, along with the publication of the *Discussion Contribution Volume*, metadata of the contributions are stored in publication databases for cross-referencing. *ARGESIM Publisher*'s DOI numbers for the **MATHMOD 2022 Discussion Contribution Volume** is within the range DOI 10.11128/arep.17.a17*nnn*, where *nnn* is the submission number of the contribution.

The **MATHMOD 2022 Proceedings** publish all accepted *Full Contributions* in a volume of the *IFAC-PapersOnLine* proceedings series (ISSN 2405-8963) at the ScienceDirect web service *www.journals.elsevier.com/ifac-papersonline/* (open access, individual contribution DOI).

Last but not least, **MATHMOD 2022** also wants to draw attention to the possibilities of **MATHMOD Postconference Publications**. Following the *IFAC* copyright regulations with possible publication of **MATHMOD 2022** contributions in *IFAC* journals, suitably adapted versions of **MATHMOD 2022** contributions which contain sufficiently new material may also be submitted to *MCMDS*, the journal *Mathematical and Computer Modelling of Dynamical* Systems, published by *Taylor and Francis.* Extended contributions with emphasis on simulation may also be submitted to *SNE Simulation Notes Europe*, the scientific journal of *EUROSIM* published by *ARGESIM Publisher*, Vienna.

But **MATHMOD** puts emphasis also on two other very important constants – the socialising constant, and the traditional constant. **MATHMOD**s are providing a – hopefully attractive – **MATHMOD Social Programme**, and **MATHMOD**s continue the tradition with connection to fine arts. Consequently, **MATHMOD 2022** starts with a talk on special views and places in Vienna, given by Inge Troch, the founder of MATHMOD. **MATHMOD 2022** presents a *Social Lecture* on modelling and simulation *Landscape Archaeology*, introducing into the techniques and methodologies of archaeological prospection. **MATHMOD 2022** continues the cooperation with Vlatko Ceric, professor emeritus for stochastics and modelling at University Zagreb, who creates graphics in style of *Algorithmic Art* for **MATHMOD** design – the title page of these proceedings show design from algorithmic art series Amulets, *www.veric.net.*
MATHMOD 2022 celebrates the Viennese Café tradition with the **Café Simulation**, a Viennese-type Café, especially established for **MATHMOD** near the conference office. And finally yet importantly, **MATHMOD 2022** continues the tradition the provide conference bags produced at a workshop for handicapped people, this time a rucksack-type sport bag with 'MATHMOD 2022 Vienna' embroidery.

As organizers we want to express our sincere thanks to all of you for your help in making the **MATHMOD 2022** conference a success – first to the **MATHMOD 2022** participants, authors, and plenary lecturers. In particular, we appreciate the support of our sponsors and co-sponsors. Special thanks go to the members of the *International Program Committee*, who did a great job in organizing the review process. A big thank goes to the organizers of the **MATHMOD Minisymposia** – playing a key role for the success of **MATHMOD 2022**.

Moreover, we are proud of the excellent work of all staff members – a big applause to our about 20 helping hands for **MATHMOD 2022**. Finally, we thank the *IFAC* publication team for the excellent cooperation, and the *ARGESIM Publisher's* people for support.

MATHMOD Conference Series – a mathematical model with constants, parameters, and variables: we hope the frequency becomes a constant again, and we would be glad to meet many variables at **11th MATHMOD** in February 2025.

Felix Breitenecker, Wolfgang Kemmetmüller, Andreas Körner, Andreas Kugi, Inge Troch
Vienna, July 2022

MATHMOD 2022 – 10th Vienna International Conference on Mathematical Modelling

Sponsored and organized by

TU Wien
Inst. f. Analysis and Scientific Computing and Automation and Control Institute

Co-Sponsored by

- **IFAC** International Federation of Automatic Control → *www.ifac.org*
- **ARGESIM** Vienna – Arbeitsgemeinschaft Simulation News, Wien → *www.argesim.org*
- EUROSIM – Federation of European Simulation Societies → *www.eurosim.info*
- ASIM – German Simulation Society (Arbeitsgemeinschaft Simulation) → *www.asim-gi.org*

Mutual Co-Sponsors

VDI / VDE – GMA – Society for Measurement and Automatic Control
GAMM Society for Applied Mathematics and Mechanics
OCG Austrian Computer Society
OVE - Österreichischer Verband für Elektrotechnik
OEMG Austrian Mathematical Society
GMAR - Österreichische Gesellschaft für Mess-, Automatisierung- und Robotertechnik

Financial Co-Sponsors

The Mathworks, Europe → *www.mathworks.de*
Vienna Convention Bureau → *www.vienna.convention.at*

International Programme Committee

Andreas KUGI, Austria (Chair) Austria
Biao HUANG, Canada (Co-Chair)
Wolfgang KEMMETMÜLLER, Austria (Co-Chair)
Inge TROCH, Austria (Editor)
K. AMPOUNTOLAS, Greece
H. ASCHEMANN, Germany
A. BACA, Austria
F. BASILE, Italy
C. BIANCA, France
G. BLOESCHL, Austria
P. BOGAERTS, Belgium
F. BREITENECKER, Austria
P. BUCHHOLZ, Germany
K. CHUDEJ, Germany
A. DEUTSCHMANN-OLEK, A
R. DYCZIJ-EDLINGER, D
P, EBERHARD, Germany
H, ECKER, Austria
S. ENGELL, Germany
L. ERIKSSON, Sweden
G. FERRETTI, Italy
S. FUCHSHUMER, Austria
F. GIRI, France
Y. LE GORREC, France
K. GRAICHEN, Germany
J. T. GRAVDAHL, Norway
R. GRINO, Spain
E. GRUENBACHER, Austria
M. GUENTHER, Germany
B. HAASDONK, Germany
L. JADACHOWSKI, Austria
A. KOERNER, Austria
B. LIE, Norway
B. MANHARTSGRUBER, A
W. MATHIS, Germany
T. MEURER, Germany
G. MUSIC, Slovenia
C. OTT, Germany
C. PINTO, Portugal
M. RAKOTONDRABE, France
G. RIZZELLO, Germany
J. RUDOLPH, Germany
J. Z. SASIADEK, Canada
O. SAWODNY, Germany
R. SCHENKENDORF, Austria
D. SEILER-THULL, Germany
T. STYKEL, Germany
A. URQUIA, Spain
J. F. M. VAN IMPE, Belgium
S. WENZEL, Germany
L. J. YEBRA, Spain
W. ZHAO, China

National Organizing Committee

Andreas KÖRNER (Chair)
Andreas DEUTSCHMANN-OLEK (Co-Chair)
Felix BREITENECKER (Co-Chair)
Sibylle KUSTER (Conf. Ass.)

MATHMOD 2022 Invited Lectures

- Mathematical Modeling in Climate Research: Characteristics and Challenges
  Thomas Slawig, Kiel University, Germany
- A Mathematical Diesel Engine Model, its Evolution and Impact on Clean and Efficient Marine Transportation
  Lars Eriksson, Linköping University, Sweden
- Challenges in Modelling and Detecting the Impact of Human Aptitudes and Preferences in Economics and Finance
  Marina Dolfin, University of Messina, Italy.
- Landscape Archaeology as an Interface between Natural Sciences and Humanities
  Michael Doneus, Department of Prehistoric and Historical Archaeology, University of Vienna

MATHMOD 2022 Minisymposia

- Recent Advances in Model Reduction and Surrogate Modeling
- Advances in Mathematical and Numerical Modelling of Cardiac Function
- Uncertainty Quantification for Dynamical Systems in Science and Engineering
- Modeling and Simulation in Environmental Informatics and Geosciences
- Mathematical Modeling and Control of (Bio-)chemical Processes
- Port-Hamiltonian Systems
- Modeling and Control of Smart Material Systems and Structures
- Modeling in Sport and Kinesiology

MATHMOD 2022 Thematic Sessions

- Electrical Systems
- Machine Learning and Data-Based Models
- Infinite-Dimensional Systems
- Modeling for Control & Model-Based Control
- Thermodynamic and Fluidic Systems
- Model Reduction
- Mechanical Systems & Robotics
- Model-Based Estimation
- Infectious Disease Modeling
- Economics, Management & Production Planning
- Biotechnical, Biochemical and Chemical Engineering Processes
- Biology, Physiology and Medicine

List of Content

Error estimates for data-driven optimal control by leveraging results for autonomous systems ⋆

Sebastian Peitz * **Katharina Bieker** **

* *Department of Computer Science, Paderborn University, Germany (e-mail: sebastian.peitz@upb.de).*
** *Department of Mathematics, Paderborn University, Germany.*

This work pursues the central task to efficiently solve *optimal control problems* for complex – and thus, expensive-to-evaluate – dynamical systems with the help of data-driven surrogate models. Mathematically speaking, we consider the following problem over the time horizon $p \cdot \Delta t$:

$$\min_{u \in U^p} J(y) = \min_{u \in U^p} \sum_{i=0}^{p-1} P(y_{i+1}) \qquad \text{(I)}$$
$$\text{s.t.} \quad y_{i+1} = \Phi(y_i, u_i), \qquad i = 0, 1, 2, \ldots,$$

where y_i and $u_i \in U$ are the system state and control at time instant $t_i = i\Delta t$. The objective function (for instance, the distance to some desired trajectory y^{ref}) is denoted by P, and Φ describes the flow of the underlying dynamical system (e.g., an ordinary or a partial differential equation) over the time increment Δt. The solution of (I) yields the optimal control u^* and corresponding state y^*.

A substantial challenge that we often face is the fact that the efficient prediction (and, by extension, control) of complex dynamical systems is hindered by the fact that the system dynamics are either very expensive to simulate or even unknown. Researchers have been investigating ways to accelerate the solution by using data for decades, the *Proper Orthogonal Decomposition (POD)* being an early and very prominent example (Sirovich, 1987). More recently, the major advances in data science and machine learning have lead to a plethora of new possibilities, for instance artificial neural networks, sparse regression for the identification of nonlinear dynamics (Brunton et al., 2016), or numerical approximations of the *Koopman operator* (Rowley et al., 2009; Klus et al., 2020), which describes the linear dynamics of observable functions. These methods facilitate the efficient simulation and prediction of high-dimensional spatio-temporal dynamics using measurement data, without requiring prior system knowledge. For control systems, a drawback is that the construction of surrogate models with inputs is often much more tedious and also problem-specific and data hungry (Bieker et al., 2020).

The approach we present here to solve (I) via surrogate models while avoiding the aforementioned issues is based on modifying the control problem instead of adjusting the surrogate modeling to the control setting. The resulting framework, which we call *QuaSiModO*, consists of the following steps (cf. also Figure 1):

(1) **Qua**ntization of the the admissible control U (for instance by replacing the interval $U = [u^{\min}, u^{\max}]$ by the bounds $V = \{u^{\min}, u^{\max}\}$);
(2) **Si**mulation of the autonomous systems with fixed inputs (e.g., $\Phi_{u^{\min/\max}}(y) = \Phi(y, u^{\min/\max})$;
(3) **Mod**eling of the individual systems via an arbitrary "off-the-shelf" surrogate modeling technique;
(4) **O**ptimization using the resulting set of autonomous surrogate models and relaxation techniques.

This interplay between continuous and integer control modeling as well as between the full system state and observed quantities (e.g., measurements) allows us to utilize the best of both worlds, namely

- integer controls for efficient data-driven modeling,
- continuous control inputs for real-time control, and
- existing error bounds for predictive models.

QuaSiModO successively transforms Problem (I) into related control problems that – as long as the predictive surrogate model is sufficiently accurate – yield optimal trajectories y^* that are close to one another. From (I) to (II), we quantize the control, meaning that only a finite set $V \subseteq U$ of inputs is feasible. This allows us to replace the non-autonomous dynamical system $\Phi(y, u)$ by a finite set of autonomous systems $\Phi_{u^j}(y)$, each corresponding

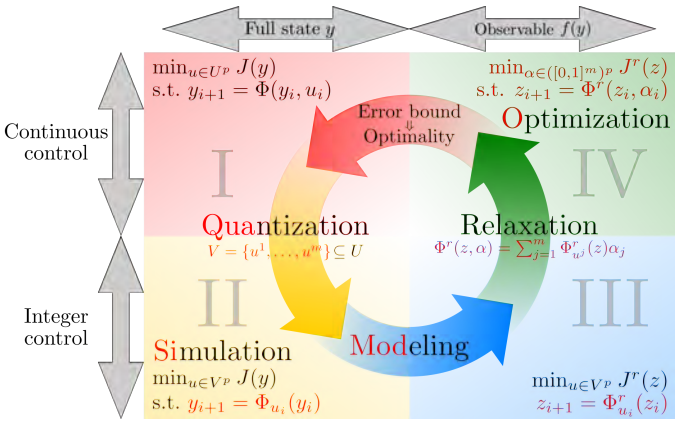

Fig. 1. The QuaSiModO framework consisting of the four steps Quantization, Simulation, Modeling and Optimization (Peitz and Bieker, 2021).

⋆ This research has been funded by the European Union and the German Federal State of North Rhine-Westphalia within the EFRE.NRW project "SET CPS", and by the DFG Priority Programme 1962 "Non-smooth and Complementarity-based Distributed Parameter Systems".

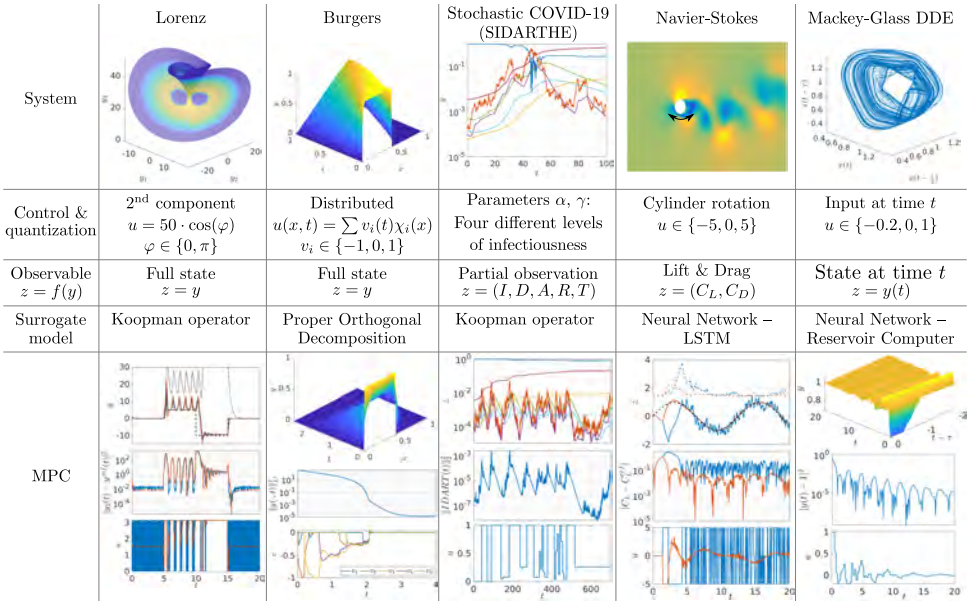

Fig. 2. QuaSiModO applied to various combinations of systems and surrogate models for model predictive control.

to one entry $u^j \in V$. While introducing an artificial drawback from the control perspective (Problem (II) is a mixed-integer optimal control problem), we can now easily introduce an equivalent Problem (III) that is based on surrogate models $\Phi^r_{u^i}(z)$ for a reduced quantity $z = f(y)$. Here, the function f is an *observable* which maps measurements from the state space of the full system to the space of measurements (which may be of significantly smaller dimension). As the transformation from (II) to (III) acts on a set of autonomous systems, we can approximate the individual systems Φ_{u^j} from individual measurement data sets, using whichever method we prefer.

In order to mitigate the disadvantages with respect to the complexity of the control problem, the problem of selecting an optimal input from V is relaxed by determining the optimal convex combination of the autonomous systems:

$$\begin{aligned} &\min_{\alpha \in ([0,1]^m)^p} J^r(z) = \min_{\alpha \in ([0,1]^m)^p} \sum_{i=0}^{p-1} P^r(z_{i+1}) \\ &\text{s.t.} \quad z_{i+1} = \sum_{j=1}^{m} \alpha_{i,j} \Phi^r_{u^j}(z_i), \qquad \sum_{j=1}^{m} \alpha_{i,j} = 1. \end{aligned} \tag{IV}$$

Problem (IV) is again continuous – with respect to the input α. For control affine systems, we can directly apply $u^* = \sum_{j=1}^m \alpha^*_j u^j$ to the real system. For non-affine systems, we use the sum up rounding algorithm from (Sager et al., 2012), by which a control corresponding to one of the quantized inputs is applied to the real system.

Besides the ability to include arbitrary models, an important aspect is that existing error bounds for the chosen surrogate model can easily be included, see (Peitz and Bieker, 2021) for a detailed description The availability of error bounds is of particular importance for engineering systems, where safety is of utmost importance (e.g., for aircraft or autonomous vehicles). The bounds guarantee the performance of a controller and – more importantly – will automatically become stronger with future developments in the field of data-driven modeling.

We have tested the QuaSiModO framework on a variety of dynamical systems, observable functions and surrogate modeling techniques, cf. Figure 2, a detailed description is given in (Peitz and Bieker, 2021). For instance, we can control the lift force acting on a cylinder (determined by the velocity and pressure fields governed by the 2D Navier–Stokes equations) without any knowledge of the flow field using the standard LSTM framework included in *TensorFlow*, and stabilize the Mackey-Glass equation using a standard echo state network. This highlights the flexibility and broad applicability of the method and the success of the technique in constructing data-driven feedback controllers.

REFERENCES

Bieker, K., Peitz, S., Brunton, S.L., Kutz, J.N., and Dellnitz, M. (2020). Deep model predictive flow control with limited sensor data and online learning. *Theoretical and Computational Fluid Dynamics*, 34, 577–591.

Brunton, S.L., Proctor, J.L., and Kutz, J.N. (2016). Discovering governing equations from data by sparse identification of nonlinear dynamical systems. *Proceedings of the National Academy of Sciences*, 113(15), 3932–3937.

Klus, S., Nüske, F., Peitz, S., Niemann, J.H., Clementi, C., and Schütte, C. (2020). Data-driven approximation of the Koopman generator: Model reduction, system identification, and control. *Physica D: Nonlinear Phenomena*, 406, 132416.

Peitz, S. and Bieker, K. (2021). On the Universal Transformation of Data-Driven Models to Control Systems. *arXiv:2021.04722*.

Rowley, C.W., Mezić, I., Bagheri, S., Schlatter, P., and Henningson, D.S. (2009). Spectral analysis of nonlinear flows. *Journal of Fluid Mechanics*, 641, 115–127.

Sager, S., Bock, H.G., and Diehl, M. (2012). The integer approximation error in mixed-integer optimal control. *Mathematical Programming*, 133(1-2), 1–23.

Sirovich, L. (1987). Turbulence and the dynamics of coherent structures part I: coherent structures. *Quarterly of Applied Mathematics*, XLV(3), 561–571.

Uncertainty and sensitivity analysis of model outputs in process industries: A critical review and perspectives in the era of digitalization and artificial intelligence

Gürkan Sin

Department of Chemical and Biochemical Engineering, Process and Systems Engineering Centre (PROSYS), Technical University of Denmark, Copenhagen, Denmark; gsi@kt.dtu.dk).

Abstract

In today's chemical industries commercial software tools employing state-of-the-art models and advanced optimization and control algorithms are used at different stages of the project life cycle, from early stages performing scale-up and conceptual process design, front-end engineering design to retrofitting and optimization studies at the plant commissioning/operation stage. The impact of advanced process modeling and simulation, optimization and control is profound and has become mainstream in the chemical industries due to the significant economic benefits achieved. These are amongst crown achievements of the process systems engineering community in Chemical Engineering discipline through research in mathematical programming, modeling, process synthesis and design and process control that has been performed in the past decades. Today there are new driving forces affecting the bottom line of chemical industries but also universities alike namely digitalization, machine learning/Artificial Intelligence (AI), climate change, decarbonization, sector coupling through renewable energy, etc. These technologies open up new horizons for industry to become more efficient, to decrease CO_2 footprint and to develop innovative products and services. As model-based engineering becomes more established as enabling technology to address these challenges, in this talk we review the critical role of uncertainty and sensitivity analysis methods starting from the fundamental theory of Monte Carlo integration to sensitivity analysis using variance decomposition methods. Here an important distinction between when a study is about uncertainty and when it is about sensitivity analysis will be discussed. A number of applications of uncertainty and sensitivity analysis from process systems engineering which employs largely first principles/mechanistic models are presented: These examples include a range of engineering problems related to model identification/parameter estimation (in process/property modeling) to process synthesis and design and optimization. From these experiences, a critical analysis of the theory and pitfalls encountered in the application of uncertainty & sensitivity analysis in wider process systems engineering is presented. In the second part of the talk, a critical attention is given to the need to provide model prediction error (uncertainty quantification) of machine learning as well as deep learning/graph neural network models that are becoming popular in this emerging AI paradigm. While a wide range of methods for uncertainty assessment for such deep learning models are proposed from the larger deep learning community (from ensemble modeling to last layer dropout, etc), these methods are mostly pragmatic and heuristics in nature. Therefore the importance of benchmarking and critically assessing the quality of uncertainty quantification methods should remain an important point of attention. This aspect will be discussed on a study that deals property prediction of chemical compounds using graph neural networks.

Stepping back from these particular examples, and looking ahead at the big picture, we see that many engineering decisions relies on computational analysis/calculations that employs a range of models some increasingly sophisticated (be it mechanistic, machine learning/deep learning or a hybrid combination). In this regard, proper identification and systematic study of potential sources

of uncertainty and assessment of their consequences to such decisions will remain relevant and important problem. This field is truly fascinating with many scientific and engineering challenges to address.

Convergence of Solutions of Shape Design Problems For Fluid Flow at Long Time Horizons ⋆

John Sebastian H. Simon *

* *Division of Mathematical and Physical Sciences, Graduate School of Natural Science and Technology, Kanazawa University, Kanazawa 920-1192, Japan (e-mail: john.simon@stu.kanazawa-u.ac.jp, jhsimon1729@gmail.com).*

1. INTRODUCTION

Let $\mathcal{D} \subset \mathbb{R}^2$ be a non-empty open bounded connected domain, $\omega \subsetneq \mathcal{D}$, and consider the following set of admissible domains

$$\mathcal{O}_\omega = \{\Omega \subset \mathcal{U} : \Omega \supset \omega,\ \Omega \text{ is open, bounded, connected, and at least of class } C^{0,1}\}.$$

Let $\boldsymbol{f} \in L^2(\mathcal{D};\mathbb{R}^2)$ be a stationary fluid source function, which can be interpreted as the force that steers the fluid at a constant pace—an example of this is a fluid pump and fluid outlet that act on the fluid at the same rate— and $\Omega \in \mathcal{O}_\omega$. The time-dependent Navier–Stokes equations on the interval $(0,T)$ is given by

$$\begin{cases} \partial_t \boldsymbol{u} - \nu\Delta\boldsymbol{u} + \gamma(\boldsymbol{u}\cdot\nabla)\boldsymbol{u} + \nabla p = \boldsymbol{f} & \text{in } \Omega\times(0,T), \\ \nabla\cdot\boldsymbol{u} = 0 & \text{in } \Omega\times(0,T), \\ \boldsymbol{u} = 0 & \text{in } \partial\Omega\times(0,T), \\ \boldsymbol{u} = \boldsymbol{u}_0 & \text{in } \Omega\times\{0\}, \end{cases} \tag{1}$$

where $\boldsymbol{u}$ and p correspond to the dynamic fluid velocity and pressure, respectively, and $\boldsymbol{u}_0 \in L^2(\mathcal{U};\mathbb{R}^2)$ is the initial velocity that satisfies $\nabla\cdot\boldsymbol{u}_0 = 0$ in Ω. The parameter $\nu > 0$ denotes the fluid viscosity. On the other hand, we call $\gamma \geq 0$ the *convection parameter*. We also look at the stationary Navier–Stokes equations

$$\begin{cases} -\nu\Delta\boldsymbol{v} + \gamma(\boldsymbol{v}\cdot\nabla)\boldsymbol{v} + \nabla q = \boldsymbol{f} & \text{in } \Omega, \\ \nabla\cdot\boldsymbol{v} = 0 & \text{in } \Omega, \\ \boldsymbol{v} = 0 & \text{in } \partial\Omega, \end{cases} \tag{2}$$

where $\boldsymbol{v}$ and q are the equilibrium fluid velocity and pressure, respectively.

On both equations, if $\gamma = 1$ we reduce to the usual Navier–Stokes equations, while $\gamma = 0$ gives us the Stokes equations.

We focus on the analysis of two shape optimization problems governed by equations (1) and (2). In particular, given a static desired velocity $\boldsymbol{u}_D \in L^2(\omega;\mathbb{R}^2)$, we consider the time-average problem

$$\left.\begin{array}{c} \min\limits_{\Omega\in\mathcal{O}_\omega} J_T(\Omega) := \dfrac{\nu}{T}\displaystyle\int_0^T \|\boldsymbol{u}(t) - \boldsymbol{u}_D\|^2_{L^2(\omega;\mathbb{R}^{2\times 2})}\,\mathrm{d}t \\ \text{subject to (1),} \end{array}\right\} \tag{3}$$

and the stationary shape design problem

$$\left.\begin{array}{c} \min\limits_{\Omega\in\mathcal{O}_\omega} J_s(\Omega) := \nu\|\boldsymbol{v} - \boldsymbol{u}_D\|^2_{L^2(\omega;\mathbb{R}^2)} \\ \text{subject to (2).} \end{array}\right\} \tag{4}$$

We denote the solutions of (3) and (4) by Ω_T and Ω_s. Our goal is to show that

$$|J_T^* - J_s^*| \leq c\left(\frac{1}{T} + \frac{1}{\sqrt{T}} + \frac{\gamma}{2^{1/2}}\right) \tag{5}$$

where $J_T^* := J_T(\Omega_T)$, $J_s^* := J_s(\Omega_s)$, and the constant $c := c(\boldsymbol{u}_0, \boldsymbol{u}_D, \boldsymbol{f}, 1/\nu, \mathcal{U}) > 0$ is independent of T.

Inequality (5) attempts to answer the contention that solutions to dynamic fluid shape design problems are close to the solution of the equilibrium problem. This assumption is one of the reasons why majority of shape optimization problems involving fluid deals with the stationary state equations rather than the time-dependent case.

Remark 1. Note that when $\gamma = 0$, both systems (1) and (2) can be realized as parabolic and elliptic problems, respectively, and inequality (5) reduces to the estimate of Trelat et al. (2018).

Our result is summarized in the following theorem.

Theorem 2. Suppose that $\boldsymbol{f} \in L^2(\mathcal{U};\mathbb{R}^2)$, $\boldsymbol{u}_0 \in H(\Omega) \cap L^2(\mathcal{U};\mathbb{R}^2)$, and $\boldsymbol{u}_D \in L^2(\omega;\mathbb{R}^2)$. If $J_T^* := J_T(\Omega_T)$ and $J_s^* := J_s(\Omega_s)$, where Ω_T and Ω_s are the solutions of (3) and (4), respectively; then there exists $c > 0$, independent of T, such that (5) holds.

As a consequence, we obtain a sense of convergence of solutions of (3) to a solution of (4). We formalize this result below.

Corollary 3. Suppose that the assumptions in Theorem 2 hold. Then there exists $\Omega^* \in \mathcal{O}_\omega$, such that $\Omega_T \xrightarrow{\chi} \Omega^*$ as $T \to \infty$, and that $|J_s^* - J_s(\Omega^*)| \leq 2^{1/2}c\gamma$, where $c > 0$ is the same constant as in Theorem 2. Here, the symbol $\xrightarrow{\chi}$ denotes the domain convergence with respect the the indicator functions in L^∞-topology.

2. NUMERICAL REALIZATION

To solve the problem numerically, we rely on a gradient descent method induced by the identity perturbation operator. For more details, we refer to Delfour and Zolesio

⋆ This work is supported by the Japanese Government Ministry of Education, Culture, Sports, Science and Technology (MEXT) Scholarship.

(2011). We compute the shape derivative of the objective functions in the sense of Hadamard's, i.e., the shape derivative of a given objective function $\mathcal{J} : \mathcal{O}_\omega \to \mathbb{R}$ in the direction of $\theta \in \Theta$ is denoted and defined as $d\mathcal{J}(\Omega)\theta = \lim_{\tau \searrow 0} \frac{\mathcal{J}(\Omega_\tau) - \mathcal{J}(\Omega)}{\tau}$.

The shape derivative of J_T and J_s have already been computed (see Kasumba and Kunisch (2012), and Mohammadi and Pironneau (2010) among others), hence we skip such step in this exposition. Nevertheless, such derivatives are given below

$$dJ_T(\Omega)\theta = \frac{\nu}{T}\int_0^T \left[\int_{\partial\Omega} (\partial_{\boldsymbol{n}}\boldsymbol{u}(t)\cdot\partial_{\boldsymbol{n}}\boldsymbol{w}(t))\theta\cdot\boldsymbol{n}\,\mathrm{d}\sigma + \int_\Omega \nabla\cdot(\chi_\omega|\boldsymbol{u}(t)-\boldsymbol{u}_D|^2\theta)\,\mathrm{d}x\right]\mathrm{d}t,$$

$$dJ_s(\Omega)\theta = \nu\left[\int_{\partial\Omega} (\partial_{\boldsymbol{n}}\boldsymbol{v}\cdot\partial_{\boldsymbol{n}}\boldsymbol{z})\theta\cdot\boldsymbol{n}\,\mathrm{d}\sigma + \int_\Omega \nabla\cdot(\chi_\omega|\boldsymbol{v}-\boldsymbol{u}_D|^2\theta)\,\mathrm{d}x\right],$$

where $\boldsymbol{w} \in L^\infty(I;H(\Omega)) \cap L^2(I;V(\Omega))$ is the time dependent adjoint variable that satisfies the variational problem

$$\begin{aligned}&{}_{V^*(\Omega)}\langle -\partial_t\boldsymbol{w}(t),\boldsymbol{\varphi}\rangle_{V(\Omega)} + \nu(\nabla\boldsymbol{w}(t),\nabla\boldsymbol{\varphi})_\Omega\\ &+\gamma[((\boldsymbol{\varphi}\cdot\nabla)\boldsymbol{u}(t),\boldsymbol{w}(t))_\Omega - ((\boldsymbol{u}(t)\cdot\nabla)\boldsymbol{w}(t),\boldsymbol{\varphi})_\Omega]\\ &= 2(\boldsymbol{u}(t)-\boldsymbol{u}_D,\boldsymbol{\varphi})_\omega \quad \forall\boldsymbol{\varphi}\in V(\Omega),\end{aligned}$$

and the transversality condition $\boldsymbol{w}(T) = 0$, while $\boldsymbol{z} \in V(\Omega)$ solves the equation

$$\begin{aligned}&\nu(\nabla\boldsymbol{z},\nabla\boldsymbol{\varphi})_\Omega + \gamma[((\boldsymbol{\varphi}\cdot\nabla)\boldsymbol{v},\boldsymbol{z})_\Omega - ((\boldsymbol{v}\cdot\nabla)\boldsymbol{z},\boldsymbol{\varphi})_\Omega]\\ &= 2(\boldsymbol{v}-\boldsymbol{u}_D,\boldsymbol{\varphi})_\omega \quad \forall\boldsymbol{\varphi}\in V(\Omega).\end{aligned}$$

Note that both derivatives can be expressed with the Zolesio-Hadamard structure, i.e., we can write

$$d\mathcal{J}(\Omega)\theta = \int_{\partial\Omega} \nabla J\boldsymbol{n}\cdot\theta\,\mathrm{d}\sigma,$$

where ∇J is called the shape gradient.These shape gradients will be the basis of our descent directions, i.e., by choosing $\theta = -\nabla J\boldsymbol{n}$ in $\partial\Omega$ we are assured that

$$d\mathcal{J}(\Omega)\theta = -\|\theta\|^2_{L^2(\partial\Omega;\mathbb{R}^2)} < 0.$$

Numerically though, such choice of descent direction may cause oscillations on the perturbed domains. Because of that, we shall resort to a traction method that intends to extend the choice of θ to the whole domain, say for example by a Robin boundary problem, see Azegami and Takeuchi (2006).

The variational equations are solved using Galerkin finite element methods. The stationary Navier–Stokes equations is solved using Newton's method, the dynamic Navier–Stokes equations and the time-dependent adjoint equation are solved using a Lagrange–Galerkin method based on characteristics, and the stationary adjoint equation is solved by the usual Galerkin method.

2.1 Numerical Implementation

For simplicity, we choose $\boldsymbol{f} = \frac{1}{10}(y^3, -x^3)$, the desired function is the solution of the Stokes equations with $\nu = 1/5$ in a domain enclosed in a circle that satisfies $x^2 + y^2 = 4$, and the domain $\omega \subset \mathbb{R}^2$ is the set $\{(x,y)\mathbb{R}^2 : x^2 + y^2 \leq 1\}$. The shape optimization problems are then solved with parameter values $\nu = \gamma = 1$, and with the initial velocity $\boldsymbol{u} = 0$.

To illustrate the convergence of the solutions of the time-dependent problems, we have Figure 1. Figure 1(A) shows that the boundary of the solutions $\partial\Omega_{T,h}$ becomes closer to the boundary $\Omega_{s,h}$ as the terminal time T gets bigger. Figure 1(B) shows the log-log plot of the gap $|J_T - J_s|$ versus the terminal time T. In the same figure, we plotted the plots of $\mathcal{O}(T^{-1})$ and $\mathcal{O}(T^{-1/2})$. Coincidental with the theoretical result, for lower values of T the order of convergence nearly follows $\mathcal{O}(T^{-1/2})$, while we observe a convergence that is similar with $\mathcal{O}(T^{-1})$ for higher values of T.

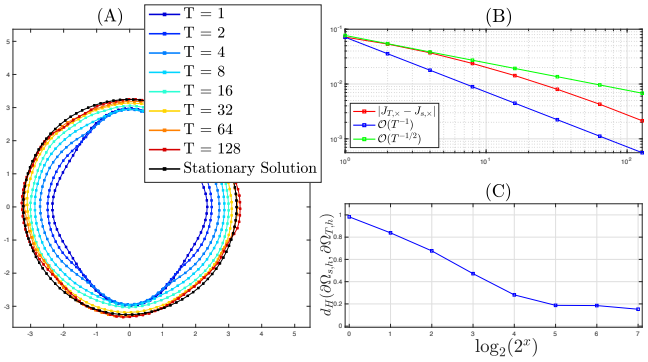

Fig. 1. Illustration of how the boundary of the shape solution of the time-dependent problem (3) converges to the boundary of the solution of the equilibrium problem (4) as T gets larger (A); log-log plots of $|J_{T,\times} - J_{s,\times}|$, $\mathcal{O}(T^{-1})$, and $\mathcal{O}(T^{-1/2})$(B); trend of the Hausdorff distance between the solutions of (3) and (4) (C).

Lastly, we quantified the convergence of the boundaries by virtue of the Hausdorff distance. We observe in Figure 1(C) that the Hausdorff distance indeed gets smaller as the value of x, which is such that $T = 2^x$, increases.

REFERENCES

Azegami, H. and Takeuchi, K. (2006). A smoothing method for shape optimization: Traction method using the Robin condition. *International Journal of Computational Methods*, 03(01), 21–33. doi: 10.1142/S0219876206000709.

Delfour, M. and Zolesio, J.P. (2011). *Shapes and Geometries: Metrics, Analysis, Differential Calculus, and Optimization*. Society for Industrial and Applied Mathematics, 2 edition.

Kasumba, H. and Kunisch, K. (2012). Vortex control in channel flows using translational invariant cost functionals. *Computational Optimization and Applications*, 52(3), 691–717. doi:10.1007/s10589-011-9434-y.

Mohammadi, B. and Pironneau, O. (2010). *Applied Shape Optimization for Fluids*. Numerical Mathematics and Scientific Computation. Oxford University Press.

Trelat, E., Zhang, C., and Zuazua, E. (2018). Optimal shape design for 2d heat equations in large time. *Inverse Problems in Science and Engineering*, 3(1), 255–269.

Hybrid Dynamical Modeling of Polycrystalline Shape Memory Alloy Wire Transducers

Michele A. Mandolino * **Francesco Ferrante** **

* *Department of Systems Engineering, Department of Material Science and Engineering, Saarland University, Saarbrücken, Germany (e-mail: michele.mandolino@imsl.uni-saarland.de).*
** *Department of Engineering, University of Perugia, Perugia, Italy (e-mail: francesco.ferrante@unipg.it)*

Keywords: Mechatronics, Model Simplification and Optimization, Discrete-Event Systems.

1. INTRODUCTION

Shape Memory Alloys (SMAs) are a class of smart materials which exhibit different thermo-mechanical properties than conventional metals. When SMA material is heated, transformations in the crystal lattice structure are induced, which generate a macroscopic change in shape on the order of 4-8%. This effect can be exploited for the development of novel actuators that react to an external thermal input with a mechanical deformation (Ballew and Seelecke (2019)). In most applications, SMA material is shaped as a thin wire. In this way, the thermal activation can be simply induced via an electric current, thus resulting in a mechatronic tendon-like actuator.

Despite their remarkable benefits such as compactness, lightweight, and high energy density, SMA materials are characterized by a highly nonlinear response, which is mainly due to a load-, temperature-, and rate-dependent hysteresis. Accurate modeling and compensation of such hysteresis is fundamental for the development of high-performance SMA applications. The goal of this work is to provide an accurate and numerically efficient model, which can be used to perform accurate simulations, model-based design optimization, and control of complex structures driven by polycrystalline SMAs. Our approach is based on a reformulation of the physics-based Müller-Achenbach-Seelecke (MAS) model for polycrystalline SMA wires (Rizzello et al. (2019)) within the hybrid dynamical framework proposed by Goebel et al. (2012). In this way, we are able to significantly reduce the numerical complexity and computation time, without losing numerical accuracy and physical interpretability. In future research, the model will be used for hybrid control of SMA systems.

2. SHAPE MEMORY ALLOY MODEL

In the scientific literature, there are plenty mathematical models which describe the behavior of SMA material (Khandelwal and Buravalla (2009)). Due to the different approaches pursued, we can classify them in numerical and analytical/physics-based models. The former are the most computationally efficient ones, but are not suitable for predicting material response to change of external conditions (e.g., load stress, external temperature, structure which is coupled with the SMA). The latter, instead, have a highly sophisticated and detailed description but, in turn, are characterized by strong nonlinearities and require high simulation time.

With the aim to obtaining fast and accurate predictions, in this work we propose a novel physics-based model for one-dimensional polycrystalline SMA wires. To provide meaningful simulation results, the model needs to reproduce as many physical effects as possible. A valuable baseline is offered by the mesoscopic MAS model for polycrystalline SMA material presented by Rizzello et al. (2019). Such a model is based on a novel bookkeping algorithm that reproduces the time evolution of smooth hysteresis loops, as well as inner loops, while maintaining all physical information of the basic single-crystal MAS model (Ballew and Seelecke (2019)). Despite those advantages, the model is affected by slow simulation time due to strong nonlinearities and numerical stiffness of the resulting ODEs.

3. HYBRID DYNAMICAL MODEL

Using the work of Rizzello et al. (2019) as starting point, in this section we summarize the theoretical reformulation which permits to overcome the aforementioned numerical limitations. A potential way to improve the physical model implementation consists of eliminating the stiff dynamics of phase transformations, and substitute it with instantaneous hybrid transitions. This approach is similar to what already exploited in a previous work on single-crystal SMA model (Mandolino et al. (2021)), which will now be generalized to more challenging polycrystalline SMAs. The adopted hybrid framework for the SMA model implementation is based on the hybrid theory of Goebel et al. (2012).

A generic stress-strain hysteresis of a superelastic polycrystalline SMA wire is shown in Fig. 1(a). The material produces different pathways (or branches) depending on the entity of a mechanical load applied. By observing this behavior, we can determine three operating modes, each one with well-defined physical interpretations:

(1) **AM**: Austenite to Martensite (or Loading) branch;
(2) **MA**: Martensite to Austenite (or Unloading) branch;

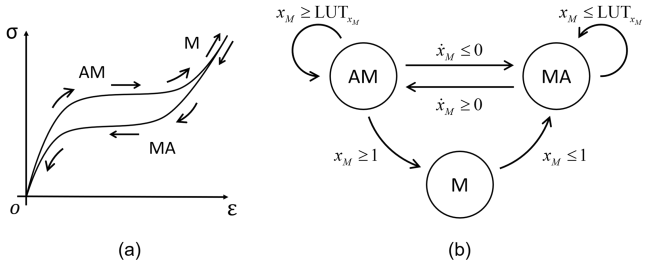

Fig. 1. Example of a qualitative stress-strain hysteresis of polycrystalline SMA wire (a) and the corresponding hybrid automaton with *modes* and *edges* (b).

(3) **M**: Full Martensite branch.

The finite state machine which defines the transition logic between those modes is sketched in Fig. 1(b). A hypothetical operating sequence of the model is as follows. A superelastic SMA wire starts in a full austenitic condition (*mode* **AM**). When subject to an increasing mechanical load, the amount of austenitic crystal lattice reduces while the martensitic one increases. If the load exceeds a certain threshold (dictated by material specifics and external inputs), the SMA wire transforms completely into martensite (*mode* **M**). When the material works below the load threshold and, at the same time, the mechanical load is decreased, the system changes gradually from martensite to austenite (*mode* **MA**). Minor hysteresis loops, which appear when performing partial loading and unloading, are handled by the same **AM** and **MA** *modes*, by considering a novel properly computed unloading branch, see Rizzello et al. (2019) for details. Note that such minor hysteresis loops are not shown in Fig. 1(a), for the ease of clarity.

The finite state machine in Fig. 1(b) can be represented through a generic hybrid system defined as follows:

$$\mathcal{H}\colon \begin{cases} \dot{x} &= f(x,u) \quad (x,u) \in C \\ x^+ &\in G(x) \quad (x,u) \in D \end{cases}. \tag{1}$$

The states $x := [\varepsilon\ T\ q]^\intercal \in \mathbb{X}$, $\mathbb{X} := \mathbb{R}_{\geq 0} \times \mathbb{R}_{\geq 0} \times \{\mathbf{AM}, \mathbf{MA}, \mathbf{M}\}$, correspond to the SMA strain, temperature, and operative mode. The inputs $u := [v\ J\ T_E]^\intercal \in \mathbb{U}$, $\mathbb{U} := \mathbb{R} \times \mathbb{R}_{\geq 0} \times \mathbb{R}_{\geq 0}$, represent wire speed, input power, and environmental temperature, respectively. The output is simply $y := F \in \mathbb{Y}$, $\mathbb{Y} := \mathbb{R}_{\geq 0}$, i.e., the SMA force. Sets f and C describe the continuous-time subset of the system by the respective differential equations and state constraints, while G and D describe the discrete-time subset by difference equations or inclusions and jump constraints. The state-space form of the hybrid SMA model is:

$$\begin{cases} \dot{\varepsilon} &= v\, l_0^{-1} \\ \dot{T} &= [J - \lambda A_s (T - T_E) + \dot{L}_{x_M^{(i)}}](\Omega \rho_V c_V - L_T)^{-1} \\ F &= \pi r_0^2 (\varepsilon - \varepsilon_T x_M^{(i)})[E_M^{-1} x_M^{(i)} + E_A^{-1}(1 - x_M^{(i)})]^{-1} \end{cases} \tag{2}$$

A detailed description of f, G, C, and D, as well as variable $x_M^{(i)}$ associated to mode (i), is omitted for conciseness.

4. SIMULATION RESULTS

In this section, the behavior of the polycrystalline MAS model from Rizzello et al. (2019) will be compared with the new hybrid one, as well as with experimental stress-strain curves. All simulations are performed in Matlab/Simulink environment. Experimental data and model parameters of a superelastic SMA wire are derived from Rizzello et al. (2019). Due to its nonlinearities, the MAS model requires a stiff solver (i.e., *ode15s*). On the other hand, thanks to its simpler structure, the hybrid reformulation can be also integrated with simpler non-stiff solver (i.e., *ode45*). Different unloading paths are tested, corresponding to two strain rates of 10^{-4} s^{-1} and 10^{-2} s^{-1}, respectively. Simulations results, shown in Fig. 2, demonstrate how the two implementations are practically equivalent in terms of numerical results. An experimental rate-dependency of the hysteresis is also observed, which is well reproduced by both models. The total simulation time of the hybrid model, however, is almost 5.6 times smaller than the one of the MAS, i.e., 36.82 s vs. 206.64 s.

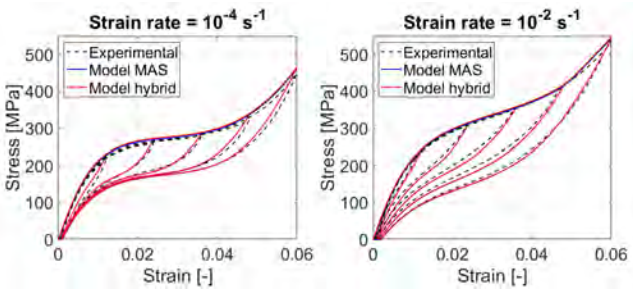

Fig. 2. Hysteresis results for different internal loops at different strain rate: $10^{-4}s^1$ (left) and $10^{-2}s^1$ (right)

5. CONCLUSION

In this paper, a novel physics-based hybrid model for polycrystalline SMA wires is developed and tested. It takes advantage of the hybrid modeling theory to significantly minimize the model complexity, thus allowing to reducing the simulation time without losing accuracy. Future research will focus on using the hybrid polycrystalline model to describe complex SMA systems, as well as on developing hybrid control laws for hysteresis compensation.

REFERENCES

Ballew, W. and Seelecke, S. (2019). Mesoscopic free energy as a framework for modeling shape memory alloys. *Journal of Intelligent Material Systems and Structures*, 30, 1969–2012.

Goebel, R., Sanfelice, R.G., and Teel, A.R. (2012). *Hybrid Dynamical Systems: Modeling, Stability, and Robustness*. Princeton University Press, New Jersey.

Khandelwal, A. and Buravalla, V. (2009). Models for shape memory alloy behavior: an overview of modeling approaches. *The International Journal of Structural Changes in Solids*, 1(1), 111–148.

Mandolino, M.A., Ferrante, F., and Rizzello, G. (2021). A hybrid dynamical modeling framework for shape memory alloy wire actuated structures. *IEEE Robotics and Automation Letters*, 6(2), 3886–3893.

Rizzello, G., Mandolino, M.A., Schmidt, M., Naso, D., and Seelecke, S. (2019). An accurate dynamic model for polycrystalline shape memory alloy wire actuators and sensors. *Smart Materials and Structures*, 28(2), 025020.

Ecosystem services from urban trees in Berlin: a feasibility study based on open data

Lisa Möller, Michael Schwalb, Lucas Tiedemann, Jochen Wittmann *

**Hochschule für Technik und Wirtschaft Berlin, University of Applied Sciences,*
Fachbereich 2, Environmental Informatics;
Wilhelminenhofstrasse 75A, 12459 Berlin, Germany
(Tel: +49 30 5019 3308; e-mail :wittmann@htw-berlin.de).

Abstract:

Using the i-Tree software, this paper provides an overview of the ecosystem services of urban trees in Berlin. The purpose of this study is to determine the feasibility of research studies concerning the ecosystem services of Berlin's urban trees based on the Berlin Geoportal. The purpose of this paper is to show how public cadastral data can be used to assess ecosystem services provided by trees. The modeling of the data is done by the software i-Tree. The paper focuses on defining the requirements for data provision and illustrates the process of data preparation using the Berlin tree cadastre as an example. In addition, an approach to fill in incomplete data sets using linear regression was made. The results of the analysis should highlight which further information on urban trees would be necessary to improve the informative value of future studies and, based on this, to improve the structure of the tree population and to enable the continuous provision of benefits by urban trees.

Keywords: i-Tree, urban trees, regression analysis, GIS, ecosystem services, feasibility study

1. INTRODUCTION

Ecosystem services refer to the benefits provided by urban trees, meadows and parks, among others. Several studies also indicate that urban trees improve air quality (Manes, et al., 2012; Soares, et al., 2011; Wang, et al., 2018).
The objective of this work shall be to identify and assess the ecosystem services provided by Berlin's urban trees and urban tree species. This study aims to determine the feasibility of research studies concerning the ecosystem services of Berlin's urban trees based exclusively on open data from the Berlin Geoportal. The study does not draw on additional forestry knowledge and is carried out without the assistance of public authorities. Only freely accessible urban tree data is used. This paper aims to highlight what further information on urban trees would be necessary to improve the results of future studies.

2. DATA AND METHODOLOGY

In order to get a more detailed overview of the street trees in Berlin, the tree data of the geoportal will be processed so that they can be analysed with the software i-Tree. Special attention will be paid to relevant parameters needed in i-Tree, which cannot be derived from the Geoportal database.

2.1 Description of the data from Berlin Geoportal

The data source for Berlin's street and plant tree inventory in the Geoportal is the tree cadastre of the Berlin (Geoportal Berlin, 2018). More than 900,000 active trees and their data are recorded in the Berlin tree register.
For the further evaluation of the data in i-Tree, the trunk circumference is the most relevant. In total, the database was able to provide 559,903 values for this category. Another relevant value for the subsequent evaluation is the height of the tree. Here the database was able to output 362,793 values. Only 266,663 values provided information about Berlin's tree canopy. This means that less than half of the total tree population allows a statement about the tree crown.

2.2 Definition of the data requirements in iTree

i-Tree has been developed and configured for the USA and its domestic tree species. Nevertheless, the tool is used in European and Asian studies as well (Scholz, et al., 2016; Wang, et al., 2018; Moser, et al., 2017).
The only mandatory values required for an evaluation are the tree species and the trunk diameter. The values for size, health and thinning of the tree crown are also recommended by i-Tree (USDA Forest Service, 2021). However, these values are only available for some of the trees in Berlin. i-Tree will thus fall back on comparative values and interpolations. Furthermore, it is recommended to specify the tree height. This value is available for some of the trees. For

the remaining trees, the height is estimated using the algorithm described in 2.3.

2.3 Adaptation and optimisation of the data set

The data set of the Berlin tree cadastre cannot be fed into i-Tree without adjustments. To achieve better results, some incomplete data points are supplemented by estimated values. This method is used for the tree height. This step is taken because out of the total 565,363 entries in the tree cadastre, about 36% do not have a value for tree height.
The following table summarises the missing entries in the data set necessary for our investigations.

Table 1. characteristics of the tree cadastre dataset

Data set total	Height missing	Art Botanically absent	Trunk circumference missing
565.363	203.010	1.198	5.932

For the used dataset, an attempt is made to determine the characteristic of tree height, which is missing for some trees, by means of the regression.
To evaluate the quality of the regression, the coefficient of determination R^2 was determined with the value 0.578. Thus, 57.8% of the variability of the tree height can be described by the independent variables tree species and trunk circumference (Lange & Bender, 2007).
i-Tree does not recognise some of the tree species from the tree cadastre dataset. Therefore, out of 475,856 trees, only 361,690 are taken over by i-Tree. To reduce the size of this gap, the tree species not recognised by i-Tree were extracted and a tree of the same genus with similar average height and diameter values was chosen as an alternative designation. This heuristic allowed 34,700 additional trees to be recognised when imported in i-Tree.

3 COMPARISON AND RESULTS

3.1 Ecosystem services of the tree species

In total, urban trees in Berlin sequestered 3,916 tonnes of carbon per year. The Littleleaf Linden stands out the most. Table 2 shows the 5 most important tree species of Berlin sorted by total number of trees in relation to carbon sequestration and oxygen production. Additionally, Wych Elm is listed as having the best values in the areas of carbon sequestration and oxygen production.

Table 2: Comparison of ecosystem services of tree species

Tree species	Numb Trees	Carbon bond [t]	per tree	Oxygen [t]	per tree
Littleleaf Linden	56.678	658,79	0,0116	1.756,76	0,0310
Norway Maple	54.422	550,30	0,0101	1.476,47	0,0271
English Oak	28.304	342,31	0,0121	912,82	0,0323
Horse Chestnut	17.381	280,53	0,0161	748,07	0,0430
Bigleaf Linden	17.176	224,22	0,0131	597,93	0,0348
Wych Elm	1.473	31,13	0,0211	83,01	0,0564

The Wych Elm has a small share of 0.4 % of the total tree population in Berlin. If the values of carbon sequestration per tree of the three trees listed first is compared, the low value per tree is striking. Trees that are not so frequently represented sometimes have a higher carbon sequestration.

4. CONCLUSION

In this study, the individual ecosystem services of Berlin's urban trees were examined and evaluated. It was found that the services can only compensate for a small part of the resulting emissions. Nevertheless, qualitative services, such as shade and the associated reduction of the temperature in the city, as well as the beautification of the cityscape and the resulting improvement in the subjective quality of life, speak in favour of optimising and expanding the tree population in Berlin. The type of tree is significantly responsible for the quality of the ecosystem service provided by a tree. Berlin should therefore take tree species and their benefits into account when designing the future tree landscape and the planting of new trees. In addition, the improvement and detailing of the existing data of the Berlin tree cadastre should be fundamental for further investigations. The improved data basis can provide political decision-makers with important information to improve the structure of the tree population and to enable a continuous benefit endowment of urban trees.

REFERENCES

Geoportal Berlin. (2018). *ArcGIS - Baumkataster Berlin*. Available at: https://www.arcgis.com/home/webmap/viewer.html?layers=05c3f9d7dea6422b86e30967811bddd7. Accessed: 15 04 2021

Lange, S., & Bender, R. (2007). Lineare Regression und Korrelation. *Deutsche medizinische Wochenschrift*, p. 9 - 11.

Manes, F., Incerti, G., Salvatori, E., Vitale, M., Ricotta, C., & Costanza, R. (2012). Urban ecosystem services: tree diversity and stability of tropospheric ozone removal. *Ecological Applications*, p. 349–360.

Moser, A., Rötzer, T., Pauleit, S., & Pretzsch, H. (2017). Stadtbäume: Wachstum, Funktionen und Leistungen – Risiken und Forschungsperspektiven. *Allgemeine Forst- und Jagdzeitung*, p. 94-111.

Scholz, T., Ronchi, S., & Hof, A. (2016). Ökosystemdienstleistungen von Stadtbäumen in urban-industriellen Stadtlandschaften – Analyse, Bewertung und Kartierung mit Baumkatastern. *AGIT – Journal für Angewandte Geoinformatik*.

Soares, A. L., Rego, F. C., McPherson, E. G., Simpson, J. R., Peper, P. J., & Xiao, Q. (2011). Benefits and costs of street trees in Lisbon, Portugal. *Urban Forestry & Urban Greening*, p. 69-78.

USDA Forest Service. (2021). *i-Tree Eco User's Manual*. Available at: https://www.itreetools.org/documents/275/EcoV6_UsersManual.2021.04.19.pdf. Accessed: 02 05 2021

Wang, X., Yao, J., Yu, S., Miao, C., Chen, W., & He, X. (2018). Street Trees in a Chinese Forest City: Structure, Benefits and Costs. *Sustainability*.

Sparse Bayesian System Identification for Dynamical Systems with Neuronized Priors

Prem R. Mohan Ram * **Ulrich Römer** ** **Richard Semaan** ***

* *Institut für Dynamik und Schwingungen, Technische Universität Braunschweig, Germany (e-mail: p.mohan-ram@tu-braunschweig.de).*
** *Institut für Dynamik und Schwingungen, Technische Universität Braunschweig, Germany (e-mail: u.roemer@tu-braunschweig.de).*
*** *Institut für Strömungsmechanik, Technische Universität Braunschweig, Germany (e-mail: r.semaan@tu-braunschweig.de).*

Abstract: This work is concerned with learning the dynamics of technical systems from data within a sparse Bayesian framework. The approach employs a basis representation of the unknown dynamics function, similar to the sparse identification of nonlinear dynamics (SINDy) approach, which is combined with a Bayesian procedure for parameter estimation. We propose to use the recently introduced neuronized priors as a unified approach to enforce sparsity in a dynamical systems context, and illustrate the method with an academic example.

Keywords: Uncertainty, dynamic systems, parameter estimation, parameter identification, probabilistic simulation.

1. INTRODUCTION

Learning the dynamics of a system from data is receiving considerable attention at present. Here, we focus on autonomous systems of the form

$$\dot{\mathbf{x}}(t) = \mathbf{f}(\mathbf{x}(t)), \quad \mathbf{x}(0) = \mathbf{x}_0, \tag{1}$$

where $\mathbf{x}(t) \in \mathbb{R}^n$, $\mathbf{f} : \mathbb{R}^n \to \mathbb{R}^n, t \in (0, T]$ and $\dot{\mathbf{x}} = \mathrm{d}\mathbf{x}/\mathrm{d}t$. One particularly popular paradigm, the sparse identification of nonlinear dynamics (SINDy) Brunton et al. (2016a), represents the unkonwn dynamics $\mathbf{f}$ as a linear combination of library basis functions as

$$f_i(\mathbf{x}) \approx \boldsymbol{\Theta}(\mathbf{x})\boldsymbol{\xi}_i, \tag{2}$$

where $\boldsymbol{\xi}_i \in \mathbb{R}^p$, $i = 1, \ldots, n$ are the parameters to be identified and $\boldsymbol{\Theta}$ represents the library of basis functions. For notational convenience, all parameter vectors are collected in a matrix as $\boldsymbol{\Xi} = [\boldsymbol{\xi}_1 \cdots \boldsymbol{\xi}_n]$. Popular choices of basis functions are polynomials or splines, which are able to accurately approximate large classes of functions. In the original paper Brunton et al. (2016a), regression with iterative thresholding was used to estimate the parameters from data of $\dot{\mathbf{x}}(t)$. Since then, extensions in many different directions have been proposed. Control scenarios were addressed in Brunton et al. (2016b), whereas uncertainty was included through a Bayesian extension in Fuentes et al. (2021). Another Bayesian approach, also including noisy observations of the state directly, was introduced in Galioto and Gorodetsky (2020), which contained the original SINDy approach as a special case. Also, there exist deep learning based approaches, such as Goyal and Benner (2021) to learn the model as a black box. In contrast, we aim for a white-box model for which a bases library approach is better suited.

Despite these contributions, several challenges remain. Enforcing sparsity in a Bayesian framework is challenging and may require to work with complicated prior formulations. Also, jointly handling all sources of uncertainty goes beyond the linear regression setting and the computational complexity will grow quickly. Here, we report and extend on our work pre-published in Ram et al. (2021).

2. BAYESIAN SYSTEM IDENTIFICATION

In this section we present our approach to estimate the unknown parameters $\boldsymbol{\Xi}$, while simultaneously accounting for observation, process and model uncertainty. Therefore, we apply a suitable approximation method in time, an explicit Runge Kutta method for the sake of simplicity, which yields

$$\mathbf{x}_{i+1} = \mathbf{x}_i + \Psi_h(\boldsymbol{\Theta}(\mathbf{x}_i)\boldsymbol{\Xi}), \quad \mathbf{x}_0 = \mathbf{x}_0, \tag{3}$$

where $i = 0, \ldots, m-1$, $\mathbf{x}_i \approx \mathbf{x}(t_i)$ and Ψ_h specifies the discrete Runge Kutta time propagator on the time grid with uniform grid size h. Then, we introduce the stochastic state space model

$$\mathbf{x}_{i+1} = \mathbf{x}_i + \Psi_h(\boldsymbol{\Theta}(\mathbf{x}_i)\boldsymbol{\Xi}) + \boldsymbol{\eta}_i, \tag{4}$$

$$\mathbf{y}_j = \mathbf{x}_j + \boldsymbol{\varepsilon}_j, \tag{5}$$

where $j = 1, \ldots, k$ indicates the observation time. Note that the considered example employs the full state, which is why we employ an observation of the full state in (5). However, the method can easily be extended to cover more general state-to-observation maps. Also, the process and observation noise are assumed to be distributed as $\boldsymbol{\eta}_i \sim \mathcal{N}(0, \sigma_\eta^2 \mathbb{I})$ and $\boldsymbol{\varepsilon}_j \sim \mathcal{N}(0, \sigma_\varepsilon^2 \mathbb{I})$, respectively. This setting is close to the one considered in Galioto and Gorodetsky

⋆ The authors acknowledge internal funding by the faculty of mechanical engineering at Technische Universität Braunschweig.

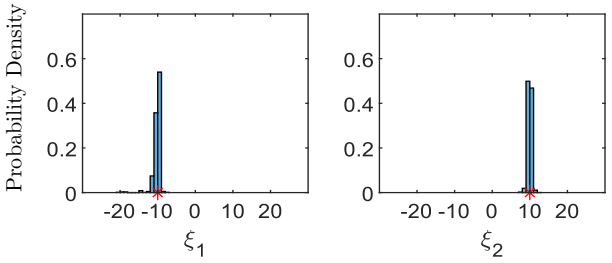

Fig. 1. Posterior histograms of ξ_i and true values (red stars).

(2020), where the joint distribution $p(\boldsymbol{\Xi}, \mathbf{X})$, with $\boldsymbol{X}$ collecting all states $\boldsymbol{x}_i$ into a matrix, was inferred with a Kalman-type filter. Because we are mainly interested in the marginal distribution

$$p(\boldsymbol{\Xi}) = \int p(\boldsymbol{\Xi}, \mathbf{X}) \, \mathrm{d}\mathbf{X}, \tag{6}$$

we pursue a different path and focus on updating the parameters directly. We employ an ensemble of N states, propagated in time according to $p(\mathbf{x}_{i+1}|\mathbf{x}_i)$ and base inference on the average Likelihood

$$\hat{L}(\mathbf{Y}|\boldsymbol{\Xi}) = \frac{1}{N} \sum_{i=1}^{N} \prod_{j=1}^{k} \frac{1}{\sqrt{(2\pi)^k \sigma_\varepsilon^2}} \exp\left(-\frac{|\mathbf{y}_j - \mathbf{x}_j^{(i)}|^2}{2\sigma_\varepsilon^2} \right), \tag{7}$$

which ensures robustness against process noise, see also Conrad et al. (2017). We then update the posterior distribution with Bayes' law as

$$p(\boldsymbol{\Xi}|\mathbf{Y}) \propto \hat{L}(\mathbf{Y}|\boldsymbol{\Xi}) p(\boldsymbol{\Xi}), \tag{8}$$

which we sample with Markov Chain Monte Carlo methods. In addition to employing the average Likelihood, another original contribution is the use of a generalized formulation of sparsity priors given as

$$\xi_i = T(\alpha_i - \alpha_0) w_i, \tag{9}$$

where $w_i \sim \mathcal{N}(0, \tau_w)$, $\alpha_i \sim \mathcal{N}(0, 1)$ and T is an activation function from neural network methods, which motivates the name neuronized prior, see Shin and Liu (2021). Through different choices for T we can recover various priors, such as Lasso, Horseshoe and Spike and Slab priors. The case of spike and slab prior is of particular interest, because it allows to obtain zero inclusion probabilities of individual basis functions in the library and hence, model selection can be carried out as well.

3. NUMERICAL EXAMPLE

Here, we present an application to estimate the coefficients of the first equation of the Lorenz system

$$\begin{aligned} \dot{x}_1 &= c_1(x_2 - x_1), \\ \dot{x}_2 &= 28x_1 - x_1x_3 - x_2, \\ \dot{x}_3 &= x_1x_2 - 2.67x_3. \end{aligned} \tag{10}$$

First, c_1 is set to a value of 10, and data $\boldsymbol{y}_j$ is simulated by propagating the initial state $[x_1^0, x_2^0, x_3^0]^\top = [-8, 8, 27]^\top$ using MATLAB's `ODE23` solver. Observation noise with $\sigma_\varepsilon = 0.01$ is added to generate the data. A total simulation time of 1.5 units, with $h = 10^{-4}$ is considered.

For the above application, a basis library $\Theta = [x_1, \, x_2, \, x_3, \, x_1x_2, \, x_1x_3, \, x_2x_3]$ is employed, and corresponding coefficients $\xi_1, \xi_2, \ldots, \xi_6$ are to be estimated. The standard deviation of the process noise σ_η is calibrated with an empirical Bayes approach, as outlined in Conrad et al. (2017), which leads to $\sigma_\eta = 256$ in the current case.

To obtain the posterior given by (8), an Affine Invariant Ensemble MCMC sampler (AIES) is employed. To facilitate straightforward model selection, the ReLu activation function $T(\alpha_i - \alpha_0) = \max(0, \alpha_i - \alpha_0)$ is chosen. With the help of a grid search, the neuronised prior's hyperparameters α_0 and τ_w are assigned values -0.25 and 0.1, respectively. A burn-in of 50% is considered and 75% of the AIES walkers are discarded as bad chains.

The resulting posterior histograms for the first two coefficients are plotted in Figure 1. It can be seen that the posteriors for both the coefficients are centered around their true values denoted by red stars. Also, the resulting posteriors for the coefficients $\xi_3, \xi_4, \ldots, \xi_6$ yield $P(\xi_i = 0) > 0.5$. Hence, a median model selection would remove those ξ_i for which $P(\xi_i = 0) > 0.5$ and successfully recover the original Lorenz system. The histograms for the coefficients $\xi_3, \xi_4, \ldots, \xi_6$ haven't been presented here as they resemble concentrated spikes at zero, with negligible spread.

We shall investigate the performance of the method with different, more complex, examples in the future.

REFERENCES

Brunton, S.L., Proctor, J.L., and Kutz, J.N. (2016a). Discovering governing equations from data by sparse identification of nonlinear dynamical systems. *Proceedings of the national academy of sciences*, 113(15), 3932–3937.

Brunton, S.L., Proctor, J.L., and Kutz, J.N. (2016b). Sparse identification of nonlinear dynamics with control (sindyc). *IFAC-PapersOnLine*, 49(18), 710–715.

Conrad, P.R., Girolami, M., Särkkä, S., Stuart, A., and Zygalakis, K. (2017). Statistical analysis of differential equations: introducing probability measures on numerical solutions. *Statistics and Computing*, 27(4), 1065–1082.

Fuentes, R., Nayek, R., Gardner, P., Dervilis, N., Rogers, T., Worden, K., and Cross, E. (2021). Equation discovery for nonlinear dynamical systems: A Bayesian viewpoint. *Mechanical Systems and Signal Processing*, 154, 107528.

Galioto, N. and Gorodetsky, A. (2020). Bayesian system id: optimal management of parameter, model, and measurement uncertainty. *Nonlinear Dynamics*, 102, 241–267.

Goyal, P. and Benner, P. (2021). Learning dynamics from noisy measurements using deep learning with a runge-kutta constraint. *arXiv preprint arXiv:2109.11446*.

Ram, P.R.M., Römer, U., and Semaan, R. (2021). Bayesian dynamical system identification with unified sparsity priors and model uncertainty. *arXiv preprint arXiv:2103.05090*.

Shin, M. and Liu, J.S. (2021). Neuronized priors for Bayesian sparse linear regression. *Journal of the American Statistical Association*, 1–43.

Electromechanical modeling of cardiac arrhythmias

Matteo Salvador [*] **Francesco Regazzoni** [*] **Stefano Pagani** [*]
Luca Dede' [*] **Alfio Quarteroni** [*,**]

[*] *MOX - Dipartimento di Matematica, Politecnico di Milano, P.zza Leonardo da Vinci 32, 20133 Milano, Italy.*
[**] *Mathematics Institute, École Polytechnique Fédérale de Lausanne, Av. Piccard, CH-1015 Lausanne, Switzerland (Professor Emeritus).*

1. INTRODUCTION

Cardiac arrhythmias arise from an abnormality in the rhythm of the human heart. Among them, ventricular tachycardia (VT), which manifests with a fast heart rate, is one of the most life threatening rhythm disorders. VT may be classified as hemodynamically stable or unstable, depending on the capability of the heart to effectively pump blood in the circulatory system. In the former case antiarrhythmic drugs are generally employed, while in the latter case cardioversion is needed. According to the specific pathogenesis, the stability of the VT remains the same or changes over time. Moreover, it may also degenerate towards ventricular fibrillation (VF), a life-threatening condition in which the ventricular activity is fully disorganized and chaotic, leading to heart failure.

In the clinical framework, these pathological scenarios can be hardly ever fully investigated and predicted for all patients. For this reason, biophysically detailed computational heart models could be used to provide a deeper understanding of the hemodynamic response to VT and to characterize the electromechanical substrate leading to dangerous arrhythmias.

Electrophysiological simulations are well-established for scar-related VT identification and treatment on human ventricles (Arevalo et al. (2016); Prakosa et al. (2018)). On the contrary, patient-specific electromechanical models coupled with closed-loop cardiovascular circulation have been just recently used to enhance our knowledge on VT (Salvador et al. (2021)). Indeed, the physiological processes that couple mechanical and electrical activity of the human heart, known as mechano-electric feedbacks (MEFs), are relevant and not fully elucidated (Kohl et al. (2013); Colli Franzone et al. (2017); Keldermann et al. (2010)). Moreover, the identification of the hemodynamic nature of the VT has significant clinical implications.

In this study we analyze the impact of different modeling choices for the left ventricle (LV) myocardial deformation and the recruitment of nonselective stretch-activated channels (SACs) by combining electrophysiology, mechanics and hemodynamics in several numerical simulations. Furthermore, we also show that our computational model reproduces both hemodynamically stable and hemodynamically unstable VT.

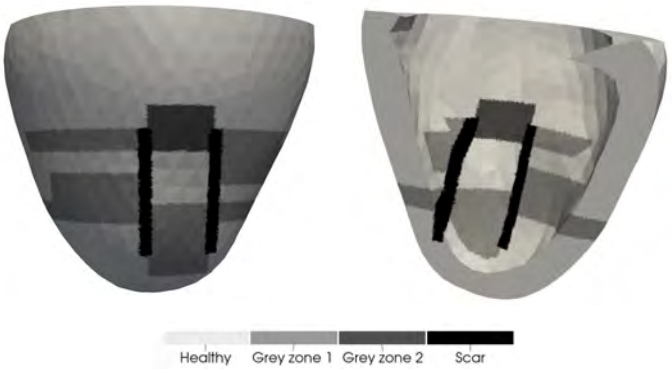

Fig. 1. Zygote LV with an idealized distribution of scars, grey zones and non-remodeled regions over the myocardium.

2. MATHEMATICAL MODELS AND METHODS

We consider the LV processed from the Zygote 3D heart model endowed with a fiber architecture generated by means of the Bayer-Blake-Plank-Trayanova algorithm and an idealized distribution of ischemic regions (Fig. 1). For cardiac electrophysiology, we employ the monodomain equation coupled with the ten Tusscher-Panfilov ionic model. In particular, we consider the monodomain equation with several degrees of complexity in MEFs mathematical modeling to assess similarities and differences in the outcomes of the numerical simulations during VT. We use a biophysically detailed and anatomically accurate active stress model to describe the active force generation mechanisms. The passive mechanical behavior of the myocardium is modeled through the Guccione constitutive law. We consider the interaction with the pericardium by means of spring-damper boundary conditions at the epicardium of the LV, while we prescribe energy-consistent boundary conditions at the base of the LV to model the interaction with the part of the heart beyond the artificial ventricular base. Regarding blood circulation, we rely on a 0D closed-loop model, consisting of a compartmental description of the cardiac chambers, systemic and pulmonary, arterial and venous circulatory networks, based on an electrical analogy. The different compartments are modeled as RLC (resistance, inductance, capacitance) circuits, while cardiac valves are described as diodes (Regazzoni et al. (2022)).

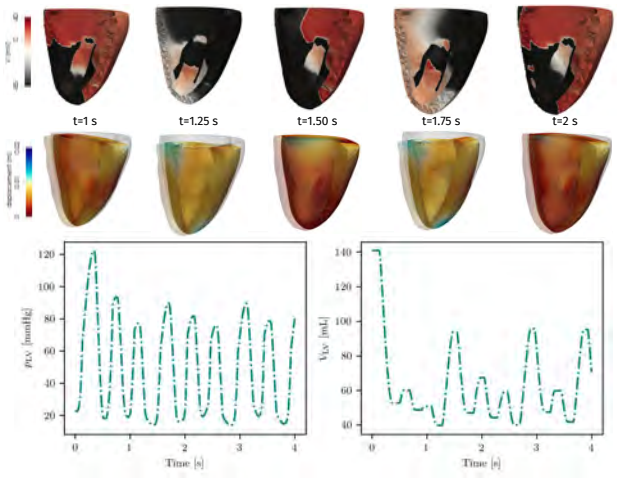

Fig. 2. Coupled effects of electrophysiology, mechanics and hemodynamics for a numerical simulation with geometric MEFs and SACs. The extra stimuli in the upper right part of the LV, which is driven by SACs, activate the LV electrophysiologically and mechanically. This has a direct impact on both pressure and volume transients, which in turn have an effect on the electromechanical behavior of the LV.

We adopt a segregated-intergrid-staggered scheme to numerically discretize this 3D-0D coupled problem (Regazzoni et al. (2022)). Indeed, the core models are solved sequentially by employing different space and time resolutions according to the specific requirements of electrophysiology, activation and mechanics.

3. DISCUSSION

We studied the effects of geometric and physiological MEFs on a realistic LV geometry endowed with an idealized distribution of infarct and peri-infarct zones. We performed numerical simulations of cardiac electromechanics coupled with closed-loop cardiovascular circulation under VT (Fig. 2).

First, we saw that if a VT is triggered by a certain stimulation protocol and by neglecting all MEFs, the very same pacing protocol induces a VT for all possible combinations of MEFs that we considered. Moreover, our electromechanical framework allows for the hemodynamic classification of the VT, which can be either stable or unstable, and permits to capture mechanically relevant indications under VT, such as the incomplete relaxation of sarcomeres.

With respect to electrophysiological simulations, we observed several differences on the morphology of the VT by combining electrophysiology, activation, mechanics and hemodynamics. In particular, geometric MEFs do not affect wave stability and may alter the VT basis cycle length, along with its exit site. On the other hand, the recruitment of SACs may generate extra stimuli, which may change wave stability. These extra stimuli are driven by myocardial contraction and are induced by changes in the action potential duration or its resting value. We conclude that both geometric and physiological MEFs define important contributions in electromechanical models, especially when numerical simulations under arrhythmia are carried out.

ACKNOWLEDGEMENTS

This project has received funding from the European Research Council (ERC) under the European Union's Horizon 2020 research and innovation programme (grant agreement No 740132, iHEART - An Integrated Heart Model for the simulation of the cardiac function, P.I. Prof. A. Quarteroni).

REFERENCES

Arevalo, H., Vadakkumpadan, F., Guallar, E., and et al. (2016). Arrhythmia risk stratification of patients after myocardial infarction using personalized heart models. *Nature Communications*, 7, 113–128.

Colli Franzone, P., Pavarino, L.F., and Scacchi, S. (2017). Effects of mechanical feedback on the stability of cardiac scroll waves: A bidomain electro-mechanical simulation study. *Chaos*, 27, 093905.

Keldermann, R.H., Nash, M.P., Gelderblom, H., and et al. (2010). Electromechanical wavebreak in a model of the human left ventricle. *American Journal of Physiology-Heart and Circulatory Physiology*, 299(1), H134–H143.

Kohl, P., Sachs, F., and Franz, M.R. (2013). *Cardiac Mechano-Electric Coupling and Arrhythmias*. Oxford University Press.

Prakosa, A., Arevalo, H., Dongdong, D., and et al. (2018). Personalized virtual-heart technology for guiding the ablation of infarct-related ventricular tachycardia. *Nature Biomedical Engineering*, 2, 732–740.

Regazzoni, F., Salvador, M., Africa, P., and et al. (2022). A cardiac electromechanical model coupled with a lumped-parameter model for closed-loop blood circulation. *Journal of Computational Physics*, 457, 111083.

Salvador, M., Fedele, M., Africa, P.C., and et al. (2021). Electromechanical modeling of human ventricles with ischemic cardiomyopathy: numerical simulations in sinus rhythm and under arrhythmia. *Computers in Biology and Medicine*, 136, 104674.

Impact of Bony Geometry on Static Optimization Based Estimations of Muscle Activations and Forces

Hans Kainz* Willi Koller* Paul Kaufmann* Fabian Unglaube Andreas Kranzl** Arnold Baca***

**Centre for Sport Science and University Sports, Department of Biomechanics, Kinesiology and Computer Science in Sport, University of Vienna, Vienna, Austria.*
*** Laboratory of Gait and Movement Analysis, Orthopedic Hospital Vienna-Speising, Vienna, Austria*

1. INTRODUCTION

Musculoskeletal simulations are widely used to increase our insight in healthy and pathological movements (Kainz *et al.*, 2019; Buehler *et al.*, 2021). Typically, a generic musculoskeletal model is scaled to a participant and afterwards employed to calculate joint angles and estimate musculoskeletal loadings (Delp *et al.*, 2007). This approach, however, neglects subject-specific musculoskeletal geometry (Kainz, Wesseling and Jonkers, 2021).

At the femur the neck-shaft angle (NSA) and femoral anteversion angle (AVA) are the most important anatomical features (Bobroff *et al.*, 1999). Recently, two bone-deformation tools have been developed which enable to modify the anatomical features of the femur (Modenese, Barzan and Carty, 2021; Veerkamp *et al.*, 2021). Modifying the NSA and AVA affect hip joint contact forces (Kainz *et al.*, 2020). Furthermore, personalizing the AVA has been shown to increase the accuracy of hip joint contact force calculations (Modenese, Barzan and Carty, 2021).

The impact of personalized femoral geometry on muscle activations and forces has not been assessed yet and therefore was the aim of the current study. We hypothesized that modifying the femoral geometry will alter muscle activations and forces. Furthermore, we assumed that a personalized femoral geometry would improve the agreement between the muscle activations obtained from the simulations and the experimentally measured electromyography (EMG) signals.

2. METHODS

We collected and analysed data of one typically developing boy (age: 8 years; height: 137 cm; weight: 40 kg). Three-dimensional motion capture data (10 cameras, Vicon Motion Systems, Oxford, UK and three force plates, Kistler Instruments AG, Switzerland) and EMG data of lower limb muscles (16-channel, menios GmbH, Ratingen, Germany) were collected during one static trial and several walking trials. Additionally, we collected magnetic resonance images (Siemens, Magnetom Sola, 1,5T) of both femurs using a T1-weighted 3D gradient echo sequence with a resolution of 0.7 x 0.7 x 0.7 mm.

Magnetic resonance images (MRI) of each femur were segmented using 3D Slicer (slicer.org) and used to calculate the subject-specific NSA and AVA based on a previously developed Matlab script (Kainz *et al.*, 2020).

For the musculoskeletal simulations, we first used the torsion tool (Veerkamp *et al.*, 2021) to create the following nine models:

- Ref: Model based on the NSA and AVA obtained from the MRI images
- NSA-20,-10,+10,+20: Ref models with altered NSA from -20 to +20 degrees
- AVA-20,-10,+10,+20: Ref models with altered AVA from -20 to +20 degrees

Afterwards, we scaled each model to the anthropometry of our participant based on the location of surface markers and estimated joint centres (Kainz *et al.*, 2017).

Joint kinematics, joint kinetics, muscle activations, muscle forces and joint contact forces were calculated for each model using OpenSim 4.1 (Delp *et al.*, 2007). Muscle activations and forces were estimated using static optimization, while minimizing the sum of squared muscle activations.

We compared muscle activations and forces of the gastrocnemius medialis, soleus, rectus femoris and gluteus medius muscles between the different models. Furthermore, we compared the EMG data with the activations from the simulations and quantified how much hip, knee and ankle joint contact forces differ between models.

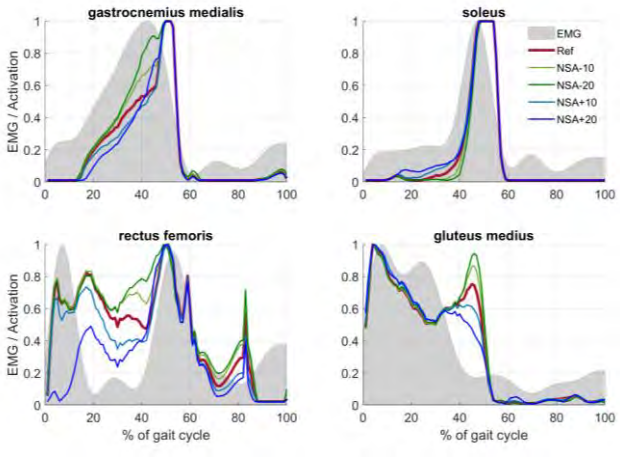

Fig. 1. EMG data and muscle activations from models with altered NSA.

3. RESULTS

Altering the NSA and AVA had an impact on the activations and forces of all our analysed muscles (Fig. 1 and 2). Activations from our simulations showed a reasonable agreement with the EMG data (Fig. 1). Both, altering the NSA and AVA had a big impact on hip and knee joint contact forces and a minor impact on ankle joint contact forces (Fig. 3). The AVA had a larger impact on joint contact forces compared to the NSA. Due to the page limit, only figures for the altered NSA are shown in this abstract.

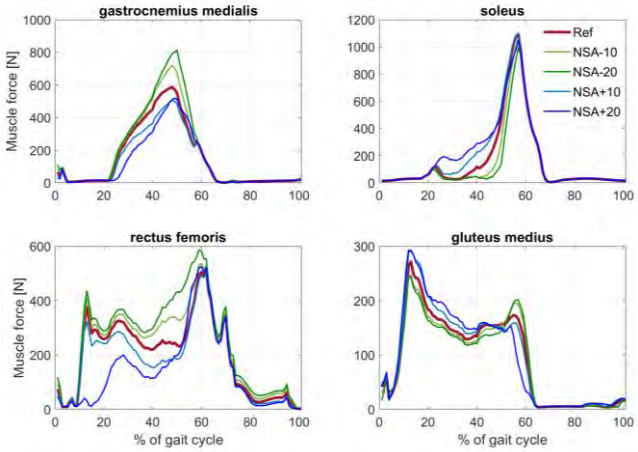

Fig. 2. Muscle forces from models with altered NSA.

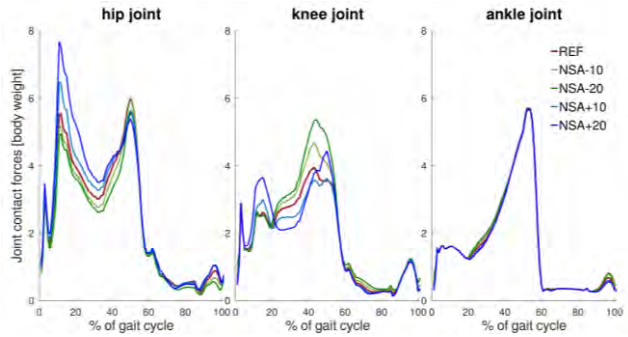

Fig. 3. Joint contact forces from models with altered NSA.

4. DISCUSSION

In agreement with our hypothesis, we showed that altering the femoral geometry affects muscle activations and forces from all analysed muscles. Although modifying the NSA and AVA did not change the moment arms of the gastrocnemius and soleus muscles, it had an impact on these muscles due to the global optimization used to estimate muscle forces. This also explains why altering the femoral geometry influences the knee and ankle joint contact forces, additionally to the hip joint contact forces.

We assumed that the personalized geometry will improve the agreement between EMG and muscle activation from the simulations. From our primary results based on one participant (Fig. 1), we cannot confirm this assumption. Several factors influence the estimation of muscle forces additionally to the bony geometry. Our models included generic muscle properties (e.g. maximum isometric muscle forces), which might not present the muscles of our participant and influences our results (Kainz *et al.*, 2018). Furthermore, different optimization approaches will likely lead to a different distribution of muscle forces (Wesseling *et al.*, 2015).

In conclusion, this is the first study, which showed that the femoral geometry affects muscle and joint contact forces at all joints. More comprehensive studies are needed to evaluate if the personalized femoral geometry can improve the accuracy of muscle force calculations in musculoskeletal simulations.

REFERENCES

Bobroff, E. D. *et al.* (1999) 'Femoral anteversion and neck-shaft angle in children with cerebral palsy.', *Clinical orthopaedics and related research*, (364), pp. 194–204.

Buehler, C. *et al.* (2021) 'Quantifying Muscle Forces and Joint Loading During Hip Exercises Performed With and Without an Elastic Resistance Band', *Frontiers in Sports and Active Living*, 0, p. 223.

Delp, S. L. *et al.* (2007) 'OpenSim: Open-Source Software to Create and Analyze Dynamic Simulations of Movement', *IEEE Transactions on Biomedical Engineering*, 54(11), pp. 1940–1950.

Kainz, H. *et al.* (2017) 'Accuracy and Reliability of Marker Based Approaches to Scale the Pelvis, Thigh and Shank Segments in Musculoskeletal Models', *Journal of Applied Biomechanics*, pp. 1–21.

Kainz, H. *et al.* (2018) 'The influence of maximum isometric muscle force scaling on estimated muscle forces from musculoskeletal models of children with cerebral palsy', *Gait & Posture*, 65, pp. 213–220.

Kainz, H. *et al.* (2019) 'Selective dorsal rhizotomy improves muscle forces during walking in children with spastic cerebral palsy.', *Clinical biomechanics (Bristol, Avon)*, 65, pp. 26–33.

Kainz, H. *et al.* (2020) 'A multi-scale modelling framework combining musculoskeletal rigid-body simulations with adaptive finite element analyses, to evaluate the impact of femoral geometry on hip joint contact forces and femoral bone growth', *PloS one*, 15(7), p. e0235966.

Kainz, H., Wesseling, M. and Jonkers, I. (2021) 'Generic scaled versus subject-specific models for the calculation of musculoskeletal loading in cerebral palsy gait: Effect of personalized musculoskeletal geometry outweighs the effect of personalized neural control', *Clinical Biomechanics*, 87, p. 105402.

Modenese, L., Barzan, M. and Carty, C. P. (2021) 'Dependency of lower limb joint reaction forces on femoral version', *Gait & Posture*, 88, pp. 318–321.

Veerkamp, K. *et al.* (2021) 'Torsion Tool: An automated tool for personalising femoral and tibial geometries in OpenSim musculoskeletal models', *Journal of Biomechanics*, 125, p. 110589.

Wesseling, M. *et al.* (2015) 'Muscle optimization techniques impact the magnitude of calculated hip joint contact forces', *Journal of Orthopaedic Research*, 33(3), pp. 430–438.

Calibration of a green roof hydrological model using global sensitivity analysis

A. Hégo * **F. Collin** * **H. Garnier** * **R. Claverie** **

* *Université de Lorraine, CNRS, CRAN, F-54000, Nancy, France (axelle.hego, floriane.collin, hugues.garnier@univ-lorraine.fr)*
** *Cerema Est, Team research group, F-54510, Tomblaine, France (remy.claverie@cerema.fr)*

Abstract:
Green roofs are a sustainable solution to manage water runoff from rain events in urban areas. Modeling hydrological phenomena of green roofs over long period is challenging because of the difficulties to both characterize the soil parameters and to take into account the dynamics of the vegetation and the meteorological variables. The water retention capacity is represented by the Van Genuchten - Mualem model implemented in Hydrus-1D©. For the calibration of the model, global sensitivity analysis is exploited to quantify the effects of parameter uncertainties on the water retention capacity. The results of this study highlight the most influential parameters on the water retention capacity and lead to an efficient reduction of the parameter uncertainties.

Keywords: Calibration, global sensitivity analysis, green roof, Van Genuchten - Mualem model

1. INTRODUCTION

In the last decade, soil imperviousness has been one of the main urban issues in the Northeast of France. In case of strong rain events, runoff can lead to the discharge of high volume of water and can cause water system saturation. Among all urban-water regulation systems, Green Roofs (GR) can be used to store and delay the release of rainwater to sewers [Li and Badcock Jr (2014)]. GR are also considered as a sustainable solution that offers benefits such as building insulation, urban heat island cooling during summer and air pollution control.

2. GREEN ROOF HYDROLOGICAL MODELLING

The hydrological performances of GR are directly linked to the outflow of a GR which is mainly related to the water content inside the layers. In order to investigate these performances, the water content needs to be measured and simulated.
Real data have been collected on an in-situ experimental GR installed in Tomblaine, North-East of France. A period of one year has been chosen from January to December 2020 which represents different hydrological phenomena shown in black in Figure 2.
Few models exist to describe the hydrological behavior of soil and can be adapted for GR characteristics such as soil parameters of the different layers, dimension, type of vegetation, etc. In this study, the dynamic of the water content is described by two elements. The first element describes the hydrological infiltration throughout unsaturated porous media and depends on soil parameters. The second element represents the water extracted from the soil due to the vegetation and the weather conditions.
All these models and equations are implemented in Hydrus-1D© software to simulate hydrological behavior [Simunek et al. (2008)]. This software allows the set up of the GR structure, boundary conditions, meteorological data, soil and vegetation parameters in order to reproduce the GR real configuration and can be used as a gray box model with:

- 1 input: rainfall;
- 1 output: Volumetric Water Content VWC;
- 6 soil parameters: θ_s, θ_r, n, K_s, α and l;
- 5 meteorological variables;
- 4 vegetation parameters: crop height $CropH$, leaf index area LAI, $Albedo$ and root depth $RootD$.

The aim of this study is to improve the calibration of this model to get closer to the behavior of the real GR. The challenge is that some of the model parameters, such as the soil or vegetation parameters, are complex to determine as they are difficult to measure accurately through experiments. All the parameter uncertainties are propagated through the simulation of water content and can be analysed to help the calibration. Methods of Global Sensitivity Analysis (GSA) can be applied to quantify the parameter uncertainty impact on the model output. These methods are described in [Hégo et al. (2021)] and will not be detailed here.
In this study, the effects of vegetation and soil parameters are simultaneously analysed in order to provide information to calibrate this new configuration of the GR model. The uncertainties of the parameters θ_s, α, n, $CropH$, LAI and $RootD$ will be analysed. The other parameters are not considered uncertain.

3. MODEL CALIBRATION

Global sensitivity analysis allows to quantify parameter influence on the output model. The least influential parameters are set to their nominal values. This allows to reduce

the number of parameters to estimate. The study can then be focused on the most influential parameters. The idea is to iteratively reduce the initial interval of variations of the most influential parameters, in order to converge to the optimal value. For this purpose, the normalized root mean square deviation between the simulated and measured output is used as objective function to minimize.

The proposed calibration approach can be summarized with these steps:

1. Application of GSA with a large uncertainty interval defined by domain experts;
2. Computation of the error between measured data and the simulated model output generated during the GSA;
3. Reduction of the interval according GSA results and error analysis;
4. Exploration of parameter combinations to find the optimal one.

GSA approach allows to obtain sensitivity index dynamics over time and to point out influence evolution. First-order S_i and total sensitivity S_{T_i} indices are represented at the top of Figure 1. S_i represents the influence of only one parameter and S_{T_i} represents the influence of a parameter and all its interaction. It is worth noting that first-order and total indices are not equal for the parameters α, n and LAI. Higher-order indices are non-zero that means there is influence of interaction between parameters. Sensitivity indices of these three parameter interactions (second-order $S_{i,q}$) are represented at the bottom of Figure 1.

To calibrate the influential parameters α, n and LAI, an objective function is defined. The normalized root mean square deviation ($nRMSD$) is defined as the quality criteria.

$$nRMSD = \frac{\sqrt{\left(\sum_{t=1}^{T}(y_{sim}(t) - y_{obs}(t))^2\right)/T}}{y_{obs}^{max} - y_{obs}^{min}}$$

where y_{sim} and y_{obs} denote respectively the simulated and observed output and $t = 1, ..., T$.
The objective is to find the parameter combinations which minimize $nRMSD$ during periods of interest. These periods of interest are defined following sensitivity index dynamics and correspond to wet period (e.g. 0 to 2000 h), drying period (e.g. 3560 to 4045 h) and when it rains during drying periods (e.g. 2800 h). The $nRMSD$ is computed for each period and each model evaluation (generated for GSA). The optimal parameter combination is presented in red on Figure 2. The absolute error between the simulated and measured VWC is plotted at the bottom of the figure.

4. DISCUSSIONS AND PERSPECTIVES

In this paper, a calibration approach based on GSA is applied to a GR model in order to reproduce a real configuration. GSA highlights the influence of the parameter uncertainties over time on the model output (Figure 1). The uncertainty interval of the model parameter have been reduced and nominal values have been proposed to reproduce the specific green roof configuration. The simulated data for nominal values are close to the observed data, however some errors are persistent (Figure 2). These differences can be caused by several reasons. For instance, the

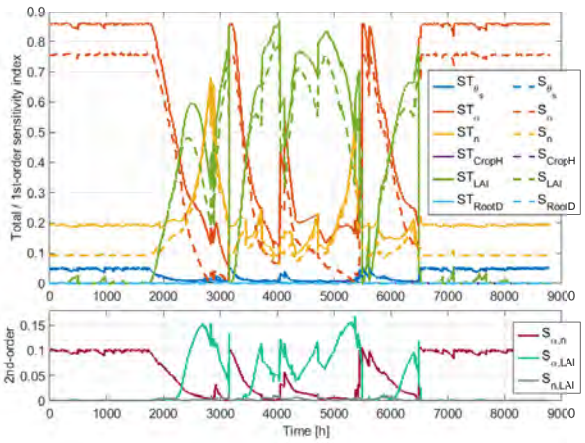

Fig. 1. Sensitivity indices applied to quantify parameter effects on VWC. At the top, total index with solid line and first-order index with dashed line and at the bottom, second-order index.

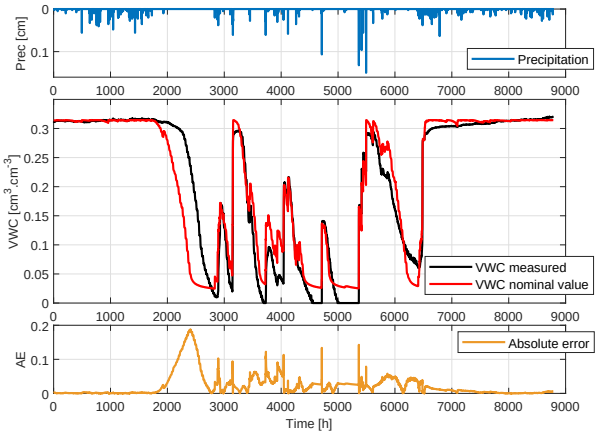

Fig. 2. Comparison of the simulated (red) and measured (black) VWC, absolute error (orange) between the simulated and measured VWC and rainfall (blue).

assumption of constant vegetation parameters could have impacted the simulated soil drying. The time-variations of vegetation parameters can be investigated but raise difficulties for sample generation. Moreover, these differences can also highlight the limits of the models and Hydrus-1D©. All green roof phenomena may not be exactly reproducible by simulation.

REFERENCES

Hégo, A., Collin, F., Garnier, H., and Claverie, R. (2021). Approaches for green roof dynamic model analysis using gsa. *IFAC-PapersOnLine*, 54(7), 613–618.

Li, Y. and Badcock Jr, R. (2014). Green roof hydrologic performance and modeling: a review. *Water Science & Technology*, 69(4), 727–738.

Simunek, J., Sejna, M., Saito, H., Sakai, M., and van Genuchten., M. (2008). *The HYDRUS-1D software package for simulating one-dimensional movement of water, heat, and multiple solutes in variably saturated media.* Department of Environmental Sciences University of California Riverside, Riverside, California.

Uncertainty Quantification for Molecular Models via Stochastic Gradient MCMC

Stephan Thaler *§, **Julija Zavadlav** * † ‡

* *Professorship of Multiscale Modeling of Fluid Materials, TUM School of Engineering and Design, Technical University of Munich, Germany*
† *Munich Data Science Institute, Technical University of Munich, Germany*
§ *e-mail: stephan.thaler@tum.de*
‡ *e-mail: julija.zavadlav@tum.de*

Abstract: The quality of molecular dynamics (MD) simulations critically depends on the employed potential energy model. Accurate uncertainty quantification (UQ) of these models could increase trust in MD simulation predictions and promote progress in the field of active learning of neural network (NN) potentials. Bayesian methods promise reliable uncertainty estimates, but the high computational cost of training via classical Markov Chain Monte Carlo (MCMC) schemes has prevented their application to deep NN potentials. In this work, we propose stochastic gradient MCMC methods as a computationally efficient option for Bayesian UQ of MD potentials. The stochastic gradient Langevin dynamics method yields promising results for a tabulated coarse-grained water model and could thus be a feasible approach for NN potentials. Additionally, we illustrate the inherent limit of Bayesian UQ imposed by the functional form of the employed model.

Keywords: Bayesian inference, Uncertainty Quantification, Molecular dynamics

1. INTRODUCTION

Molecular dynamics (MD) simulations are the computational backbone of fields such as soft-matter physics and material science. The quality of MD simulations critically depends on the employed potential energy model defining particle interactions. Potentials are parametrized to match data from experiments (Thaler and Zavadlav (2021)) or high fidelity simulations. Given that experimental data and high fidelity simulations are expensive and only sparsely available, potentials are regularly applied outside the training domain. Hence, uncertainty quantification (UQ) of MD simulations is important to assess the trustworthiness of predictions (Zavadlav et al. (2019)).
An intriguing application of UQ in MD is active learning (Zhang et al. (2019)) of neural network (NN) potentials (Behler and Parrinello (2007)) from density functional theory (DFT) data. Active learning promises to minimize the number of expensive DFT simulations by quantifying the uncertainty of input states and iteratively augmenting the training data set only with states for which the NN potential is most uncertain. However, the efficiency of active learning hinges on the quality of UQ estimates. The common approach to UQ using NN ensembles (Hansen and Salamon (1990)) was found to be only marginally more informative than random selection of states (Kahle and Zipoli (2021)). While Bayesian NNs appear to yield more reliable uncertainty estimates, the high computational training cost of classical Markov Chain Monte Carlo (MCMC) schemes have prevented the application to real-world problems so far (Kahle and Zipoli (2021)).
In this work, we propose stochastic gradient MCMC methods (SG-MCMC) as a computationally efficient option for Bayesian UQ of MD potentials. Results for a tabulated coarse-grained (CG) model of water showcase reasonable uncertainty predictions.

2. METHODS

Bayesian UQ is centered around Bayes' theorem. The aim is to compute the posterior distribution $p(\boldsymbol{\theta}|\mathcal{D},\mathcal{M})$ of model parameters $\boldsymbol{\theta}$ for a given data set $\mathcal{D}$ and model $\mathcal{M}$. MCMC is the gold-standard for approximating the posterior, which requires at least one evaluation of the likelihood $p(\mathcal{D}|\boldsymbol{\theta},\mathcal{M})$ and the prior $p(\boldsymbol{\theta}|\mathcal{M})$ for each update of $\boldsymbol{\theta}$. As computing the likelihood requires evaluation of the model for each data point in $\mathcal{D}$, training on large data sets with expensive models (e.g. NN potentials) quickly becomes infeasible. By contrast, SG-MCMC schemes evaluate the likelihood $p(\boldsymbol{\theta}|\tilde{\mathcal{D}},\mathcal{M})$ (and its gradient) only on a mini-batch $\tilde{\mathcal{D}} \subset \mathcal{D}$, allowing many updates of $\boldsymbol{\theta}$ per pass over $\mathcal{D}$ - analogous to stochastic gradient descent in maximum likelihood estimation. In the simplest case of the stochastic gradient Langevin dynamics method (Welling and Teh (2011)), learning rates λ_n at step n are required to converge to 0 such that generated samples of $\boldsymbol{\theta}$ are asymptotically unbiased, e.g. via a polynomial step size decay $\lambda_n = a(n+1)^{-\gamma}$, with decay rate γ and initial learning rate a . Hence, the increased computational efficiency comes at the cost of generating a biased estimate of $p(\boldsymbol{\theta}|\mathcal{D},\mathcal{M})$ for a finite number of update steps.
To assess the quality of uncertainty estimates from SG-MCMC schemes, we learn a single-site CG water model parametrized by the control points of a cubic spline via

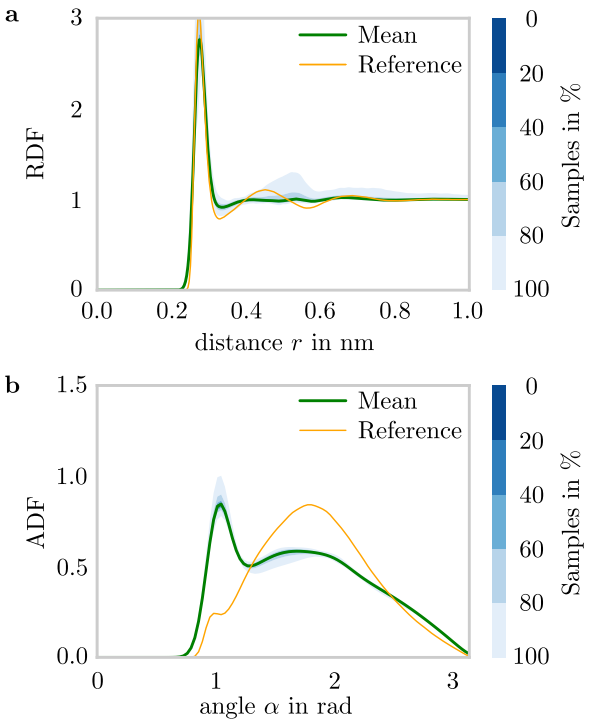

Fig. 1. Mean and credible interval of the predicted radial (RDF, **a**) and angular distribution function (ADF, **b**), together with the atomistic ground truth.

force-matching (Noid et al. (2008)). The ground-truth data consisting of 10^5 de-correlated states are obtained from a simulation of 905 water molecules in a cubic box of side length 3 nm with the atomistic SPC/FW (Wu et al. (2006)) water model at a temperature $T = 300$ K. We choose a uniform prior and assume a Gaussian likelihood with identity covariance matrix, where the variance σ^2 is treated as a learnable model parameter. The spline control points are initialized to the corresponding values of the potential of mean force (Reith et al. (2003)) and σ to 200 kJ / (mol nm). We approximate the posterior distribution via the stochastic gradient Langevin dynamics method (Welling and Teh (2011)) with the polynomial learning rate schedule ($a = 10^{-8}$, $\gamma = 0.33$). We train for 5 epochs with a mini-batch size of 5 and generate 1000 MCMC samples after the learning rate is reduced below $\alpha = 6 \cdot 10^{-10}$.

3. RESULTS

We evaluate the quality of the learned potential based on predicted observables by reference to the atomistic ground-truth. The mean predicted radial distribution function (RDF) deviates from the atomistic reference (Fig. 1 **a**), which is in line with tabulated 2-body potentials parametrized via maximum likelihood estimation (Scherer and Andrienko (2018)). The deviation results from the fact that the 2-body tabulated potential is a weak approximation to the distinct 3-body properties of water (Scherer and Andrienko (2018)). Importantly, the credible interval contains most of the ground truth RDF such that the extent of the deviation can be anticipated by practitioners. By contrast, the mean predicted angular distribution function (ADF) fails to reproduce the atomistic reference, but the narrow credible interval suggests high confidence in the incorrect prediction (Fig. 1 **b**).

Note that this UQ failure is not caused by a sub-optimal approximation of the true $p(\boldsymbol{\theta}|\mathcal{D}, \mathcal{M})$ from the SG-MCMC scheme, but rather stems from the (implicit) conditioning of Bayes' theorem on the model $\mathcal{M}$: By definition, $p(\boldsymbol{\theta}|\mathcal{D}, \mathcal{M})$ describes the posterior probability of all possible parameters $\boldsymbol{\theta}$ of $\mathcal{M}$. Effects that cannot be captured by any $\boldsymbol{\theta}$ cannot be represented in the uncertainty prediction. In this particular example, the ADF is predominantly determined by 3-body forces which cannot be represented by $\boldsymbol{\theta}$ in a 2-body potential. Hence, interpretation of results from Bayesian UQ critically depends on the employed $\mathcal{M}$.

4. CONCLUSION

Our results suggest that SG-MCMC methods could promote the application of UQ in MD simulations by reducing the computational burden of full-batch MCMC methods. However, further studies including investigation of the merits of more advanced SG-MCMC schemes, the number of necessary MCMC samples for reliable UQ results, as well as applying Bayesian UQ to highly expressive models such as NN potentials are required before obtained uncertainty estimates can be trusted in practice.

ACKNOWLEDGEMENTS

We thank Paul Fuchs for providing Fig. 1.

REFERENCES

Behler, J. and Parrinello, M. (2007). Generalized neural-network representation of high-dimensional potential-energy surfaces. *PRL*, 98(14), 146401.

Hansen, L.K. and Salamon, P. (1990). Neural network ensembles. *IEEE PAMI*, 12(10), 993–1001.

Kahle, L. and Zipoli, F. (2021). On the quality of uncertainty estimates from neural network potential ensembles. URL `arXiv:2108.05748`.

Noid, W., Chu, J.W., Ayton, G.S., Krishna, V., Izvekov, S., Voth, G.A., Das, A., and Andersen, H.C. (2008). The multiscale coarse-graining method. I. A rigorous bridge between atomistic and coarse-grained models. *J. Chem. Phys.*, 128(24), 244114.

Reith, D., Pütz, M., and Müller-Plathe, F. (2003). Deriving effective mesoscale potentials from atomistic simulations. *J. Comput. Chem.*, 24(13), 1624–1636.

Scherer, C. and Andrienko, D. (2018). Understanding three-body contributions to coarse-grained force fields. *Phys. Chem. Chem. Phys.*, 20(34), 22387–22394.

Thaler, S. and Zavadlav, J. (2021). Learning neural network potentials from experimental data via differentiable trajectory reweighting. *Nat. Commun.*, 12, 6884.

Welling, M. and Teh, Y.W. (2011). Bayesian learning via stochastic gradient langevin dynamics. In *ICML'11*.

Wu, Y., Tepper, H.L., and Voth, G.A. (2006). Flexible simple point-charge water model with improved liquid-state properties. *J. Chem. Phys.*, 124(2), 024503.

Zavadlav, J., Arampatzis, G., and Koumoutsakos, P. (2019). Bayesian selection for coarse-grained models of liquid water. *Sci. Rep.*, 9(1), 99.

Zhang, L., Lin, D.Y., Wang, H., Car, R., and Weinan, E. (2019). Active learning of uniformly accurate interatomic potentials for materials simulation. *Phys. Rev. Mater.*, 3(2), 023804.

Extended Abstract: Damage Modeling for the Tree-Like Network with Fractional-Order Calculus ⋆

Xiangyu Ni, Bill Goodwine *

* *Department of Aerospace and Mechanical Engineering, University of Notre Dame, IN 46556 USA (e-mail: bill@controls.ame.nd.edu)*

Keywords: Fractional differential equations, mathematical modeling, large scale systems.

Introduction: This paper shows that a tree-like network with damage can be modeled as the product of a fractional-order (FO) nominal plant and a FO multiplicative disturbance, which is well structured and completely characterized by the damage amount at each damaged component. Such way of modeling brings insight about that damaged network's behavior and helps us design robust controllers under uncertain damages and identify the damage.

We study the network in Fig. 1, motivated by a viscoelastic model from Heymans and Bauwens (1994) and also studied in Goodwine (2014); Leyden (2018); Mayes (2012). Considering only integer-order calculus, that system can only be modeled by an infinite continued fraction. Existing literature, *e.g.*, Goodwine (2014), shows that, if FO calculus is allowed, then the undamaged version of that system is exactly half order which has a concise representation. This paper shows that for such a damaged network, its transfer function can still be written in a structured way.

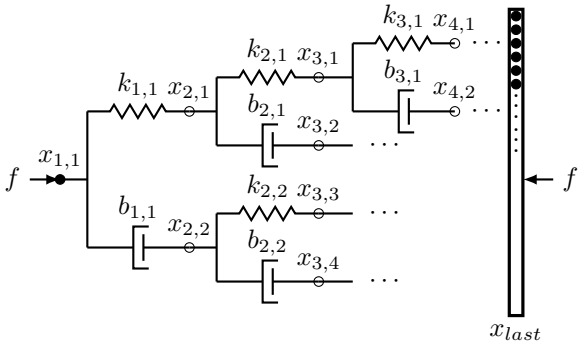

Fig. 1. The tree model.

It can be shown that the transfer function $\widetilde{G}(s)$ from the input force, f, to the distance between $x_{1,1}$ and x_{last} of such model satisfies the recurrence formula given by

$$\widetilde{G}(s) = \frac{1}{\dfrac{1}{\dfrac{1}{\widetilde{k}} + \widetilde{G}_U(s)} + \dfrac{1}{\dfrac{1}{\widetilde{b}s} + \widetilde{G}_L(s)}}. \tag{1}$$

Moving one generation deeper, the transfer function from the input force to the distance between $x_{2,1}$ and x_{last} is $\widetilde{G}_U(s)$; similarly, $\widetilde{G}_L(s)$ is that between $x_{2,2}$ and x_{last}. The spring constant connecting $x_{1,1}$ to $x_{2,1}$ is denoted by $\widetilde{k}$, and $\widetilde{b}$ denotes the damper constant connecting $x_{1,1}$ to $x_{2,2}$. Fig. 2 illustrates the meaning of above elements.

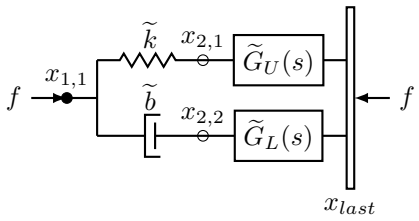

Fig. 2. An illustration about recurrence formula, Eq. (1).

We call the tree model *undamaged* when all spring and all damper constants are same, that is $k_{g,n} = k$ and $b_{g,n} = b$ for all $g = 1, 2, \ldots$ and $n = 1, 2, \ldots, 2^{g-1}$. For each damage case, we assume that there is either only one spring or only one damper having a constant different from its corresponding undamaged value. We further assume that the damaged spring (damper) constant k_d (b_d) is defined by a factor of ϵ, *i.e.*, $k_d = \epsilon k$ or $b_d = \epsilon b$, where ϵ is called the damage amount and $0 < \epsilon < 1$.

As shown in Goodwine (2014) and as is well-known, for the undamaged case, the transfer function from the input force $f(t)$ to the relative distance between $x_{1,1}(t)$ and $x_{\text{last}}(t)$ for the undamaged tree is given by

$$G_\infty(s) = \frac{X_{1,1}(s) - X_{\text{last}}(s)}{F(s)} = \frac{1}{\sqrt{kbs}}. \tag{2}$$

Eq. (1) can be viewed as a mapping from $(\widetilde{G}_U(s), \widetilde{G}_L(s))$ to $\widetilde{G}(s)$, which builds up the tree generation by generation regardless of whether the model is undamaged or damaged.

The existing literature outlined above shows that the undamaged tree's transfer function $G_\infty(s)$ in Eq. (2) can be obtained by replacing $(\widetilde{G}(s), \widetilde{G}_U(s), \widetilde{G}_L(s), \widetilde{k}, \widetilde{b})$ with $(G_\infty(s), G_\infty(s), G_\infty(s), k, b)$ in Eq. (1), *i.e.*, the undamaged transfer function between $x_{1,1}$ and x_{last} is the same as the one between $x_{2,1}$ and x_{last}, and also the one between $x_{2,2}$ and x_{last}.

In a similar manner and using self-similarity, every damage case can also be computed by using Eq. (1) repeatedly. However, repeatedly applying the above process will result

⋆ The partial support of the US NSF Award CMMI 1826079 is gratefully acknowledged.

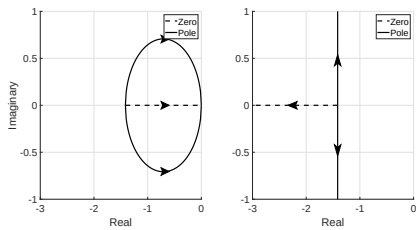

Fig. 3. Half-order ZP locus when the damage occurs at the first generation and $\epsilon \in [0, 1]$. When $\epsilon = 1$, all half-order ZP are at $-\sqrt{k/b}$. (For this plot, $k = 2$ and $b = 1$.) Left: $l = k_{1,1}$. Right: $l = b_{1,1}$.

in a very complicated transfer function. In fact, both transfer functions $\widetilde{G}_U(s)$ and $\widetilde{G}_L(s)$ have the same formula as Eq. (1) due to the self-similarity. Therefore, with integer-order calculus, the transfer function for the entire tree is a complicated infinite continued fraction.

Main Result: The main result of this work is that the damaged tree's transfer function can be written as

$$G_l(s) = G_\infty(s)\Delta_l(s),$$

where the disturbance $\Delta_l(s)$ is well structured and can be determined completely by the damage amount ϵ of a damaged component l. Those two features are the key points which make such way of modeling useful in different applications. See Ni (2021) for a complete analysis.

Claim: For each damage case outlined above, its damaged transfer function $G_l(s)$ from the input force to the relative distance between $x_{1,1}$ and x_{last} can be modeled as a FO nominal plant with a FO multiplicative disturbance,

$$G_l(s) = G_\infty(s)\Delta_l(s), \tag{3}$$

where $G_\infty(s)$ is the undamaged transfer function defined by Eq. (2). Moreover, $\Delta(s)$ is structured as

$$\Delta_l(s) = \frac{N(s)}{D(s)} = \frac{\prod_{j=1}^{2g}(s^{\frac{1}{2}} + z_j)}{\prod_{j=1}^{2g}(s^{\frac{1}{2}} + p_j)} \tag{4}$$

where g denotes the g-th generation at which the damaged component l locates, and $-z_j$ and $-p_j$ are called as half-order zeros and poles. In addition, z_1 is fixed at $\sqrt{k/b}$ regardless of the damage location or amount ϵ.

Claim: $\Delta_l(s)$ Depends on ϵ only at each l.

When the damage happens at the first generation, the relation between $\Delta_l(s)$ and ϵ can be expressed in closed-form. Fig. 3 shows the locus for those half-order zeros and poles when the damage happens at the first generation, and when the damage amount ϵ varies from 1 (no damage) to 0 (complete damage).

For all the other damage locations deeper into the network than the first generation, the relation between $\Delta_l(s)$ and ϵ cannot be easily expressed in a closed form. However,we can still obtain those locus by using a nonlinear equation solver. Fig. 4 shows the locus for those half-order zeros and poles, which are built up numerically, when the damage happens at the second generation with damage $\epsilon \in [0, 1]$.

Since it is possible to get this kind of locus for each damaged component, $\Delta_l(s)$ clearly has only one degree of freedom, namely ϵ, at each damaged component l. That is, as long as either one pole or one zero (other than $-z_1$

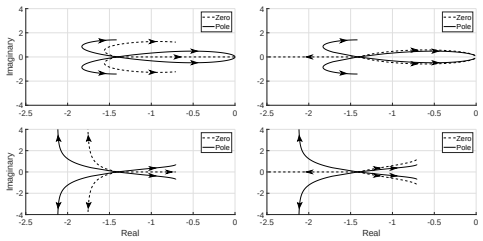

Fig. 4. Half-order ZP locus when the damage occurs at the second generation, and $\epsilon \in [1, 0]$. When $\epsilon = 1$, all half-order zeros and poles are at $-\sqrt{k/b}$. (For this plot, $k = 2$ and $b = 1$.) Upper left: $l = k_{2,1}$. Upper right: $l = k_{2,2}$. Lower left: $l = b_{2,1}$. Lower right: $l = b_{2,2}$.

which always stays at $-\sqrt{k/b}$) is known, all the other zeros and poles can be determined through ϵ, thus $\Delta_l(s)$ is determined thereby.

Utility of These Results: Because the disturbance $\Delta_l(s)$ is completely determined by the damage amount ϵ of a damaged component l, we can use the above result to identify a damage tree network's damage amount ϵ. Specifically, we can formulate that damage identification problem as an optimization problem. For instance, when a damage occurs at $k_{2,1}$, given a frequency domain measurement $\Delta_{k_{2,1}}(s)$, we can identify its damage amount ϵ by solving the following optimization problem,

$$\min_{\epsilon} \sum \frac{\|\widetilde{\Delta}_{k_{2,1}}(s) - \Delta_{k_{2,1}}(s)\|}{\|\Delta_{k_{2,1}}(s)\|}$$

$$\text{where} \quad \widetilde{\Delta}_{k_{2,1}}(s) = \frac{\prod_{j=1}^{4}(s^{\frac{1}{2}} + z_j)}{\prod_{j=1}^{4}(s^{\frac{1}{2}} + p_j)}$$

and $z_j = z_j(\epsilon)$, $p_j = p_j(\epsilon)$ for all $j = 1, \ldots, 4$. The functions $z_j(\epsilon)$ and $p_j(\epsilon)$ are already known by fitting the ZP locus as shown in Fig. 4. We have successfully identified the damage amount ϵ by using `fmincon()` to solve the above optimization problem.

Applications:

(1) Providing insights about how damage affects the network.
(2) Robust control.
(3) Identification of samage for a damaged network.

REFERENCES

Goodwine, B. (2014). Modeling a multi-robot system with fractional-order differential equations. In *2014 IEEE International Conference on Robotics and Automation (ICRA)*, 1763–1768. IEEE.

Heymans, N. and Bauwens, J.C. (1994). Fractal rheological models and fractional differential equations for viscoelastic behavior. *Rheologica acta*, 33(3), 210–219.

Leyden, K. (2018). *System Monitoring by Tracking Fractional Order*. University of Notre Dame.

Mayes, J. (2012). *Reduction and approximation in large and infinite potential-driven flow networks*. Citeseer.

Ni, X. (2021). *Frequency Response of Self-Similar Dynamic Networks with Applications to Health Monitoring and Control*. Ph.D. thesis. URL `https://curate.nd.edu/show/kh04dn43855`.

A 3D-0D closed-loop Model of the Heart and the Circulatory System ⋆

Matthias A.F. Gsell * **Christoph M. Augustin** *
Elias Karabelas ** **Gernot Plank** *

* *Biophysics Department, Medical University of Graz, Austria, (e-mail: {matthias.gsell,christoph.augustin,gernot.plank}@medunigraz.at).*
** *Institute of Mathematics and Scientific Computing, University of Graz, Austria, (e-mail: elias.karabelas@uni-graz.at)*

1. INTRODUCTION

In industrialized countries, cardiovascular diseases are the primary cause of mortality and morbidity. Due to the complex multiphysics nature of cardiovascular function, the optimal treatment remains challenging. In the recent years, personalized computer models of electrophysiology (EP) became an important tool to predict intervention outcomes or to improve therapy stratification and planning. Problems of cardiac electromechanics (EM) are even more challenging. Beside the deformation of the heart, also the bi-directional interaction with the systemic and pulmonary vascular system plays a major role in EM simulations. A fully coupled fluid-structure interaction problem would yield the most detailed insights but is computationally expensive. Simpler lumped models of the circulatory system are able to predict physiological behaviors at a much lower computational cost. In this work, we discuss the coupling of a 3D bi-ventricular model with the closed-loop 0D *CircAdapt* model and we show its ability to predict physiological behaviors under experimental standard protocols.

2. METHODS

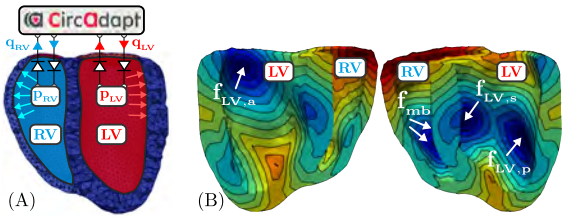

Fig. 1. (A) Bi-ventricular model setup and (B) activation sequence induced by five fasciles used for EP.

2.1 3D Electromechanical PDE Model

The tissue is modeled as a nearly incompressible, hyperelastic, orthotropic material with a nonlinear stress-strain relation using Cauchy's equation of motion

$$\rho_0 \ddot{\mathbf{u}} - \nabla \cdot \mathbf{FS}(\mathbf{u}) = \mathbf{0} \quad in \quad \Omega_0 \times (0,T) \tag{1}$$

for a final time $T > 0$, where $\mathbf{F}$ denotes the deformation gradient, $\mathbf{S}$ is the second Piola-Kirchhoff stress tensor, ρ_0 is the tissue density and Ω_0 denotes the reference configuration. Normal stress boundary conditions are applied at the endocardium

$$\mathbf{FS}(\mathbf{u})\mathbf{N} = -p\, J\, \mathbf{F}^{-\top}\, \mathbf{N} \quad on \quad \Gamma_{0,\text{endo}} \times (0,T) \tag{2}$$

with pressure p, outer normal vector $\mathbf{N}$ of the reference enodicardial surface $\Gamma_{0,\text{endo}}$ and the Jacobian determinant $J = \det\mathbf{F}$. Appropriate spring type boundary conditions are imposed at the remaining boundary of the geometry, see Fig. 1(A).

Passive and active tissue properties are simulated by decomposing the total stress $\mathbf{S}$ into a passive $\mathbf{S}_p$ and active $\mathbf{S}_a$ part, i.e. $\mathbf{S} = \mathbf{S}_p + \mathbf{S}_a$. The passive stress is modeled by the constitutive equation

$$\mathbf{S}_p = 2\frac{\partial \Psi(\mathbf{C})}{\partial \mathbf{C}}$$

with the right Cauchy-Green strain tensor $\mathbf{C} = \mathbf{F}^\top\mathbf{F}$ and the strain-energy function Ψ which is given by

$$\Psi(\mathbf{C}) = \frac{\kappa}{2}\big(\log\, J\big)^2 + \frac{a}{2}\big(\exp(\mathcal{Q}) - 1\big). \tag{3}$$

The first term in (3) penalizes local volume changes scaled by the bulk modulus $\kappa \gg 0\,\text{kPa}$ and the second term models a Fung-type material with a scaling factor $a > 0$ and $\mathcal{Q}$ according to Usyk et al. (2000).

Active stress $\mathbf{S}_a$ is assumed to be orthotropic with full contractile force along myocyte fiber direction $\mathbf{f}_0$ plus 40 % contractile force in sheet direction $\mathbf{s}_0$, i.e.

$$\mathbf{S}_a = S_a(\mathbf{f}_0 \cdot \mathbf{C}\mathbf{f}_0)^{-1}\mathbf{f}_0 \otimes \mathbf{f}_0 + 0.4\, S_a(\mathbf{s}_0 \cdot \mathbf{C}\mathbf{s}_0)^{-1}\mathbf{s}_0 \otimes \mathbf{s}_0$$

with a simplified phenomenological length dependent active stress transient S_a, see Niederer et al. (2011).

The EP, which serves as a trigger for the active stress generation, was modeled by a recently developed reaction-Eikonal approach which combines a standard reaction-diffusion model based on the monodomain equation with an Eikonal model, see Neic et al. (2017).

2.2 0D CircAdapt ODE Model

The *CircAdapt* model, see Arts et al. (2005), is a lumped 0D model enabling real-time simulations of the entire

⋆ The project received funding fom the European Union's Horizon 2020 research and innovation programme and the Austrian Science Fund (FWF).

cardiovascular system by concatenating modules (tubes, valves, chambers, ...) yielding a system of 26 ordinary differential equations. A detailed description of the model and the underlying equations can be found in Augustin et al. (2021).

2.3 0D-3D Coupling and Numerical Framework

To couple the ODE with the PDE model, the 0D cavities in the *CircAdapt* model are replaced by the 3D models discussed in Sec. 2.1. Furthermore, the pressure p within the cavities is introduced as an additional unknown and a supplementary equation enforcing the equality of the cavity volume is added in order to close the formulation. The resulting nonlinear saddle point problem reads

$$\begin{aligned} K(\mathbf{u},t) + G(p,t) &= 0 \\ V^{\mathrm{PDE}}(\mathbf{u},t) - V^{\mathrm{ODE}}(p,t) &= 0 \end{aligned} \tag{4}$$

where V^{PDE} is the cavity volume of the PDE model, V^{ODE} is the cavity volume predicted by the *CircAdapt* model and K and G are operators realizing (1) and (2), respectively.

The saddle point problem (4) is linearized by applying a Newton scheme and solved within the Cardiac Arrhythmia Research Package (CARP) framework, see Vigmond et al. (2008), using a finite element approach.

3. RESULTS

To demonstrate the predictive power of the coupled model, physiological experiments such as altering loading conditions and contractility are performed with a bi-ventricular PDE model. Therefore, 20 heart beats with tuned model parameters are simulated to arrive a stable limit cycle which matches measured baseline conditions. The response of the model to changes in (A) systemic afterload, (B) left aterial preload and (C) left ventricular contractility are probed by changing (A) the systemic resistance, (B) the cross sectional area of the pulmonary vein and (C) the peak active stress, respectively. The response of the coupled model on the pressure-volume diagram is depicted in Fig. 2 (acute response) and Fig. 3 (limit cycle response).

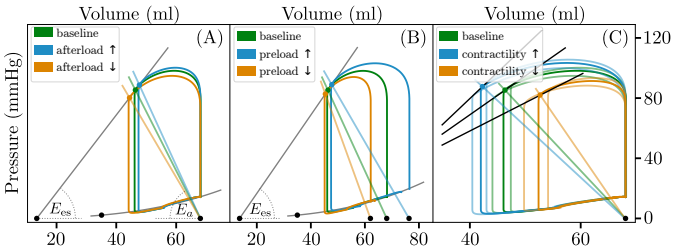

Fig. 2. Acute response to changes in (A) afterload, (B) preload and (C) contractility.

4. DISCUSSION

The coupled model is capable to reproduce the expected physiological behaviors in the left ventricular pressure-volume diagram, see Fig. 2 and Fig. 3. Altering afterload is reflected in pivoting the slope of the arterial elastance

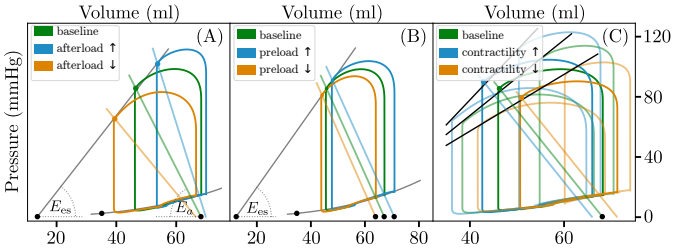

Fig. 3. Limit cycle response to changes in (A) afterload, (B) preload and (C) contractility.

curve E_a. Only marginal affects are observed in the acute case, Fig. 2(A), but significant changes are witnessed after stabilization to a limit cycle, Fig. 3(A). Changing preload conditions increased/decreased the stroke volume (SV) of the left ventricle due to the Frank-Starling mechanism and shifted E_a according to the changed end-diastolic volume. The slope of the end-systolic pressure volume relation E_{es} remains the same as under baseline conditions, see Fig. 2(B) and Fig. 3(B). Altering contractility increased/decreased the SV and E_{es} (sampled by perturbing afterload) is steepened/flattened as expected. In the acute response, Fig. 2(C), E_a was affected but after stabilization E_a was the same for all states, see Fig. 3(C).

REFERENCES

Arts, T., Delhaas, T., Bovendeerd, P., Verbeek, X., and Prinzen, F.W. (2005). Adaptation to mechanical load determines shape and properties of heart and circulation: the CircAdapt model. *American Journal of Physiology-Heart and Circulatory Physiology*, 288(4), H1943–H1954. doi:10.1152/ajpheart.00444.2004.

Augustin, C.M., Gsell, M.A., Karabelas, E., Willemen, E., Prinzen, F.W., Lumens, J., Vigmond, E.J., and Plank, G. (2021). A computationally efficient physiologically comprehensive 3D-0D closed-loop model of the heart and circulation. *Computer Methods in Applied Mechanics and Engineering*, 386, 114092. doi: 10.1016/j.cma.2021.114092.

Neic, A., Campos, F.O., Prassl, A.J., Niederer, S.A., Bishop, M.J., Vigmond, E.J., and Plank, G. (2017). Efficient computation of electrograms and ECGs in human whole heart simulations using a reaction-eikonal model. *Journal of Computational Physics*, 346, 191–211. doi:10.1016/j.jcp.2017.06.020.

Niederer, S.A., Plank, G., Chinchapatnam, P., Ginks, M., Lamata, P., Rhode, K.S., Rinaldi, C.A., Razavi, R., and Smith, N.P. (2011). Length-dependent tension in the failing heart and the efficacy of cardiac resynchronization therapy. *Cardiovascular Research*, 89(2), 336–343. doi:10.1093/cvr/cvq318.

Usyk, T.P., Mazhari, R., and McCulloch, A.D. (2000). Effect of laminar orthotropic myofiber architecture on regional stress and strain in the canine left ventricle. *Journal of Elasticity*, 61(1-3), 143–164. doi: 10.1023/A:1010883920374.

Vigmond, E.J., Weber dos Santos, R., Prassl, A.J., Deo, M., and Plank, G. (2008). Solvers for the cardiac bidomain equations. *Progress in Biophysics and Molecular Biology*, 96(1-3), 3–18. doi: 10.1016/j.pbiomolbio.2007.07.012.

Bipartite Graph Modeling of Critical Driving Scenarios - an Occupant Safety Perspective

Florian Bechler [*,**] **Jörg Fehr** [**] **Fabian T. Neininger** [*]
Stefan Knöß [*] **Bernhard Grotz** [*]

[*] *ZF Friedrichshafen AG, Safe Mobility Systems, 88046 Friedrichshafen, Germany (e-mail: {florian.bechler, fabian.neininger, stefan.knoess, bernhard.grotz}@zf.com)*
[**] *Institute of Engineering and Computational Mechanics, University of Stuttgart, Pfaffenwaldring 9, 70569 Stuttgart, Germany (e-mail: joerg.fehr@itm.uni-stuttgart.de)*

1. INTRODUCTION AND MOTIVATION

The automotive industry is currently undergoing major changes. While mobility concepts and drive technologies change, vehicle safety remains of utmost importance and enables new mobility concepts. Currently, the field of vehicle safety systems can be divided into active and passive systems. Within this definition, active systems prevent a crash while passive systems mitigate crash consequences for the occupants. Each system has its intrinsic operating time, activation logic, and principle of action. With the constantly increasing development of enhanced sensor technology for the vehicle's interior and exterior, this can be used for predictive safety strategies Grotz et al. (2021). In addition to improved data availability and increased interconnection between former separated systems, this promises holistically coordinating all safety systems. This approach targets an improved scenario-based occupant protection. To bring vehicle safety from trigger-based activation of individual components and actuators to holistic and comprehensible safety decision-making, a mathematical description of the environment is the crucial first step to begin with the interdisciplinary modeling, simulation and optimization cycle.

In the following, a base scenario is shown and in Section 2 the novel approach of mathematically formulating a driving scenario, from an occupant perspective, as a bipartite graph is presented.

In Fig. 1 the driving scenario is depicted, labelling the vehicle under consideration (ego vehicle) in green. The other road users and potential accident opponents, referred to as bullets hereinafter, in black. Figure 1(a), describes an uncritical driving scene on a two-lane road. Only one passenger, the driver, occupies the the vehicle. If the car ahead decelerates, ideally detectable via the taillights, the ego vehicle needs to react and has different options. If the time-to-collision (TTC) is greater than the time-to-brake (TTB), it is still possible to stop before a collision occurs. However, if the TTC is smaller than the TTB, or if a rear-end collision with a following vehicle (B_2) should be avoided, a front collision will occur. Since the left lane is blocked (B_3) and there is also an obstacle (O) on the right side, an evasive maneuver influences the safety strategy. In the presented scenario, the driver is leaning slightly to the front left, as depicted in Fig. 1(b), i.e. the driver is adjusting something on his mirror.

Emergency braking followed by a collision may not be the ideal safety strategy, as the belt does not well couple the occupant to the vehicle's deceleration, hence the performance of the airbag is reduced. Since the passenger seat is not occupied, a collision on the passenger's right side of the vehicle, as shown in Fig. 1(c), would help to make the impact less critical for the occupant by better exploiting the safety potential of the airbag as the driver is slightly moved towards the center during the impact.

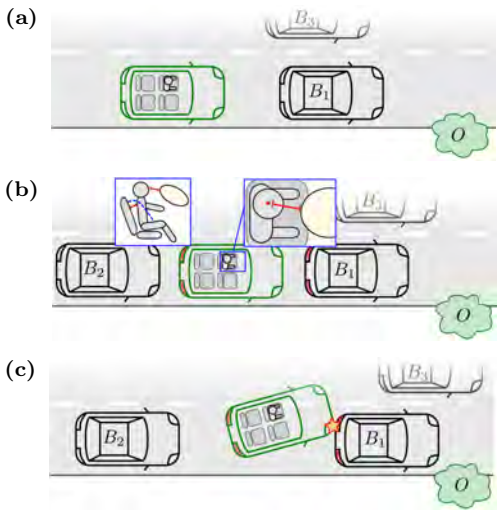

Fig. 1: Driving scenarios (a)-(c) with ego vehicle (green) and bullet vehicles (black).

This presented scenario shows how challenging it is to find the optimized safety strategy which maximizes the benefits of available safety systems for occupant protection. The task becomes even more difficult when considering multiple occupants, the driver's attention status, possible occlusions in the environment, the lack of sensor information, scenario states such as the TTC or the safety parameters of the passive safety devices, e.g. seatbelt pretensioner trigger.

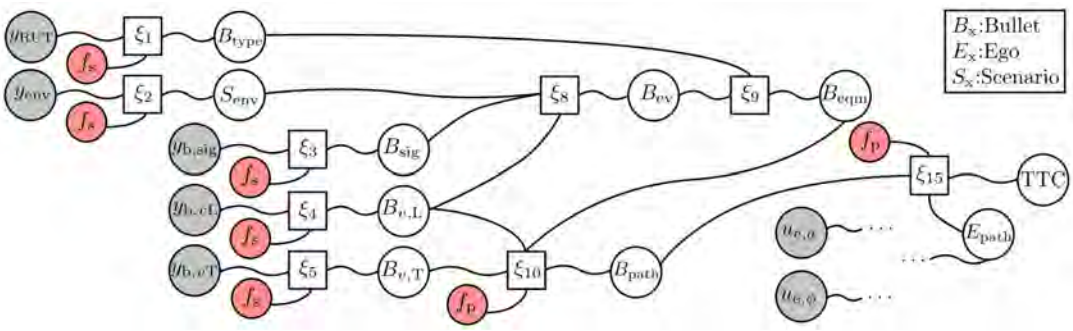

Fig. 2: Branch of a bipartite graph representing a driving scenario with measured inputs (grey) and uncertainties (red).

2. MODELING

In order to later decide on a safety strategy for the occupant online, calculations has to be simplified. Thus surrogate models need to be derived for some state relationships. The overall model must be able to combine physical models with data-driven models and expert knowledge and allow for the implementation of uncertainties and probabilities. The following description is limited to a mathematical framework without describing the entire mathematical modeling, which is not the scope of the presented work.

A bipartite graph is used to represent the relationships of the variables and to meet the needs of the model. This approach is presented in Gienger (2021) for process monitoring and fault detection. Figure 2 shows a branch of the overall model. As a bipartite graph, it represents how the TTC can be inferred from sensor data of the environment and the ego vehicle.

The vertices of the graph $\mathcal{G} = (\mathcal{V},\mathcal{U})$ can be split in two groups, where $\mathcal{V}$ represents the variable nodes (circles) and $\mathcal{U}$ represents factor nodes (rectangles), such that every edge conntects between these groups. Variable nodes consist of observable nodes $\{y_{\mathrm{RUT}}$, y_{env}, $y_{b,\{\mathrm{sig},v\mathrm{L},v\mathrm{T}\}}$, $u_{\mathrm{e},\{a,\phi\}}\}$ and latent variables $\{S_{\mathrm{env}}$, TTC, $B_{\{\mathrm{type,sig,ev,eqm,path},v\mathrm{L},v\mathrm{T}\}}$, $E_{\mathrm{path}}\}$ which are unknown and correspond to the states of the system. The red variable nodes describe the sensor uncertainties f_{s} and the process uncertainties f_{p} resulting from inaccurate sensing and errors in the mathematical model. The factor nodes $\xi_{1,\dots,15}$ represent the functional dependencies between adjacent variable nodes. This representation of the system dynamics helps to understand the system structure and sets the basis for later implementation. The measured inputs $y_{\mathrm{RUT}} \in \{$car, pedestrian, truck, etc.$\}$ which describe the road user type under observation, and $y_{\mathrm{env}} \in \{$crossing, left/right lane, turn, etc.$\}$ describe the current environment give information about which maneuvers the observed bullet may potentially execute. The derived states B_{type} and S_{env} contain the probabilities of the measured inputs. Combined with some evidence $y_{\mathrm{b,sig}} \in \{[0,1];[0,1]\}$ representing the status of the turning signals of the bullet, $y_{\mathrm{b},v\mathrm{L}}$ and $y_{\mathrm{b},v\mathrm{T}}$ representing the measured lateral and tangential velocity of the bullet and their states including the uncertainties $B_{\{\mathrm{sig},v\mathrm{L},v\mathrm{T}\}}$, an equation of motion B_{eqm} for the most likely maneuver is selected. The evaluation of the selected equation B_{eqm} with the measured velocities results in a predicted path B_{path}. This procedure is similar to the approach presented by Schreier et al. (2016). For the ego vehicle and its input states $u_{\mathrm{e},a}$, describing the acceleration, and $u_{\mathrm{e},\phi}$, describing the steering angle, a graph is defined leading to a predicted ego path E_{path}. This branch is omitted in Fig. 2 for better readability. Given the two paths, the TTC is calculated with a process uncertainty f_{p}. So in this branch of the bipartite graph a TTC is derived from both a probabilistic model to assume a maneuver of the bullet and a physical model in forms of the equation of motion.

3. CONCLUSION AND OUTLOOK

The interconnection between active and passive safety systems in different driving scenarios can offer enormous benefits for the occupant's safety. A mathematical description of the traffic environment is mandatory to decide model-based when and which system should intervene. In this work, an approach was presented how a complex traffic scenario can be described mathematically and how the relationships of different variables can be represented. The representation as a bipartite graph can combine different modeling approaches, including probabilities and uncertainties and attaching a decision tree as in Bungartz et al. (2013) Ch. 3-4. This leads to the goal of finding a holistic safety strategy that helps to optimally utilize the safety potentials of the individual components. In further investigations, the branches of the graph will be extended and different modeling approaches will be used and tested in a simulation environment. For state dependencies that either cannot be physically described or can only be calculated with great computational effort naturalistic driving- and crash databases like, e.g. the AMP or GIDAS will be used.

REFERENCES

Bungartz, H.J., Zimmer, S., Buchholz, M., and Pflüger, D. (2013). *Modellbildung und Simulation Eine anwendungsorientierte Einführung.* Springer Spektrum, Wiesbaden.

Gienger, A. (2021). *Combining Model- and Data-based Methods for Process Monitoring and Fault Diagnosis (in German).* Dissertation. Shaker Verlag, Aachen.

Grotz, B., Straßburger, P., Huf, A., and Roig, L. (2021). Predictive safety - preception-based activation of pre-crash systems. *ATZ worldwide*, 1, 18–24.

Schreier, M., Willert, V., and Jürgen, A. (2016). Bayesian, maneuver-based, long-term trajectory prediction and criticality assessment for driver assistance systems. In *2016 IEEE Intelligent Transportation Systems (ITSC)*, 334–341.

Neural networks based real-time simulations of cardiac electromechanics

Francesco Regazzoni [*] **Matteo Salvador** [*] **Luca Dedè** [*]
Alfio Quarteroni [*,**]

[*] *MOX - Dipartimento di Matematica, Politecnico di Milano, P.zza Leonardo da Vinci 32, 20133 Milano, Italy.*
[**] *Mathematics Institute, École Polytechnique Fédérale de Lausanne, Av. Piccard, CH-1015 Lausanne, Switzerland (Professor Emeritus).*

Abstract: We propose a non-intrusive method, based on Artificial Neural Networks (ANNs), that builds reduced-order models (ROMs) approximating the dynamics of 3D cardiac electromechanics. Our Machine Learning method allows for real-time numerical simulations of the cardiac function, accounting for the dependence on a set of parameters associated with the full-order model (FOM) to be surrogated. The ANN-based ROM is trained from a collection of pressure-volume transients obtained through the FOM and it can then be coupled with hemodynamic models for the blood circulation external to the heart, in the same manner as the original electromechanical model, but at a dramatically lower computational cost. We demonstrate the effectiveness of the proposed method in two relevant contexts in cardiac modeling. First, we employ the ANN-based ROM to perform a global sensitivity analysis on both the electromechanical and hemodynamic models. Second, we perform a Bayesian estimation of two parameters starting from noisy measurements of two scalar outputs. In both these cases, replacing the FOM of cardiac electromechanics with the ANN-based ROM makes it possible to perform in a few hours of computational time the numerical simulations that would be unaffordable if carried out with the FOM, because of their overwhelming computational cost.

Keywords: Cardiac Electromechanics, Machine Learning, Reduced Order Modeling, Global Sensitivity Analysis, Bayesian Parameter Estimation

1. INTRODUCTION

The clinical exploitation of cardiac numerical simulations is seriously hampered by their overwhelming computational cost (several hours of computational time even on supercomputer platforms, see e.g. Quarteroni et al. (2019)). A promising approach to address this issue is to replace the computationally expensive cardiac electromechanical model, say the full-order model (FOM), with a reduced version of it, the reduced-order model (ROM), to be called any time new parameters come in. The ROM is built from a database of numerical simulations obtained by solving the FOM.

Recently, this framework has been applied in the context of cardiac modeling, primarily by using Machine Learning algorithms, including Gaussian Process emulators (GPEs) and Artificial Neural Networks (ANNs) (see e.g. Dabiri et al. (2019); Longobardi et al. (2020)). These emulators are trained to fit the map that links the model parameters with a set of scalar outputs of interest, known as quantities of interest (QoIs), which are clinically meaningful biomarkers.

[⋆] This project has received funding from the European Research Council (ERC) under the European Union's Horizon 2020 research and innovation programme (grant agreement No 740132, iHEART - An Integrated Heart Model for the simulation of the cardiac function, P.I. Prof. A. Quarteroni).

2. METHODS

We propose a Machine Learning method to build a ROM of cardiac electromechanical models, which differs in many respects from existing approaches. We rely on the ANN-based method that we proposed in Regazzoni et al. (2019), which can learn a time-dependent differential equation from a collection of input-output pairs. In contrast to existing approaches, we only surrogate the time-dependent pressure-volume relationship of a cardiac chamber, while we do not reduce the model describing external circulation (see Fig. 1). The latter is indeed either a low dimensional 0D windkessel or closed-loop circulation model comprised of a few state variables (up to two dozens), which does not require further reduction. Unlike emulators, for which the online phase consists in evaluations of the map linking model parameters to QoIs, with our approach the online phase consists instead in numerical simulations, in which the ANN-based ROM of the electromechanical model is coupled with the circulation model, at a very low computational cost.

Our ANN-based ROM consists of a system of Ordinary Differential Equations (ODEs), whose right-hand side is represented by an ANN. The inputs of the ANN are (1) the state variables of the ROM, whose dimension is one of the hyper-parameters of the model; (2) the blood pressure at the current time, that is an input for the

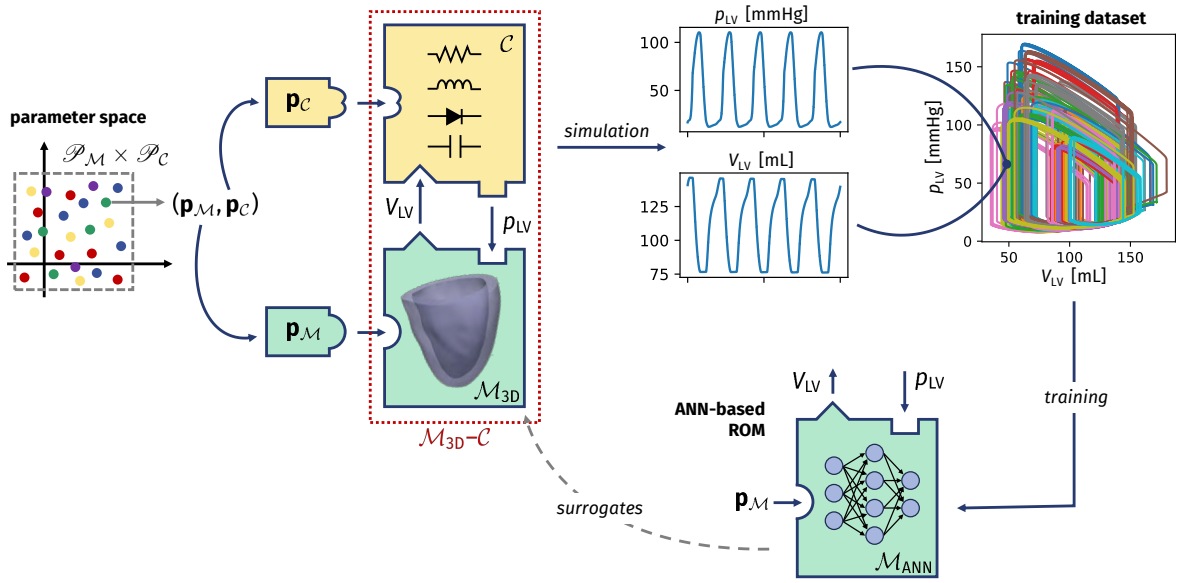

Fig. 1. The training data are generated by sampling the parameter space and by solving the electromechanical model $\mathcal{M}_{3D}$, coupled with the circulation model $\mathcal{C}$, for each parameter instance. Then, once the ANN-based ROM ($\mathcal{M}_{ANN}$) has been trained, it can be coupled to the model $\mathcal{C}$, thus surrogating the $\mathcal{M}_{3D}$ model.

FOM; (3) the parameters of the FOM (e.g. fiber direction, electrical conductivities, active contractility, stiffness of the myocardium); (4) the coordinates of a point that moves on a unitary circumference with the same frequency of the heartbeat, in order to take into account the periodicity of the FOM. The output of the ANN consists instead in the time-derivative of the state variables. By numerically solving this system of ODEs, it is possible to simulate the cardiac dynamics described by the ROM. To train the weights and the biases of the ANN associated with the ROM, we use the Machine Learning algorithm proposed in Regazzoni et al. (2019) by exploiting the open-source library accompanying the manuscript itself.

3. RESULTS

We present two test cases in which we employ the ANN-based ROM. We carry out a global sensitivity analysis to assess the influence of the parameters of the electromechanical and hemodynamic models on a list of outputs of clinical interest. Then, we perform a Bayesian estimation of a couple of parameters (belonging to the electromechanical and hemodynamic models, respectively), starting from the noisy measurement of a couple of scalar quantities (namely maximum and minimum arterial pressure). In both the cases, performing through the FOM the large number of numerical simulations that are needed would not have been possible, due to their high computational cost (it would in fact have taken tens of years on a supercomputer platform). Replacing the FOM with its ANN-based surrogate allowed us to obtain the results in a few hours of computation. By taking into account that the generation of the numerical simulations contained in the training set required less than 7 days on the same computational platform, our ANN-based ROM allowed us to reduce the total computational time by more than 3'000 times.

4. CONCLUSIONS

We presented a Machine Learning algorithm to build ANN-based ROMs of cardiac electromechanical models. Our algorithm is capable of learning, on the basis of pressure and volume transients generated with the FOM, a system of differential equations that approximate the dynamics of the cardiac chamber to be surrogated. This differential equation, linking pressure and volume of a cardiac chamber, is coupled with lumped-parameter models of cardiac hemodynamics, thus allowing for the simulation of the cardiac function at a dramatically reduced computational cost with respect to the original FOM. As a matter of fact, our ROM permits to perform numerical simulations in real-time. Moreover, thanks to its non-intrusive nature, the proposed algorithm can be easily applied to other electromechanical models besides the one considered in this work.

REFERENCES

Dabiri, Y., Van der Velden, A., Sack, K.L., Choy, J.S., Kassab, G.S., and Guccione, J.M. (2019). Prediction of left ventricular mechanics using machine learning. *Frontiers in physics*, 7, 117.

Longobardi, S., Lewalle, A., Coveney, S., Sjaastad, I., Espe, E.K.S., Louch, W.E., Musante, C.J., Sher, A., and Niederer, S.A. (2020). Predicting left ventricular contractile function via gaussian process emulation in aortic-banded rats. *Philosophical Transactions of the Royal Society A*, 378(2173), 20190334.

Quarteroni, A., Dedè, L., Manzoni, A., and Vergara, C. (2019). *Mathematical modelling of the human cardiovascular system: data, numerical approximation, clinical applications*. Cambridge Monographs on Applied and Computational Mathematics. Cambridge University Press.

Regazzoni, F., Dedè, L., and Quarteroni, A. (2019). Machine learning for fast and reliable solution of time-dependent differential equations. *Journal of Computational Physics*, 397, 108852.

Data-driven nonlinear system identification of a closed-loop CSTR

Sarmilan Santhakumaran * **Yuri A. W. Shardt** ** **Jesse Rejek** * **Christine Maul** *

* *Covestro Deutschland AG, Leverkusen, 51365 Germany (e-mail: {sarmilan.santhakumaran}; {jesse.rejek}; {christine.maul}@covestro.com).*
** *Technical University of Ilmenau, Ilmenau, 98694 Germany, Germany, (e-mail: yuri.shardt@tu-ilmenau.de)*

1. INTRODUCTION

Recently, data-driven system identification using sparse regression with L_1 regularisation solved the problem to identify simultaneously functional structure and the related parameter estimates [Brunton et al. (2016)]. Based on this open-loop framework, the objectives of this paper are to theoretically examine the performance of the data-driven nonlinear system identification using a sequential threshold least-squares (STLSQ) algorithm based on sparse regression with L_1 regularisation for closed-loop processes. Additionally, the effect of normalisation on the proposed method is discussed. In order to evaluate the method, a CSTR model with a PI controller to control the reactor temperature is chosen as benchmark system and the model is identified using the proposed framework. Finally, the validation of the proposed method using simulation results are presented.

2. SPARSE IDENTIFICATION OF NONLINEAR DYNAMICS

The sparse identification framework seeks to identify dynamic systems in the form of

$$\frac{dx(t)}{dt} = f(x(t)),\ x(t_0) = x_0, \tag{1}$$

describing the temporal behaviour of the state vector $x(t) \in \mathbb{R}^n$. Data-driven system identification consists of the identification of nonlinear candidates using the properties of dictionary learning and regularisation [Brunton et al. (2016)]. The resulting regression problem can be written as:

$$\min_{\Xi} \|\Theta(X) \cdot \Xi - \dot{X}\|_2 + \lambda \cdot \|\Xi\|_1. \tag{2}$$

where the output of the regression is the matrix $\Xi \in \mathbb{R}^{(\sum d_i) \times n}, i = 1, 2, .., H$, which contains the model coefficients for each candidate function from the dictionary function $\Theta(X)$ fit to the data matrix $X \in \mathbb{R}^{m \times n}$ and its derivative obtained from the process $\dot{X} \in \mathbb{R}^{m \times n}$. $\lambda \in \mathbb{R}$ denotes the regularisation parameter. In order to improve the optimisation performance, [Brunton et al. (2016), Wang et al. (2011)] recommend the normalisation of the dictionary function. The idea can be transferred to a closed-loop identification by adding a manipulated variable into the regression problem. Reformulating the regression problem in an augmented state-space form can account for PI controllers commonly used in practical applications. The resulting state-space form is

$$\frac{dx}{dt} = a(x) + K_p \cdot (w - y) + K_I \cdot z, \tag{3}$$

$$\frac{dz}{dt} = w - y, \tag{4}$$

$$y = x. \tag{5}$$

where $x \in \mathbb{R}$ is a single state, $y \in \mathbb{R}$ is the system output, $w \in \mathbb{R}$ is the reference value to which the system should be controlled, $z \in \mathbb{R}$ is the auxiliary state and $K_p \in \mathbb{R}$ and $K_I \in \mathbb{R}$ are, respectively, the proportional and integral gains.

3. SIMULATION AND RESULTS

In order to evaluate the performance of the proposed solution in a continuous time environment, a CSTR model was used. The state-space model consists of the mass balance, the energy balance and the PI controller structure. The nonlinear part of the model is represented by the reaction kinetics containing the Arrhenius equation. The model parameters are given in Table 1 and the model is

$$\begin{aligned}
\frac{dc_A}{dt} &= \frac{q}{V} \cdot (c_{Af} - c_A) - rA \\
\frac{dT}{dt} &= \frac{q}{V} \cdot (T_f - T) - \frac{\Delta H_R}{(\rho \cdot c_p)} \cdot rA + \\
&\quad \frac{U \cdot A}{(V \cdot \rho \cdot c_p)} \cdot (T_c - T) + PI \\
\frac{dz}{dt} &= T_{ref} - T \\
rA &= k_0 \cdot e^{-E/R \cdot T} \cdot c_A^2 \\
PI &= K_p \cdot (T_{ref} - T) + K_I \cdot z.
\end{aligned} \tag{6}$$

where $T \in \mathbb{R}$ is the reactor temperature, $c_A \in \mathbb{R}$ is the concentration of the considered component, $z \in \mathbb{R}$ describes the integrated control error state and $PI \in \mathbb{R}$ is the PI-controller structure. Parameters and initial conditions of the model are shown in Table 1.
The model equations were implemented and solved in Python to obtain data for the identification. The identification was performed with a threshold of $\lambda = 0.9$, ten iterations in the STLSQ algorithm, and a normalised dictionary. The resulting coefficient matrix containing the

	$\frac{dc_A}{dt}$	$\frac{dT}{dt}$	$\frac{dz}{dt}$	
1	20	$1.41 \cdot 10^4$	380	Other model coefficients
T	0	−37	−1	
c_A	−5	0	0	
z	0	180	0	PI controller
$T^2 \cdot e^{-E/R \cdot T}$	0	0	0	
$T^2 \cdot e^{-E/R \cdot c_A}$	0	0	0	
$c_A^2 \cdot e^{-E/R \cdot T}$	$-8.46 \cdot 10^6$	$4.21 \cdot 10^8$	0	Reaction kinetics
$c_A^2 \cdot e^{-E/R \cdot c_A}$	0	0	0	
$z^2 \cdot e^{-E/R \cdot T}$	0	0	0	
$z^2 \cdot e^{-E/R \cdot c_A}$	0	0	0	

Fig. 1. Result of sparse identification with nonlinear dynamics applied to the CSTR model with PI temperature controller described by Equation 6.

candidate functions as rows and the differential equations as columns is shown in Figure 1. It can be observed that the appropriate candidate functions representing the actual dynamics were identified and a sparse solution was obtained. The candidate functions and coefficients chosen by the identification are the same as specified in the input model (see Table 1). The coefficient of determination $R^2 = 1$ confirms that the resulting model is appropriate. To produce different dynamical responses of the model and evaluate the effect of normalisation, the initial conditions of the CSTR model with PI controller were randomly varied to produce 51 different data sets for identification. Figure 2 shows the number of nonzero coefficients in the identified model equations as a function of the initial conditions. When no normalisation is performed (red triangles), none of the models has the desired nine nonzero coefficients, while with normalisation (blue triangles), the desired model is found in most cases. It was shown that, with respect to the sparsity of the model, the normalisation has a significant effect and improves the identification. Furthermore, it is assumed that the normalisation of the dictionary improves the predictive capacity of the models.

Table 1. Parameters and initial conditions of the model

q	Volumetric Flowrate ($5\,\mathrm{m^3/h}$)
V	Reactor Volume ($1\,\mathrm{m^3}$)
ρ	Density of Mixture ($1000\,\mathrm{kg/m^3}$)
c_p	Heat Capacity of Mixture ($0.231\,\mathrm{kJ/(kg \cdot K)}$)
ΔH_R	Heat of Reaction ($-1.15 \cdot 10^4\,\mathrm{kJ/kmol}$)
E	Activation Energy ($50000\,\mathrm{kJ/kmol}$)
R	Gas Constant ($8.314\,\mathrm{kJ/(kmol \cdot K)}$)
k_0	Reaction Constant ($8.46 \cdot 10^6\,\mathrm{m^3/(kmol \cdot h)}$)
U	Heat Transfer Coeff. ($5000\,\mathrm{kJ/(m^3 \cdot h)}$)
A	Heat Transfer Area ($1\,\mathrm{m^3}$)
T_f	Feed Temperature ($350\,\mathrm{K}$)
c_{Af}	Feed Concentration Comp. A ($4\,\mathrm{kmol/m^3}$)
T_c	Cooling Jacket Temperature ($395\,\mathrm{K}$)
T_{ref}	Controller Reference Temperature ($380\,\mathrm{K}$)
K_p	Controller Proportional Gain ($10\,1/\mathrm{h}$)
K_I	Controller Integral Gain ($180\,1/\mathrm{h^2}$)
c_{A0}	Initial Concentration Comp. A ($2.2\,\mathrm{kmol/m^3}$)
T_0	Initial Temperature ($325\,\mathrm{K}$)

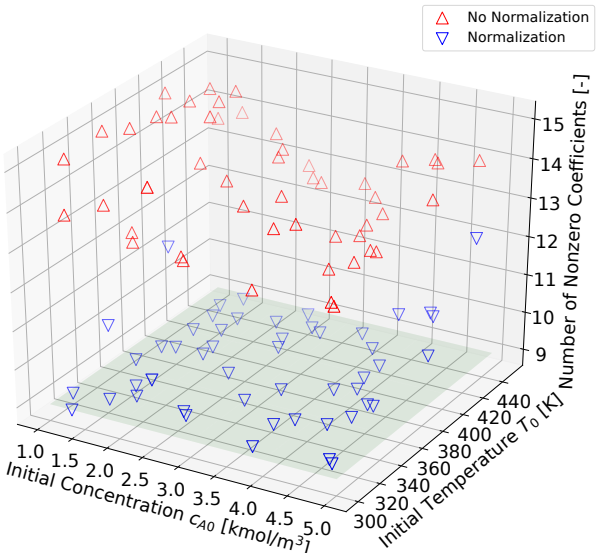

Fig. 2. Number of nonzero coefficients of the 51 identified models as a function of the initial conditions c_{A0}, T_0.

4. CONCLUSION

The effect of normalising the dictionary of candidate functions was evaluated with 51 data sets obtained from varying the initial conditions of the model. It was shown that both process dynamics and controller dynamics can be identified accurately ($R^2 = 1$). The normalisation of the dictionary was shown to be beneficial to promote sparsity. In future work, the proposed framework could be tested with data coming from black-box models, e.g., from the process simulation environment UniSim Design. Also, real process data could be used or additional Gaussian white noise could be added to the input data. In order to determine the performance limit of the proposed framework, local differentiation methods, e.g., the Savitzky-Golay filter, or global differentiation methods, e.g., the total variation derivative, could be evaluated. Furthermore, the framework could be extended to also allow the identification of the differential part of a proportional-integral-differential (PID) controller and other controller structures.

REFERENCES

Brunton, S.L., Proctor, J.L., and Kutz, J.N. (2016). Discovering governing equations from data by sparse identification of nonlinear dynamical systems. *Proceedings of the national academy of sciences*, 113(15), 3932–3937.

Wang, W.X., Yang, R., Lai, Y.C., Kovanis, V., and Grebogi, C. (2011). Predicting catastrophes in nonlinear dynamical systems by compressive sensing. *Physical review letters*, 106(15), 154101.

Parameter Space Reduction for Four-chamber Electromechanics Simulations Using Gaussian Processes Emulators

Marina Strocchi [*] **Stefano Longobardi** [*]
Christoph M. Augustin [**] **Matthias A. F. Gsell** [**]
Edward J. Vigmond [***] **Gernot Plank** [**] **Chris J. Oates** [****]
Richard D. Wilkinson [†] **Steven A. Niederer** [*]

[*] *King's College London, London, UK (e-mail: marina.strocchi@kcl.ac.uk).*
[**] *Medical University of Graz, Graz, Austria*
[***] *IHU Liryc, Electrophysiology and Heart Modeling Institute, Bordeaux, France*
[****] *Newcastle University, Newcastle upon Tyne, UK*
[†] *University of Nottingham, Nottingham, UK*

Keywords: Gaussian Processes, Sensitivity Analysis, Cell Models, Parameter Estimation.

1. INTRODUCTION

Cardiac physiology results from coordinated interactions across multiple scales, from proteins through to whole heart function. Physics-based computational models can encode these multi-scale processes. Calibrating these models to clinical data measuring whole heart function potentially provides a virtual heart assay to identify the tissue and cellular scale mechanisms underpinning these clinical observations. However, these models have large numbers of parameters and are computationally intensive, making model calibration challenging. In this context, machine learning methods for parameter reduction and estimation can be of great help in reducing the number of required simulation runs and therefore make parameter fitting possible.

2. METHODS

In this paper, we applied Gaussian processes emulators (GPE), Sobol variance-based global sensitivity analysis (GSA) and Bayesian history matching (HM) to the ToR-ORd model (Tomek et al., 2019) for human ventricular action potential and the Land model for human cellular active contraction (Land et al., 2017). The code for GPE training, GSA and HM is available online and is described in detail in (Longobardi et al., 2020). All simulations were run with a basic cycle length of 1000 ms for 100 beats to reach a near limit cycle. The calcium and the active tension transients from the last beat were used to extract features of interest, that were then used to evaluate parameter importance.

We selected 29 parameters of the ToR-ORd model representing ion channel conductivity, pump and exchanger maximum flux, the maximum fluxes of the calcium pathways and buffering concentrations to study their effect on the resulting calcium transient. Four separate GPE were trained to predict the following key calcium transient features: 1) diastolic calcium, 2) transient amplitude, 3) time to peak and 4) time to reach 90% relaxation. We used 2175 latin hypercube samples and the parameter space bounds were set to $\pm 25\%$ from their default values. Using the GPE we performed a Sobol GSA to compute the total effect of each parameter on each output feature. The parameters were ranked according to their maximum effect across all outputs. These values were then normalised to sum up to 1 and the most important parameters cumulatively explaining 90% of the output variance were selected as the most important, while the others were discarded.

A HM was then run on this subset of parameters to identify areas of the parameter space that led to physiological output features. Literature experimental data for human ventricular calcium transient were used as target values. The implausibility measure of each parameter combination was computed as in (Longobardi et al., 2020), to quantify discrepancy between GPE prediction and target experimental observations, accounting for both experimental data and GPE uncertainty. We ran five HM iterations (or waves) with a cutoff on the implausibility measure of 3.5 and a sixth wave with a cutoff of 3.0.

The non-implausible areas on the ToR-ORd model parameters were then used to define calcium transients to input to the Land model. A GSA on all 17 Land model parameters and the 10 selected ToR-ORd model parameter was run to detect important parameters for the following active tension features: 1) peak tension, 2) time to peak, 3) maximum time derivative, 4) minimum time derivative, 5) twitch duration and 6) rest tension. The GSA was applied for three experiments: isometric twitch with 0 and 0.1 constant strains and isotonic twitch.

We finally applied HM on the Land model fixing the ToR-ORd parameters to their default value to identify which parameter space regions led to physiological active tension. The target values for the HM were set to be the active tension transient features obtained in the Land model original paper (Land et al., 2017) and their standard deviation was set to 10% of their value. In this case, we ran only two waves with 3.5 cutoff on the implausibility measure and one last third wave with cutoff of 3.

3. RESULTS

Ranking the ToR-ORd model parameters according to their maximum total effect on the calcium features showed that, as expected, the most important parameters were directly related to either calcium ion channel or pump conductivities or to other calcium handling regulatory processes (e.g. diffusion inside the cell, calmodulin binding or contraction proteins). The GSA allowed us to reduce the number of parameter from 29 to 10, as the 10 most important parameters were enough to explain 90% of the output variance.

These 10 parameters were then used in the HM to restrict the parameter space to areas leading to physiological calcium transients. Figure 1 shows the initial calcium transients (blue) and the ones resulting from the restricted regions until the last HM wave (red). The corresponding simulated feature values from the initial (blue) and the restricted (red) space are compared with the experimental data (black). The HM allows us to restrict the parameter space to ensure the simulations give physiological values for all features. For the last HM wave (red) all simulations result in physiologically plausible calcium transients.

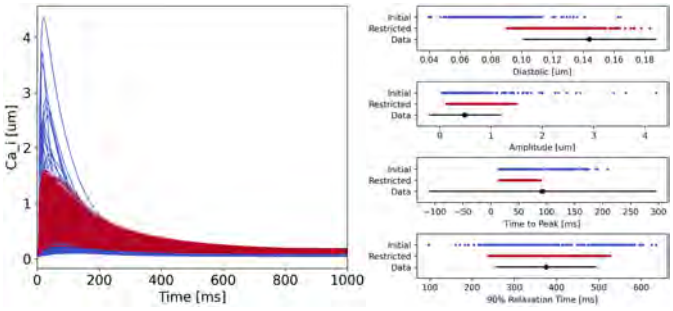

Fig. 1. **ToR-ORd HM Results.** Calcium transients (left) and extracted features (right) from the initial (blue) and from the restricted (red) parameter space. Experimental data ranges are shown in black.

The GSA on the Land model allowed us to reduce the parameters from 17 to 9. Furthermore, according to our analysis, only 4 of the original 29 ToR-ORd model parameters were necessary to explain 90% variance of the active tension transient. Therefore, the GSA allowed us to reduce the number of parameters in the ToR-ORd+Land model from 46 parameters down to 13 to explain 90% of the variance in the tension transient which drives whole heart simulations.

The HM allowed us to restrict the kinetic parameters of the Land model to values that led to physiological active tension transient when coupled with the ToR-ORd model. (Figure 2). The blue curves obtained with the initial sampling are far away from the target active tension transient from the original publication in (Land et al., 2017), while the red curves obtained by sampling the restricted regions are close to the target curve.

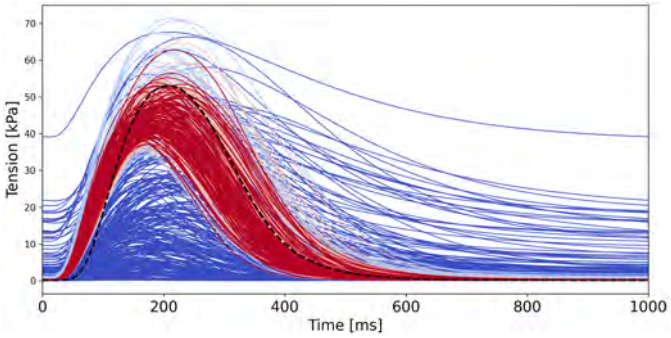

Fig. 2. **ToR-ORd+Land model HM Results.** Active tension transients from the initial (blue) and from the restricted (red) parameter space compared to the target active tension transient from (Land et al., 2017).

4. CONCLUSION

This work shows how GPE, GSA and HM can provide a systematic workflow to fit models to available experimental and clinical data while keeping the number of required simulation runs at a treatable level.

ACKNOWLEDGEMENTS

This study received support from the UK Engineering and Physical Sciences Research Council (EP/M012492/1, NS/A000049/1, EP/L015226/1, EP/P01268X/1 and EP/P010741), the Wellcome EPSRC Centre for Medical Engineering (NS/A000049/1 and WT 203148/Z/16/Z), the British Heart Foundation (PG/15/91/31812 and PG/13/37/30280), the National Institute of Health (NIH R01-HL152256), the European Research Council (ERC PREDICT-HF 864055) and Kings Health Partners London National Institute for Health Research (NIHR) Biomedical Research Centre. Prof Chris Oates was supported by the Lloyd's Register Foundation through the Alan Turing Institute, UK.

REFERENCES

Land, S., Park-Holohan, S.J., Smith, N.P., dos Remedios, C.G., Kentish, J.C., and Niederer, S.A. (2017). A model of cardiac contraction based on novel measurements of tension development in human cardiomyocytes. *J Mol Cell Cardiol*, 106, 68–83.

Longobardi, S., Lewalle, A., Coveney, S., Sjaastad, I., Espe, E.K., Louch, W.E., Musante, C.J., Sher, A., and Niederer, S.A. (2020). Predicting left ventricular contractile function via gaussian process emulation in aortic-banded rats. *Philosophical Transactions of the Royal Society A*, 378(2173), 20190334.

Tomek, J., Bueno-Orovio, A., Passini, E., Zhou, X., Minchole, A., Britton, O., Bartolucci, C., Severi, S., Shrier, A., Virag, L., et al. (2019). Development, calibration, and validation of a novel human ventricular myocyte model in health, disease, and drug block. *Elife*, 8, e48890.

Assessment and forecast of EDA Company Viability in Case of Disruptive Technological Events

Galia Marinova*. Aida Bitri**

**Technical University of Sofia, 8 Kl. Ohridski Blvd, 1000, Bulgaria, (gim@tu-sofia.bg).*
*** Technical University of Sofia, 8 Kl. Ohridski Blvd, 1000, Bulgaria;*
Aleksander Moisiu University, 1001 Durres, Albania, (aidabitri@uamd.edu.al).

Abstract: This paper proposes a model to analyze, assess and forecast the viability of Electronic Design Automation (EDA) companies that operate in a dynamic environment. Due to the technological advancements and the specific characteristics of this industry, companies that operate in the market are under continuous pressure to innovate their products, to find new policies of investment, strategies and forms of business model organization to maintain viability. Knowledge-intensive industries, like EDA, are known for needing continuous access to new knowledge, talents, and experts and a lot of research and development activity. Not all companies can provide in time the necessary results and innovation to compete in the market, so most of them dissolve, merge, or are being acquired.

Keywords: EDA industry, Company viability, Forecasting, Disruptive Technologies, Technological factors.

1. INTRODUCTION

The research in the current paper is in the framework of a study of the dynamics of Electronic Design Automation (EDA) companies. EDA is a relatively new business sector emerging, following, and enabling the first the semiconductor and later the high-tech industry, manufacturing, and mass production. The first data available are from the year 1961, the sector is about 60 years old. EDA companies need highly specialized staff with STEM expertise. EDA companies are strongly affected by technology development factors and disruptive technological events (innovations) lead to numerous mergers and acquisitions (M&A), emerging start-ups, and the disappearance of those who cannot follow. Paper (Bitri, A. et al, 2020) addresses the global place of EDA companies (EDA_C) and their business models (BM) in the current hyperconnected world, paper (Marinova, G. et al, 2021b**)** proposes formalization and parameters of the BM of an EDA company and paper (Marinova, G. et al, 2021a**)** describes a project of Database with parameters' values for several hundreds of EDA companies. Some initial observations and first statistical data are presented in the paper. Vu that the total number of EDA companies doesn't overpass 1000 and there are about 10 leaders with more than 70% of global market shares the study is fully representative.
The paper proposes a formalization of the Viability of an (EDA) Company in case of disruptive technological events or innovation. It will allow to predict the effect of a disruptive technological event (innovation) on the Viability of EDA company and to help adjust its investments and BM for increasing its Viability.
The study described in (Marinova, G. et al, 2021b) identifies 3 main technological factors: TF1 – The Moor's Law; TF2 – The System integration Law; TF3 - The technological disruptive innovation events – specified by a list of events (innovations) in years. The current paper focuses on the effect of TF3 which has rather a random character and the effect is strongly disruptive.
On a graph from (Marinova, G. et al, 2021a) are presented the numbers of funded and M&A EDA companies in years, concerning TF3 events. The formalization of the Viability of EDA companies in the paper considers the effect of TF3.
The current market expanders for EDA companies are Internet of things IoT and Digital twins. Some of the incoming technological disruptions are nanotechnologies, quantum computers, bioinspired engineering. The formalization of the Viability will help to determine which of the EDA_C has the potential to survive the new Disruptive technological events and/or adapt and expand generation technological innovations themselves or profiting from market expanders.

2. PROBLEM DEFINITION AND GENERAL FORMULATION OF THE VIABILITY IN EDA

The following definitions and notations are adopted:
$\boldsymbol{\mathcal{V}}$ – The viability of a company;
EDA_C(J) – Electronic design automation company J where J=1, N;
N - number of EDA companies studied;TF3(I) – Technology factor 3, technological innovation(I), Technological innovations are listed in time per year;
$\boldsymbol{\mathcal{V}}$(EDA_C(J)) – viability of EDA_C(J);
$\boldsymbol{\mathcal{G}}$(TF3(I)) – generator of the innovation TF3(I);
$\boldsymbol{\mathcal{R}}$(TF3(I)) – reaction to TF3(I) with a Delay $\boldsymbol{\mathcal{D}}$(J,I);
$\boldsymbol{\mathcal{D}max}$ – maximal delay admissible for viability;
D(J, I) – delay of the reaction of the company EDA_C(J) to the innovation TF3(I); FD – factor of the delay;
The investment of the EDA company in R&D is a precondition for the generation of innovations G(TF3(I)).

Table I Feathers of the tool as the main product of EDA_C

Interfaces/Periphery	Math	SW&HW description languages	Processing power	Models	Application area Market
• Graphics • Multimedia • Data acquisition (signal, image) records or real-time. • Communications • Measurements + equipment, devices and testbench setups associated to interfaces	• General math • System of nonlinear integro-differential equations • Digital synthesis and analysis • Digital signal processing • Finite element method • Boundary element method • Finite state machine • Approximations • Topological Place&Route methods • Telegraph equations • Probability&Statistics • Optimization • AI(DNN) • 3D	C C++ CSharp Phyton Matlab VHDL Verilog	Computer Super-computer	Models Digital twins Ips	•Semiconductor •Telecom •Data Centers •Cybersecurity •Automotive •Avionics •Military •Industry •Cyberphysical systems •IoT

The reaction and its delay are a result of the Sensing and Learning processes (Marinova, G. et al, 2021a**)** in the EDA company and it is related to Human resources HR talents (T_HR) and the connection with academia CA(J).
The viability of the EDA company can be expressed as:
$\mathcal{V}$(EDA_C(J)=$\mathcal{G}$(TF3(I))+$\mathcal{R}$(TF3(J)xF$\mathcal{D}$=
$\mathcal{G}$(TF3(I))+$\mathcal{R}$)TF3(I),$\mathcal{D}$(J,TF3(I))<$\mathcal{D}max$)

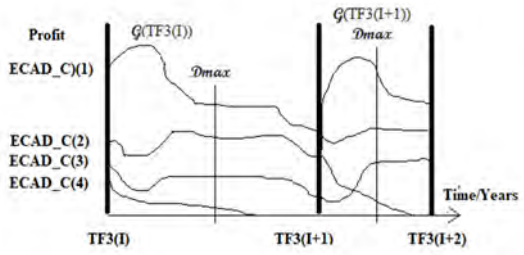

Figure 1. Profit curves of EDA companies

Figure 1 draws a hypothetical curve of the profit of an EDA_C between consecutive Technological disruption events TF3(I), TF3(I+1) and TF3(I+2). If EDA_C generated the TF(I), its profit is maximal, the profit of other EDA_C depends on their Reactions and the Delays of the reactions. A delay superior to $\mathcal{D}max$ leads the EDA_C to disappearance.
This definition of the viability can be implemented to formalize the viability and the rules for its forecast.

3. FEATHERS OF THE TOOL AS A MAIN PRODUCT EDA COMPANY

The main business of an EDA_C is to develop tools. Table I presents the feathers of the tool as the main product of EDA_C and its connection to the market. The feathers are categorized into 6 groups: Interfaces, Mathematical methods, and Solvers (Math), Software and hardware description languages (SW&HW_DL), Processing power (PP), or computer where to tool is run, Models and Application area (AA) representing the Market. These feathers can be connected to innovations, business models and viability of EDA companies.

4. CONCLUSIONS

This paper proposes a model to evaluate the viability of a Business Model that operated in a dynamic environment, such as the Electronic Design Automation Industry. The time and the delay to react to a new technological event or innovation generated by the competitor might be disruptive for the company.

ACKNOWLEDGMENT

This study is realized and partly supported by the CEEPUS network CIII-BG-1103-06-2122, and by the Bulgarian National Science Fund − the project "Mathematical models, methods and algorithms for solving hard optimization problems to achieve high security in communications and better economic sustainability", Grant No: KP-06-N52/7

REFERENCES

Bitri, A., Marinova, G., Hajrizi, E. (2020) Identifying business model characteristics through BM canvas: a case of EDA industry. New Approaches in Innovation, Technology, Education and Development, 143-153.

Marinova, G., Bitri, A. (2021) Data Analysis Environment to Study the Dynamics in Electronic Design Automation Industry, IFAC Conf. TECIS'2021, 14-18 Sept. 2021, Moscow, Russia.

Marinova, G., Bitri, A. (2018) New Business Model for EDA Industry in the Internet of Everything Future. ICEST'2018, June 2018 Sozopol, Bulgaria, pp. 63-66.

Marinova, G., Bitri, A. (2021) Review on Formalization of Business Model Evaluation for Technological Companies with Focus on the Electronic Design Automation Industry, IFAC Conf. TECIS'2021, Sept.2021, Moscow, Russia.

Loeffler, J. (2018). No More Transistors: The End of Moore's Law. [online] Interestingengineering.com. Available at: https://interestingengineering.com/no-more-transistors-the-end-of-moores-law.

An integrated multiscale CFD model of the human heart

Alberto Zingaro [*,⋆] **Luca Dede'** [*] **Alfio Quarteroni** [*,**]

[*] *MOX, Dipartimento di Matematica, Politecnico di Milano, Piazza Leonardo da Vinci 32, 20133, Milan, Italy.*
[**] *Chair of Modeling and Scientific Computing (CMCS), Institute of Mathematics, École Polytechnique Fédérale de Lausanne, Station 8, Av. Piccard, CH-1015 Lausanne, Switzerland (Professor Emeritus).*

Abstract: We introduce a CFD model for the numerical simulation of the heart hemodynamics in both physiological and pathological conditions, by accounting for all the physical processes that influence cardiac flows: moving domain and interaction with electromechanics, transitional-turbulent flows, cardiac valves and coupling with the external circulation. To impose a physiological displacement of the domain boundary, we employ a 3D ventricular electromechanical model coupled to a lumped-parameter (0D) closed-loop model of the circulation and the remaining cardiac chambers. To extend the ventricular motion to the endocardium of the remaining heart, we introduce a novel preprocessing procedure that combines an harmonic extension of the electromechanical displacement with the motion of the atria based on the 0D model. We thus obtain a one-way coupled electromechanics-fluid dynamics model in the ventricle(s). To better match the 3D CFD with blood circulation, we also couple the 3D CFD model to the 0D circulation model. We obtain a multiscale coupled 3D-0D fluid dynamics model that we solve via a segregated numerical scheme. We carry out numerical simulations for a healthy heart and we validate our model by showing that significant hemodynamic indicators are correctly reproduced.

Keywords: Cardiac hemodynamics, cardiac valves, circulation, transitional flows, mitral valve regurgitation, computational fluid dynamics, multiscale models, finite element method.

1. INTRODUCTION

The study of cardiac blood flow aims at enhancing the knowledge of the heart physiology, assessing the pathological conditions and possibly improving the clinical treatment and therapeutics. In the clinical routine, blood flow analysis is conventionally based on imaging techniques. However, their space and time resolution is not accurate enough to capture small-scales features as recirculation regions, possible regions of transition to turbulence and the formation, interaction and dissipation of small coherent structures. Furthermore, imaging-based techniques cannot provide relevant fluid dynamics indicators such as the wall shear stress (WSS) which is correlated with the function and the remodeling of the heart chambers (Ngo et al. (2019)). In this respect, computer based numerical simulations – also known as in silico simulations – of the heart and circulation represent a valuable tool to quantitatively assess the cardiac function and to enhance the understanding of cardiovascular diseases.

The numerical simulations of cardiac blood flows should account for several aspects that characterize heart's hemodynamics (Chnafa et al. (2014)). The strong interaction between the fluid and the electromechanical activity of the heart yields a complex multiscale and multiphysics system involving the interaction of several physical processes. Furthermore, the cardiac valves affect the blood motion and change the topology of the fluid domain during the heartbeat. In addition, a CFD simulation of the heart should also account for the transitional regime of the blood flow occurring in the heart chambers and, eventually, also for the strict influence between the local dynamics and the hemodynamics of the surrounding circulatory system. In this work, we introduce a CFD model of the heart accounting for all the aforementioned aspects.

2. MODELS AND METHODS

We model the blood flow in the heart chambers via the incompressible Navier-Stokes (NS) equations expressed in an Arbitrary Lagrangian Eulerian (ALE) framework to account for moving domains. To model the presence of valves in the fluid, we use the Resistive Immersed Implicit Surface (RIIS) method, in which the effect of the immersed surface in the blood is enforced via a penalization technique by introducing a resistive term in the momentum balance of the NS equations (Fedele et al. (2017)).

To prescribe a physiological displacement to the domain boundary, we employ the ventricular electromechanics (EM) model developed in Regazzoni et al. (2022); Piersanti et al. (2022) coupled to the surrounding circulation described by a 0D lumped-parameter hemodynamic model. We introduce a novel procedure that combines an

⋆ alberto.zingaro@polimi.it

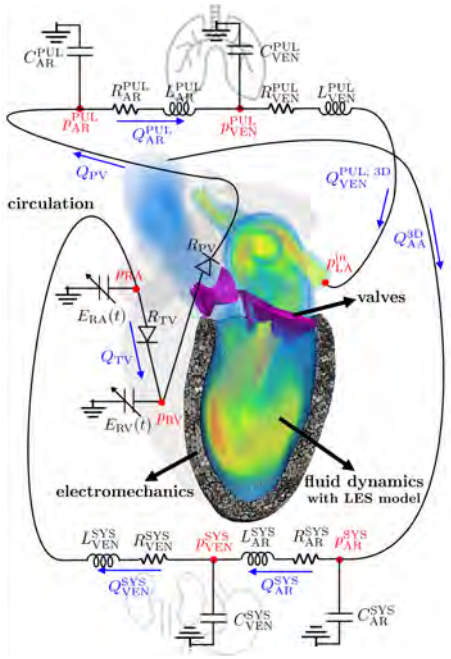

Fig. 1. The integrated multiscale CFD model of the heart.

harmonic extension of the the ventricular displacement on the remaining heart chamber(s) based on Laplace-Beltrami equation, and a volume-based model of the atria tuned on the basis of the 0D circulation model (Zingaro et al. (2022)). This yields an integrated and multiphysics problem in which fluid dynamics is one-way coupled to EM in the ventricle(s). The model introduced can directly be applied also to the right heart and to the whole heart geometry.

To address the reciprocal influence between the hemodynamics of the heart chambers and the one of the surrounding cardiocirculatory system, we rely on the geometric multiscale modeling (Quarteroni et al. (2016)). We couple the 3D CFD model of the heart with the 0D lumped parameter model closed-loop model of the circulation introduced in Regazzoni et al. (2022). The interfaces conditions of the 3D-0D CFD model consists of the enforcement of the continuity of pressures and flowrates on the artificially chopped boundaries. In Figure 1 we represent the overall integrated and multiscale computational model.

We discretize the NS-ALE-RIIS equations in space via the finite element (FE) method and in time by means of backward differentiation formulas. We use a Variational Multiscale - Large Eddy Simulation method (Forti and Dede' (2015)) to get a stable formulation of the NS equations discretized by means of FE method; to stabilize the advection-dominated regime and to account for turbulence modeling within the framework of LES (Zingaro et al. (2021)). We discretize the system of ODEs of the 0D circulation model through a 4^{th} order explicit Runge-Kutta scheme. We numerically solve the 3D-0D CFD model by means of a segregated numerical scheme (Zingaro et al. (2022)).

3. NUMERICAL RESULTS

We simulate the heart hemodynamics in physiological conditions and we show that several hemodynamic indicators and flow patterns are correctly reproduced by the computational model when compared with in-vivo data. Furthermore, we simulate pathological scenarios as mitral valve regurgitation and we quantify clinical indicators to grade the severity of the pathology.

ACKNOWLEDGEMENTS

This work has been supported by the ERC Advanced Grant iHEART, "An Integrated Heart Model for the simulation of the cardiac function", 2017–2022, P.I. A. Quarteroni (ERC-2016-ADG, project ID: 740132).

REFERENCES

Chnafa, C., Mendez, S., and Nicoud, F. (2014). Image-based large-eddy simulation in a realistic left heart. *Computers & Fluids*, 94, 173–187.

Fedele, M., Faggiano, E., Dede', L., and Quarteroni, A. (2017). A patient-specific aortic valve model based on moving resistive immersed implicit surfaces. *Biomechanics and Modeling in Mechanobiology*, 16(5), 1779–1803.

Forti, D. and Dede', L. (2015). Semi-implicit BDF time discretization of the Navier–Stokes equations with VMS-LES modeling in a high performance computing framework. *Computers & Fluids*, 117, 168–182.

Ngo, M.T., Kim, C.I., Jung, J., Chung, G.H., Lee, D.H., and Kwak, H.S. (2019). Four-dimensional flow magnetic resonance imaging for assessment of velocity magnitudes and flow patterns in the human carotid artery bifurcation: Comparison with computational fluid dynamics. *Diagnostics*, 9(4), 223.

Piersanti, R., Regazzoni, F., Salvador, M., Corno, A.F., Vergara, C., Quarteroni, A., et al. (2022). 3d–0d closed-loop model for the simulation of cardiac biventricular electromechanics. *Computer Methods in Applied Mechanics and Engineering*, 391, 114607.

Quarteroni, A., Veneziani, A., and Vergara, C. (2016). Geometric multiscale modeling of the cardiovascular system, between theory and practice. *Computer Methods in Applied Mechanics and Engineering*, 302, 193–252.

Regazzoni, F., Salvador, M., Africa, P., Fedele, M., Dedè, L., and Quarteroni, A. (2022). A cardiac electromechanical model coupled with a lumped-parameter model for closed-loop blood circulation. *Journal of Computational Physics*, 457, 111083.

Zingaro, A., Dede', L., Menghini, F., and Quarteroni, A. (2021). Hemodynamics of the heart's left atrium based on a Variational Multiscale-Les numerical method. *European Journal of Mechanics-B/Fluids*, 89, 380–400.

Zingaro, A., Fumagalli, I., Dede, L., Fedele, M., Africa, P.C., Corno, A.F., and Quarteroni, A. (2022). A geometric multiscale model for the numerical simulation of blood flow in the human left heart. *Discrete and Continuous Dynamical Systems-S*, 15(8), 2391–2427.

Structure Graph of Production: A basic concept for process data integration and analysis

Wan Li*, Michael Winter*, Christian Roos, Tobias Kleinert***

** Chair of Information and Automation Systems for Process and Material Technology, RWTH Aachen University 52064 Aachen, Germany (e-mail: {w.li, m.winter, kleinert}@plt.rwth-aachen.de)*
*** International Partners in Glass Research (IPGR) e.V., Krantzstr. 7, 52070 Aachen (e-mail: Christian.roos@ipgr.com)*

Keywords: interdisciplinary modelling, integrated system model, causal graph, knowledge representation

1. INTRODUCTION

With the development of Industry 4.0 technologies, numerous manufacturers are establishing production digitization as their corporate strategy to maintain and increase competitiveness. More and more data on production facilities and processes are collected and stored to answer recurring questions e.g., causes of machine downtimes or product quality defects, so that measures for correcting the failure can be intervened as early as possible.

For such cause-effect analysis, influencing factors have to be gathered, evaluated, and visually represented. Potential influencing factors can be found using priori knowledge about the production plant, e.g., the plant structure presented in a CAE (computer aided engineering) model or the project configuration in a control application program. Such prior knowledge is considered as context information to the production data of the plant, however, there is usually no direct link created to the production data. Therefore, influencing factors and their belonging production data have to be gathered and interrelated with laborious manual efforts, and the established relationships are often not reusable for new tasks of causal analysis. In addition, heterogeneity in production data regarding, e.g., data structure and sampling rate, complicates the integration of production data needed for analysis. Furthermore, the influencing factors found have to be represented in an easy human-readable way. At last, saving the context information, the influencing factors, and their relationships in a reusable way is challenging as well.

To address the above described challenges in managing and representing of production data for data analysis purposes, manufacturers need a sensible and practical concept. In this paper, we present a novel and generalized concept, the *Structure Graph of Production (SGP).*

2. CONCEPT OF THE SGP

The SGP is a graph model based on the *phase model of production (PMP)* (Polke 1992). It includes property clusters representing components of the considered production system, and relationships between the properties as well as the PMP elements (Fig. 1).

A production system in the current consideration is composed of production processes, machines, raw materials, produced (intermediate) products, and field devices (including actuators, measuring devices), which are abstractly modelled with clusters of properties of these components (Fig. 1).

Nodes and relationships are the most basic model elements that build the property clusters and the PMP. Fig. 1. shows the generalized SGP class with nodes and relationships, which are specialized as shown in Fig. 4 and Fig. 5, respectively.

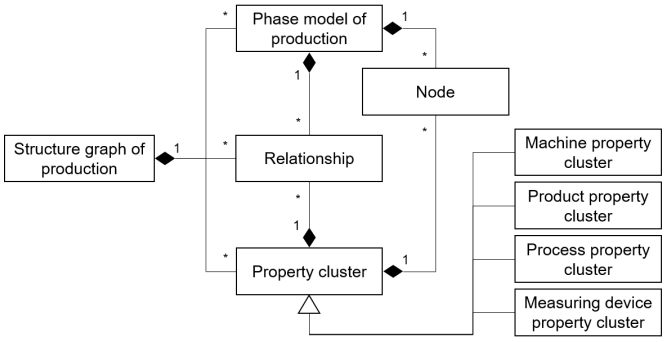

Fig. 1. General SGP class model

In the following, the concept of SGP is explained with a demonstrative example of a heating system of our laboratory plant. Its piping and instrumentation diagram (P&ID) is shown in Fig. 2. Pump N13 feeds the outflow from an upstream tank B1 into a heat exchanger and feeds it further to the downstream processes through valve Y16. A temperature sensor (T15) and a flow meter (F17) measures the process and product properties, respectively. The pumping power, heating power and valve opening are controlled automatically.

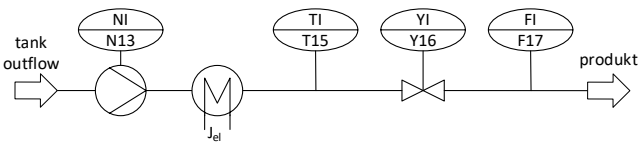

Fig. 2. P&ID of a part of a laboratory plant

With the given information, the SGP is created as shown in Fig. 3. The processes and products are modelled as PMP

represented by the blue nodes and edges. The respective properties of the heating system components are modelled as nodes and clusters on the side of the PMP elements, which are pipelines with actuators and sensors as well as water.

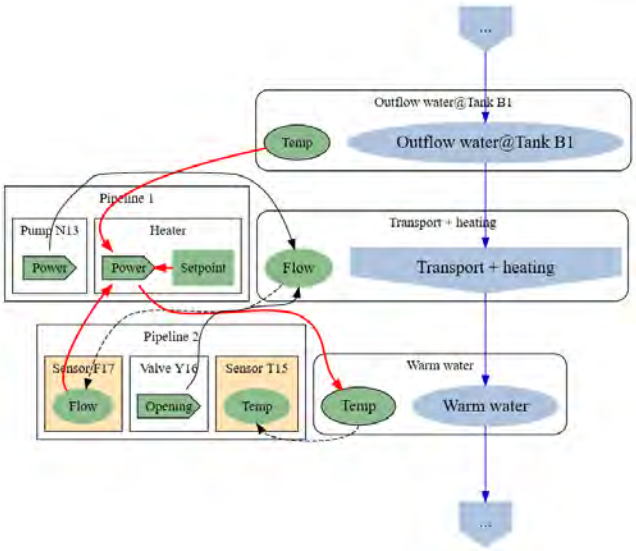

Fig. 3. SGP model of the heating process shown in Fig. 2

Each node (Fig. 4) in SGP has a uniquely identifiable *ID* that can be represented by a textual label. The class node has two subclasses: structural node and property node. A *structural node* can either be a product node (e.g., "warm water") or a process node (e.g., "transport + heating"), representing process steps or products in the PMP. A *Property node* (e.g., the green nodes) describes either a certain aspect of a machine, a product, a process or a measuring device. Each property node has two further attributes: (1) *Associated cluster* to which the node belongs to; (2) *Associated data variable* with basic metadata (e.g., name, data type and location) which are referencing the data stored in a database. The nodes are displayed in corresponding colors and shapes, depending on controllability, control mode and measurability.

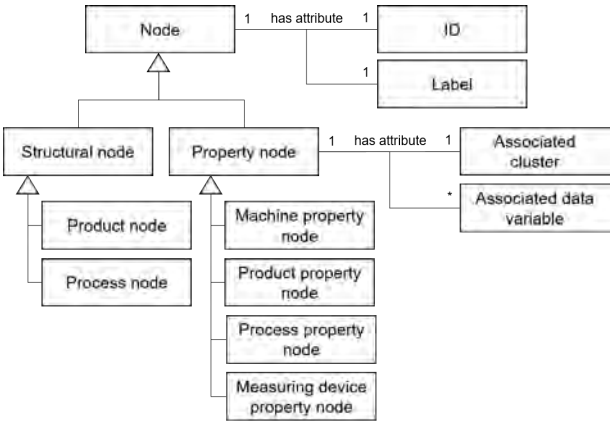

Fig. 4. Node class model

A *relationship* (Fig. 5) is modelled as an *edge* in the graph model, which is represented by a directed line pointing from a source node to a target node. Each relationship is uniquely identifiable in an SGP by its *ID* or by a node tuple (source node, target node). A relationship has two subclasses: structural or influencing relationship. A *structural relationship* represents the direction of the *material flow* in the PMP, or the *data flow* between the property nodes of a measuring device cluster and a machine, product or process cluster, respectively. An *influencing relationship* (causal or correlational) indicates that the source node may have an influence on the target node with a certain probability and intensity, which can be determined by using methods of either data analysis, experimental observation, or expert knowledge (see Section 4). When an influencing relationship is valid, its attribute *isValidated* is set TRUE.

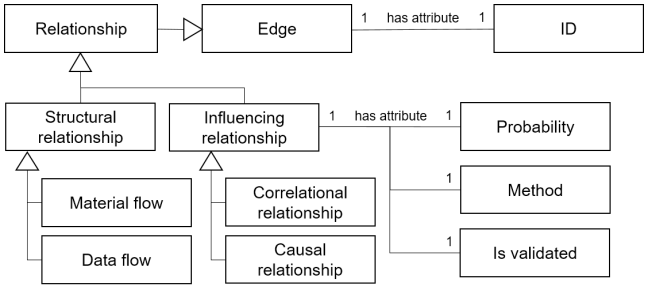

Fig. 5. Relationship class model

6. DISCUSSION

Causal questions can be answered with a combination of process model and data analysis (Pearl 2018). In the concept of SGP, prior knowledge about the production plant is modelled as PMP and clusters of the production system properties. The PMP containing structural relationships and nodes forms the fundamental structure of the SGP, which allows categorization and association of property clusters. The PMP model implies also time constraints for inferencing causal and influencing relationships, because the structural nodes in PMP are arranged regarding the execution sequence of the production processes. In addition, measurements stored in databases are associated with properties of process steps, products and machines using the attribute *associated data variable*. Thus, semantics and metadata of measurements are available, such that the measured data can be extracted, integrated and prepared in an efficient way. Influencing factors of a certain property can be gathered using existing relationships and topological distances between the property nodes. Furthermore, PMP allows the property nodes to be presented in a structured way, so that human can easily interact with the SGP and carry out causal analysis. With the above advantages, the SGP provides a basis for a straight through data integration and analysis. In future work, we will specify the modelling systematics of SGP, and develop SGP towards automated data integration and analysis. Moreover, aspects of changeability, scalability and user-friendly visualization will also be considered.

REFERENCES

Pearl, J. (2018). *The book of why: the new science of cause and effect*. Chap. 10. Basic Books, New York, U.S.

Polke, M. (1992). Phasenmodell der Produktion als nicht-mathematische Präsentationsform für Automatisierungs-aufgaben. *Entwurf komplexer Automatisierungs-systeme*, Braunschweig, Germany

Tensor-train approximation of the chemical master equation and its application for parameter inference

Ion Gabriel Ion [*,**] **Christian Wildner** [**]
Dimitrios Loukrezis [*,**] **Heinz Koeppl** [*,**,***]
Herbert De Gersem [*,**]

[*] *Centre for Computational Engineering, Technische Universität Darmstadt (e-mail: ion@temf.tu-darmstadt.de).*
[**] *Department of Electrical Engineering, Technische Universität Darmstad.*
[***] *Centre for Synthetic Biology, Technische Universität Darmstadt.*

1. INTRODUCTION

Traditional chemical kinetic models use ordinary differential equations (ODEs) to predict the concentrations of the involved molecule types (Gillespie (1992)). The evolution of the corresponding probability distribution is given by the chemical master equation (CME) which, in principle, can be solved by numerical integration. Unfortunately, the computational cost grows exponentially with the number of species, due to the fact that the system states must be labeled explicitly to cast the CME into a ODE. A framework for performing Bayesian inference tasks for the parameter-dependent CME is suggested, by exploiting the so called tensor-train (TT) decomposition to approximate the joint distribution over the CME states and parameters (see Ion et al. (2021)). For that purpose, we construct an explicit representation of the evolution operator in the TT format and show that it can be constructed without ever assembling the corresponding matrix. The TT format has the advantage that the storage requirement scales linearly with respect to the number of dimensions, while at the same time being a numerically robust tensor decomposition. To that end, we combine the state space and the parameter space into a higher-dimensional tensor-product space. The parameter dependence is expressed by means of a B-spline basis. Since typically every reaction is governed by an individual rate constant, the parameters can be seamlessly included in the tensor representation, thus allowing for efficiently solving the joint system. In practice, however, the system parameters are often unknown. Therefore, we develop a framework for filtering, smoothing, and parameter inference based on the efficient TT representation of the joint system.

2. TENSOR-TRAIN DECOMPOSITION FOR THE CHEMICAL MASTER EQUATION

2.1 Chemical master equation

The chemical master equation describes the time evolution of the probability mass function (PMF) of well-mixed reaction system with d species (Gillespie (1992)). After the state space truncation of the PMF $\mathbf{p}$ to a $n_1 \times \cdots \times n_d$ tensor, the CME is represented as a large linear system of ODEs

$$\frac{\mathrm{d}\mathbf{p}(t)}{\mathrm{d}t} = \mathbf{A}\mathbf{p}(t),$$

where $\mathbf{A}$ is a tensor operator with size $(n_1 \times \cdots \times n_d) \times (n_1 \times \cdots \times n_d)$. Parameters that govern the reactions can be included in the framework, leading to the following parameter dependent CME

$$\frac{\mathrm{d}\mathbf{p}(t,\boldsymbol{\theta})}{\mathrm{d}t} = \mathbf{A}(\boldsymbol{\theta})\,\mathbf{p}(t,\boldsymbol{\theta}). \tag{1}$$

For the joint state-parameter density together with the time dependency, a tensor-product basis representation in used:

$$\mathsf{p}_{\boldsymbol{i}}(t,\boldsymbol{\theta}) \approx \sum_j \sum_{\boldsymbol{l}} \mathbf{p}_{\boldsymbol{i}\boldsymbol{l}j} b_j(t) L_{\boldsymbol{l}}(\boldsymbol{\theta}), \tag{2}$$

where $\mathbf{p}$ is $d + N_p + 1$ dimensional tensor, $\{b_j\}_j$ is the basis for the time dependency (Chebyshev polynomials) and $\{L_{\boldsymbol{l}}\}_{\boldsymbol{l}}$ is a tensor-product basis for the parameter to accommodate parameter dependency (product of univariate B-splines). Galerkin projection is then used to derive an extended multilinear system for $\mathbf{p}$. Since the unknown $\mathbf{p}$ is high-dimensional, the storage requirements grow exponentially and therefore compression schemes are employed for the unknown $\mathbf{p}$ and the multilinear system.

2.2 Tensor-trains

An array $\mathbf{x}$ of shape $n_1 \times \cdots \times n_d$ is said to be in the TT format if it can be elementwise written as

$$\mathbf{x}_{\boldsymbol{i}} = \sum_{r_1=1}^{R_1} \sum_{r_2=1}^{R_2} \cdots \sum_{r_{d-1}=1}^{R_{d-1}} \mathbf{g}^{(1)}_{1 i_1 r_1} \mathbf{g}^{(2)}_{r_1 i_2 r_2} \cdots \mathbf{g}^{(d)}_{r_{d-1} i_d 1}, \tag{3}$$

where the three-dimensional tensors $\mathbf{g}^{(k)}$ are called the TT-cores and $\boldsymbol{R} = (1, R_1, ..., R_{d-1}, 1)$ are called the TT-ranks (Oseledets (2011) provides a detailed look). The storage complexity becomes linear with respect to d and once the tensors are converted in the TT-format, the basic operations (elementwise addition, multiplication, summing over indices) can be efficiently performed without building the full d-dimensional object. The construction of a low-rank TT-decomposition provides an error bound and rank reduction can be also performed within a given accuracy (see Oseledets (2011) for more details). In addition

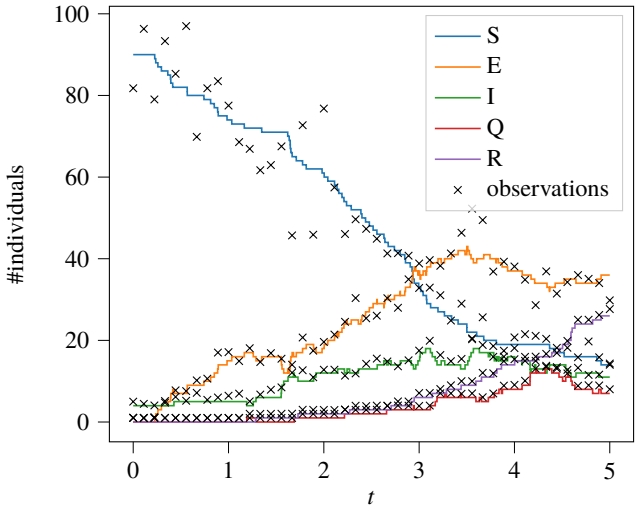

Fig. 1. Noisy observation sample for the SEIQR model (sample size is 45).

to that, multilinear systems can be solved directly in the TT-format using optimization based methods (see Dolgov and Savostyanov (2014)). The CME operator **A** presented in the previous section can be directly represented in the TT-format and the multilinear system arising from the Galerkin projection can be as well solved in the TT-format.

2.3 Inference tasks

Given a number of noisy observations of a system governed by a CME with unknown governing parameters, one can be interested in finding those parameters. A probabilistic description of the distribution over the parameter space (called posterior) can be obtained using Bayes rule. As presented in Ion et al. (2021), updating the posterior implies solving the CME and constructing the likelihood (conditional probability of observing the data given the underlying state of the system). Both of the steps are efficiently performed using the TT-format without being affected by the curse of dimensionality, since both the observation model and the CME operator can be computed directly in the TT-format. A prior PDF over the parameters can be included in the framework.

3. RESULTS

Numerical experiments have been performed to showcase the advantages of the proposed framework in terms of accuracy and computational efficiency Ion et al. (2021). Among them, we present here only he SEIQR model. It has 5 species: susceptible (S), exposed (E), infected (I), quarantined (Q) and recovered (R) involved in 9 reactions with 4 parameters assumed as unknown. From a sample path, noisy observations are generated (see Fig. 1) and the TT CME solver is used to infer the parameters with the dimension of the parameter space basis is 64 for every parameter. Marginals of the posterior are shown in Fig. 2, comparing the obtained posterior with the prior (green dashed line) and also displaying the exact parameter.

The execution time for a TT-solver is $\approx$ 55 minutes with a maximum posterior size in the QTT-format of $\approx$ 30 MB. As a comparison, the chosen state truncation

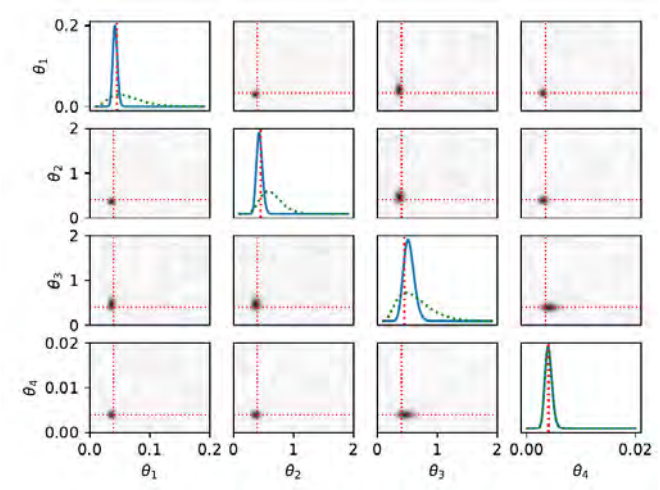

Fig. 2. Posterior marginal distributions for the four unknown reaction rates of the SEIQR model. The exact parameters are marked with the red dashed lines and the prior with green dashed lines.

of $(128, 64, 64, 32, 32)$ would require $\approx$ 4.2 GB only for storing the state for one parameter realization. The storage complexity for the parameter-dependent CME operator in the QTT format is $\approx$ 200 KB.

4. CONCLUSION

We presented a method based on the TT decomposition to solve the CME, either in its standard form or including parameter dependencies, and approximate the joint distribution over the state-parameter space, including the time dependency as well. Using the considered TT-framework, inference tasks such as parameter identification can be performed accurately and efficiently.

ACKNOWLEDGEMENTS

The work of I.G. Ion is supported by the Graduate School Computational Engineering within the Centre for Computational Engineering at Technische Universität Darmstadt. D. Loukrezis is supported by the German Federal Ministry for Education and Research (BMBF) via the research contract 05K19RDB.

REFERENCES

Dolgov, S.V. and Savostyanov, D.V. (2014). Alternating minimal energy methods for linear systems in higher dimensions. *SIAM Journal on Scientific Computing*, 36(5), A2248–A2271. doi:10.1137/140953289.

Gillespie, D.T. (1992). A rigorous derivation of the chemical master equation. *Physica A: Statistical Mechanics and its Applications*, 188(1), 404–425. doi: https://doi.org/10.1016/0378-4371(92)90283-V.

Ion, I.G., Wildner, C., Loukrezis, D., Koeppl, H., and De Gersem, H. (2021). Tensor-train approximation of the chemical master equation and its application for parameter inference. *The Journal of Chemical Physics*, 155(3), 034102. doi:10.1063/5.0045521.

Oseledets, I. (2011). Tensor-train decomposition. *SIAM J. Sci. Comput.*, 33, 2295–2317.

Non-linear RF Device Behavioral Models based on Hammerstein-Wiener Systems

Martin K. Steiger * **Kai Bittner** * **Hans-Georg Brachtendorf** *

* *University of Applied Sciences Upper Austria, 4232 Hagenberg, Austria*

Abstract: Creating behavioral models for radio frequency (RF) devices is a challenging task. Most approaches require a substantial prior knowledge of the physical structure in order to be able to generate suitable mathematical models for the desired characteristics. However, since it is usually not attractive for manufacturers to pass on extensive knowledge about internal components to third parties, one has to rely mainly on black- or gray-box models. An approach is to fit a parameterized model based on representative measurement data, following the example of the Hammerstein-Wiener models. With this approach, only simple linear least squares problems have to be solved and special structures encourage the use of efficient solution methods. In this paper, the general fitting procedure will be discussed and suggestions for successful device modeling will be provided

Keywords: Nonlinear system identification, Frequency domain identification, Time series, Gray box modeling, Recursive identification

1. INTRODUCTION

In order to integrate various new components from different manufacturers into device simulators, the dynamic behavior of the component under defined operating conditions must be determined as precisely as possible. However, since the physical structure or other internal components are rarely published by the respective semiconductor manufacturers for such purposes, the simulation software usually relies on the models they provide. If these do not exist at all, or only for special simulators, one is faced with a problem. The only remaining option is to create a gray-box model, which is associated with various challenges.

2. HAMMERSTEIN-WIENER MODELS

The main challenge one is facing when creating a gray-box model is the choice of an appropriate structure. Here a variety of possible models may apply, ranging from classical RF approaches such as the X-parameter model or even AI models such as neural networks. In this paper, the focus is on a model that is composed of classical elements of signal and system theory, the so-called Hammerstein-Wiener model, and its possible application in the field of RF devices.

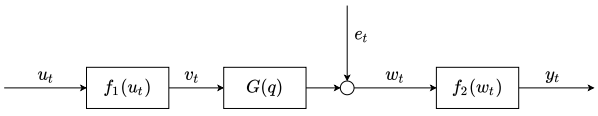

Fig. 1. Hammerstein-Wiener Block Diagram

2.1 Structural Overview

As displayed in Figure 1, a Hammerstein-Wiener model consists of a series connection of an arbitrary non-linear mapping function $f_1(\cdot)$, a discrete LTI system $G(q)$ with the delay operator q^{-1} and another non-linear function $f_2(\cdot)$. We assume that all of these sub-blocks can be described with a set of parameters which may be adapted to fit the input and output measurement data of an actual RF device. Since the Hammerstein-Wiener model is a discrete-time system, these must be available in the form of time domain samples

$$\begin{aligned} Y &= (y_1 \cdots y_N) \\ U &= (u_1 \cdots u_N) \end{aligned} \tag{1}$$

where N is the number of measurement samples. In the following considerations we assume u_t, y_t etc. to be a single sample out of a given measurement series. Based on the block diagram in Figure 1, the Hammerstein-Wiener model is given by

$$\begin{aligned} v_t &= f_1(u_t) \\ w_t &= G(q)v_t + e_t \\ y_t &= f_2(w_t) = f_2\left[G(q)f_1(u_t) + e_t\right] \end{aligned} \tag{2}$$

where $f_1(\cdot)$ and $f_2(\cdot)$ are set to be continuous, $f_2(\cdot)$ is furthermore monotone and invertible and w_t is disturbed by a sample e_t of a stationary stochastic process with zero mean. $G(q)$ is an arbitrary transfer function containing the delay operator q^{-1}. The nonlinear functions f_1 and f_2 are approximated with cubic splines as defined in Zhu (2002)

$$\begin{aligned} f_1(u_t) &= \sum_{k=1}^{m_1-2} \alpha_k |u_t - \tilde{u}_k|^3 + \alpha_{m_1-1} + \alpha_{m_1} u_t \\ f_2(w_t) &= \sum_{k=1}^{m_2-2} \beta_k |w_t - \tilde{w}_k|^3 + \beta_{m_2-1} + \beta_{m_2} w_t \end{aligned} \tag{3}$$

where $\tilde{u}_k$ and $\tilde{w}_k$ represent the spline knot sequences. It is established practice to select the spline knots according to the dynamic range of the function argument. However, this formulation cannot be applied as it is, since w_t can not be measured. It is replaced in the course of this section. For the linear time-invariant system $G(q)$ we select a

Box-Jenkins model, which may be replaced with a higher order auto-regressive model with exogenous input (ARX) of order n that reads

$$A(q)w_t = B(q)v_t + e_t \tag{4}$$
$$w_t = B_1 v_{t-1} + ... + B_n v_{t-n} - A_1 w_{t-1} - ... - A_n w_{t-n}$$

Since the stochastic process e is used to approximate the model error, the objective function $V(\Theta, Z)$ for the upcoming optimization is given by

$$e_t = A(q) f_2^{-1}(y_t) - B(q) f_1(u_t) \tag{5}$$
$$f_2{}^{-1}(y_t) = \sum_{k=1}^{m_2-2} \gamma_{|} y_t - \tilde{y}_k|^3 + \gamma_{m_2-1} + \gamma_{m_2} y_t$$
$$Z = [u_1, ..., u_N, y_1, ..., y_N], \Theta = [A_1, ..., B_1, ..., \gamma_1, ..., \alpha_1, ...]$$
$$V(\Theta, Z) = \frac{1}{N} \sum_{t=1}^{N} e_t^2$$

where the inverse of f_2 is approximated with another spline model with measurable input dynamics for y_t and Θ contains the parameters of the Hammerstein-Wiener model.

2.2 Optimization Process

The starting point for the following iterative optimization procedure also defined in Zhu (2002) is based on a small-signal analysis of a non-linear device. With low dynamic ranges, these usually behave almost linearly, which simplifies an initial estimate of the linear ARX model. For this purpose, the following optimization criterion is defined

$$\sum_{t=1}^{N} \left(A_{(0)}(q) f_2^{-1}{}_{(0)}(y_t) - B_{(0)}(q) f_{1(0)}(u_t) \right)^2 \rightarrow \min \tag{6}$$

where $A_{(0)}(q)$ and $B_{(0)}(q)$ represent the initial ARX coefficients. The non-linear functions $f_1(\cdot)$ and $f_2^{-1}(\cdot)$ are set as identity for this initial estimate. For the subsequent optimization the following steps are repeated until a target norm has been reached. Therefore we are introducing an iteration index i and mark fixed components with the hat-notation

Step 1: Determine the spline coefficients α_k for f_1 by solving a linear least square problem for fixed $\hat{A}_{(i)}(q)$, $\hat{B}_{(i)}(q)$ and $\hat{f}_{2(i)}^{-1}(y_t)$

$$\sum_{t=1}^{N} \left(\hat{A}_{(i)}(q) \hat{f}_{2(i)}^{-1}(y_t) - \hat{B}_{(i)}(q) f_{1(i+1)}(u_t) \right)^2 \rightarrow \min$$

Step 2: Determine the spline coefficients γ_k for f_2^{-1} by solving a linear least square problem, where $\hat{A}_{(i)}(q)$, $\hat{B}_{(i)}(q)$ and $\hat{f}_{1(i+1)}[u_t]$ are fixed

$$\sum_{t=1}^{N} \left(\hat{A}_{(i)}(q) f_{2(i+1)}^{-1}(y_t) - \hat{B}_{(i)}(q) \hat{f}_{1(i+1)}(u_t) \right)^2 \rightarrow \min$$

Step 3: The last part of the optimization procedure is analogous to the initial ARX step but with the previously computed splines for $f_1(u_t)$ and $f_2^{-1}(y_t)$. Then one solves the least squares problem

$$\sum_{t=1}^{N} \left(A_{(i+1)}(q) \hat{f}_{2(i+1)}^{-1}(y_t) - B_{(i+1)}(q) \hat{f}_{1(i+1)}(u_t) \right)^2 \rightarrow \min$$

2.3 Modifications

The original idea of this optimization procedure originates from Zhu (2002), but is associated with several limitations there. For example, it is assumed that u_t, y_t and the Hammerstein-Wiener model parameters each represent scalar values. It is therefore only possible to model Single-Input Single-Output (SISO) systems with this approach. However, since this assumption is inadequate for RF devices with multiple ports, a notation for modeling Multiple-Input Multiple-Output (MIMO) systems is proposed in the following where $u_t \in \mathbb{R}^K$ and $y_t \in \mathbb{R}^L$. There are various possibilities to modify the given structure of the Hammerstein-Wiener model so that multivariate data can be approximated. One option are multivariate splines, but a simpler solution is a higher-dimensional ARX model in which the coefficients are represented by matrices. $A_1 ... A_n \in \mathbb{R}^{LxK}$ and $B_1 ... B_n \in \mathbb{R}^{LxK}$ therefore applies. Then it is sufficient to apply scalar spline functions to every element within u_t and w_t similarly to the scalar case in Section 2.2. Another improvement is the use of b-Splines, where the order can be defined flexibly.

3. NUMERICAL TEST

The variants of the Hammerstein-Wiener models presented here have so far proven themselves in practical use, although the proof of convergence is still work in progress. In the course of this work, mainly models from the Cadence AWR Design Environment were used for verification. An example of a frequency-dependent non-linear common emitter amplifier with a two-tone signal at the input port is provided in Figure 2. As expected, the actual measurement data show attenuated artifacts around the harmonics of the input signal (100 kHz), which a Hammerstein-Wiener model ($n = 3$, $m_1 = m_2 = 11$) approximates accurately.

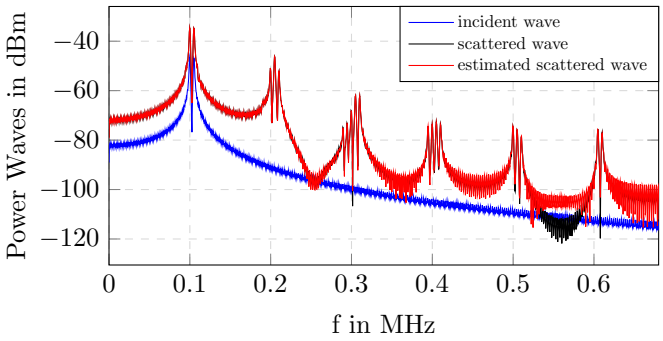

Fig. 2. Scattered Wave Approximation at Port 1

ACKNOWLEDGEMENTS

This project AMOR ATCZ203 has been co-financed by the European Union using financial means of the European Regional Development Fund (INTERREG) for sustainable cross boarder cooperation. Further information on INTERREG Austria-Czech Republic is available at https://www.at-cz.eu/at.

REFERENCES

Zhu, Y. (2002). Estimation of an n-l-n hammerstein-wiener model. *IFAC Proceedings Volumes*, 35(1), 247–252. doi:https://doi.org/10.3182/20020721-6-ES-1901.01027. 15th IFAC World Congress.

Implementation of Recurrence Analysis algorithms in a dashboard for practical application in Football.

Sebastian Hermann*. Martin Lames **. Hendrik Meth *.**

**Faculty of Information and Communication, Stuttgart Media University, Stuttgart, Germany*
(e-mail: sh318@hdm-stuttgart.de)
*** Faculty of Sports and Health Sciences, Technical University of Munich, Munich, Germany*
(e-mail: martin.lames@tum.de),
**** Faculty of Information and Communication, Stuttgart Media University, Stuttgart, Germany*
(e-mail: meth @hdm-stuttgart.de)

1. INTRODUCTION

Football matches are subject to a temporal sequence of different events that result from a series of upstream chains of interaction between players, positional groupings or teams whose goals either conflict or harmonise. In this context, the prevailing idea is to see football matches as dynamic interaction processes with evolving behaviour (Gréhaigne et al., 1997; Lames & McGarry, 2007; Hughes & Franks, 2008). Complex techniques and methods are necessary to adequately analyse these processes (Lames & McGarry, 2007).

Recurrence analysis represents such a method as it examines approximations of a trajectory in a phase space (Lames & Plück, 2015). The core component of the recurrence analysis is the recurrence plot (RP), which visualises the recurring patterns in a matrix (Eckmann et al., 1987). The method is completed by the recurrence quantification analysis (RQA), which expresses the texture and typology of the recurrence plot in a number by means of statistically calculated key figures (see Marwan et al., 2007).

Applications of the recurrence method in professional football can be found in the work of Lames & Plück (2015), Stöckl et al. (2017) and Lames et al. (2021). The results of these studies are promising, as they demonstrate the representational capacity of RPs in football matches (Lames & Plück, 2015), the unpredictability of the players' behaviour (Stöckl et al., 2017), significant correlations with common performance indicators (Lames et al., 2021) and a correlation of RPs and RQA parameters to open play (ibid.).

It is noticable that in all the studies, the recurrence analysis was carried out without the aid of method-specific analysis tools. Instead, the calculations and plots were executed programmatically and with the help of mathematical programming and visualisation libraries (e.g. Lames et al., 2021). This circumstance is consistent with the authors' knowledge that, at the time of writing, no tool exists for carrying out recurrence analyses in professional football. Furthermore, the method was only used in a scientific context. For practical application, an intuitive and easy-to-use tool is still missing, with the help of which flexible recurrence views are possible within a very short time.

The aim of this study is to present a user-friendly dashboard that can be used to conduct performance analyses in professional soccer including the recurrence method. In pursuit of this goal, it is investigated how the practicability of the recurrence method can be increased and which contents and information are additionally relevant for a comprehensive performance analysis.

2. MODELLING

2.1 RPs

The recurrence plot is a graphical preparation of a square matrix whose coefficients express the approximation of a trajectory at the corresponding time points t=i and t=j. In terms of soccer, the axes correspond to the match time points in seconds. To form a coefficient, the Euclidean distance between the positions at time points i and j is first calculated. The distance is then matched with the recurrence threshold. If the distance equals or falls below the threshold, the recurrence condition is fulfilled for this point. Graphically, the corresponding pixel is coloured black, whereas a non-recurrent point is coded white.

2.2 RQA

We adopted seven recurrence parameters from Marwan et al. (2007). Recurrence Rate (RR) simply counts the recurrence points in the whole RP and provides the rate of these points compared to all points in the RP. Determinism (DET) is the ratio between the recurrence points that lie on a diagonal line of length l with $l \geq l_{min}$ ($l_{min}=3$ in our case) and the total number of recurrence points. Laminarity (LAM) means very much the same as DET, but for vertical lines instead of diagonal ones. Average diagonal line length (LL) is defined as the average of all diagonal lines with $l \geq l_{min}$. Trapping Time (TT) is analogous to LL but is the average vertical line length of all lines with $l \geq l_{min}$. Entropy (ENTR) is the Shannon entropy of the different diagonal line lengths $\geq l_{min}$. ENTR-V is the entropy of the vertical lines.

2.3 Technologies

21 matches of a German Bundesliga team from the 2019/2020 season were used as a sample. The data was preprocessed using the Python programming language and its common data processing libraries. The tool was implemented with the help of Plotly's framework Dash, which enables the development of web-based analysis applications using Python.

3. RESULTS

A recurrence-based dashboard was designed that forms the basis for comprehensive match analyses in practice. Central to the development is the idea of bundling several analysis functions in one tool, so that the RP is contextualised by diagrams, graphics, key figures as well as cross-media content such as match videos. For this reason, the RP is used as an interactive control, whereby the user receives specific information by selecting an area. The dashboard shows extracts of the game video before and after a selected point on the x-axis in the RP and the corresponding part of the game on the y-axis. Practicality has been increased in that sports analysts are able to use the dashboard to quickly search for points of interest in the RP as the relevant video clips are easily accessible. This also makes it easier to find similar clips that might not be easy to find if they were not marked by specific events, e.g. during a set. In addition, a pitch visualisation was integrated, showing the players' positions from a bird's eye view. From this, more detailed interpretations of the positional play at the selected points in time can be derived. Furthermore, filtering by tactical groupings or individual players provides information about commonalities in the behaviour of players in certain positions. In addition to the interactive RP, the analysis tool also contains RQA parameters and performance indicators such as average speed, which allow further aspects of the game to be quantified (Fig. 1).

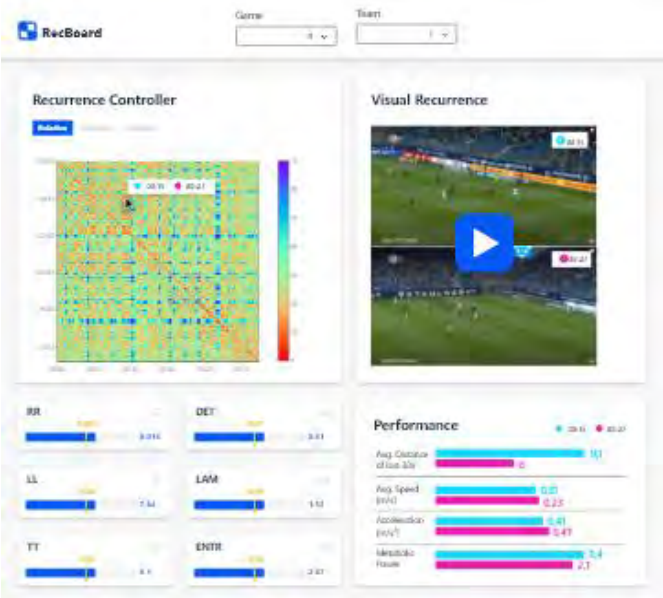

Fig. 1: User interface draft of the RP analysis tool with RP as controller, video display of the selected scenes, local performance indicators as well as recurrence parameters and filtering options.

4. CONCLUSIONS

In this abstract, we presented a dashboard that can be used to perform recurrence analysis in professional soccer games. It shows how recurrence analysis can be integrated into notational performance analysis and what information is useful in this context.

Future work could deal with the further development of the dashboard. On the one hand, new functionalities could improve the practicability and produce innovative insights in performance analysis. At this point, the flexible nature of dashboards should be emphasised, which makes it possible to analyse any key figures and analysis methods simultaneously. On the other hand, the dashboard could be extended to other application scenarios. One possibility would be to include training operations in the match analysis. This could bridge the gap between training and match analysis, for example by examining the implementation of specifically trained tactics in the match. Although this work is aimed overall at football, it is to be expected that other top sports can also benefit from such a recurrence-focused dashboard. Particularly obvious are implementations in those sports for which empirical data already exists in connection with recurrence analysis (e.g. golf, Stöckl et al. 2017).

REFERENCES

Eckmann, J.-P., Kamphorst, S. O. & Ruelle, D. (1987). Recurrence Plots of Dynamical Systems. *Europhysics Letters (EPL)*, 4(9), 973–977.

Grehaigne, J.-F., Bouthier, D. & David, B. (1997). Dynamic-system analysis of opponent relationships in collective actions in soccer. *Journal of Sports Sciences*, 15, 137–149.

Hughes, M., & Franks, I. M. (2008). The essentials of performance analysis. *London: E. & FN Spon.*

Lames, M., & McGarry, T. (2007). On the search for reliable performance indicators in game sports. *International Journal of Performance Analysis in Sport*, 7(1), 62-79.

Lames, M. & Plück, D. (2015). Modeling soccer matches by recurrence analyses. IFAC-PapersOnLine, 48(1), 788–789. https://doi.org/10.1016/j.ifacol.2015.05.181

Lames, M., Hermann, S., Prüßner, R. & Meth, H. (2021). Football Match Dynamics Explored by Recurrence Analysis. *Frontiers in Psychology*, 12, 747058. https://doi.org/10.3389/fpsyg.2021.747058

Marwan, N., Romano, M. C., Thiel, M., & Kurths, J. (2007). Recurrence plots for the analysis of complex systems. *Physics reports*, 438(5-6), 237-329.

Stöckl, M., Plück, D., & Lames, M. (2017). Modelling game sports as complex systems–application of recurrence analysis to golf and soccer. *Mathematical and Computer Modelling of Dynamical Systems*, 23(4), 399-415.

Coupled computational modeling of cardiac electrophysiology, mechanics and fluid dynamics ⋆

Michele Bucelli [*,***] **Luca Dede'** [*] **Alfio Quarteroni** [*,**]

[*] *MOX, Department of Mathematics, Politecnico di Milano, P.zza Leonardo da Vinci 32, 20133 Milan, Italy.*
[**] *Mathematics Institute, EPFL, Av. Piccard, CH-1015 Lausanne, Switzerland (Professor Emeritus).*
[***] *Corresponding author; e-mail: michele.bucelli@polimi.it*

Abstract: We propose a computational model of a human heart including three-dimensional descriptions for electrophysiology, solid mechanics and fluid dynamics of the blood, aiming at reproducing the feedback mechanisms that occur within the heart. The model is obtained combining standalone physical models used in the cardiac modeling literature, introducing coupling terms, resulting in a multi-way coupled integrated model. We numerically solve the model with a staggered scheme. Fluid dynamics and solid mechanics are coupled implicitly with a monolithic scheme. The staggered scheme allows to select different timesteps for the different core models, leveraging the multiscale and multiphysics nature of the model. Simulations results on a realistic human heart model are consistent with the behavior shown by healthy hearts.

Keywords: Cardiovascular modeling, Heart, Multiphysics, Electrophysiology, Cardiac electromechanics, Fluid-structure interaction, Hemodynamics, Finite element analysis

1. INTRODUCTION

We aim at a multi-way coupled computational model that integrates three dimensional descriptions of cardiac electrophysiology (EP), active and passive mechanics and blood dynamics (individually referred to as core models). Such a model has the capability of capturing the feedback mechanisms between the different components of the heart. We refer to the model as electro-mechanics-fluid dynamics (EMF)

Due to the large size of an EMF model, fully coupled computational models of this kind are seldom considered in literature, e.g. in Hosoi et al. (2010), Santiago et al. (2018). Nonetheless, the core models have been studied in detail either in a standalone way or with reduced coupling to other models (see e.g. Augustin et al. (2016), Gurev et al. (2011), Regazzoni et al. (2022), Nordsletten et al. (2011), This et al. (2020), Zingaro et al. (2022)).

We leverage previously developed core models, introducing couplings between them. We solve the EMF model with a staggered scheme in time, exploiting its multiphysics and multiscale nature, and relying on finite elements for the space discretization. Numerical results, obtained on a realistic human heart, showcase the ability of the computational model to reconstruct physiological behavior.

⋆ This project has received funding from the European Research Council (ERC) under the European Union's Horizon 2020 research and innovation programme (grant agreement No 740132, iHEART - An Integrated Heart Model for the simulation of the cardiac function, P.I. Prof. A. Quarteroni).

2. MODELS AND NUMERICAL METHODS

The EMF model has four major components: EP, activation, solid mechanics and fluid dynamics. For EP, we use the monodomain equation (Colli Franzone et al. (2014)) coupled with the ionic model of Ten Tusscher and Panfilov (2006). Active force generation, in the active stress framework, is obtained with the model presented in Regazzoni et al. (2018). The muscle displacement is modeled using elastodynamics equations, as described e.g. in Regazzoni et al. (2022), fed with the activation state computed by the activation model to compute the active stress contribution. We use Guccione and Neo-Hooke constitutive models for passive mechanics. Fluid dynamics of the blood are described by ALE incompressible Navier-Stokes equations (see e.g. Zingaro et al. (2022)). Valves are included with the Resistive Immersed Implicit Surface method (Fedele et al. (2017)), choosing the opening and closing times based on computed pressures. Fluid and solid are coupled by imposing continuity of velocity and stresses at the interface, see Bazilevs et al. (2013), resulting in a fluid-structure interaction (FSI) problem.

We discretize the EMF model in time with a staggered scheme. We solve the EP equations for a few small timesteps. We then solve the activation model, and the FSI equations. All couplings are treated explicitly, except for the FSI coupling, due to stability concerns. We discretize in space with finite elements on a hexahedral grid, with a finer grid for EP, nested into the one for mechanics, and with a conforming fluid-solid interface. The FSI problem is discretized monolithically and solved with Newton method and GMRES, with a block-triangular preconditioner using

SIMPLE (Deparis et al. (2014)) and AMG to approximate fluid and mechanics blocks.

3. NUMERICAL SIMULATIONS

We consider a human cardiac model, under physiological conditions. We generate fibers with rule-based algorithms (Piersanti et al. (2021)). We use boundary conditions mimicking the presence of the pericardial sac for the outer wall of the myocardium (Regazzoni et al. (2022)), and simplified boundary conditions of Neumann and resistive type for fluid inlets and outlet. The results are qualitatively consistent with the deformations observed in medical images. Moreover, major biomarkers such as ventricular volume and pressure are captured effectively by the model. The model shows the potential of reproducing effectively the behavior of the human heart under physiological conditions.

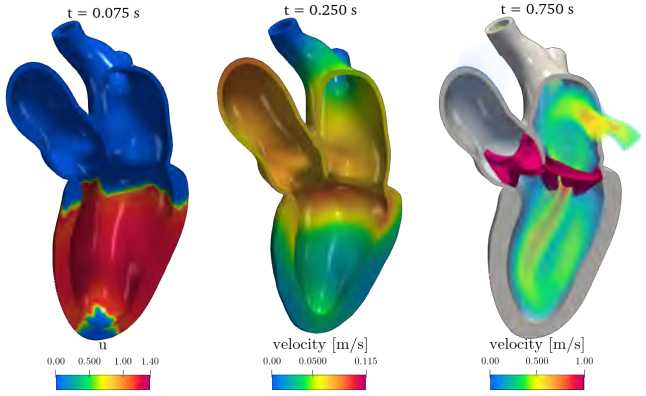

Fig. 1. Three snapshots of a numerical EMF simulation: EP (left), solid velocity (center), fluid velocity (right).

ACKNOWLEDGEMENTS

This project has received funding from the European Research Council (ERC) under the European Union's Horizon 2020 research and innovation programme (grant agreement No 740132, iHEART - An Integrated Heart Model for the simulation of the cardiac function, P.I. Prof. A. Quarteroni).

The authors acknowledge the CINECA award under the ISCRA C initiative, for the availability of HPC resources and support (IsC92_HeartEMF, P.I. Michele Bucelli, 2021).

REFERENCES

Augustin, C.M., Crozier, A., Neic, A., Prassl, A.J., Karabelas, E., Ferreira da Silva, T., Fernandes, J.F., Campos, F., Kuehne, T., and Plank, G. (2016). Patient-specific modeling of left ventricular electromechanics as a driver for haemodynamic analysis. *EP Europace*, 18, iv121–iv129.

Bazilevs, Y., Takizawa, K., and Tezduyar, T.E. (2013). *Computational fluid-structure interaction: methods and applications*. John Wiley & Sons.

Colli Franzone, P., Pavarino, L., and Scacchi, S. (2014). *Mathematical Cardiac Electrophysiology*. Springer.

Deparis, S., Grandperrin, G., and Quarteroni, A. (2014). Parallel preconditioners for the unsteady Navier–Stokes equations and applications to hemodynamics simulations. *Computers & Fluids*, 92, 253–273.

Fedele, M., Faggiano, E., Dedè, L., and Quarteroni, A. (2017). A patient-specific aortic valve model based on moving resistive immersed implicit surfaces. *Biomechanics and Modeling in Mechanobiology*, 16(5).

Gurev, V., Lee, T., Constantino, J., Arevalo, H., and Trayanova, N.A. (2011). Models of cardiac electromechanics based on individual hearts imaging data: Image-based electromechanical models of the heart. *Biomechanics and Modeling in Mechanobiology*, 10(3), 295–306.

Hosoi, A., Washio, T., Okada, J.i., Kadooka, Y., Nakajima, K., and Hisada, T. (2010). A multi-scale heart simulation on massively parallel computers. In *SC'10: Proceedings of the 2010 ACM/IEEE International Conference for High Performance Computing, Networking, Storage and Analysis*, 1–11. IEEE.

Nordsletten, D., McCormick, M., Kilner, P.J., Hunter, P., Kay, D., and Smith, N.P. (2011). Fluid-solid coupling for the investigation of diastolic and systolic human left ventricular function. *International Journal for Numerical Methods in Biomedical Engineering*, 27, 1017–1039.

Piersanti, R., Africa, P.C., Fedele, M., Vergara, C., Dede', L., Corno, A.F., and Quarteroni, A. (2021). Modeling cardiac muscle fibers in ventricular and atrial electrophysiology simulations. *Computer Methods in Applied Mechanics and Engineering*, 373, 113468.

Regazzoni, F., Salvador, M., Africa, P., Fedele, M., Dedè, L., and Quarteroni, A. (2022). A cardiac electromechanical model coupled with a lumped-parameter model for closed-loop blood circulation. *Journal of Computational Physics*, 457, 111083.

Regazzoni, F., Dedè, L., and Quarteroni, A. (2018). Active contraction of cardiac cells: a reduced model for sarcomere dynamics with cooperative interactions. *Biomechanics and Modeling in Mechanobiology*, 17(6), 1663–1686.

Santiago, A., Aguado-Sierra, J., Zavala-Aké, M., Doste-Beltran, R., Gòmez, S., Arìs, R., Cajas, J.C., and Casoni, E. (2018). Fully coupled fluid-electro-mechanical model of the human heart for supercomputers. *International Journal for Numerical Methods in Biomedical Engineering*, 34, e3140.

Ten Tusscher, K.H. and Panfilov, A.V. (2006). Alternans and spiral breakup in a human ventricular tissue model. *American Journal of Physiology - Heart and Circulatory Physiology*, 291(3), 1088–1100.

This, A., Boilevin-Kayl, L., Fernández, M.A., and Gerbeau, J.F. (2020). Augmented resistive immersed surfaces valve model for the simulation of cardiac hemodynamics with isovolumetric phases. *International Journal for Numerical Methods in Biomedical Engineering*, 36(3), 1–26.

Zingaro, A., Fumagalli, I., Dede, L., Fedele, M., Africa, P.C., Corno, A.F., and Quarteroni, A. (2022). A geometric multiscale model for the numerical simulation of blood flow in the human left heart. *Discrete and Continuous Dynamical Systems-S*.

Uncertainty Investigation of PEPT Measurement in the Cardiovascular System

Hamed Keramati*. Adelaide de Vecchi.**
Steven Niederer***

** School of Biomedical Engineering and Imaging Sciences, King's College London, London, UK, (e-mail: hamed.keramati@kcl.ac.uk)*
*** School of Biomedical Engineering and Imaging Sciences, King's College London, London, UK, (e-mail: adelaide.de_vecchi@kcl.ac.uk)*
**** School of Biomedical Engineering and Imaging Sciences, King's College London, London, UK, (e-mail: steven.niederer@kcl.ac.uk)*

1. INTRODUCTION

Positron emission particle tracking (PEPT) has been known and used for industrial flow tracking in opaque flow fields such as chemical reactors, food processors, and granulators. Because of its abilities, such as tracking a single or limited number of particles, PEPT has promising potential for biomedical imaging applications.

Both PEPT and positron emission tomography (PET) are based on the annihilation of a positron when meeting an electron, which results in a release of two gamma rays (511 keV) at virtually 180 degrees. By triangulation of the relevant coincidences, the location of the annihilation is calculated (Ingram et al. 2007, Seville et al. 2009).

Cheng et al. (2011) investigated the standard deviations of the position measurements and showed the effect of various factors such as the number of the lines of response (LORs) and relative position of the tracer and the detector on the accuracy of the measurements in a hydrocyclone. The details for labelling the resin spheres as well as the algorithm for the triangulation and elimination of random coincidence was described by Cheng et al. (2011). It has been shown that the conventional PET and PEPT tracking algorithms need improvement to be optimized for a single particle (Jung et al. 2020, Schmitzer et al. 2019) and multiple particles (Langford et al. 2016, Langford et al. 2017) tracking.

To assess the potential of clinical applications of PEPT for coronary disease diagnosis, we investigated the errors associated with the reconstruction of the velocity profile from multiple particles in a vessel with a stenotic obstruction.

2. METHOD

To investigate the uncertainty of the blood velocity measurement using the information from a limited number of particles, computational models with an axisymmetric stenosed geometry and steady flows with various Reynolds numbers (Re=50, 100, 200, and 250) were created. ANSYS FLUENT was used to simulate the laminar fluid flow in the stenosed artery using computational fluid dynamics (CFD) techniques. The total axial length of the stenosis was assumed to be 1 cm. The wall was assumed to be rigid; therefore, no deformation was considered.

Particle tracking was conducted using an in-house Python code. The effects of the number of particles and particle tracking time step were analysed. The particles were randomly seeded into the inlet of the flow field with a uniform distribution. To reconstruct the profile using the particles information, we compared 4^{th} and 6^{th} order polynomial fitting. We modified the fitting procedure to capture the negative axial velocities downstream of the stenosis.

Due to the order of magnitude of the Stokes number, i.e., the relaxation time of the particles over the typical time scale of the flow, the drag force exerted on the particles was neglected. The root-mean-square error (RMSE) between the fitted and the CFD solution was calculated as a metric of the accuracy of the predicted profile. The radioactivity of the tracers bound to the radionuclide (^{18}F) is between 13 and 55 MBq per particle; therefore, gathering the information of the location of the particles is restricted by the particle tracking time step not the radioactivity of the tracer.

3. RESULTS AND DISCUSSION

Figure 1 shows the velocity profile for one of the cases (Re=250) around the stenosis.

The reconstruction of the velocity profile using a limited number of particles showed acceptable agreement, i.e., an estimated error of 1% with 10 particles with Re=250, for the flow before the stenosis. However, recirculation regions were observed. Therefore, we used auxiliary points to improve the fitting of the velocity profile after the stenosis. Figure 2 shows the RMS error for various numbers of particles for the velocity profiles reconstructed with 6^{th} order polynomials. Due to better results, we only present the results corresponding to the 6^{th} order.

The RMS error was less than 3.6% with a standard deviation (SD) of 4.1% for more than seven particles and decreased to 1.5 (SD=0.18%) as the number of particles grew to 30. However, it was observed that the error did not approach zero

for velocity prediction after the stenosis when we increased the number of particles.

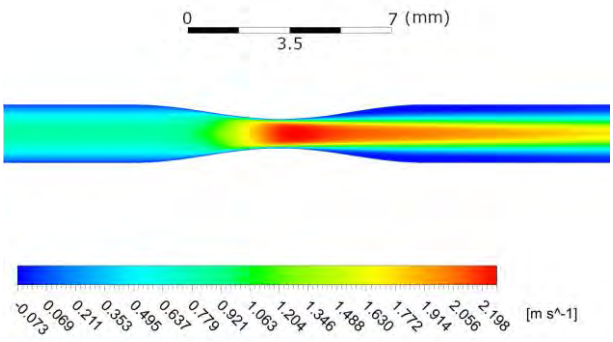

Fig. 1. The velocity contour in the case with 50% stenosis and Re=250

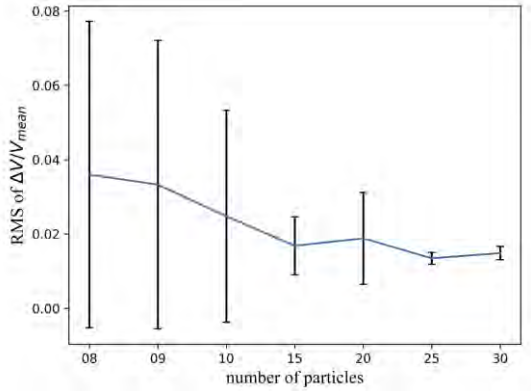

Fig. 2. RMS error between fitted and simulated velocity profiles for different number of particles. The bars show the standard deviation.

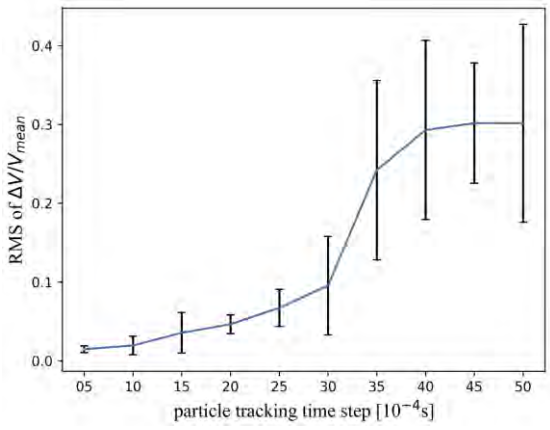

Fig. 3. RMS error between fitted and simulated velocity profiles for different particle tracking time steps. The bars show the standard deviation.

The particle tracking time step was varied from 0.5 ms to 5 ms to investigate its effect on the accuracy of the velocity reconstruction. Figure 3 presents the RMS error of the normalized velocity difference for the different temporal resolutions. The results suggest that the accuracy of the reconstructed velocity profile drops as the particle tracking time step increases. The RMS error was below 10% for tracking time steps less than 25 ms and increased to 30% (SD=12.5%) for tracking time steps larger than 40 ms, respectively. For the untreated 6th order profile, the RMS error of the normalized velocity after the stenosis, increased from 6% (SD=2%) to 39.9% (SD=38%) when Re increased from 150 to 250. However, when the modified fitting was used the RMS error remained below 10% (SD<3%) for all cases.

4. CONCLUSIONS

PEPT is a novel technology with high potential diagnostic impact in clinical applications where non-invasive assessment of blood flow velocity and subsequent derivation of pressure gradients are of critical importance, such as coronary stenosis. To determine the effects of parameters involved in PEPT, we analysed a simplified set-up for stenosed vessels with steady flow at different Reynolds numbers. We investigated the error of this method for velocity profile reconstruction after the stenosis. This methodology is currently being developed for 3D idealised and patient-specific coronary arteries to investigate the correlation of the pressure field and the reconstructed velocity field.

REFERENCES

Chang, Y.F., Ilea, C.G., Aasen, Ø.L. and Hoffmann, A.C., (2011). Particle flow in a hydrocyclone investigated by positron emission particle tracking. *Chemical Engineering Science*, 66(18), pp.4203-4211.

Ingram, A., Hausard, M., Fan, X., Parker, D.J., Seville, J.P.K., Finn, N. and Evans, M., (2007). Portable positron emission particle tracking (PEPT) for industrial use. *Proceedings of 12th International Conference on Fluidization (2007)*, pp. 13-17

Jung, K.O., Kim, T.J., Yu, J.H., Rhee, S., Zhao, W., Ha, B., Red-Horse, K., Gambhir, S.S. and Pratx, G., (2020). Whole-body tracking of single cells via positron emission tomography. *Nature biomedical engineering*, 4(8), pp.835-844.

Langford, S., Wiggins, C., Tenpenny, D. and Ruggles, A., (2016). Positron emission particle tracking (PEPT) for fluid flow measurements. *Nuclear Engineering and Design*, 302, pp.81-89.

Langford, S.T., Wiggins, C.S., Santos, R., Hauser, M., Becker, J.M. and Ruggles, A.E., (2017). Three-dimensional spatiotemporal tracking of fluorine-18 radiolabeled yeast cells via positron emission particle tracking. *PloS one*, 12(7), p.e0180503.

Schmitzer, B., Schäfers, K.P. and Wirth, B., (2019). Dynamic cell imaging in PET with optimal transport regularization. *IEEE transactions on medical imaging*, 39(5), pp.1626-1635.

Seville, J.P.K., Ingram, A., Fan, X. and Parker, D.J., (2009). Positron emission imaging in chemical engineering. *Advances in Chemical Engineering*, 37, pp.149-178.

Dynamics of a Mecanum Wheel Pair with Variable Orientation of the Rollers ⋆

Igor Zeidis * **Klaus Zimmermann** ** **Steffen Greiser** *** **Julia Marx** ****

* *Department of Mechanical Engineering, Technische Universität Ilmenau, Ilmenau, Germany (e-mail: igor.zeidis@tu-ilmenau.de)*
** *Department of Mechanical Engineering, Technische Universität Ilmenau, Ilmenau, Germany (e-mail: klaus.zimmermann@tu-ilmenau.de)*
*** *Department of Management and Technology, Hochschule Osnabrück, Osnabrück, Germany, (e-mail: s.greiser@hs-osnabrueck.de)*
**** *Department of Management and Technology, Hochschule Osnabrück, Osnabrück, Germany, (e-mail: j.marx@hs-osnabrueck.de)*

1. INTRODUCTION

The demand of mobile platforms for the motion in a constrained spaces in complex environments or personal high-maneuverability robots for disabled persons has led to the invention of new types of wheels. Beginning from the first patent received by Grabowezky in USA in 1919, engineers started developing wheels that could move not only in their own plane but, for example, perpendicularly to this plane. A key issue for the effective usage of these wheels and for the optimal control of the entire mobile system is the understanding of the physical interaction between the wheels and the environment. For this reason, the mechanics of motion with such wheels draws attention of both researchers and engineers (Campion et al. (1996), Ostrowski and Burdick (1998) and others). The motion of a platform with four Mecanum wheels is investigated in Zeidis and Zimmermann (2019) within the framework of non-holonomic mechanics. In this paper the dynamic equations of a wheel pair that contain two Mecanum wheels with controllable orientation of the rollers during motion is considered. Such a system consists of two coaxial disks with rollers attached to them as shown in Fig. 3. When one of the disks turns with respect to the other disk, the angle of inclination of the rollers relative to the wheel's plane changes. The relative rotation of the disks can be produced by a separate actuator, which allows choosing an optimal orientation of the rollers for a given trajectory.

2. MATHEMATICAL PROBLEM

The Mecanum wheel pair moves so that all its wheels have permanent contact with the underlying plane. The distance between the centers of the wheels is $2\,l$. The coordinates of the center of mass C in a fixed coordinate system XOY are x_c, y_c , the angle formed by the axis that is orthogonal to the axis of wheel pair with axis OX we denote by ψ. The angles of rotation of the wheels relative to the axes that are perpendicular to the planes of the respective wheels and pass through their centers are φ_i, and the time-dependent torques applied to the wheels are $M_i(t)$ $(i = 1\,, 2)$.

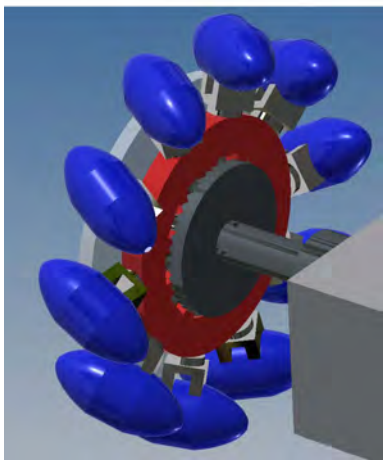

Fig. 1. Prototype of a Mecanum wheel with controllable angle of the rollers

A Mecanum wheel is a wheel with rollers fixed on its outer rim. The axis of each of the rollers forms the same angle δ $(0° \leq \delta < 90°)$ with the plane of the wheel. Each roller may rotate freely about its axis, while the wheel may roll on the roller. We will model a Mecanum wheel by a thin disk of radius R, see Fig. 2. Let $\boldsymbol{V}_K$ be the velocity of the wheel's center K, $\boldsymbol{\gamma}$ be the unit vector of the roller's axis, and φ be the angle of rotation of the wheel about the axis that is perpendicular to the wheel's plane and passes through its center. The wheels move without slip, which implies the constraint (Nejmark and Fufaev (1972))

$$\boldsymbol{V}_K \cdot \boldsymbol{\gamma} = R\,\dot{\varphi}\cos\delta\,. \tag{1}$$

⋆ This study was partly supported by the Deutsche Forschungsgemeinschaft (DFG) (project ZI 540-19/2).

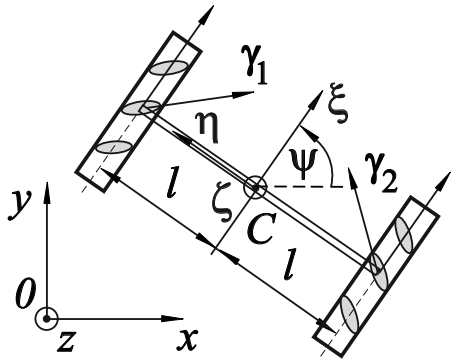

Fig. 2. Mecanum wheel pair

We introduce a wheel pair-attached coordinate system $\xi\eta\zeta$ with origin at the center of mass C of the axis between the wheel pair (Fig. 2). We point axis $C\xi$ orthogonal to the axis of the wheel pair, axis $C\eta$ along the axis of the wheel pair, and axis $C\zeta$ vertically upward. Denote by $V_{C\xi}$ and $V_{C\eta}$ the projections of the velocity of the center of mass onto the movable axes $C\xi$ and $C\eta$, respectively, and represent expression (1) as follows:

$$\begin{aligned} V_{C\xi}\cos\delta_1 - V_{C\eta}\sin\delta_1 - l\,\cos\delta_1\,\dot{\psi} &= R\,\cos\delta_1\,\dot{\varphi}_1\,, \\ V_{C\xi}\cos\delta_2 + V_{C\eta}\sin\delta_2 + l\,\cos\delta_2\,\dot{\psi} &= R\,\cos\delta_2\,\dot{\varphi}_2\,. \end{aligned} \tag{2}$$

Here the angles $\delta_1 = \delta_1(t)$, $\delta_2 = \delta_2(t)$ are given functions of time t. Then the components $\dot{x}_c$ and $\dot{y}_c$ of the velocity vector of the center of mass in the fixed reference frame are as follows:

$$\begin{aligned} \dot{x}_c &= V_{C\xi}\cos\psi - V_{C\eta}\sin\psi, \\ \dot{y}_c &= V_{C\xi}\sin\psi + V_{C\eta}\cos\psi. \end{aligned} \tag{3}$$

The configuration of the mechanical system is defined by five generalized coordinates, $q_1 = \varphi_1$, $q_2 = \varphi_2$, $q_3 = \psi$, $q_4 = x_c$, and $q_5 = y_c$. Two generalized velocities can be expressed in terms of the remaining generalized velocities by using the non-holonomic constraint equations (3). The coefficients in these equations be functions of only the independent coordinates and time t. Chaplygin's systems (Papastavridis (2002), Zimmermann et al. (2009)) are usually defined as mechanical systems with non-holonomic time-invariant constraints that are linear with respect to the generalized velocities and can be reduced to the form in which the dependent generalized velocities are expressed in terms of the independent generalized velocities in such a way that the coefficients of the independent generalized velocities are functions only of the independent generalized coordinates. In this case, the dynamic equations can be represented in a special form that are called Chaplygin's equations. Chaplygin's equations form a closed system that does not involve the constraint equations, as it is the case for systems with holonomic constraints. This remarkable property remains valid for the systems with linear time-varying constraints if the coefficients of the independent generalized velocities depend only on the independent generalized coordinates and on the time.

Fig. 3 depicts the time histories $x_c(t)$ and $y_c(t)$ of the coordinates of the wheel pair center of mass for the case where the rollers inclination angle changes periodically with a period of 2 s first from 5° to 85° and then from 85° to 5° (curves 1) and for the case where the roller inclination angle is constant and is equal to 45° (curves 2).

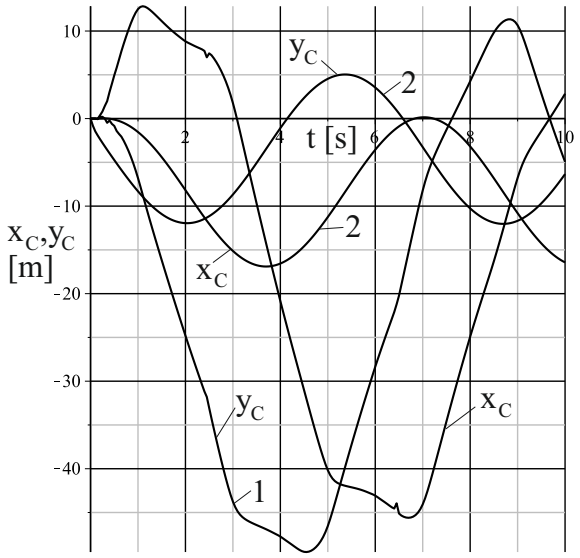

Fig. 3. The time histories of the x_c- and y_c-coordinates of the center of mass of the wheel pair for the cases of changing and constant inclination angle of the rollers

3. CONCLUSION

The equations of motion of a wheel pair with time varying change in the angle of inclination of rollers to the wheel's plane are presented. These equations can be regarded as a modification of Chaplygin's equations for non-holonomic systems with time-varying constraints. The modified equations contain additional terms as compared with the classical equations for the systems with time invariant constraints. The main property of Chaplygin's equations is that the dynamic equations can be integrated irrespective of the constraint equations. This property is retained for the modified equations. The ability of a controllable inclination angle of the rollers of the Mecanum wheels during motion enhances the kinematic possibilities of mobile robots with such wheel pairs.

REFERENCES

Campion, G., Basin, G., and D'Andrea-Novel, B. (1996). Structural properties and classification of kinematic and dynamic models of wheeled mobile robots. *IEEE Transactions on Robotics and Automation*, 12(1), 47–62.

Nejmark, J. and Fufaev, N. (1972). *Dynamics of non-holonomic systems.* American Mathematical Society, Providence.

Ostrowski, J. and Burdick, J. (1998). The geometric mechanics of undulatory robotic locomotion. *The International Journal of Robotic Research*, 17(7), 683–701.

Papastavridis, J. (2002). *Analytical Mechanics: A Comprehensive Treatise on the Dynamics of Constrained Systems for Engineers.* Oxford University Press, New York.

Zeidis, I. and Zimmermann, K. (2019). Dynamics of a four wheeled mobile robot with mecanum wheels. *ZAMM Journal of applied mathematics and mechanics*, 99(12), 1–22.

Zimmermann, K., Zeidis, I., and Behn, C. (2009). *Mechanics of terrestrial locomotion with a focus on nonpedal motion systems.* Springer, Heidelberg.

Modeling and Control of a Two-body Limbless Crawler on a Rough Inclined Plane ⋆

Nikolay Bolotnik * **Tatiana Figurina** **

* *Ishlinsky Institute for Problems in Mechanics of the Russian Academy of Sciences, Moscow 119526, Russia (e-mail: bolotnik@ipmnet.ru)*
** *Ishlinsky Institute for Problems in Mechanics of the Russian Academy of Sciences, Moscow 119526, Russia (e-mail: t_figuriva@mail.ru)*

1. INTRODUCTION

A mobile system consisting of two interacting bodies regarded as point masses is a simplest model of a worm-like limbless crawler. The interaction force plays the role of a control variable. This system can move progressively on a rough plane with Coulomb's friction acting between each of the bodies and the plane. On a horizontal plane, if both bodies did not move at the initial time instant, this system can move only along the line that connected the bodies at the initial time instant. This is the case, because no lateral impressed forces act on the system. The motion of a two-body crawling system along a straight line on a horizontal plane was studied by Chernousko (2002) and Chernousko (2011). The situation changes for an inclined plane, since the gravity force has a projection onto the direction orthogonal to the line that connects the bodies, provided that both bodies do not lie on the common line of maximum slope. The motion of a two-body crawler on an inclined plane along a line of maximum slope is addressed by Figurina (2018). The aim of this study is to show that the two-body crawler can, in principle, be driven from any initial state of rest to an arbitrarily small neighborhood of any terminal state of rest on an inclined plane, if at the initial time instant the bodies do not lie on the common line of maximal slope.

2. STATEMENT OF THE PROBLEM

Consider a system of two interacting point bodies of masses m and M, $m < M$, on a rough inclined plane. Let k be the coefficients of Coulomb's friction between the bodies and the plane, γ the inclination angle of the plane ($0 < \gamma < \pi/2$), $\mathbf{F}$ the interaction force applied by body M to body m. We assume that from a state in which both bodies lie on the common line of maximum slope and do not move, body m can be moved upward along this line, with body M remaining at rest. This assumption implies the inequality

$$\tan\gamma \le k\frac{M-m}{M+m}. \qquad (1)$$

⋆ This study was partially supported by the Ministry of Science and Higher Education of the Russian Federation within the framework of the Russian State Assignment under contract No. AAAA-A20-120011690138-6 and partially supported by RFBR Grant No. 20-01-00378.

Let at the initial time instant both bodies be not moving and the bodies do not lie on the common line of maximum slope. The issue we are interested in is whether the system can be transferred into an arbitrary terminal state of rest on the plane. We investigate this possibility in principle and do not impose constraints on the control force and the relative displacement of the bodies. In particular, the impulsive interaction force $\mathbf{F}$ that changes instantaneously the distance between the bodies is allowed and, moreover, the bodies are allowed to pass through each other. It will be shown that such a transfer can be performed by combining infinitely slow (quasistatic) motions of body m and fast motions in which the distance between the bodies changes virtually instantaneously.

3. QUASISTATIC MOTIONS

Consider the quasistatic motion of the system, i.e., the slow motions that can be regarded as a continuous sequence of equilibria. As follows from inequality (1), in the quasistatic mode, only body m can move and body M remains at rest. Introduce in the inclined plane the coordinate system Mxy (fixed for the case of the quasistatic motion), the y-axis of which points upward along the line of maximum slope (Fig.1).

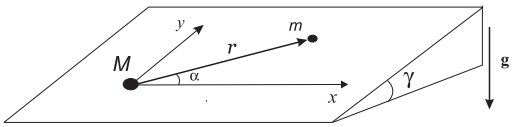

Fig. 1. Two-body system on an inclined plane.

Let r and α denote the polar coordinates of body m in the inclined plane, related to the pole M and the polar axis Mx. The trajectories of the quasistatic motion of body m for $\alpha \in (-\pi/2,\, \pi/2)$ are defined by the equation

$$\frac{dr}{d\alpha} = \pm\frac{r\sqrt{1-a^2\cos^2\alpha}}{a\cos\alpha}, \quad a = \frac{\tan\gamma}{k} < 1, \qquad (2)$$

The minus sign on the right-hand side of Eq. (2) corresponds to the repulsive motion for which the force $\mathbf{F}$, applied to body m is directed along the vector $\overrightarrow{Mm}$, and the plus sign corresponds to the attractive motion.

Let $r_{\pm}(\alpha, \alpha_0, r_0)$ denote the solution of Eq. (2) subject to the initial conditions $r(\alpha_0) = r_0$. The function r_+ (r_-) monotonically increases (decreases) as α increases in the interval $(-\pi/2, \pi/2)$. The function r_+ possesses the following properties:

$$\lim_{\alpha \to \pi/2} r_+(\alpha) \cos\alpha = \infty, \qquad \lim_{\alpha \to -\pi/2} r_+(\alpha) = 0.$$

The trajectories r_- are symmetric to r_+ about the axis Mx, i.e.,

$$r_-(\alpha, \alpha_0, r_0) = r_+(-\alpha, -\alpha_0, r_0).$$

The quasistatic trajectories of body m are plotted in Fig. 2. It can be shown that body m can move quasistatically from the point $(\alpha_0,\ r_0)$ clockwise along a curve that is arbitrarily close to the circumferential arc $r = r_0$, $\alpha \in (-\pi/2, \alpha_0]$. We will call such a motion quasistatic circumferential motions (motions along a circumference). The circumferential motions require infinitely frequent switchings between the attractive and repulsive trajectories.

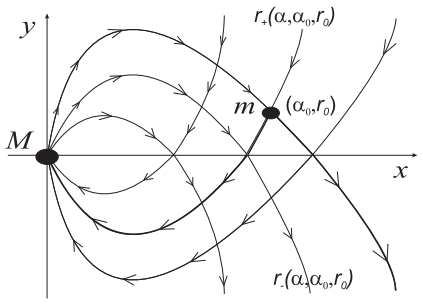

Fig. 2. Quasistatic trajectories of body m.

For $\alpha \in (\pi/2,\ 3\pi/2)$, the repulsive and attractive trajectories are symmetric with respect to the axis My to the respective trajectories for $\alpha \in (-\pi/2,\ \pi/2)$. For $\alpha \in [\alpha_0, 3\pi/2)$, body m can move quasistatically along a circumference counterclockwise.

4. FAST MOTIONS. ALGORITHMS FOR DRIVING THE SYSTEM INTO THE TERMINAL STATE

By fast motions we understand the motions that transfer the system between two states of rest in an infinitesimal time. For such motions, the interaction force of the bodies is much larger than the force of friction and, therefore, the center of mass of the system and the line that connects the bodies remain fixed. By assumption, the bodies may pass through each other and, hence, by means of a fast motion body M can be driven to any position on the initial line Mm; then the position of body m is defined uniquely.

By combining fast and quasistatic motions one can drive body m into any position on the plane, with body M remaining arbitrarily close to its initial position. We will prove this proposition for the particular case where $\alpha \in (\pi/2, 3\pi/2)$ for the initial position and $\alpha \in (-\pi/2, \pi/2)$ for the terminal position. The respective process is illustrated in Fig. 3. The starting position of body m is denoted by A and the destination position by B. The larger and smaller circles depict the successive positions of bodies M and m, respectively. The shading density of the circles decreases as the later positions are depicted. First, we proximate body m quasistatically to body M by a distance of $r = \varepsilon$. If ε is small enough, the angle α is close to $3\pi/2$. The respective position of body m corresponds to point C. After this, we perform a fast motion as a result of which bodies m and M change their positions to the positions that are symmetric to the previous positions with respect to the system's center of mass, body m comes into point D, while the change in the position of body M is less than ε. Then, body m is moved quasistatically along a circumference clockwise until it arrives at the point E that belongs to the repulsive trajectory that passes through the desired point B. Finally, body m is moved quasistatically along this repulsive trajectory into the point B. Simplifying, we can regard the described strategy (for $\varepsilon \to 0$) as proximation of bodies m and M until coincidence, with following motion of body m along an appropriate quasistatic repulsive trajectory emerging from the origin.

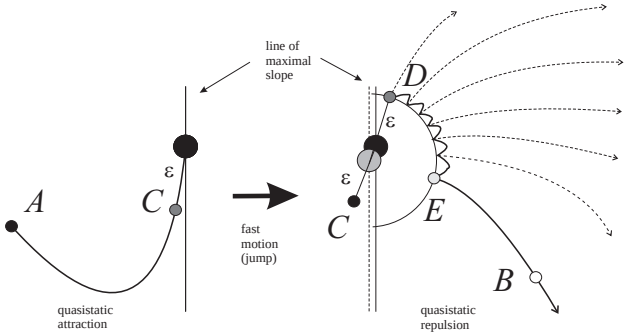

Fig. 3. Motion of body m between two prescribed points, with body M remaining close to its initial position.

The entire strategy for moving the system into the given terminal state can be briefly described as follows. By alternating fast motions of the system and quasistatic motions of body m along a circumference, we move the system into a position in which the line mM passes through the terminal position of body M. Then, by fast motion, we transfer body M into the terminal position. Finally, by using the strategy that was described above, we move body m into the terminal position, the change in the position of body M being able to be made arbitrarily small.

5. CONCLUSION

If at the initial state of rest the bodies of the crawler do not lie on a common line of maximum slope, the system can be driven into an arbitrarily small neighborhood of any terminal state of rest on an inclined rough plane by combining quasistatic and fast motions.

REFERENCES

F.L. Chernousko. The optimum rectilinear motion of a two-mass system. *J. Appl. Math. Mech.*, 66(1):1–7, 2002.

F.L. Chernousko. Analysis and optimization of the rectilinear motion of a two-body system. *J. Appl. Math. Mech.*, 75(5):493–500, 2011.

T.Yu. Figurina. On the periodic motion of a two-body system upward along an inclined straight line. In F. Breitenecker, W. Kemmetmuller, A. Korner, A. Kugi, I. Troch, editors, *MATHMOD 2018 Extended Abstract Volume*, pages 13–14. ARGESIM Publisher, Vienna, 2018.

Enhanced actuation strain of PDMS based loudspeaker membrane by using core-shell structured CNT-SiO_2 nano-inclusions

M.S. Alfonso*, E. Garnell*, D. He**, C.Rouby*, P. Molinié***, J. Bai*, O. Doaré*

* ENSTA Paris-Tech, Institut Polytechnique de Paris
**MSSMat, CNRS UMR 8579, CentraleSupélec, Université Paris-Saclay
*** GEEPS Laboratory, CentraleSupélec, Université Paris-Saclay

Abstract:
Dielectric elastomers (DEs) are flexible active materials capable of large deformations when activated by high voltage. They consist of a thin elastomeric membrane covered on each side by flexible and stretchable soft electrodes. When a high voltage (~1kV) is applied, the membrane is compressed and its surface area increases by up to 100% [1]. Because of this strong electromechanical conversion, associated to their high energy density, lightness and ability to work over a broad frequency range, they are considered as promising materials in different mechatronic applications[2], such as soft robotics[3] or fluidic pumps[4] and energy harvesting systems[5] just to name a few. On this regard, DEs have been considered also as promising materials for acoustic applications, such as loudspeakers [6]. Several prototypes have been developed and tested by several research groups, and models have been proposed to estimate their performance [7,8].
Previous studies described the electro-elastoacoustic interactions occurring in a DE membrane with the help of an electromechanical model solved numerically using finite elements. The frequency response was well predicted in a broad frequency range. Moreover, the relation between the electrode shape and the dynamical and acoustical behavior of membranes was described for the first time with the perspective to control selectively the contribution of eigenmodes to the radiated sound [9].
Although several progresses have been made in the field in these recent years, still a high actuating electric field (~10V/µm) is needed to induce large mechanical deformation of DEs, thus limiting their practical applications[10]. The major challenge in this field is to achieve a high actuation stress under a low applied electric field. A new approach based on the use of polymers loaded with conductive nano-inclusions is the subject of growing interest in scientific research. Indeed, the presence of nanoparticles leads to an increase in the dielectric constant of the material, altering their electrostriction coefficient, which is linked to the actuation deformation of the composite according to the Maxwell stress equation.
DE nanocomposites, are generally made up of random dispersions of particles without any structural optimization. In this study, we propose to manufacture and formulate isotropic self-assembled networks of core-shell nano-inclusions composed of conductive carbon nanotubes (CNT) coated by a few nanometers of SiO_2 passivation layer uniformly dispersed in flexible polymer elastic matrix (PDMS) without compromising breakdown strength (E_b) and elasticity (Y) of membrane assuring high actuation strain under a low driving electric field.
According to Maxwell stress equation $S_{Maxwell}=\varepsilon_0\beta E^2$, with $\beta= \varepsilon_r Y$ a substantial increase of the electromechanical sensitivity (β) obtained by a slight improvement of the

dielectric constant of DEs nanocomposite keeping a reasonable elastic modulus represents a safe and reliable solution to reduce the driving electric field of dielectric elastomer loudspeakers. The improvement of the electromechanical couplings in these novel elastomeric dielectric nanocomposites, following the optimizations electrodes shaping studied by Garnel *et al.* will be validated by the integration of these membranes in loudspeakers prototypes. Based on actual measurements of the tensile-dielectric properties of nanofabricated nanocomposites, we aim for improvements beyond the state of the art by obtaining high actuation stress at halved applied electric field.

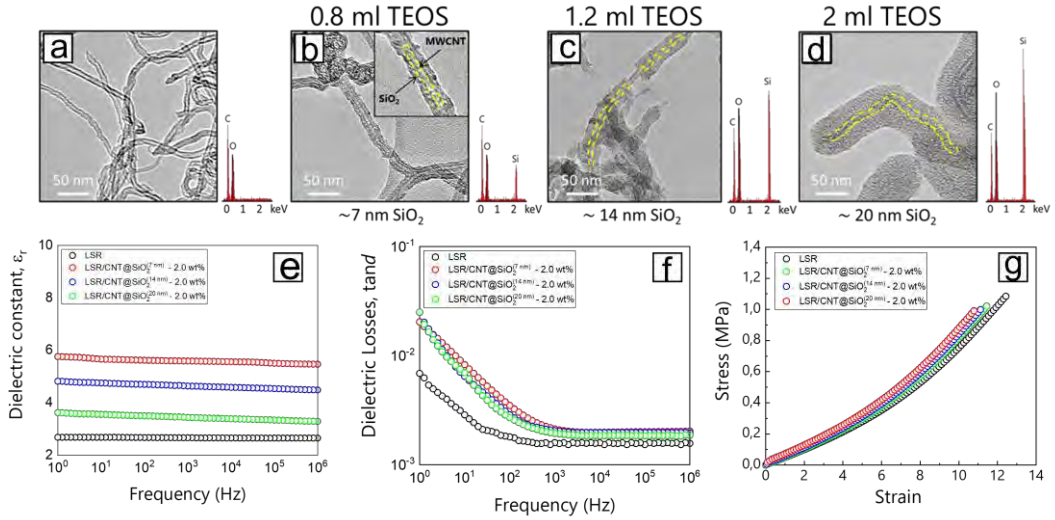

Fig. 1 – TEM/EDS images of the CNT-SiO2 prepared by sol-gel method: (a) Pristine carbon nanotubes, (b) 7 nm of SiO_2 passivation shell, (c) 14 nm of SiO_2 passivation shell, (b) 20 nm of SiO_2 passivation shell. Dielectric-tensile properties of nanofabricated nanocomposites: (e) frequency dependence of dielectric constant, (f) frequency dependence of dielectric losses and (g) Tensile stress-strain curves of the nanofabricated nanocomposites.

Keywords: Dielectric elastomers (DEs), Loudspeakers, Core-Shell nanocomposites, electromechanical sensitivity, Dielectric properties.

[1] Pelrine, R., Kornbluh, R., Pei, Q., and Joseph, J. (2000). "High-speed electrically actuated elastomers with strain greater than 100%". *Science* (287), 836-839.

[2] Gu, G.-Y., Zhu, J., Zhu, L.-M., Zhu, X. (2017). A survey on dielectric elastomer actuators for soft robots. *Bioinspiration & Biomimetics* (12), 011033.

[3] O'Halloran, A., O'Malley, F., McHugh, P. (2008). A review on dielectric elastomer actuators, technology, applications, and challenges. Journal of Applied Physics (104), 071101.

[4] Cao, C., Gao, X., Conn, A.T. (2019). A Magnetically Coupled Dielectric Elastomer Pump for Soft Robotics. *Advanced Materials Technologies* (4) 1900128

[5] Pelrine, R., Kornbluh, R.D., Eckerle, J., Jeuck, P., Oh, S., Pei, Q., Stanford, S. (2001). Dielectric elastomers: generator mode fundamentals and applications. SPIE Proceedings, (4329), 148-156.

[6] Heydt, R., Kornbluh, R., Pelrine, R., and Mason, V. (1998). "Design and performance of an electrostrictive-polymer-film acoustic actuator," *Journal of Sound and Vibration,* (215), 297-311.

[7] Garnell, E., Rouby, C., and Doaré O. (2019). Dynamics and sound radiation of a dielectric elastomer membrane. *Journal of Sound and Vibration*, (459), 114836.

[8] Garnell, E., Rouby, C., and Doaré O. (2020). Coupled vibro-acoustic modeling of a dielectric elastomer loudspeaker. *The Journal of the Acoustical Society of Americ*a, (147), 1812–1821.

[9] Garnell, E. Aksoy, B., Rouby, C., Shea H., and Doaré, O. (2021). Geometric optimization of dielectric elastomer electrodes for dynamic applications. *Applied Acoustics* (181), 108120.

[10] Zhang, J., Zhao, F., Zuo, Y.-J., Zhang, Y., Chen, X., Li, B., Zhang, N., Niu, G., Ren, W., and Z. YeImproving. (2020). Actuation strain and breakdown strength of dielectric elastomersusing core-shell structured CNT-Al_2O_3. *Composites Science and Technology* (200) 108393.

Passing Dynamics Across Top-Level Coaches: The Influence of the Quality of Opposition

Juliana Exel, Sebastian Immler, Arnold Baca

Department of Biomechanics, Kinesiology and Computer Science in Sport, Centre for Sport Science and University Sports, University of Vienna, Vienna, Austria (Tel: +43-1-4277-4888; e-mail: juliana.exel@univie.ac.at)

Abstract: The present study applied social networks analysis to objectively discriminate and describe interpersonal interaction dynamics of players coached by the top-level professionals Jürgen Klopp, Pep Guardiola, and Mauricio Pochettino, across the UEFA Champions League seasons from 2017 to 2020, considering different quality of opposition. Statistical analysis revealed that two of Jürgen Klopp's team passing network metrics differ according to the quality of opposition. Density ($U(34) = 202$; $p = 0.02$) and largest eigenvalue ($t(32) = -3.24$; $p = 0.03$) were lower when Liverpool played against strong opponents. Pochettino also showed lower values for density ($t(26) = -2.77$; $p = 0.01$) and largest eigenvalue when playing against strong opponents ($U(28) = 148$; $p = 0.01$), compared to when playing against weak opponents. Additionally, the average shortest-path length was significantly lower when playing against strong opponents ($U(28) = 148$; $p = 0.01$). This is novel evidence on sports teams' coordination and cooperation relationships through passing in football association, along seasons of a high-level European competition.

Keywords: coaching, football (soccer), notational analysis, social network analysis, collective behaviour.

1. INTRODUCTION

Previous work has dedicated efforts to unveil patterns in passing dynamics through social network analysis for the 3 finalists of the Best FIFA Men's Coach awards ins 2019: Jürgen Klopp, Pep Guardiola, and Mauricio Pochettino [1]. The authors investigated the potential of passing social networks to objectively discriminate match dynamics across different coaching framework styles. As a step forward, the analysis of teams' performance level according to specific constraints should yield practical information that can be more representative to elaborate models and help on coaches' operational decisions. Quality of opposition have been associated to influence positioning behaviour of players in matches [2], as well as a change in the average use of attacking and defensive style of play in association football [3]. Thus, we applied social networks analysis to objectively discriminate and describe interpersonal interaction dynamics of players coached by the top-level professionals Jürgen Klopp, Pep Guardiola, and Mauricio Pochettino, across the UEFA Champions League seasons from 2017 to 2020, considering different quality of opposition.

2. MATERIALS AND METHODS

2.1 Sample

In total, passing data of 92 games of the UEFA Champions League in the seasons of 2017/18, 2018/19 and 2019/20, while coaching Liverpool, Manchester City, and Tottenham Hotspur teams, were analysed, respectively. Data from the games were gathered from the media press kits of UEFA [4], and were divided according to 2 different qualities of opposition: strong (finished the group stage between the 1st and 2nd places) and weak opponents (placed in 3rd and 4th in their respective groups).

2.2 Social Network and Data Analysis

A dedicated toolbox for social network analysis [5] was applied, and the passing data from the 11 players that played most time during the matches were included. The network metrics were considered the following: local clustering coefficient, density, average shortest-path length, mean centrality, and largest eigenvalue. All variables were calculated from adjacent matrices normalized by the maximum number of passes performed, to avoid the bias of a different number of passes in each game to impact the interpretation of the results. After applying the Kolmogorov-Smirnov, for the normally distributed data, T-test was carried out. For not-normally distributed data, the U Mann-Whitney test was applied, with $p < 0.05$.

3. RESULTS

The results for the network metrics are described in Table 1. Jürgen Klopp's team passing network metrics showed to differ according to the quality of opposition. Density ($U(34) = 202$; $p = 0.02$) and largest eigenvalue ($t(32) = -3.24$; $p = 0.03$) were lower when Liverpool played against strong opponents. Pochettino also showed higher values for density ($t(26) = -2.77$; $p = 0.01$) and largest eigenvalue when playing

against strong opponents (U(28) = 148; p = 0.01), compared to when playing against weak opponents. Additionally, the average shortest-path length was significantly lower when playing against strong opponents (U(28) = 148; p = 0.01). Guardiola's network metrics were not statistically different according to the quality of opposition in the analysed matches.

Table 1. Mean ± standard deviation of passing network metrics for the coaches of Liverpool, Manchester City, and Tottenham Hotspur during 3 seasons of the UEFA Champions league (2017 to 2020), considering the quality of opposition.

		Jürgen Klopp	Pep Guardiola	Mauricio Pochettino
Matches	Strong	21	17	17
	Weak	13	12	11
Density [a.u.]	Strong	49.77 ± 26.53*	64.35 ± 21.69	45.01 ± 14.36*
	Weak	69.44 ± 26.25	63.10 ± 22.74	60.34 ± 15.81
Local clustering coefficient [a.u.]	Strong	0.54 ± 0.21	0.50 ± 0.18	0.53 ± 0.23
	Weak	0.52 ± 0.19	0.52 ± 0.20	0.56 ± 0.23
Average shortest-path length [a.u.]	Strong	2.47 ± 1.93	2.98 ± 0.44	2.57 ± 0.32*
	Weak	3.06 ± 0.59	2.83 ± 0.43	3.06 ± 0.51
Centrality dispersion [a.u.]	Strong	0.11 ± 0.03	0.14 ± 0.02	0.12 ± 0.04
	Weak	0.12 ± 0.03	0.14 ± 0.01	0.13 ± 0.03
Largest eigenvalue [a.u.]	Strong	40.23 ± 16.03*	64.16 ± 19.69	38.19 ± 12.13*
	Weak	58.67 ± 16.24	62.70 ± 13.48	50.78 ± 11.10

*Significantly different from weak (p<0.05).

4. DISCUSSION

Pep Guardiola is to be able to maintain a consistent work regarding passing, independently on his opponents, once the metrics showed no statistical difference when playing against weak and strong opponents. He presents higher largest eigenvalue overall, which indicates the promotion of a higher number of passes than the other coaches. His team also presents pairs of players less closely connected when compared to the other coaches', meaning that more intermediate players participate to connect passes among teammates [1]. He's been also reported to stand out by the capacity to adjust the important roles assigned to his players, thus affecting the centrality dispersion in the team [6]. Jürgen Klopp and Mauricio Pochettino coaching style are reported to share important similarities. Both explore more the flexibility of interpersonal linkages synergies, with fluid opportunities or levels of collaboration between all teammates [1]. The present study also found similarities for these coaches' passing networks when the quality of opposition is accounted. Both coaches had decreased values for density and largest eigenvalue when playing against stronger opponents, challenging their teams' ability in exploring passing options, thus, reducing the synergy in team coordination, when compared to the matches which they played against the weak opponents. The present results could reflect a certain difficulty in achieving the sweet spot between robustness and adaptability in the passing dynamics. Additionally, Pochettino also presented a lower average shortest-path length when playing against stronger opponents. Maybe, as a compensation for difficulties in maintaining quality of ball possessions, the exploration of interpersonal linkages synergies contributes to smaller topological distance between pairs of players and give Pochettino's team more options to distribute the ball. Therefore, it might be a sign of changing tactical patterns of plays when playing against strong opponents, which can alter the topological distances of players and altering the average shortest-path length.

5. CONCLUSIONS

Coaches' fundamental role is to elaborate and adjust the strategies underlying their teams' collective behaviour and most of coaches' work is discussed on the plane of impressions. Klopp and Pochettino, which stand out for more the flexibility of interpersonal linkages synergies in their passing dynamics, presented lower density and largest eigenvalue when playing against strong opponents. Guardiola is able to maintain his footprint which is related to integrated and coordinated connection between groups of players, thus keeping the relevant players connecting the attacking plays, regardless of the quality of opposition.

5. REFERENCES

[1] Immler, S. *et al.* (2021) 'Guardiola, Klopp, and Pochettino: The Purveyors of What? The Use of Passing Network Analysis to Identify and Compare Coaching Styles in Professional Football', *Frontiers in Sports and Active Living*, 3, p. 725554. doi:10.3389/fspor.2021.725554.

[2] Gonçalves, B. *et al.* (2019) 'Extracting spatial-temporal features that describe a team match demands when considering the effects of the quality of opposition in elite football', *PLOS ONE*. Edited by D. Boullosa, 14(8), p. e0221368. doi:10.1371/journal.pone.0221368.

[3] García-Rubio, J. *et al.* (2015) 'Effect of match venue, scoring first and quality of opposition on match outcome in the UEFA Champions League', *International Journal of Performance Analysis in Sport*, 15(2), pp. 527–539. doi:10.1080/24748668.2015.11868811

[4] UEFA (2021). UEFA press kits. Available at: https://www.uefa.com/insideuefa/mediaservices/presskits/index.html (Accessed: 11 May 2021).

[5] MIT (2011). Matlab tools for Network Analysis (2006 – 2011). Available at: http://strategic.mit.edu/downloads.php?page=matlab_networks (Accessed: 27 May 2021).

[6] Buldú, J.M. *et al.* (2019) 'Defining a historic football team: Using Network Science to analyze Guardiola's F.C. Barcelona', *Scientific Reports*, 9(1), p. 13602. doi:10.1038/s41598-019-49969-2.

Nonlinear Model Order Reduction using Diffeomorphic Transformations of a Space-Time Domain ⋆

Hendrik Kleikamp * **Mario Ohlberger** * **Stephan Rave** *

* *Institute for Analysis and Numerics, University of Münster, Germany (e-mail: hendrik.kleikamp@uni-muenster.de).*

Keywords: nonlinear model reduction, parametrized partial differential equations, conservation laws, hyperbolic equations, diffeomorphic registration, geodesic shooting, neural networks.

1. INTRODUCTION

Hyperbolic conservation laws play an important role in many applications. For instance, modeling the behavior of fluids or gases leads to conservation equations for quantities like mass, momentum, or energy. The resulting equations are typically nonlinear and exhibit phenomena like shock formation and transport. Parametrized hyperbolic equations suffer from a highly nonlinear solution manifold that cannot be approximated appropriately by a linear subspace, that is, the solution manifold has a slowly decaying Kolmogorov N-width, see for instance Ohlberger and Rave (2016). Therefore, methods that rely solely on linear combinations of ansatz-functions are not sufficient to achieve suitable reduced models. Furthermore, the formation and interaction of shocks is an additional difficulty when dealing with model order reduction for conservation laws.

In this contribution, we describe a new nonlinear model order reduction technique. The nonlinearity of the approach stems from the exponential map applied to vector fields in Euclidean space. We will thus identify diffeomorphisms, resulting from the application of the exponential map, with vector fields. Afterwards, we use standard ideas from linear model order reduction to compute a subspace of the space of vector fields. During the online phase, for a given parameter, elements from this subspace are computed and the exponential map is used to determine the corresponding diffeomorphism. This transformation is subsequently applied to a (fixed) space-time solution snapshot to obtain the approximate solution for the new parameter.

2. BASICS FROM DIFFERENTIAL GEOMETRY AND IMAGE REGISTRATION

In this section, we give a brief overview of important notions from differential geometry and introduce the basic concepts of image registration via geodesic shooting.

⋆ The authors acknowledge support by the Deutsche Forschungsgemeinschaft under Germany's Excellence Strategy EXC 2044 390685587, Mathematics Münster: Dynamics – Geometry – Structure.

2.1 Differential geometry and Lie groups

In the intersection of differential geometry and group theory, one considers so called *Lie groups*, which are groups such that group multiplication and inversion are smooth. Directly connected to the concept of Lie groups is the notion of *Lie algebras*. For a Lie group G, the corresponding Lie algebra $\mathfrak{g}$ is defined as the tangent space to the manifold G at the identity element. The *exponential map* $\exp\colon \mathfrak{g} \to G$ describes, for an element $v \in \mathfrak{g}$ of the Lie algebra, the end point of a shortest path (a *geodesic*) that starts at the identity in G in the direction given by v.

2.2 Image registration and geodesic shooting

The field of image registration has its origins in the analysis of medical image data. Given two images $u_0, u_1\colon \Omega \to \mathbb{R}^d$, treated as functions on a fixed domain $\Omega \subseteq \mathbb{R}^d$, the aim of image registration is to find a transformation $\phi\colon \Omega \to \Omega$ such that $u_0 \circ \phi^{-1} \approx u_1$. There exist several choices for the class of transformation to employ. A quite general approach uses the group of diffeomorphisms of the domain Ω. Since the group of diffeomorphisms also forms a Lie group, with the vector space of smooth vector fields on Ω being the corresponding Lie algebra, we parametrize a diffeomorphism by a single vector field to which we apply the exponential map to regain the corresponding diffeomorphism. This idea is used in the *geodesic shooting* algorithm developed in Miller et al. (2006). In the aforementioned work, the Euler-Poincaré equations for the evolution along a geodesic in the diffeomorphism group are described. Together with the corresponding adjoint equations, it is possible to formulate a gradient descent algorithm for an energy functional of the form

$$E_{u_0 \to u_1}(v_0) := \|v_0\|_V^2 + \frac{1}{\sigma^2}\|u_0 \circ \phi_1^{-1} - u_1\|_{L^2(\Omega)}^2,$$

where $v_0\colon \Omega \to \mathbb{R}^d$ denotes a vector field, $\|\cdot\|_V$ is a suitable norm on the space of vector fields, $\sigma > 0$ is a weighting parameter, and the diffeomorphism $\phi_1\colon \Omega \to \Omega$ is given as the solution at the final time $t = 1$ of the equation

$$\frac{d\phi_t}{dt} = v_t \circ \phi_t,$$

where v_t, for $t \in [0, 1]$, solves the Euler-Poincaré equation for the initial vector field v_0. It then holds $\phi_1 = \exp(v_0)$.

3. NONLINEAR APPROXIMATION SCHEME

Before describing the algorithm in detail, we introduce some more notation: We denote by $\mathcal{P} \subset \mathbb{R}^p$ for some $p \in \mathbb{N}$ the parameter space. Moreover, the space-time solution of the equation under consideration for the parameter $\mu \in \mathcal{P}$ is denoted by $u(\mu)\colon \Omega \to \mathbb{R}$. The domain Ω is a subset of $\mathbb{R}^n \times \mathbb{R}^+$, where $n \in \mathbb{N}$ is the space dimension. It therefore holds $d = n+1$ for the dimension of the domain we deform.

For simplicity, we restrict our attention to a single "topology" of the solution, which is assumed to be independent of the parameter $\mu \in \mathcal{P}$. We consider, for instance, only solutions with a single shock or solutions with two merging shocks. This means that we assume that it is possible to transform solutions into each other by means of diffeomorphic transformations of the underlying domain Ω.

The idea of using Lie groups together with their corresponding Lie algebra for model order reduction of hyperbolic equations was introduced in Ohlberger and Rave (2013), where finite-dimensional groups acting only on the spatial domain were considered, for instance the translation group. Here, we use the infinite-dimensional diffeomorphism group on the space-time domain Ω, such that shock formation and interaction are already included in the ansatz-functions.

3.1 Offline algorithm

During the offline phase, we first of all choose a reference parameter $\mu_{\text{ref}} \in \mathcal{P}$ and compute the related full-order space-time reference solution $u(\mu_{\text{ref}})$. Afterwards, we select training parameters $\mu_1, \dots, \mu_M \in \mathcal{P}$ and compute the solution snapshots $u(\mu_1), \dots, u(\mu_M)$. We do not detail the exact solution algorithm for the full-order computations, the only requirement we impose is that the solution data can be treated as a function on Ω, such that we can apply the geodesic shooting algorithm for image registration. Subsequently, vector fields $v(\mu_1), \dots, v(\mu_M)\colon \Omega \to \mathbb{R}^d$ are computed, using the geodesic shooting algorithm, such that they minimize $E_{u(\mu_{\text{ref}})\to u(\mu_1)}, \dots, E_{u(\mu_{\text{ref}})\to u(\mu_M)}$. The set of vector fields $v(\mu_1), \dots, v(\mu_M)$ is now reduced using *proper orthogonal decomposition*, similar to the procedure described in Wang et al. (2019). This step results in an orthogonal matrix V_N, whose columns span an N-dimensional subspace of the space of vector fields. Finally, an artificial neural network $\Phi\colon \mathcal{P} \to \mathbb{R}^N$ is trained to approximate the mapping $\pi\colon \mathcal{P} \to \mathbb{R}^N$ defined as $\pi(\mu) = V_N^\top v(\mu)$. The function π maps a parameter $\mu \in \mathcal{P}$ to the coefficients (with respect to the basis V_N) of the orthogonal projection of the optimal vector field $v(\mu)$ onto the subspace $\text{ran}(V_N)$.

3.2 Online algorithm

Given a new parameter $\mu \in \mathcal{P}$, a forward pass through the neural network is performed to obtain the approximate coefficients $\Phi(\mu) \approx \pi(\mu)$. Next, the vector field $v_N(\mu) = V_N\Phi(\mu)$ is computed. By applying the exponential map exp to $v_N(\mu)$, we derive the diffeomorphism $\phi_N(\mu) = \exp(v_N(\mu))$. The approximate solution for the parameter μ is now given as $u_N(\mu) = u(\mu_{\text{ref}}) \circ \phi_N^{-1}(\mu)$.

4. EXAMPLE

We present the decay of the singular values of the computed vector fields for a Burgers' equation with two merging shocks. The equation of interest reads

$$\partial_t u + u\,\partial_x u = 0, \quad u(x,0) = \begin{cases} 2, & \text{if } x \le 0.25, \\ 1, & \text{if } 0.25 < x < 0.5, \\ 0, & \text{otherwise,} \end{cases}$$

where $\mu \in [0.25, 1] =: \mathcal{P}$, and $(x,t) \in [0,1]^2 =: \Omega$. An example of a space-time solution for this equation for $\mu = 1/2$ is given in the left part of Fig. 1. Starting with the reference parameter $\mu_{\text{ref}} = 0.25$, we performed registration onto 50 snapshots for parameters uniformly selected from $\mathcal{P}$. The singular values of the vector fields together with the singular values of the space-time snapshots themselves are presented in the right part of Fig. 1. The maximum relative L_2-error of the transformed snapshots with respect to the exact solutions is roughly 6%. The plots show that the singular values of the vector fields decay much faster (even exponentially) than those of the snapshots, which means that the vector fields can be approximated more efficiently by a linear subspace than the snapshots.

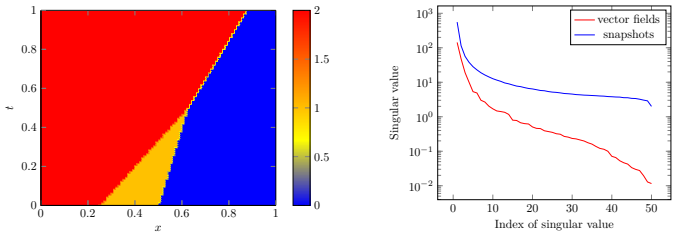

Fig. 1. Sample solution to Burgers' equation and singular values of vector fields (red) and snapshots (blue)

5. CONCLUSION

In this work we describe a new approach for nonlinear model order reduction for parametrized hyperbolic equations. Future research in this direction will be concerned with the computation of the reduced coefficients for the vector fields by solving a residual-minimization problem. Furthermore, the treatment of different solution topologies would make the algorithm more flexible.

REFERENCES

Miller, M., Trouvé, A., and Younes, L. (2006). Geodesic shooting for computational anatomy. *Journal of mathematical imaging and vision*, 24, 209–228.

Ohlberger, M. and Rave, S. (2013). Nonlinear reduced basis approximation of parameterized evolution equations via the method of freezing. *Comptes Rendus Mathematique*, 351(23), 901 – 906.

Ohlberger, M. and Rave, S. (2016). Reduced basis methods: Success, limitations and future challenges. *Proceedings of the Conference Algoritmy*, 1–12.

Wang, J., Xing, W., Kirby, R.M., and Zhang, M. (2019). Data-driven model order reduction for diffeomorphic image registration. In A.C.S. Chung, J.C. Gee, P.A. Yushkevich, and S. Bao (eds.), *Information Processing in Medical Imaging*, 694–705. Springer International Publishing, Cham.

Global analysis of SAIRS-type epidemic models

Stefania Ottaviano * **Mattia Sensi** ** **Sara Sottile** ***

* *University of Padua, Dept. of Mathematics "Tullio Levi Civita", Viale Trieste 63, 35131 Padova, Italy.*
** *Inria Sophia Antipolis - Méditerranée Research Centre, 2004 Rte des Lucioles - Biot, 06410, France.*
*** *University of Trento, Dept. of Mathematics, Via Sommarive, 14 - Povo, Trento, 38123, Italy.*

1. INTRODUCTION

Once an infectious disease starts circulating in a population, the main goal is to contain its spread. Several control strategies may be applied to control a disease, such as detection and isolation of infectious individuals or vaccination. However, the detection of infectious individuals is far from being an easy task: various diseases, such as influenza, cholera, shigella or Covid-19, are often spread by asymptomatic individuals. The presence of asymptomatic cases allows a wide circulation of a disease in the population, since they often remain unidentified. Hence, the contribution of the so called "silent spreaders" to the infection transmission dynamics should be considered in mathematical epidemic models, as in Robinson and Stilianakis (2013). Unlike the more famous and studied epidemic models, much less attention has been paid to the SAIR(S)-type models. Thus, we think that a deeper understanding of these kinds of models is needed, and could prove to be very useful in the epidemiological field.

In this work, we consider an SAIRS (Susceptible - Asymptomatic infected - symptomatic Infected - Recovered - Susceptible) model based on the one proposed in (Robinson and Stilianakis, 2013, Sec. 2), in which the authors provide only a local stability analysis. An SAIR-type model is studied in Ansumali et al. (2020), with application to SARS-CoV-2. The proposed global stability analysis regards only a simplified version of the model in Robinson and Stilianakis (2013): first, recovered people do not lose their immunity; moreover, the infection rates of the asymptomatic and symptomatic individuals are equal, as well as their recovery rates, while in Robinson and Stilianakis (2013) these parameters are considered to be potentially different. In Ottaviano et al. (2022b), we provide a global stability analysis of the model proposed in Robinson and Stilianakis (2013), and for some variations thereof. In addition, we include in our model the possibility of vaccination. In the investigation of global stability, we answer an open problem left in Ansumali et al. (2020). In particular, we study the global asymptotic stability (GAS) of the disease-free equilibrium (DFE) and provide results related to the global asymptotic stability of the endemic equilibrium (EE) for many variations of the model. We found the expression of the basic reproduction number R_0 and prove that the DFE is globally asymptotically stable if $R_0 < 1$ and unstable if $R_0 > 1$, condition under which a positive endemic equilibrium (EE) exists.

2. FORMULATION OF THE MODEL

In our model, the total population N is partitioned into four compartments, namely S, A, I, R, which represent the fraction of Susceptible, Asymptomatic infected, symptomatic Infected and Recovered individuals, respectively, such that $N = S + A + I + R$. Without loss of generality, we assume $N = 1$. The infection can be transmitted to a susceptible through contact with either an asymptomatic infected individual, at rate β_A, or a symptomatic individual, at rate β_I. From the asymptomatic compartment, an individual can either progress to the class of symptomatic infectious I, at rate α, or recover without ever developing symptoms, at rate δ_A. An infected individual with symptoms can recover at a rate δ_I. We assume that the recovered individuals do not obtain a long-life immunity and can return to the susceptible state after an average time $1/\gamma$. Furthermore, we assume that a proportion ν of susceptible individuals receive a dose of vaccine, which grants them a temporary immunity. Moreover, we consider the vital dynamics of the entire population and, for simplicity, we assume that the rate of births and deaths are the same, equal to μ; we do not distinguish between natural deaths and disease related deaths. The system of ODEs that describes the model is given by:

$$\begin{aligned}
\frac{dS(t)}{dt} &= \mu - \Big(\beta_A A(t) + \beta_I I(t)\Big) S(t) - (\mu+\nu) S(t) + \\
&\quad + \gamma R(t), \\
\frac{dA(t)}{dt} &= \Big(\beta_A A(t) + \beta_I I(t)\Big) S(t) - (\alpha + \delta_A + \mu) A(t), \\
\frac{dI(t)}{dt} &= \alpha A(t) - (\delta_I + \mu) I(t), \\
\frac{dR(t)}{dt} &= \delta_A A(t) + \delta_I I(t) + \nu S(t) - (\gamma + \mu) R(t),
\end{aligned} \tag{1}$$

with initial condition $(S(0), A(0), I(0), R(0))$ belonging to the set

$$\bar{\Gamma} = \{(S, A, I, R) \in \mathbb{R}^4_+ | S + A + I + R = 1\}, \tag{2}$$

where $\mathbb{R}^4_+$ is the non-negative orthant of $\mathbb{R}^4$. Assuming initial conditions in $\bar{\Gamma}$, $S(t) + A(t) + I(t) + R(t) = 1$, for all $t \geq 0$; hence, system (1) is equivalent to the following three-dimensional dynamical system:

$$\begin{aligned}\frac{dS(t)}{dt} &= \mu - \Big(\beta_A A(t) + \beta_I I(t)\Big)S(t) - (\mu+\nu+\gamma)S(t) + \\ &\quad + \gamma(1 - A(t) - I(t)), \\ \frac{dA(t)}{dt} &= \Big(\beta_A A(t) + \beta_I I(t)\Big)S(t) - (\alpha + \delta_A + \mu)A(t), \\ \frac{dI(t)}{dt} &= \alpha A(t) - (\delta_I + \mu)I(t),\end{aligned} \tag{3}$$

with initial condition $(S(0), A(0), I(0))$ belonging to the set

$$\Gamma = \{(S, A, I) \in \mathbb{R}^3_+ | S + A + I \leq 1\},$$

which is positively invariant for system (3). In the following, we denote with $\mathring{\Gamma}$ the interior of the set Γ.

3. RESULTS

System (3) always admits a disease-free equilibrium, given by

$$x_0 = (S_0, A_0, I_0) = \left(\frac{\mu+\gamma}{\mu+\nu+\gamma}, 0, 0\right). \tag{4}$$

The behaviour of the system is related to the basic reproduction number $\mathcal{R}_0$ of (3), given by

$$\mathcal{R}_0 = \left(\beta_A + \frac{\alpha\beta_I}{\delta_I + \mu}\right)\frac{\gamma+\mu}{(\alpha+\delta_A+\mu)(\nu+\gamma+\mu)}. \tag{5}$$

Theorem 3.1. *The disease-free equilibrium x_0 of (3) is globally asymptotically stable in Γ if $\mathcal{R}_0 < 1$, and unstable if $\mathcal{R}_0 > 1$.*

Theorem 3.2. *There exists a unique endemic equilibrium $x^* = (S^*, A^*, I^*)$ in $\mathring{\Gamma}$ for system (3) if and only if $\mathcal{R}_0 > 1$.*

In Ottaviano et al. (2022b), we analyze different variations of the model. In the case of the SAIR model (i.e. $\gamma = 0$) and when asymptomatic and symptomatic individuals have the same transmission rate and recovery rate (i.e. $\beta_A = \beta_I$ and $\delta_A = \delta_I$), we prove the following result providing an appropriate Lyapunov function.

Theorem 3.3. *The endemic equilibrium $x^* = (S^*, A^*, I^*)$ is globally asymptotically stable in $\mathring{\Gamma}$ for system (3) if $\mathcal{R}_0 > 1$.*

In the general case of the SAIRS model with different rate of transmission and recovery for the two groups of infectious individuals, we use a geometric approach for the global stability of equilibria of nonlinear autonomous differential equations proposed in Lu and Lu (2017).

Theorem 3.4. *Assume that $\mathcal{R}_0 > 1$ and $\beta_A < \delta_I$. Then, the endemic equilibrium x^* is globally asymptotically stable in $\mathring{\Gamma}$ for system (1).*

However, as illustrated by various numerical simulations in Ottaviano et al. (2022b), we are led to think that the assumption on the parameters β_A and δ_I could be relaxed.

4. EXTENSION TO A MULTI-GROUP MODEL

Later, we generalize the SAIRS model to a multi-group model, which takes into account different groups of individual among which an epidemic can spread.

In this framework, the total population is divided into n groups. We denote with S_i, A_i, I_i and R_i the fraction of Susceptible, Asymptomatic infected, symptomatic Infected and Recovered individuals in the $i-$th group, respectively, such that $S_i + A_i + I_i + R_i = 1$ at all times.

The disease can be transmitted by individuals A_i and I_i, within their group, to the susceptible S_i, with transmission rate β^A_{ii} and β^I_{ii}, respectively, but also between different groups: e.g., individuals A_j and I_j, belonging to the j-th group, may infect susceptible individuals S_i of group i with transmission rate β^A_{ij} and β^I_{ij}, respectively. We also assume that the multi-group network is undirected and connected. The disease-related parameters, that are the average time of the symptoms developing, denoted by $1/\alpha$, the recovery rates from both the infectious compartments, δ_A and δ_I, and the average time to return to the susceptible state, $1/\gamma$, do not depend on the group of origin. We assume, instead, that the proportion ν_i of vaccinated individuals depends on the group. Moreover, we consider the vital dynamics of each group, assuming that the rate of births and deaths are the same in the $i-$th group, equal to μ_i.

Even though some results on SIRS-type model in Muroya et al. (2013) and SEIRS-type model in Fan et al. (2018) have been achieved, the problem of existence and global stability of an endemic equilibrium for several multi-group models remains open, as stated in Mohapatra et al. (2015).

Our results, in Ottaviano et al. (2022a), regard a generalization of Theorems 3.1-3.3 for the multi-group type model. The problem of the global asymptotically stability of the endemic equilibrium, as in Theorem 3.4, remains open.

REFERENCES

Ansumali, S., Kaushal, S., Kumar, A., Prakash, M.K., and Vidyasagar, M. (2020). Modelling a pandemic with asymptomatic patients, impact of lockdown and herd immunity, with applications to SARS-CoV-2. *Annual reviews in control*.

Fan, D., Hao, P., Sun, D., and Wei, J. (2018). Global stability of multi-group SEIRS epidemic models with vaccination. *International Journal of Biomathematics*, 11(01), 1850006.

Lu, G. and Lu, Z. (2017). Geometric approach to global asymptotic stability for the SEIRS models in epidemiology. *Nonlinear Analysis: Real World Applications*, 36, 20–43.

Mohapatra, R., Porchia, D., and Shuai, Z. (2015). Compartmental disease models with heterogeneous populations: a survey. In *Mathematical Analysis and its Applications*, 619–631.

Muroya, Y., Enatsu, Y., and Kuniya, T. (2013). Global stability for a multi-group SIRS epidemic model with varying population sizes. *Nonlinear Analysis: Real World Applications*, 14(3), 1693–1704.

Ottaviano, S., Sensi, M., and Sottile, S. (2022a). Global stability of multi-group SAIRS epidemic models. arxiv:2202.02993.

Ottaviano, S., Sensi, M., and Sottile, S. (2022b). Global stability of SAIRS epidemic models. *Nonlinear Analysis: Real World Applications*, 65, 103501.

Robinson, M. and Stilianakis, N.I. (2013). A model for the emergence of drug resistance in the presence of asymptomatic infections. *Mathematical Biosciences*, 243(2), 163–177.

Physics-informed Neural Networks for parameter estimation in cardiac mechanics ⋆

Stefano Pagani * **Francesco Regazzoni** * **Matteo Salvador** *
Daniel Fraulin * **Filippo Zacchei** * **Alfio Quarteroni** *,**

* *MOX - Department of Mathematics, Politecnico di Milano, P.zza Leonardo da Vinci 32, 20133 Milano, Italy.*
** *Institute of Mathematics, École Polytechnique Fédérale de Lausanne, Av. Piccard, CH-1015 Lausanne, Switzerland (Professor Emeritus).*

1. INTRODUCTION

Medical imaging represents a relevant tool for diagnosing heart diseases. Different techniques are available, such as echocardiography, magnetic resonance imaging, computed tomography scans, and nuclear medicine. These are associated with an increasing space-time resolution, which may capture crucial details for the clinical decision-making process. However, the more detailed ones might have contraindications for some patients. For this reason, numerous research efforts are directed toward developing new mathematical methods to process those images (especially the most accessible ones) and extract meaningful indications. Deep Learning methods have been very successful in this area (Hernandez et al., 2020) by providing tools for the automatic segmentation of geometry and structural defects (resulting, e.g., from myocardial infarction) and for the computation of clinical biomarkers (such as cardiac motion and strains). Nevertheless, Deep Learning methods generally require large datasets for the training phase, which are not always available.

The knowledge of the physical laws governing the myocardial motion may balance this lack of data, enabling the training of the so-called physics-informed neural networks (PINNs) introduced in Raissi et al. (2019). PINNs consist of interconnected neurons, whose parameters are trained by minimizing the mismatch between the output and the available noisy data, together with additional terms encoding the partial differential equation (PDE) and the boundary conditions characterizing the physical phenomenon.

Compared to standard model personalization strategies (Chabiniok et al., 2016) based on iterative schemes requiring the numerical approximation of the forward and the adjoint problems at each iteration, PINNs enable the simultaneous numerical estimation of both the displacement and the parameters of interest. This is achieved by automatic differentiation, which provides a flexible and computationally inexpensive tool to evaluate the PDE residual and the boundary conditions in their strong form.

⋆ This project has been supported by the European Research Council (ERC) under the European Union's Horizon 2020 research and innovation programme (grant agreement No 740132, iHEART, P.I. Prof. A. Quarteroni)

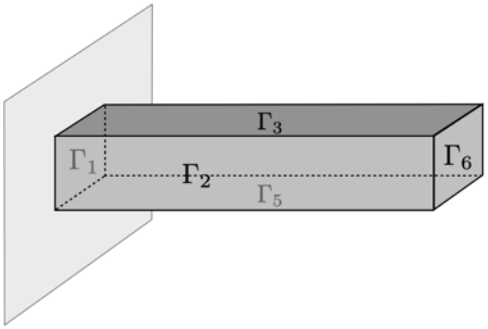

Fig. 1. Undeformed geometry of a parallelepiped with a fixed base.

In this framework, promising proofs of concept have been already presented in Zhang et al. (2020) and Nguyen-Thanh et al. (2020).

In this work, we study the feasibility of using PINNs in estimating parameters of interest for a 3D mechanical problem starting from scattered measurements of the displacement. We also focus on the effects of the density of data and the associated level of noise on the accuracy of the estimation.

2. MATHEMATICAL MODELS AND METHODS

We consider a quasi-static non-linear elastic problem to model the deformation of a parallelepiped with a fixed base (see Fig. 1) and different boundary conditions. We analyze traction, compression, and shear scenarios.

The mechanical problem for the undeformed configuration reads as follows:

$$\begin{cases} -\nabla \cdot \boldsymbol{\mathcal{P}}(\mathbf{d}) = 0 \quad \text{in } (0,L)\times(0,W)\times(0,W), \\ + \text{ B.C.}, \end{cases} \tag{1}$$

where $\mathbf{d} = \mathbf{d}(\mathbf{x})$ is the displacement, L and W define the dimensions of the parallelepiped, and $\boldsymbol{\mathcal{P}}$ is the first Piola-Kirchhoff stress tensor. Additional boundary conditions are considered for the three different scenarios (traction, compression, and shear). After introducing a hyperelastic energy $\mathcal{W} = \mathcal{W}(\boldsymbol{\mathcal{F}})$, the first Piola-Kirchhoff stress tensor $\boldsymbol{\mathcal{P}}$ can be computed as:

$$\boldsymbol{\mathcal{P}} = \frac{\partial \mathcal{W}}{\partial \boldsymbol{\mathcal{F}}} \ .$$

Among the several constitutive laws available for cardiac mechanics (Quarteroni et al., 2019), we use the following quasi-incompressible Neo-Hookean hyperelastic energy:

$$\mathcal{W} = \frac{\mu}{2}(\mathcal{J}^{-2/3}\mathrm{tr}(\boldsymbol{\mathcal{C}}) - 3) + \frac{\lambda}{4}\left((\mathcal{J}-1)^2 + \log^2(\mathcal{J})\right)$$

where $\mathcal{J} = \det(\boldsymbol{\mathcal{F}})$ is the determinant of the deformation tensor, $\boldsymbol{\mathcal{C}} = \boldsymbol{\mathcal{F}}^T\boldsymbol{\mathcal{F}}$ is the right Cauchy-Green tensor and, finally, μ and λ are the mechanical parameters (shear and bulk modulus, respectively). We construct in silico datasets by solving Eq. (1) with the Finite Element Method, by employing the Dolfin Python library (Logg et al., 2012). We sample the displacement in different locations of the computational domain, and we possibly add Gaussian noise to the pointwise values:

$$\mathbf{d}_{\mathrm{i}}^{\mathrm{obs}} = \mathbf{d}(\mathbf{x}_{\mathrm{i}}; \mu_{\mathrm{ex}}) + \epsilon_{\mathrm{i}} \qquad \epsilon_{\mathrm{i,j}} \sim \mathcal{N}(0, \sigma^2),$$

where μ_{ex} is the exact value of the parameter to be estimated. Indeed, we adopt PINNs to find the unknown parameter $\mu \subset \mathcal{P} \subset \mathbb{R}$ by solving a statistical learning problem in which the numerical solution of Eq. (1) is approximated by means of a fully-connected Neural Network $\mathcal{NN}$, formed by a set of neurons distributed over different layers. Moreover, $\mathcal{NN}$ is characterized by a set of parameters $\mathbf{W}$, namely weights and biases, which are tuned during the optimization process by solving the following PDE-constrained optimal control problem:

$$\begin{cases} \min\limits_{\mu,\mathbf{W}} \ (\mathcal{J}_{\mathrm{fit}}(\mathbf{W}) + \mathcal{J}_{\mathrm{phys}}(\mu, \mathbf{W})) \\ \text{s.t.} \quad \mathbf{d}(\mathbf{x}) = \mathcal{NN}(\mathbf{x}; \mathbf{W}). \end{cases}$$

We minimize the loss function composed of the weighted sum of different components leveraging data and physics. Specifically, the mismatch between the output of the $\mathcal{NN}$ and the available N_{obs} noisy observations is measured through the following component of the loss function:

$$\mathcal{J}_{\mathrm{fit}}(\mathbf{W}) = \frac{\omega_{\mathrm{fit}}}{N_{\mathrm{obs}}} \sum_{i=1}^{N_{\mathrm{obs}}} \|\mathcal{NN}(\mathbf{x}_{\mathrm{i}}; \mathbf{W}) - \mathbf{d}_{\mathrm{i}}^{\mathrm{obs}}\|^2.$$

Here, $\omega_{\mathrm{fit}} > 0$ is an additional hyperparameter that weights the contribution of the available data with respect to the information coming from the physical model. The latter is encoded in $\mathcal{J}_{\mathrm{phys}}$, which is made by several terms containing the residuals of the PDE and boundary conditions, expressed in the strong form:

$$\begin{aligned} \mathcal{J}_{\mathrm{phys}}(\mu, \mathbf{W}) = \omega_{\mathrm{phys}} R_{\mathrm{phys}}(\mathbf{d}; \mu, \mathbf{W}) \\ + \sum_{i=1}^{N_{\mathrm{bc}}} \omega_{\mathrm{bc}}^i B_{\mathrm{phys}}^i(\mathbf{d}; \mu, \mathbf{W}), \end{aligned}$$

with scalar hyperparameters ω_{phys} and ω_{bc}^i, $i \in 1, \ldots, N_{\mathrm{bc}}$, that leverage the contributions of the mathematical model. In particular, $\mathcal{J}_{\mathrm{phys}}$ contains a regularization term R_{phys} formed by the norm of the PDE residual:

$$R_{\mathrm{phys}}(\mathbf{d}; \mu, \mathbf{W}) = \frac{1}{N_{\mathrm{c}}} \sum_{i=1}^{N_{\mathrm{c}}} \| - \nabla \cdot \boldsymbol{\mathcal{P}}(\mathcal{NN}(\mathbf{x}_{\mathrm{i}}^c; \mathbf{W}))\|^2,$$

which is averaged over the set of collocation points $\{\mathbf{x}_{\mathrm{i}}^c\}$, $i = 1, \ldots, N_{\mathrm{c}}$.

The training of $\mathcal{NN}$ parameters, along with the estimation of the unknown parameter μ, is attained by combining the first-order ADAM optimizer (Kingma and Ba, 2014) with the second-order BFGS optimizer. Specifically, we develop a multistage training strategy that allows robustly performing data fitting and parameter estimation over a wide range of initial guesses for the $\mathcal{NN}$ parameters $\mathbf{W}$.

3. DISCUSSION

We studied the ability of PINNs to estimate the solution of Eq. (1) and the unknown parameter μ for different benchmark test cases based on a 3D non-linear elastic problem. We investigated the performances of PINNs in different setups, showing the dependence of the accuracy in parameter estimation with respect to the level of noise and density of measures. Hyperparameters may be suitably tuned by properly weighting the different components of the loss function to handle large noise and low data regimes.

PINNs have proven to be a powerful and flexible tool for solving the parameter estimation problem in this context. This will potentially lead to the clinical exploitation of PINNs. Nevertheless, finding an automatic optimal tuning of the various hyperparameters in the algorithm remains an open challenge.

REFERENCES

Chabiniok, R., Wang, V.Y., Hadjicharalambous, M., Asner, L., Lee, J., Sermesant, M., Kuhl, E., Young, A.A., Moireau, P., Nash, M.P., Chapelle, D., and Nordsletten, D.A. (2016). Multiphysics and multiscale modelling, data-model fusion and integration of organ physiology in the clinic: ventricular cardiac mechanics. *Interface Focus*, 6(2), 20150083.

Hernandez, K.A.L., Rienmüller, T., Baumgartner, D., and Baumgartner, C. (2020). Deep learning in spatiotemporal cardiac imaging: A review of methodologies and clinical usability. *Computers in Biology and Medicine*, 104200.

Kingma, D.P. and Ba, J. (2014). Adam: A method for stochastic optimization. *arXiv preprint arXiv:1412.6980*.

Logg, A., Mardal, K.A., and Wells, G. (2012). *Automated solution of differential equations by the finite element method: The FEniCS book*, volume 84. Springer Science & Business Media.

Nguyen-Thanh, V.M., Zhuang, X., and Rabczuk, T. (2020). A deep energy method for finite deformation hyperelasticity. *European Journal of Mechanics-A/Solids*, 80, 103874.

Quarteroni, A., Dede', L., Manzoni, A., and Vergara, C. (2019). *Mathematical Modelling of the Human Cardiovascular System: Data, Numerical Approximation, Clinical Applications*. Cambridge Monographs on Applied and Computational Mathematics. Cambridge University Press.

Raissi, M., Perdikaris, P., and Karniadakis, G.E. (2019). Physics-informed neural networks: A deep learning framework for solving forward and inverse problems involving nonlinear partial differential equations. *Journal of Computational Physics*, 378, 686–707.

Zhang, E., Yin, M., and Karniadakis, G.E. (2020). Physics-informed neural networks for nonhomogeneous material identification in elasticity imaging. *arXiv preprint arXiv:2009.04525*.

pyMOR – Reduced Order Modeling with Python ⋆

Linus Balicki * **René Fritze** ** **Petar Mlinarić** * **Stephan Rave** **
Jens Saak *** **Felix Schindler** **

* *Department of Mathematics, Virginia Tech, Blacksburg, USA (e-mail: {balicki,mlinaric}@vt.edu).*
** *Applied Mathematics, University of Münster, Germany (e-mail: {rene.fritze,stephan.rave,felix.schindler}@uni-muenster.de)*
*** *Max Planck Institute for Dynamics of Complex Technical Systems, Magdeburg, Germany (e-mail: saak@mpi-magdeburg.mpg.de)*

Abstract: pyMOR is a free and open source software library for writing model order reduction applications with the Python programming language. Implemented algorithms include both Reduced Basis and system-theoretic reduction methods, as well as non-intrusive approaches such as approximation with artificial neural networks. All these algorithms can be easily integrated with external high-performance PDE solver packages. In this poster contribution we give a brief overview on the design of pyMOR. Further, we will present in more details two main features of the upcoming 2022.1 release: 1. a new and unified model hierarchy, 2. new discretization routines to create these models from common analytical problem definitions using different PDE solver backends.

Keywords: model reduction, software, reduced basis method, balanced truncation, IRKA, POD, empirical interpolation, artificial neural networks

1. INTRODUCTION

Over the last decade, Model Order Reduction (MOR) has become an essential tool in mathematical modeling and simulation workflows, significantly speeding up computation times, especially in multi-query contexts such as optimization, optimal control or interactive design applications (see, e.g., Benner et al. (2020)).

Since MOR methods work on top of existing ODE/PDE solvers, their implementation is often non-trivial and requires knowledge of both the given solver and the MOR method to be implemented. pyMOR (Milk et al. (2016); Balicki et al. (2019); Mlinarić et al. (2021), `https://www.pymor.org`) is a free and open source MOR library for the Python programming language which facilitates the integration of MOR methods with high-performance solvers by expressing MOR algorithms via operations on simple solver interface classes.

In this poster contribution we give a short overview on pyMOR's design (Section 2). In Section 3 we discuss two new features of the upcoming 2022.1 release, which significantly facilitate the construction and reduction of full-order models (FOMs) in pyMOR.

⋆ Funded by the Deutsche Forschungsgemeinschaft (DFG, German Research Foundation) under Germany's Excellence Strategy EXC 2044 –390685587, Mathematics Münster: Dynamics–Geometry–Structure and under RA 3055/1-1, SA 3477/1-1: pyMOR – Nachhaltige Software zur Modell-Ordnungs-Reduktion.

2. SOFTWARE DESIGN

pyMOR's design is based on the idea of expressing all MOR operations through low-level, MOR agnostic interface classes for interacting with the solver that implements the FOM. In particular this allows to easily prototype new MOR algorithms using a lightweight discretization library, such as the toolkit shipped with pyMOR, and later use the same implementation for a large application problem implemented in a specialized high-performance code.

2.1 Interfaces

pyMOR interacts with external solvers through `VectorArrays`, `Operators` and `Models`. A `VectorArray` represents an ordered collection of vectors of the same dimension and allows the usual linear algebra operations such as inner products or linear combinations. `Operators` encapsulate matrices or nonlinear operators, which can be `applied` to `VectorArrays`. A `Model` encodes the mathematical structure of the given FOM and exposes the solvers' simulation routines via the `solve` method.

We emphasize that all required interface operations can be expected to be already implemented in the external solver. In particular, no MOR-specific code has to be added to integrate a new solver with pyMOR. The integration usually is technically realized by compiling the external solver as a Python extension module, but also network or disk-based communication is possible.

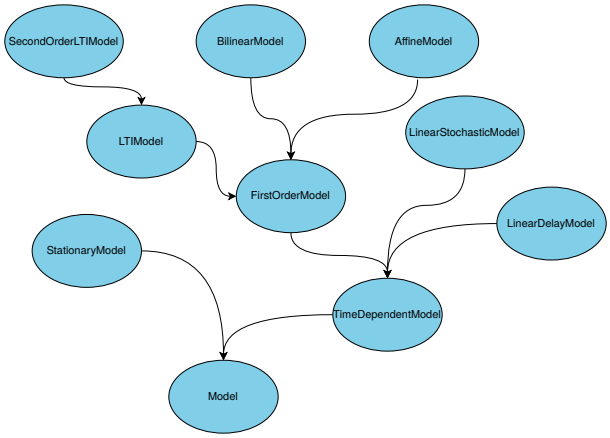

Fig. 1. Hierarchy of `Models` in pyMOR 2022.1 (subject to change). `Reductors` for a base class can be applied to each subclass in the hierarchy.

2.2 Algorithms

Based on the aforementioned interface classes, pyMOR implements various MOR algorithms such as Reduced Basis (RB) methods, Proper Orthogonal Decomposition (POD), (discrete) empirical interpolation, Balanced Truncation, the Iterative Rational Krylov Algorithm (IRKA), as well as non-intrusive data-driven methods, such as approximation with artificial neural networks. As an example, the Petrov-Galerkin projection $W^T \cdot A \cdot V$ of the full-order matrix A onto bases spanned by the columns of V and W can be written as

```
W.inner(A.apply(V)),
```

where A is given as an `Operator` and V, W are `VectorArrays`. All MOR algorithms are realized as `Reductor` objects, which transform a given full-order `Model` to a corresponding reduced-order `Model` (ROM) of similar type, where the FOM's `Operators` have been replaced by new `Operators` storing their reduced counterparts. Due to the general nature of pyMOR's interfaces, pyMOR also implements further algorithms, such as Gram-Schmidt orthonormalization, a Newton algorithm or different time steppers.

3. NEW FEATURES IN PYMOR 2022.1

In this section we highlight two main new features in pyMOR related to building and reducing `Models` in pyMOR.

3.1 A new Model hierarchy

To our knowledge, pyMOR is the only available software package which includes a large variety of both RB methods, which are geared at parameterized PDEs, as well as system-theoretic methods such as Balanced Truncation or IRKA, which originally were mainly developed for LTI systems. For years, both branches of MOR have been developed mostly independently from one another, which, so far, has also been reflected in pyMOR, where system-theoretic `reductors` operate on `LTIModels` and related classes, which are incompatible with the classes required by RB `reductors`, which operate on `StationaryModels` and `InstationaryModels`.

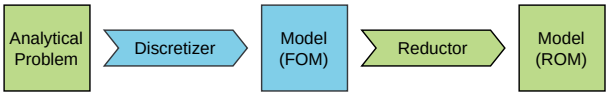

Fig. 2. Reduced-order modeling pipeline in pyMOR (blue background: solver specific code, green background: generic code).

In pyMOR 2022.1, the existing `Model` classes are refactored into a new class hierarchy that provides a unified view onto `Models` for both RB and system-theoretic methods (see Fig. 1). In particular, this allows to seamlessly apply RB `reductors` for general `FirstOrderModels` to `Models` with additional structure, such as `LTIModel`, in addition to the more specialized methods, e.g., Balanced Truncation.

3.2 Discretizers for external PDE solvers

pyMOR's builtin discretization toolkit uses `analytical-problems` as data structures to define the (parameterized) PDE problem to be solved. `Analyticalproblems` combine a definition of the computational domain with coefficient functions for the respective PDE that is given by the respective problem class. Such an `analyticalproblem` is then given as an input to a `discretizer`, which builds a corresponding `Model` using pyMOR's builtin FEM/FV `Operators`. So far, building a `Model` with an external PDE solver, even for a standard benchmark problem, required manually building the `Model` using appropriate PDE solver code and pyMOR's wrapper classes for the given solver.

Based on pyMOR's recently introduced symbolic expression library, pyMOR 2022.1 includes new `discretizers` which allow to use the same `analyticalproblems` to automatically build `Models` using external solvers, such as FEniCS, and, thus, to make use of advanced features of these solvers, such as higher-order methods or MPI parallelization. This enables a powerful reduced order modeling workflow, where the user can easily build efficient ROMs, even for complex problems, without having knowledge of the used PDE solver library (see Fig. 2).

REFERENCES

Balicki, L., Mlinarić, P., Rave, S., and Saak, J. (2019). System-theoretic model order reduction with pyMOR. *PAMM*, 19(1). doi:10.1002/pamm.201900459.

Benner, P., Schilders, W., Grivet-Talocia, S., Quarteroni, A., Rozza, G., and Miguel Silveira, L. (eds.) (2020). *Model Order Reduction: Volume 1–3*. De Gruyter.

Milk, R., Rave, S., and Schindler, F. (2016). pyMOR – Generic Algorithms and Interfaces for Model Order Reduction. *SIAM Journal of Scientific Computing*, 38(5), S194–S216. doi:10.1137/15M1026614.

Mlinarić, P., Rave, S., and Saak, J. (2021). Parametric Model Order Reduction Using pyMOR. In P. Benner, T. Breiten, H. Faßbender, M. Hinze, T. Stykel, and R. Zimmermann (eds.), *Model Reduction of Complex Dynamical Systems*, International Series of Numerical Mathematics, 357–367. Springer International Publishing, Cham. doi:10.1007/978-3-030-72983-7_17.

Hydrogen sensor fault detection in a dark fermenter based on an interval observer and adaptive thresholds

J. David Avilés * **Ixbalank Torres** **

* *Universidad Autónoma de Baja California, Mexico (e-mail: david.aviles@uabc.edu.mx).*
** *C.A. Telemática, Departamento de Ingeniería Electrónica, Universidad de Guanajuato, Mexico (e-mail: ixbalank@ugto.mx)*

Abstract: In this paper, we propose an interval observer-based fault detection strategy for a hydrogen production bioreactor in occurrence of sensor faults. Based on the dark fermenter model in presence of disturbances, we design a robust interval observer to: (i) estimate the glucose and biomass concentrations from hydrogen flow rate measurements, (ii) attenuate the influence of a disturbance, and (iii) detect the occurrence of the sensor faults by adaptive thresholds. The features of the proposed observer are assessed by numerical simulations.

Keywords: Fault detection, adaptive thresholds, interval observer, biohydrogen production.

1. INTERVAL OBSERVER-BASED SENSOR FAULT DETECTION STRATEGY

Dark fermentation is a complex hydrogen production process, it involves crucial state variables that can be estimated by state observers (software sensors). Nevertheless, kinds of malfunctions or imperfect behaviors may appear during the normal operation of the sensors used to measure the system output. They can be detected by means of different methods of fault detection.

In this paper, we consider the interval observer structure, reported in (Meslem et al., 2020), for a class of linear systems in presence of perturbations. The interval observer provides the upper and lower bounds for the trajectory of the dark fermenter state. Furthermore, we present a sensor fault detection scheme considering the adaptive thresholds for the output signal.

1.1 Interval observer

In this section we consider the 3-order linear model proposed in (Torres and Avilés, 2021) that satisfies the following Assumptions.

Assumption 1. The pair $(A,\, C)$ is detectable.

Assumption 2. We know the upper and lower bounds $\left(\overline{x}^{+}\left(t_0\right),\ \overline{x}^{-}\left(t_0\right)\right)$ for the initial condition, satisfying the following inequality

$$\overline{x}^{+}\ \left(t_0\right)\ \succeq\ \overline{x}\left(t_0\right)\ \succeq\ \overline{x}^{-}\left(t_0\right), \tag{1}$$

and the disturbance $\overline{w}\left(t\right)$ is also bounded in the following way,

$$\overline{w}^{+}\left(t\right)\ \succeq\ \overline{w}\left(t\right)\ \succeq\ \overline{w}^{-}\left(t\right), \qquad \forall t \geq 0, \tag{2}$$

where $\overline{w}^{+}\left(t\right)$ and $\overline{w}^{-}\left(t\right)$ are known bounded.

Based on the formulation in (Meslem et al., 2020), we firstly consider the linear observer with the Luenberger structure for the dark fermenter linear model presented in (Torres and Avilés, 2021), described as follows

$$\Upsilon_{\mathrm{O}_1}:\begin{cases}\dot{\xi}(t)=A\xi(t)+B_u\bar{u}(t)+L(\bar{y}(t)-\hat{\bar{y}}(t)),\\ \hat{\bar{y}}(t)=C\xi(t),\end{cases} \tag{3}$$

where $\xi\left(t\right)$ represents the estimate of the real state vector $\overline{x}\left(t\right)$ and the matrix L requires to be selected to ensure the stability property of the observer. If we define the estimation error as $e\left(t\right) \triangleq\ \overline{x}\left(t\right) - \xi\left(t\right)$, we get the estimation error dynamics in the fault-free case $f_s\left(t\right)\ =\ 0$, which are given by the following equations

$$\Upsilon_{\mathrm{E}}:\begin{cases}\ \dot{e}(t)=A_Le(t)\ +\ B_w\overline{w}(t)\,,\\ \ y_e(t)=I_3e(t),\ e\left(t_0\right)\ =\ e_0,\end{cases} \tag{4}$$

where $\overline{w}\left(t\right)$ represents the bounded unknown signals and the matrix $A_L\ =\ A - LC$. I_3 is the identity matrix of dimensions 3×3. The estimation error behavior can be analyzed using the solution of the linear system Υ_{E}, expressed as follows

$$e(t) = \Phi\left(t,\, t_0\right) e(t_0)\ +\ \sigma\left(t\right), \tag{5}$$

where

$$\sigma\left(t\right) = \int_{t_0}^{t} \Phi\left(t,\, \tau\right) B_w \overline{w}(\tau)\, d\tau, \tag{6}$$

with $\Phi\left(t,\, t_0\right)\ =\ \exp\left(A_L(t - t_0)\right)$ is the state transition matrix of the system Υ_{E} in (4).

Secondly, the observer (3) in Υ_{O_1} is combined with the interval predictor, which is given by the following equations

$$\Upsilon_{\mathrm{O}_2}:\begin{cases}\dot{\sigma}^{+}(t)=\Phi^{+}\left(t,\,t_0\right)\left(B_w^{+}\overline{w}^{+}-B_w^{-}\overline{w}^{-}\right)-\\ \qquad\qquad\Phi^{-}\left(t,\,t_0\right)\left(B_w^{+}\overline{w}^{-}-B_w^{-}\overline{w}^{+}\right),\\ \dot{\sigma}^{-}(t)=\Phi^{+}\left(t,\,t_0\right)\left(B_w^{+}\overline{w}^{-}-B_w^{-}\overline{w}^{+}\right)-\\ \qquad\qquad\Phi^{-}\left(t,\,t_0\right)\left(B_w^{+}\overline{w}^{+}-B_w^{-}\overline{w}^{-}\right),\end{cases} \tag{7}$$

$$\Upsilon_{O_3}: \begin{cases} \overline{x}^{+}(t) = \xi(t) + \Phi^{+}(t, t_0)\, e^{+}(t_0) + \\ \qquad\qquad \sigma^{+}(t) - \Phi^{-}(t, t_0)\, e^{-}(t_0), \\ \overline{x}^{-}(t) = \xi(t) + \Phi^{+}(t, t_0)\, e^{-}(t_0) + \\ \qquad\qquad \sigma^{-}(t) - \Phi^{-}(t, t_0)\, e^{+}(t_0), \end{cases} \tag{8}$$

where $\overline{x}^{+}(t)$ and $\overline{x}^{-}(t)$ stand for the upper and lower bounds of the state $\overline{x}(t)$. The matrices B_w^{+} and B_w^{-} in (7) comprise the positive decomposition of the matrix B_w. $(\Phi^{+}(t, t_0), \Phi^{-}(t, t_0))$ and $(\sigma^{+}(t), \sigma^{-}(t))$ are the positive decompositions of $\Phi(t, t_0)$ and $\sigma(t)$, respectively. Additionally, $e^{+}(t_0) = \overline{x}^{+}(t_0) - \xi(t_0)$ and $e^{-}(t_0) = \overline{x}^{-}(t_0) - \xi(t_0)$ are upper and lower bounds, positive representations, of the initial estimation error $e(t_0)$.

We design the interval observer gain L, under fault-free conditions $f_s(t) = 0$, to guarantee that the estimation error $e(t)$ converges to a neighborhood of the origin even if the dark fermenter is in presence of the perturbation $\overline{w}(t)$, as proposed in (Torres and Avilés, 2021).

1.2 Adaptive thresholds strategy

We consider the sensor fault detection using a scheme of adaptive thresholds for the output signal, stated as follows

$$\Upsilon_{\text{Test}}: \begin{cases} \overline{y}(t) \in [\overline{y}^{-}(t),\ \overline{y}^{+}(t)], & \text{if} \quad f_s(t) = 0, \\ \overline{y}(t) \notin [\overline{y}^{-}(t),\ \overline{y}^{+}(t)], & \text{if} \quad f_s(t) \neq 0, \end{cases} \tag{9}$$

where $\overline{y}^{-} = C\overline{x}^{-}$ and $\overline{y}^{+} = C\overline{x}^{+}$. Thus, the plant is fault free when the output signal is inside the set, limited by the adaptive thresholds (the upper and lower estimates), while a fault is indicated in the plant when the output is outside the set, $[\overline{y}^{-}(t), \overline{y}^{+}(t)]$.

2. RESULTS AND DISCUSSION

Simulations of the biohydrogen production process and the Luenberger observer Υ_{O_1} combined with the interval predictor $(\Upsilon_{O_2}, \Upsilon_{O_3})$ have been performed in Matlab for the inputs Q_{in} and Glu_{in} used in (Torres and Avilés, 2021).

We set the following conditions for simulations on the dark fermenter in order to analyze the sensor fault detection strategy proposed. The first one considers the case with a noise variation up to 1% on the hydrogen flow rate sensor during the time period from the beginning of the simulations to day 15, from day 25 to day 35, from day 40 to day 50, and from day 60 to the end of the simulations. This condition corresponds to the sensor fault-free condition. Moreover, we take a noise variation of 10% on the measured variable during the time-period from day 15 to day 25 and from day 50 to day 60, while from day 30 to day 40 an offset of 25% is added to the measured output. These last conditions correspond to sensor fault conditions.

Figure 1a shows the glucose concentration in the dark fermenter, Figure 1b shows the biomass concentration in the dark fermenter, while Figure 1c shows the produced hydrogen flow rate. In green lines the bioreactor simulations, in dashed red line the estimation by the Luenberger observer, and in blue line the lower and the upper estimations by the interval predictor. The behavior of the interval observer is shown in the three figures, where the upper and lower estimations preserve the partial ordering with respect of the trajectories of the bioreactor state when there is no occurrence of faults $f_s = 0$, taking an adequate initialization, and reducing the influence of the unknown inlet glucose concentration. In particular, if there is the presence of sensor faults $f_s \neq 0$, the trajectories of the outputs are outside the interval set given by the lower and upper estimations $\overline{y}(t) \notin [\overline{y}^{-}(t),\ \overline{y}^{+}(t)]$. This fact validates the adaptive thresholds strategy to detect sensor faults.

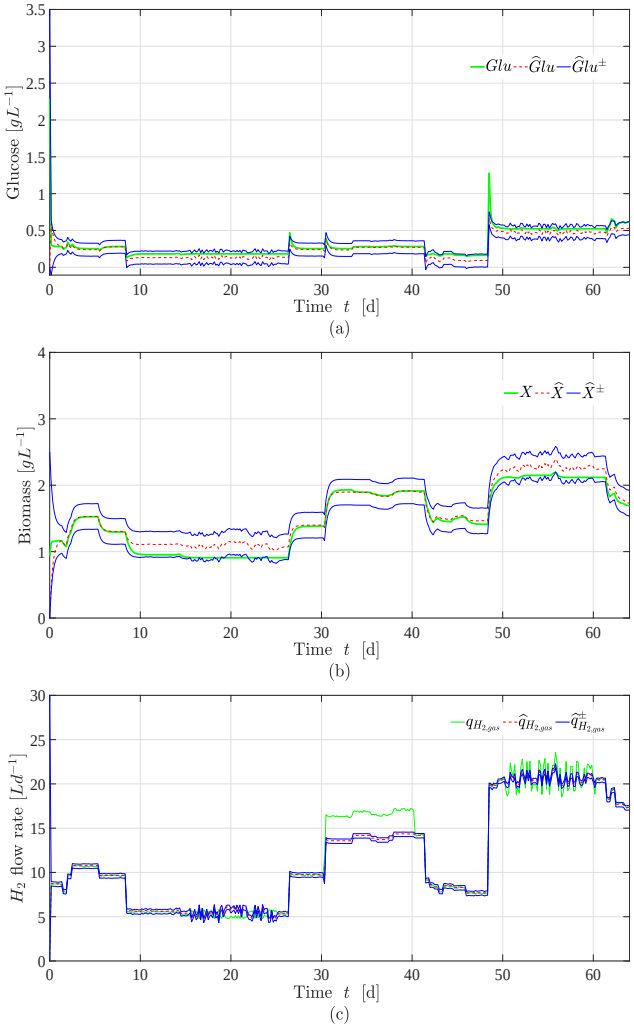

Fig. 1. Biohydrogen production dark fermenter estimations. In green line the bioreactor data, in dotted red line the estimation by the Luenberger observer, and their lower and upper estimations in blue lines. (a) Glucose. (b) Biomass. (c) Hydrogen flow rate.

3. CONCLUSIONS

In this paper, an interval observer to detect sensor faults in a hydrogen production bioreactor was presented. The simulation results validated the effectiveness of the proposed method. Besides, its performance guaranteed robustness against measurement noise and the exogenous disturbance.

REFERENCES

Meslem, N., Martinez, J., Ramdani, N., and Besançon, G. (2020). An interval observer for uncertain continuous-time linear systems. *International Journal of Robust and Nonlinear Control*, 30(5), 1886–1902.

Torres, I. and Avilés, J.D. (2021). Observer-based sensor fault detection in a dark fermenter for hydrogen production. *IEEE Control Systems Letters*, 5(5), 1621–1626. doi:10.1109/LCSYS.2020.3042391.

An adaptive model hierarchy for data-augmented training of kernel models for reactive flow ⋆

B. Haasdonk * **M. Ohlberger** ** **F. Schindler** **

* *Institute of Applied Analysis and Numerical Simulation, Pfaffenwaldring 57, D-70569 Stuttgart (e-mail:* `haasdonk@mathematik.uni-stuttgart.de`*).*
** *Mathematics Münster, Westfälische Wilhelms-Universität Münster, Einsteinstr. 62, D-48149 Münster (e-mail:* {`mario.ohlberger,felix.schindler`}`@uni-muenster.de`*)*

1. REFERENCE MODEL

We are interested in constructing efficient and accurate models to approximate time-dependent quantities of interest (QoI) $f \in L^2\big(\mathcal{P}; L^2([0,T])\big)$ in the context of reactive flow, with $T > 0$ and where $\mathcal{P} \subset \mathbb{R}^p$ for $p \geq 1$ denotes the set of possible input parameters. As a class of QoI functions, we consider those obtained by applying linear functionals $s_\mu \in V'$ to solution trajectories $c_\mu \in L^2(0,T;V)$ of, e.g., parametric parabolic partial differential equations. Thus, $f(\mu;t) := s_\mu(c_\mu(t))$, where for each parameter $\mu \in \mathcal{P}$, the concentration c_μ with $\partial_t c_\mu \in L^2(0,T;V')$ and initial condition $c_0 \in V$ is the unique weak solution of

$$\langle \partial_t c_\mu, v\rangle + a_\mu(c_\mu, v) = l_\mu(v) \quad \forall\, v \in V,\ c_\mu(0) = c_0. \quad (1)$$

Here, $V \subset H^1(\Omega) \subset L^2(\Omega) \subset V'$ denotes a Gelfand triple of Hilbert-spaces associated with a spatial Lipschitz-domain Ω and, for $\mu \in \mathcal{P}$, $l_\mu \in V'$ denotes a continuous linear functional and $a_\mu : V \times V \to \mathbb{R}$ a continuous coercive bilinear form.

As a basic model for reactive flow in catalytic filters, (1) could stem from a single-phase one-dimensional linear advection-diffusion-reaction problem with Dammköhler- and Péclet-numbers as input (thus $p = 2$), where c models the dimensionless molar concentration of a species and the break-through curve s measures the concentration at the outflow, as detailed in Gavrilenko et al. (2022).

Since direct evaluations of f are not available, we resort to a full order model (FOM) as reference model, yielding

$$f_h : \mathcal{P} \to \mathbb{R}^{N_T} \text{ for } N_T \geq 1, \quad f_h(\mu;t) := s_\mu(c_{h,\mu}(t)), \quad (2)$$

which we assume to be a sufficiently accurate approximation of the QoI. For simplicity, we consider a P^1-conforming Finite Element space $V_h \subset V$ and obtain the FOM solution trajectory $c_{h,\mu} \in L^2(0,T;V_h)$ by Galerkin projection of (1) onto V_h and an implicit Euler approximation of the temporal derivative.

⋆ Funded by BMBF under contracts 05M20PMA and 05M20VSA. Funded by the Deutsche Forschungsgemeinschaft (DFG, German Research Foundation) under contracts OH 98/11-1 and SCHI 1493/1-1, as well as under Germany's Excellence Strategy EXC 2044 390685587, Mathematics Münster: Dynamics – Geometry – Structure, and EXC 2075 390740016, Stuttgart Center for Simulation Science (SimTech).

2. SURROGATE MODELS

The evaluation of (2) may be arbitrarily costly, in particular in multi- or large-scale scenarios where $\dim V_h \gg 1$, but also if $N_T \gg 1$ due to long-time integration or when a high resolution of f_h is required. We thus seek to build a machine learning (ML) based surrogate model

$$f_{\mathrm{ml}} : \mathcal{P} \to \mathbb{R}^{N_T},\ f_{\mathrm{ml}}(\mu;t_n) \approx f_h(\mu;t_n)\ \forall 1 \leq n \leq N_T, \quad (3)$$

to predict all values $\{f_{\mathrm{ml}}(\mu;t_n)\}_{n=1}^{N_T}$ at once, without time-integration. Such models based on Neural Networks or Kernels typically rely on a large amount of training data

$$\big\{\big(\mu, f_h(\mu)\big) \,\big|\, \mu \in \mathcal{P}_{\mathrm{train}}\big\}, \quad \mathcal{P}_{\mathrm{train}} \subset \mathcal{P}, \quad |\mathcal{P}_{\mathrm{train}}| \gg 1, \quad (4)$$

rendering their training prohibitively expensive in the aforementioned scenarios; we refer to Gavrilenko et al. (2022) and the references therein and in particular to Santin and Haasdonk (2021). In Gavrilenko et al. (2022) we thus seek to employ an intermediate surrogate to generate sufficient training data.

2.1 Structure preserving Reduced Basis models

The idea of projection-based model order reduction by Reduced Basis (RB) methods is to approximate the state c_h in a low-dimensional subspace $V_{\mathrm{rb}} \subset V_h$ and to obtain online-efficient approximations of f_h by Galerkin projection of the FOM detailed in Section 1 onto V_{rb} and a precomputation of all quantities involving V_h in a possibly expensive offline-computation; we refer to Milk et al. (2016) and the references therein. Using such structure preserving reduced order models (ROM)s we obtain RB trajectories $c_{\mathrm{rb},\mu} \in L^2(0,T;V_{\mathrm{rb}})$ and a RB model

$$f_{\mathrm{rb}} : \mathcal{P} \to \mathbb{R}^{N_T}, \qquad f_{\mathrm{rb}}(\mu;t) := s_\mu(c_{\mathrm{rb},\mu}(t)), \quad (5)$$

with a computational complexity independent of $\dim V_h$, the solution of which, however, still requires time-integration.

The quality and efficiency of RB models hinges on the problem adapted RB space V_{rb} which could be constructed in an iterative manner steered by a posteriori error estimates using the POD-greedy algorithm from Haasdonk (2013). Instead, we obtain by the method of snapshots

$$V_{\mathrm{rb}} := \langle \texttt{POD}(\{c_{h,\mu} \,|\, \mu \in \mathcal{P}_{\mathrm{rb}}\rangle\,, \qquad \text{with } \mathcal{P}_{\mathrm{rb}} \subset \mathcal{P} \quad (6)$$

consisting of only few a priori selected parameters (e.g. the outermost four points in $\mathcal{P}$), where we use the hierarchic approximate POD from Himpe et al. (2018) for $N_T \gg 1$ to avoid computing the SVD of a dense snapshot Gramian of size N_T^2.

2.2 Kernel models

While still requiring time-integration, we can afford to use RB ROMs to generate a sufficient amount of training data $X_{\text{train}} = \{(\mu, f_{\text{rb}}(\mu)) \,|\, \mu \in \mathcal{P}_{\text{ml}}\} \cup \{(\mu, f_h(\mu) \,|\, \mu \in \mathcal{P}_{\text{rb}})\}$, augmented by the FOM-data available as a side-effect from generating V_{rb}. Using this data, we obtain the ML model f_{ml} from (3) using the vectorial greedy orthogonal kernel algorithm from Santin and Haasdonk (2021).

While resulting in substantial computational gains, the presented approach from Gavrilenko et al. (2022) still relies on the traditional offline/online splitting of the computational process to train the RB ROM as well as the ML model to be valid for all of $\mathcal{P}$, requiring a priori choices regarding $\mathcal{P}_{\text{rb}}$ and $\mathcal{P}_{\text{ml}}$ with a significant impact on the overall performance and applicability of these models.

3. AN ADAPTIVE MODEL HIERARCHY

Keil et al. (2021) introduced an approach beyond the classical offline/online splitting where a RB ROM is adaptively enriched based on rigorous a posteriori error estimates, following the path of an optimization procedure through the parameter space. Similarly, we propose an adaptive enrichment yielding a hierarchy of FOM, RB ROM and ML models, based on the standard residual-based a posteriori estimate on the RB output error, $\|f_h(\mu) - f_{\text{rb}}(\mu)\|_{L^2([0,T]))} \leq \Delta_{\text{rb}}(\mu)$, for which we refer to the references in Milk et al. (2016).

Algorithm 1 Adaptive QoI model generation

Require: ROM tolerance $\varepsilon > 0$, ML trust/train criteria
$X_{\text{train}} = \emptyset$, $\Phi_{\text{RB}} = \{\}$, $V_{\text{rb}} := \langle \Phi_{\text{rb}} \rangle$, $f_{\text{ml}} := 0$
for all $\mu \in \mathcal{P}$ selected by outer loop **do**
  if ML model is trustworthy **then return** $f_{\text{ml}}(\mu)$
  else
    compute $f_{\text{rb}}(\mu)$, $\Delta_{\text{rb}}(\mu)$
    if $\Delta_{\text{rb}}(\mu) \leq \varepsilon$ **then**
      collect $X_{\text{train}} = X_{\text{train}} \cup \{(\mu, f_{\text{rb}}(\mu))\}$
      (optionally) fit ML model, **return** $f_{\text{rb}}(\mu)$
    else $\Pi_{\Phi_{\text{rb}}}$: orth. proj. onto $\langle \Phi_{\text{rb}} \rangle$
      compute $f_h(\mu)$
      enrich $\Phi_{\text{rb}} = \Phi_{\text{rb}} \cup \texttt{POD}(c_h(\mu) - \Pi_{\Phi_{\text{rb}}}[c_h(\mu)])$
      update RB ROM
      collect $X_{\text{train}} = X_{\text{train}} \cup \{(\mu, f_h(\mu))\}$
      (optionally) fit ML model, **return** $f_h(\mu)$

As a means to judge if a ML model is trustworthy, we propose a manual validation using the following a posteriori error estimate on the ML QoI error. While not as cheaply computable as f_{ml}, it still allows to validate the ML model without computing f_h.

Proposition 1. (ML model a posteriori error estimate). Let $f_{\text{rb}}(\mu)$, $f_{\text{ml}}(\mu) \in \mathbb{R}^{N_T}$ denote the RB ROM and ML model approximations of $f_h(\mu)$, respectively, and let $\Delta_{\text{rb}}(\mu)$ denote an upper bound on the RB-output error. We then have by triangle inequality for all $\mu \in \mathcal{P}$

$$\|f_h(\mu) - f_{\text{ml}}(\mu)\|_{L^2([0,T])} \leq \Delta_{\text{rb}}(\mu) + \|f_{\text{rb}}(\mu) - f_{\text{ml}}(\mu)\|_{L^2([0,T])}, \tag{7}$$

where the right hand side is computable with a computational complexity independent of $\dim V_h$.

Applying Algorithm 1 to the example of one-dimensional single-phase reactive flow from the last row of Table 1 in Gavrilenko et al. (2022), with $\dim \mathcal{P} = 2$, $N_T = 24576$ time steps, $\dim V_h = 65537$ gives the behaviour shown in Figure 1, where we set $\varepsilon = 10^{-2}$, retrain the ML model every 10 collected samples and unconditionally trust the ML model as soon as $|X_{\text{train}}| \geq 50$.[1] For the considered diffusion dominated regime, we only require a single evaluation of f_h (yielding a $\dim V_{\text{rb}} = 15$-dimensional RB ROM), which results in even further computational savings, compared to the results obtained in Gavrilenko et al. (2022).

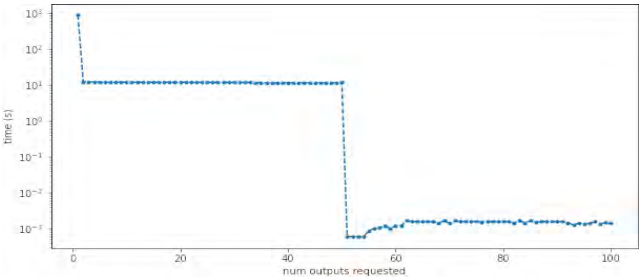

Fig. 1. Each dot correspond to the input-to-output query time of the adaptive model from Algorithm 1 applied to Gavrilenko et al. (2022).

REFERENCES

Gavrilenko, P., Haasdonk, B., Iliev, O., Ohlberger, M., Schindler, F., Toktaliev, P., Wenzel, T., and Youssef, M. (2022). A full order, reduced order and machine learning model pipeline for efficient prediction of reactive flows. In *Large-Scale Scientific Computing*, 378–386. Springer International Publishing.

Haasdonk, B. (2013). Convergence rates of the POD-greedy method. *ESAIM Math. Model. Numer. Anal.*, 47(3), 859–873.

Himpe, C., Leibner, T., and Rave, S. (2018). Hierarchical Approximate Proper Orthogonal Decomposition. *SIAM Journal on Scientific Computing*, 40(5), A3267–A3292.

Keil, T., Mechelli, L., Ohlberger, M., Schindler, F., and Volkwein, S. (2021). A non-conforming dual approach for adaptive trust-region reduced basis approximation of PDE-constrained parameter optimization. *ESAIM Math. Model. Numer. Anal.*, 55(3), 1239–1269.

Milk, R., Rave, S., and Schindler, F. (2016). pyMOR – generic algorithms and interfaces for model order reduction. *SIAM J. Sci. Comput.*, 38(5), S194–S216.

Santin, G. and Haasdonk, B. (2021). Kernel methods for surrogate modeling. In P. Benner, S. Grivet-Talocia, A. Quarteroni, G. Rozza, W. Schilders, and L.M. Silveira (eds.), *Model Order Reduction*, volume 2, 311–353. De Gruyter.

[1] The experiments were performed using `pyMOR` from Milk et al. (2016) and `dune-gdt` from `https://docs.dune-gdt.org/`.

Periodic Regimes of Motion of Capsule System along Straight Line with Dry Friction ⋆

Tatiana Figurina Dmitri Knyazkov

Ishlinsky Institute for Problems in Mechanics RAS,
Prospekt Vernadskogo 101-1, Moscow, 119526 Russia
(e-mail: t_figurina@mail.ru, Dmitri.Knyazkov@gmail.com)

1. INTRODUCTION

The capsule system driven by a periodically moving internal mass was considered in a number of papers, see Chernousko (2008); Yan et al. (2017). Different control and optimization problems were solved for such systems. The solution of such problems is always searched among the motions with periodic velocity of the capsule, because such motions provide prolonged positive averaged displacement of the system. But the uniqueness and stability of such periodic regimes of motion is not sufficiently studied. For the case when the medium resistance is a monotonous continuous function of the velocity of the capsule and the velocity of the internal mass relative to the capsule is continuous, it was proved, that the periodic regime of motion exists, is unique, and the velocity of all other motions converge to the periodic one exponentially, see Knyaz'kov and Figurina (2020). The same results were obtained in Figurina and Knyazkov (2022) for a system of several interacting bodies and capsules.

In the current paper, a capsule system with an internal mass moves on a plane with dry friction, and the relative velocity of the mass has discontinuities (jumps). These jumps may occur due to collisions in the system. It is proved, that the periodic regime of motion exists and the velocity of any motion converges to the periodic velocity exponentially or in finite time. In contrary to the results obtained in Knyaz'kov and Figurina (2020); Figurina and Knyazkov (2022) for similar locomotion systems, in the current paper, the periodic by velocity motion may be non-unique. This non-uniqueness appears due to jumps in velocity of the capsule for the case of dry friction between the capsule and the plane.

2. PROBLEM STATEMENT

The capsule of mass M contains an internal body of mass m. The position $l(t)$ of the internal mass relative to the capsule changes periodically as a result of some forces, that are internal for the system:

$$l(t+T) = l(t).$$

The capsule moves with the velocity $v(t)$ along a straight line on a rough plane (see Fig. 1). Dry friction force R acts on the capsule. The equation of motion can be written as

$$\dot{v} = u + r(v,u), \tag{1}$$

⋆ This study was supported by Russian Science Foundation, Project No. 18-11-00307, https://rscf.ru/en/project/18-11-00307/

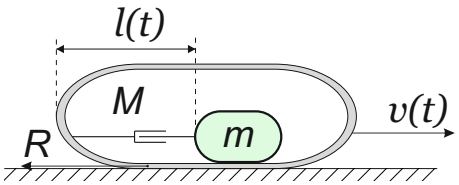

Fig. 1. Scheme of the motion

where r is the normalized dry friction force, $r = \frac{R}{M+m}$, u is the normalized relative acceleration of the internal mass, $u = -\frac{m}{M+m}\ddot{l}$. According to Coulomb's law of dry friction,

$$r(v,u) = \begin{cases} -\mu\,\mathrm{sign}v, & v \neq 0, \\ -u, & v = 0,\ |u| \leq \mu, \\ -\mu\,\mathrm{sign}u, & v = 0,\ |u| > \mu, \end{cases} \tag{2}$$

where $\mu = kg$, k is the coefficient of dry friction, g is the gravitational acceleration. We assume, that for $t \in [0,T]$

$$u(t) = u_0(t) + \sum_{i=1}^{N} d_i \delta(t - t_i),$$

where δ is Dirac delta function, $u_0(t)$ is a periodic piecewise-continuous function. As far as the relative motion of the internal mass is periodic, we have

$$u(t+T) = u(t), \qquad t \geq 0, \tag{3}$$

$$\int_0^T u(t)dt = 0. \tag{4}$$

The details of the statement of the problem can be found in Knyaz'kov and Figurina (2020). We are interested in the existence, uniqueness, and stability of the periodic solution $v_*(t)$ of the problem (1)-(4), such that

$$v_*(t+T) = v_*(t).$$

3. MAIN RESULTS

The following results regarding the periodic solution $v_*(t)$ and the behavior of velocities $v(t)$ of motions with any initial velocity are obtained.

Lemma 1. The distance between any two solutions $v(t)$, $\tilde{v}(t)$ of the equation (1) does not increase:

$$\frac{d}{dt}|v(t) - \tilde{v}(t)| \leq 0.$$

It follows from (1) and (2). From Lemma 1, the following corollary can be easily obtained.

Corollary 1. If there exist two periodic solutions v_*, $\tilde{v}_*$ of the equation (1), they differ by a constant:

$$v_*(t) = \tilde{v}_*(t) + C.$$

Theorem 1. The periodic solution $v_*(t)$ of the problem (1)-(4) exists. If the periodic solution is non-unique, then the set of periodic solutions consists of all the solutions with initial values from an interval $[v_*^{min}(0), v_*^{max}(0)]$.

Proof. The idea of the proof is the following. For the initial values $v^+(0) = \max |u_0(t)|T + \sum_{i=1}^{N} |d_i|$, $v^-(0) = -v^+(0)$, we have $v^+(0) \geq v^+(T)$, $v^-(0) \leq v^-(T)$. Due to continuity, there exists such $v_*(0) \in [v^-(0), v^+(0)]$ that the corresponding solution $v_*(t)$ is periodic.

Let v_*^{min}, v_*^{max} are periodic solutions with minimum (maximum) possible initial values, $v(0) \in (v_*^{min}(0), v_*^{max}(0))$. Due to Lemma 1, the distances $|v_*^{min} - v|$, $|v_*^{max} - v|$ between the solutions do not increase. From Corollary 1, $v_*^{max} = v_*^{min} + C$. Thus, $v = v_*^{min} + \widetilde{C}$, and v is periodic.

The behavior of non-periodic solutions is described by the following theorem.

Theorem 2. Any solution $v(t)$ of the problem (1)-(4) such that $v(0) > v_*^{max}(0)$ converges to the periodic solution $v_*^{max}(t)$. Any solution $v(t)$ of the problem such that $v(0) < v_*^{min}(0)$ converges to the periodic solution $v_*^{min}(t)$.

Proof. Due to Lemma 1, any solution v with $v(0) > v_*^{max}(0)$ tends to $v_*^{max} + C$. It can be shown that $v_*^{max} + C$ is also the solution of (1)-(4). By definition, v_*^{max} is the periodic solution with the maximum possible initial value $v_*^{max}(0)$, hence, $C = 0$ and v converges to v_*^{max}. The second part of the theorem is proved in a similar way.

The following theorem gives a criteria for the type of this convergence.

Theorem 3. (A) Solution $v(t)$ such that $v(0) > v_*^{max}(0)$ converges to the periodic solution $v_*^{max}(t)$ in a finite time if and only if there exists a time instant τ such that $v_*^{max}(\tau) = 0$, and either $v_*^{max}(t) < 0$, $|u(t)| \leq \mu$ or $v_*^{max}(t) \equiv 0$, $-\mu \leq u(t) < \mu$ take place in some left vicinity of the point τ.

(B) Solution $v(t)$ such that $v(0) < v_*^{min}(0)$ converges to the periodic solution $v_*^{min}(t)$ in a finite time if and only if there exists a time instant τ such that $v_*^{min}(\tau) = 0$, and either $v_*^{min}(0) > 0$, $|u(t)| \leq \mu$ or $v_*^{min}(t) \equiv 0$, $-\mu < u(t) \leq \mu$ take place in some left vicinity of the point τ.

(C) If a non-periodic solution $v(t)$ does not converges to the periodic solution $v_*^{max}(t)$ (or $v_*^{min}(t)$) in a finite time, it converges to $v_*^{max}(t)$ (or $v_*^{min}(t)$) exponentially.

Proof. Let v be a non-periodic solution such that $v(0) > v_*^{max}(0)$. If $v_*^{max}(t) \equiv 0$, $-\mu \leq u(t) < \mu$ for $t \in [\tau - a, \tau]$, then a distance between $v(t)$ and $v_*^{max}(t)$ decreases by a constant value over every time period. If $v_*^{max}(t) < 0$, $|u(t)| \leq \mu$ for $t \in [\tau - a, \tau)$, then there exists such time moment $t_0 \in [\tau - a + nT, \tau + nT]$ that $v(t_0) = 0$, $v(t) = 0$, $t \in (t_0, \tau + nT]$, and $v(t) = v_*^{max}(t)$ for all $t \geq \tau + nT$. Thus, part (A) is proved. (B) is proved in a similar way.

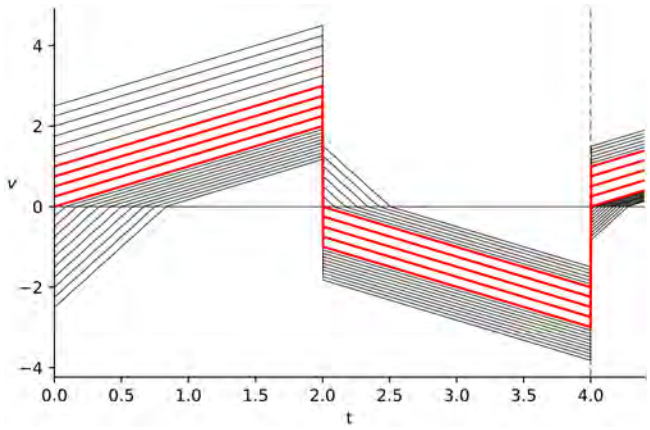

Fig. 2. Example of non-uniqueness of the periodic regime

If a non-periodic v does not converge to v_* in a finite time, there is infinite number of intervals where v and v_* have different signs. From (1), (2), the distance between v and v_* decreases with the rate 2μ on these intervals. It can be proved that the total length of these intervals is sufficiently large, thus, the exponential convergence takes place.

Consider the example, that illustrates the behavior of the velocities $v(t)$ for different initial velocities $v(0)$.

Example. Let's take take $\mu = 1$, $T = 4$, $u(t) = u_0(t) - 3\delta(t - T/2) + 3\delta(t - T)$, where $u_0(t) = 2$ for $t \in [0, T/2)$ and $u_0(t) = -2$ for $t \in [T/2, T)$. The corresponding velocities for different initial values are shown in Fig. 2. The velocities of periodic and non-periodic regimes are shown by red and black colors correspondingly. Here we have $v_*^{min}(0) = 0$, $v_*^{max}(0) = 1$.

If the initial velocity of the capsule $v(0)$ is greater than $v_*^{max}(0)$, then $v(t)$ converges to the motion with $v_*^{max}(t)$, and average velocity of the capsule is directed to the right. If the initial velocity of the capsule $v(0)$ is less than $v_*^{min}(0)$, then $v(t)$ converges to the motion with $v_*^{min}(t)$, and average velocity of the capsule is directed to the left. And there exists some initial velocity $v(0) \in [v_*^{min}(0), v_*^{max}(0)]$, that the capsule returns to its initial state at the end of each time period. This can be used to control vibro-driven capsule robots, because it gives us the ability to influence the direction of movement of the capsule only by specifying its initial velocity. Note, that all periodic solutions $v_*(t)$ with initial velocities $v_*(0) \in [v_*^{min}(0), v_*^{max}(0)]$ are not asymptotically stable.

REFERENCES

Chernousko, F.L. (2008). On the optimal motion of a body with an internal mass in a resistive medium. *J. Vib. Control*, 14(1-2), 197–208.

Figurina, T. and Knyazkov, D. (2022). Periodic gaits of a locomotion system of interacting bodies. *Meccanica*. doi:10.1007/s11012-022-01473-0.

Knyaz'kov, D.Y. and Figurina, T.Y. (2020). On the existence, uniqueness, and stability of periodic modes of motion of a locomotion system with a mobile internal mass. *J. Comput. Syst. Sci. Int.*, 59, 129–137.

Yan, Y., Liu, Y., and Liao, M. (2017). A comparative study of the vibro-impact capsule systems with one-sided and two-sided constraints. *Nonlinear Dyn.*, 89, 1063–1087.

An Alternative Algorithm for Unstable Balanced Truncation ⋆

Peter Benner *

* *Max Planck Institute for Dynamics of Complex Technical Systems, Sandtorstr. 1, 39106 Magdeburg, Germany (e-mail: benner@mpi-magdeburg.mpg.de).*

Abstract: Model reduction of stable linear-time invariant systems by balanced truncation is well-established in systems and control engineering. For unstable systems, several alternatives have been suggested, with linear-quadratic Gaussian balanced truncation arguably the most prominent one. Here, we discuss an alternative method that can be computed in a potentially more efficient way.

Keywords: Model Reduction, Balanced Truncation, Algebraic Riccati Equations, Numerical Methods, Sign Function Method.

1. INTRODUCTION

Balancing-related model order reduction (MOR) is one of the main techniques for reducing the complexity of linear dynamical systems

$$\dot{x}(t) = Ax(t) + Bu(t), \qquad y(t) = Cx(t), \tag{1}$$

and is particularly popular in systems and control engineering due to its beneficial properties for control system design (e.g. Antoulas (2005); Benner (2009); Baur et al. (2014); Benner et al. (2021)). The basic principle is to use two symmetric positive semidefinite matrices P, Q and a contragredient transformation to find a coordinate system in which they are equal and diagonal. Then one projects the dynamics of (1) onto the dominant subspace of $P = Q$ in this coordinate system. This is always possible if the system is controllable and observable, and can still be used on the controllable and observable subspaces for MOR purposes.

The most common choice (Moore (1981)) for P, Q is to use the system (reachability and obervability) Gramians which solve the two "dual" Lyapunov equations

$$AP + PA^T + BB^T = 0, \tag{2a}$$
$$A^TQ + QA + C^TC = 0. \tag{2b}$$

Note that for the usual SR or BFSR procedures to compute a reduced-order model from A, B, C and P, Q, one needs (approximations of) full-rank or Cholesky factors of P, Q, i.e. one works with S, R satisfying

$$P = SS^T, \qquad Q = R^TR$$

approximately. A prerequisite for this to be a successful is that A is stable, i.e., has all its eigenvalues in the open left half of the complex plane. The resulting method is commonly called *Balanced Truncation (BT)*.

⋆ Partially supported by the DFG Research Training Group 2297 "Mathematical Complexity Reduction (MathCoRe)" in Magdeburg.

2. BT FOR UNSTABLE SYSTEMS

One possibility to apply balancing-based MOR for unstable systems is to use *LQG balanced truncation (LQGBT)* (Jonckheere and Silverman (1983)). Here, $(P, Q) = (X_s, Y_s)$ is chosen, where X_s and Y_s are the unique stabilizing solutions of the algebraic Riccati equations (AREs) corresponding to the linear-quadratic regulator (LQR) and Kalman-Bucy filter problems related to (1):

$$A^TX + XA - XBB^TX + C^TC = 0, \tag{3a}$$
$$AY + YA^T - YC^TCY + BB^T = 0. \tag{3b}$$

An alternative to LQGBT is *closed-loop balancing* (Wortelboer (1994)). The idea is to first stabilize the system and then to use the Gramians of the closed-loop system in the balance-and-truncate procedure. Suppose one chooses for the stabilization X_s, the stabilizing solution of the LQR ARE (3a). This requires to first compute the unique stabilizing solution X_s of the LQR Riccati equation and then to apply the feedback law

$$u_s(t) = -B^TX_sx(t) + u(t)$$

to (1), resulting in the *closed-loop system*

$$\dot{x}_s(t) = (A - BB^TX_s)x_s(t) + Bu(t),\ y_s(t) = Cx_s(t). \tag{4}$$

Then, *closed-loop balanced truncation (CLBT)* uses the solutions P_s, Q_s of the Lyapunov equations

$$(A - BB^TX_s)P_s + P_s(A - BB^TX_s)^T + BB^T = 0, \tag{5a}$$
$$(A - BB^TX_s)^TQ_s + Q_s(A - BB^TX_s) + C^TC = 0. \tag{5b}$$

As it turns out, P_s can simply be computed by applying the sign function to the Hamiltonian matrix

$$\begin{bmatrix} A & -BB^T \\ -C^TC & -A^T \end{bmatrix} \tag{6}$$

associated to the LTI system (1), without ever computing X_s. In particular, P_s can be read off from $\operatorname{sign}(H)$ without further computation! This follows from the following corollary of the proof of (Kenney et al., 1989, Theorem 1).

Corollary 1. Let (A, B) be stabilizable, and (A, C) be detectable. Then the unique stabilizing solution X_s to the

ARE (3a) exists and is symmetric positive semidefinite. Hence, $A - BB^T X_s$ is stable, (5a) as well as (5b) have unique solutions $P_s = P_s^T \geq 0$, $Q_s = Q_s^T \geq 0$, resp., and it holds

$$\operatorname{sign}(H) = \begin{bmatrix} -I + 2P_s X_s & -2P_s \\ 2X_s P_s X_s - 2X_s & I - 2X_s P_s \end{bmatrix}. \qquad (7)$$

How to get Q_s solving (5b) is not so straightforward, though. It should be computed using any Lyapunov solver where one would then also need X_s to set up the coefficient matrix $A - BB^T X_s$.

It is interesting to note that the observability Gramian of yet another stabilized system can also be read off from $\operatorname{sign}(H)$. Here, one uses as "closed-loop matrix" $A - Y_s C^T C$, which is stable under the same assumptions as used in Corollary 1. The observability Gramian $\tilde{Q}_s$ of this stable LTI system solves the Lyapunov equation

$$(A - Y_s C^T C)^T \tilde{Q} + \tilde{Q}(A - Y_s C^T C) + C^T C = 0. \qquad (8)$$

Now, $\tilde{Q}_s$ can be obtained from the $(1,2)$-block of the sign function applied to the Hamiltonian matrix corresponding to (3b) which is nothing but H^T with H as in (6). As $\operatorname{sign}(H^T) = (\operatorname{sign}(H))^T$, we can read-off $\tilde{Q}_s$ from the $(2,1)$-block of $\operatorname{sign}(H)$. BT could now also be based on $(P, Q) = (P_s, \tilde{Q}_s)$, which to the best of our knowledge has not been described in the literature. As we will see from the numerical example below, this new balancing-based MOR method for unstable systems yields very good results, comparable to LQGBT.

2.1 Numerical Example

We use the eady data from the SLICOT benchmark collection [1]. Here, $n = 598$, $m = p = 1$. We computed reduced-order models (ROMs) of order $r = 17$ using BT and LQGBT as implemented in MORLAB (Benner and Werner (2020)). We also computed a ROM based on $(P_s, \tilde{Q}_s)$ as suggested above, where we used `signm` from MORLAB to compute $\operatorname{sign}(H)$ and read off the $(1,2)$- and $(2,1)$-blocks to get P_s and $\tilde{Q}_s$. We then obtained approximate full-rank factors of both matrices using truncated SVDs, and passed them to `srrom` from MORLAB to compute the reduced-order model, using the rank parameter set to $r = 17$. For now, we call this method "CLBT2". Fig. 1 shows the Bode magnitude plot for the full-order model and the three computed ROMs, where the graphs are indistinguishable in the "eyeball norm". The Bode magnitude plot of the errors for the three ROMs is displayed in Fig. 2. Here, the interesting fact arises that the error plots of LQGBT and CLBT2 coincide, and differ from that of BT. This supports the conjecture that CLBT2 and LQGBT actually compute the same ROM, i.e., that they are equivalent.

3. OUTLOOK

The discussion of the conjecture that the new "CLBT2" method is really just another (and potentially) more efficient implementation of LQBT will be part of the talk delivered at MATHMOD 2022. The proof of this conjecture will be reported elsewhere, as it requires more space than available here.

[1] `https://morwiki.mpi-magdeburg.mpg.de/morwiki/index.php/Earth_Atmosphere`

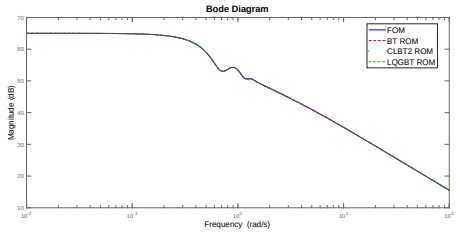

Fig. 1. Frequency responses for the full- and reduced-order models using the "eady data".

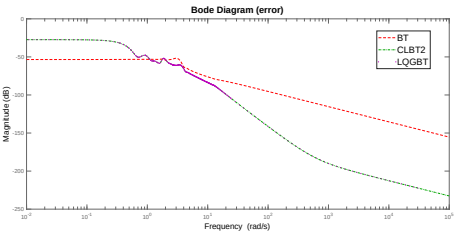

Fig. 2. Frequency responses for the errors of the reduced-order models using the "eady data".

ACKNOWLEDGEMENTS

The author would like to thank Federico Poloni (University of Pisa) for inviting him to a research stay in Pisa, where the work reported here was triggered as a side effect of the actual project we worked on.

REFERENCES

Antoulas, A.C. (2005). *Approximation of Large-Scale Dynamical Systems*, volume 6 of *Adv. Des. Control*. SIAM Publications, Philadelphia, PA.

Baur, U., Benner, P., and Feng, L. (2014). Model order reduction for linear and nonlinear systems: A system-theoretic perspective. *Arch. Comput. Methods Eng.*, 21(4), 331–358.

Benner, P. (2009). System-theoretic methods for model reduction of large-scale systems: Simulation, control, and inverse problems. In *ARGESIM Report (MATHMOD 2009 Proceedings)*, volume 35, 126–145.

Benner, P., Grivet-Talocia, S., Quarteroni, A., Rozza, G., Schilders, W.H.A., and Silveira, L.M. (eds.) (2021). *Model Order Reduction. Volume 1: System- and Data-Driven Methods and Algorithms*. De Gruyter, Berlin.

Benner, P. and Werner, S.W.R. (2020). MORLAB – A model order reduction framework in MATLAB and Octave. In A.M. Bigatti, J. Carette, J.H. Davenport, M. Joswig, and T. de Wolff (eds.), *Mathematical Software – ICMS 2020*, volume 12097 of *Lecture Notes in Comput. Sci.*, 432–441. Springer International Publishing, Cham.

Jonckheere, E.A. and Silverman, L.M. (1983). A new set of invariants for linear systems—application to reduced order compensator. *IEEE Trans. Autom. Control*, 28, 953–964.

Kenney, C., Laub, A.J., and Jonckheere, E.A. (1989). Positive and negative solutions of dual Riccati equations by matrix sign function iteration. *Systems Control Lett.*, 13, 109–116.

Moore, B.C. (1981). Principal component analysis in linear systems: controllability, observability, and model reduction. *IEEE Trans. Autom. Control*, AC–26(1), 17–32.

Wortelboer, P.M.R. (1994). *Frequency-weighted Balanced Reduction of Closed-loop Mechanical Servo-systems: Theory and Tools*. Ph.D. Thesis, Delft University of Technology, Delft, NL.

A Two-Dimensional Port-Hamiltonian Model for Coupled Heat Transfer

J. Jäschke * **M. Ehrhardt** * **M. Günther** *

* *University of Wuppertal, Chair of Applied Mathematics and Numerical Analysis, 42119 Wuppertal, Germany (e-mail: {jaeschke, ehrhardt, guenther}@uni-wuppertal.de)*

Abstract: The problem of conjugate heat transfer in gas turbine blades and their cooling ducts is investigated by constructing a highly simplified mathematical model that focuses on the relevant coupling structures and aims to reduce the unrelated complexity as much as possible. Then, the Port-Hamiltonian formalism is applied to the model and its subsystems, and the interconnections are investigated. Finally, a simple spatial discretization is applied to the system to investigate the properties of the resulting finite-dimensional Port-Hamiltonian system and to determine whether the order of coupling and discretization has an effect on the resulting semi-discrete system.

Keywords: Port-Hamiltonian System, Conjugate Heat Transfer, Coupled System, Thermodynamics, heat equation, cooling channel

1. INTRODUCTION

In this discussion contribution we propose a simplified mathematical model of the coupled system of a heated blade and a cooling channel as it appears in modern gas turbines. First we develop a port-Hamiltonian system (PHS) formulation for each of the subsystems and investigate the coupling structure of their interconnection in order to determine whether the coupling of the two subsystems forms a PHS for the overall system. Next we propose some spatial discretization of the PHS and study whether the resulting semi-discrete systems form finite-dimensional PHS and whether there is a difference between the coupling of the discretized systems and the discretization of the coupled system. For details we refer to Jäschke et al. (2021).

2. THE MODEL SYSTEM

First, let us introduce the mathematical model of the coupled system under investigation. $\Omega_m = (0,1)\times(0,1) \subset \mathbb{R}^2$ denotes the spatial domain of the blade metal. The heat equation on Ω_m is given by

$$\frac{\partial T}{\partial t}(x,y,t) = \frac{1}{c_m \rho_m} \operatorname{div}\left(\lambda \operatorname{grad} T(x,y,t)\right), \ (x,y) \in \Omega_m. \tag{1}$$

In Figure 1 we give a rough sketch of the model setting.

The left, upper and lower boundary ($x = 0$, $y = 0$ and $y = 1$), denoted by $\partial\Omega_{ext}$, are in contact with a thermal reservoir with a given temperature T_{ext}, leading to:

$$-\lambda \frac{\partial T}{\partial x}(x,y,t) = h_0\big(T_{\text{ext}}(t) - T(x,y,t)\big), \ x = 0, y \in [0,1] \tag{2}$$

$$-\lambda \frac{\partial T}{\partial y}(x,y,t) = h_0\big(T_{\text{ext}}(t) - T(x,y,t)\big), \ x \in (0,1), \ y = 0 \tag{3}$$

$$\lambda \frac{\partial T}{\partial y}(x,y,t) = h_0\big(T_{\text{ext}}(t) - T(x,y,t)\big), \ x \in (0,1), y = 1 \tag{4}$$

The right boundary $\partial\Omega_c$ ($x = 1$) is in contact with the cooling channel, so that $\partial\Omega_m = \partial\Omega_{\text{ext}} \cup \partial\Omega_c$ and

$$-\lambda \frac{\partial T}{\partial x}(1,y,t) = h_1\big(T(1,y,t) - \Theta(y,t)\big), \ (1,y) \in \partial\Omega, \tag{5}$$

with the temperature of the cooling channel Θ that is governed by a transport equation with an additional source term describing the heat flux into the cooling channel:

$$\frac{\partial \Theta}{\partial t}(y,t) = -v \frac{\partial \Theta}{\partial y}(y,t) + \frac{h_1}{c_c \rho_c}\big(T(1,y,t) - \Theta(y,t)\big), \tag{6}$$

$$\Theta(0,t) = \Theta_{\text{in}}(t). \tag{7}$$

3. PORT-HAMILTONIAN FORMULATION

We formulate the PHS for each subsystem using quadratic Hamiltonians. For the heat equation in the metal rod we

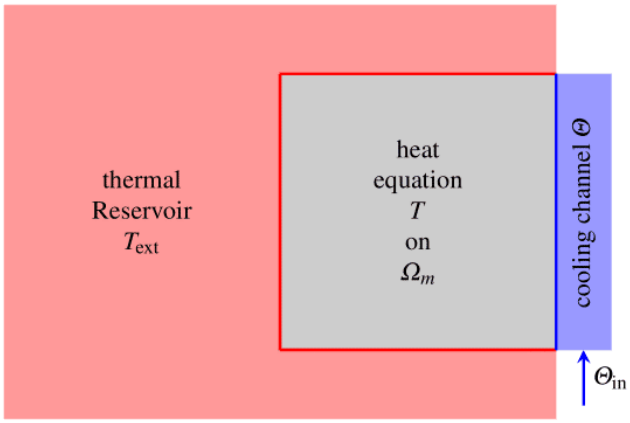

Fig. 1. Schematic of the 2D model system with $\partial\Omega_{\text{ext}}$ marked as a red line and $\partial\Omega_c$ as a blue line.

choose the Hamiltonian, cf. Serhani et al. (2019)

$$H(t) = \frac{1}{2}\int_{\Omega_m} \rho(\boldsymbol{x}) c_m(\boldsymbol{x})\, T(t,\boldsymbol{x})^2 \,\mathrm{d}\boldsymbol{x}, \tag{8}$$

with temperature $T(t,\boldsymbol{x})$ and c_m is the *isochoric specific heat capacity* that does not depend on the temperature.

We now choose the usual flow and effort variables

$$e_T = \delta_T H = T, \qquad f_T = \partial_t T, \tag{9}$$

with δ_T denoting the variational derivative w.r.t. T and the measure $\rho c_m \,\mathrm{d}x$.

Next, the first law of thermodynamics yields

$$\rho(\boldsymbol{x}) c_m(\boldsymbol{x})\, \partial_t T(t,\boldsymbol{x}) = -\operatorname{div} \boldsymbol{\Phi}_Q(t,\boldsymbol{x}), \tag{10}$$

with the heat flux Φ_Q. The (isotropic) Fourier's law gives

$$\boldsymbol{\Phi}_Q(t,\boldsymbol{x}) = -\lambda \operatorname{grad} T(t,\boldsymbol{x}). \tag{11}$$

Therefore we introduce the additional flow and effort variables similar to Serhani et al. (2019)

$$\boldsymbol{e}_Q = \boldsymbol{\Phi}_Q, \quad \boldsymbol{f}_Q = -\operatorname{grad} T, \tag{12}$$

to obtain the system of equations

$$\begin{pmatrix} \rho c_m f_T \\ \boldsymbol{f}_Q \end{pmatrix} = \begin{pmatrix} 0 & -\operatorname{div} \\ -\operatorname{grad} & 0 \end{pmatrix} \begin{pmatrix} e_T \\ \boldsymbol{e}_Q \end{pmatrix}, \tag{13}$$

$$\boldsymbol{e}_Q = \lambda \boldsymbol{f}_Q. \tag{14}$$

The time derivative of the Hamiltonian reads

$$d_t H = -\int_{\Omega_m} \boldsymbol{e}_Q \boldsymbol{f}_Q \,\mathrm{d}x - \int_{\partial\Omega_m} e_T(\boldsymbol{e}_Q \boldsymbol{n}) \,\mathrm{d}\gamma, \tag{15}$$

i.e. the same boundary port variables as Serhani et al. (2019). To replicate the boundary conditions, we set

$$\boldsymbol{e}_Q \boldsymbol{n} = \boldsymbol{\Phi}_Q \boldsymbol{n} = h_0 \left(T - T_{\text{ext}}\right) \text{on } \partial\Omega_{ext} \tag{16}$$

so equation (15) becomes

$$\begin{aligned} d_t H = &-\int_{\Omega_m} \boldsymbol{e}_Q \boldsymbol{f}_Q \,\mathrm{d}x \\ &- \int_{\partial\Omega_{ext}} h_0 e_T^2 \,\mathrm{d}\gamma + \int_{\partial\Omega_{ext}} h_0 e_T T_{\text{ext}} \,\mathrm{d}\gamma \end{aligned} \tag{17}$$

turning the boundary port of (15) into two new boundary ports and additional dissipative terms on the boundary.

For the treatment of the cooling channel we refer to Jäschke et al. (2021), providing us with a PHS that has an input $T(1,y,t)$ and an output $h_1\big(T(1,y,t) - \Theta(y,t)\big)$.

To obtain a PH formulation of the model system by coupling the PHS we need the following equality:

$$-\lambda \frac{\partial T}{\partial x}(1,y,t) = h_1\big(T(1,y,t) - \Theta(y,t)\big). \tag{18}$$

With the inputs and outputs of the two systems we find

$$e_1 = T(1,y,t), \quad f_1 = -\boldsymbol{\Phi}_Q \boldsymbol{n} = \lambda \frac{\partial T}{\partial x}(1,y,t), \tag{19}$$

$$e_2 = h_1\big(T(1,y,t) - \Theta(y,t)\big), \quad f_2 = T(1,y,t). \tag{20}$$

The 'gyrative' interconnection, cf. Cervera et al. (2007)

$$f_2 = e_1, \quad f_1 = -e_2, \tag{21}$$

is a Dirac structure, and obviously satisfies (18). Therefore, the combined system is again a port-Hamiltonian system.

4. DISCRETIZED COUPLED SYSTEMS

We employ a standard finite difference discretization to the PHS and due to its simplicity we can easily write down the matrices of the discretized system. Here, spatial grid variables are indicated by an underscore, e.g. $\underline{x}$.

We consider a uniform spatial grid with $N+1$ points and define $\underline{T} \in \mathbb{R}^{N\cdot M}$, such that $\underline{T}$ is defined on an offset grid, i.e. $\underline{T}_{i+jN} \approx T(\underline{x}_i + \frac{\Delta x}{2}, \underline{y}_j + \frac{\Delta y}{2})$. Meanwhile, the heat fluxes $\underline{\Phi_x} \in \mathbb{R}^{N\cdot M}$ and $\underline{\Phi_y} \in \mathbb{R}^{N(M+1)}$ are defined on a grid offset in only the y- and x-direction, respectively, i.e. $\underline{\Phi_x}_{i+Nj} \approx \Phi_x(\underline{x}_i, \underline{y}_j + \frac{\Delta y}{2})$ and $\underline{\Phi_y}_{i+Nj} \approx \Phi_y(\underline{x}_i + \frac{\Delta x}{2}, \underline{y}_j)$. We discretize the Hamiltonian (8) w.r.t. space using the midpoint rule

$$\underline{H} = \frac{1}{2}\rho c_m \Delta x \Delta y\, \underline{T}^\top \underline{T}, \tag{22}$$

giving us the internal energy change as flow variable and the temperature as effort variable:

$$\underline{f}^{(T)} = \rho c_m \Delta x \Delta y \frac{\partial \underline{T}}{\partial t}, \quad \underline{e}^{(T)} = \underline{T}. \tag{23}$$

The PHS modelling the cooling channel is disrectized similarly, cf. Jäschke et al. (2021).

Now the two PHS are coupled, results in a system with the Hamiltonian

$$H = \frac{1}{2}\int_\Omega \rho(\boldsymbol{x}) c_m(\boldsymbol{x})\, T(t,\boldsymbol{x})^2 \,\mathrm{d}\boldsymbol{x} + \frac{1}{2}\int_0^1 \rho_c c_c\, \Theta^2(y,t) \,\mathrm{d}y. \tag{24}$$

Discretizing T, Θ with a proper midpoint rule yields

$$\underline{H} = \frac{1}{2}\rho c_m \Delta x \Delta y\, \underline{T}^\top \underline{T} + \frac{1}{2}\Delta y \sum_{i=0}^{M-1} \rho_c c_c \underline{\Theta}_i^2, \tag{25}$$

the same Hamiltonian produced by coupling the two discretized PHS. We then obtain the following system:

$$\begin{pmatrix} f^{(T)} \\ 0 \\ 0 \\ f^{(\Theta)} \end{pmatrix} = \begin{pmatrix} 0 & J_x & J_y & 0 \\ -J_x^\top & -R_x & 0 & B_{x,N} \\ -J_y^\top & 0 & -R_y & 0 \\ 0 & -B_{x,N}^\top & 0 & J_\Theta - R_\Theta \end{pmatrix} \begin{pmatrix} e^{(T)} \\ \underline{\Phi_x} \\ \underline{\Phi_y} \\ e^{(\Theta)} \end{pmatrix} + B \begin{pmatrix} T_{\text{ext}}(\underline{x}_0, \underline{y} + \frac{\Delta y}{2}) \\ T_{\text{ext}}(\underline{x} + \frac{\Delta x}{2}, \underline{y}_0) \\ T_{\text{ext}}(\underline{x} + \frac{\Delta x}{2}, \underline{y}_M) \\ v\rho c_c \Theta_{in} \end{pmatrix}, \quad \widetilde{w} = B^\top \big(e^{(T)}, \underline{\Phi_x}, \underline{\Phi_y}, e^{(\Theta)}\big)^\top,$$

which is a PHDAE with J_Θ skew-symmetric and R_x, R_y, R_Θ symmetric.

At least in this case, for the discretization chosen here, there is therefore no difference between coupling the discretized systems and discretizing the coupled system.

REFERENCES

Cervera, J., van der Schaft, A., and Baños, A. (2007). Interconnection of port-Hamiltonian systems and composition of Dirac structures. *Automatica*, 43(2), 212–225.

Jäschke, J., Ehrhardt, M., Günther, M., and Jacob, B. (2021). A two-dimensional port-Hamiltonian model for coupled heat transfer. IMACM Preprint 21/28.

Serhani, A., Haine, G., and Matignon, D. (2019). Anisotropic heterogeneous n-D heat equation with boundary control and observation: I. Modeling as port-Hamiltonian system. *IFAC-PapersOnLine*, 52(7), 51–56.

Modeling Whole Heart Muscle Fibers in Cardiac Computational Models

Roberto Piersanti [*,⋆] **Christian Vergara** [**] **Luca Dedè** [*]
Alfio Quarteroni [*,***]

[*] *Modellistica e Calcolo Scientifico (MOX), Dipartimento di Matematica, Politecnico di Milano, Milan, Italy*
[**] *LaBS, Dipartimento di Chimica, Materiali e Ingegneria Chimica "Giulio Natta" Politecnico di Milano, Milan, Italy*
[***] *Mathematics Institute (Professor Emeritus) 'Ecole Polytechnique Fédérale de Lausanne, Lausanne, Switzerland*

Abstract: A crucial issue in simulating the heart function is accounting and modeling the arrangement of myocardial fibers that characterizes the cardiac tissue. Aggregations of myofibers, namely the results of cardiomyocytes orientation, plays a key role in the electric signal propagation and in the myocardial contraction. This motivates the need to accurately include muscular fibers in cardiac computational models (CCM). Rule-Based-Methods (RBMs), which provide a surrogate of myocardial fibers field, are one of the most used strategy to prescribe fiber orientation in CCM. In this work, we present a Laplace-Dirichlet-Rule-Based-Method (LDRBM), a particular class of RBMs, for generating myocardial whole heart fibers directly on full heart computational geometries. The methodology is straightforward and can be easily applied to any four-chambers models. The heart LDRBM includes a detailed myocardial fiber architecture and is able to quantitatively reproduce almost all the features of the different four-chambers, particularly those of the right ventricle and the atrial bundles.

Keywords: Cardiac fiber architecture, Fiber reconstruction, Finite element method, Laplace-Dirichlet-Rule-Based-Methods, Whole heart modeling.

1. INTRODUCTION

In cardiac computational models (CCM), a major issue consists in modeling the complex arrangement of myocardial fibers that characterizes the cardiac tissue. Aggregations of myofibers determine how the electric potential propagates within the muscle and also the mechanical contraction [Punske et al. (2005); Gil et al. (2019)]. This motivates the need to accurately include fiber orientations in order to obtain physically meaningful results.

Due to the difficulties of reconstructing cardiac muscle fibers from medical imaging [Toussaint et al. (2013)], a widely used strategy, for generating myofiber orientations in CCM, relies on the so-called *Rule-Based Methods* (RBMs) [Potse et al. (2006)].

Laplace-Dirichlet-Rule-Based Methods (LDRBMs) are the most used RBMs for prescribing ventricular fibers in CCM. LDRBMs, which rely on the solution of Laplace boundary-value problems, have been recently reviewed and analysed under a communal mathematical description [Piersanti et al. (2021)].

Regarding the atria, several RBMs have been developed, using either semi-automatic rule-based approaches [Fastl et al. (2018)], atlas-based methods [Roney et al. (2020)] or manually prescribing the atrial fiber orientations [Krueger et al. (2010)]. All the former procedures require manual intervention and often are designed for specific morphologies. Only recently, a LDRBM has been proposed for the atria [Piersanti et al. (2021)].

Prescribing the myofibers architecture is significantly more challenging in full heart geometries. Many of the existing four-chambers heart models embed only the ventricular fibers [Strocchi et al. (2020)], include simplified architecture for the atria [Land and Niederer (2018)] or adopt different RBMs for the ventricles and the atria [Gerach et al. (2021)]. To the best of our knowledge, none of whole heart computational studies makes use of a unique RBM to directly embed reliable and detailed cardiac myofiber architecture that takes into account different fiber orientations specific of the four chambers.

In this work we present a LDRBM for the generation of full heart myofibers architecture, that is able to reproduce all the important characteristic features of the four chambers, needed to provide a realistic cardiac musculature. Our newly developed method is built upon the combination of the ventricular and atrial LDRBMs presented in [Piersanti et al. (2021)] and on a novel definition of several inter-heart distances by means of Laplace problems.

2. METHODOLOGY

To properly represent the cardiac fiber architecture, throughout the whole heart computational domain, the heart LDRBM defines several inter-heart and intra-heart

⋆ e-mail: roberto.piersanti@polimi.it

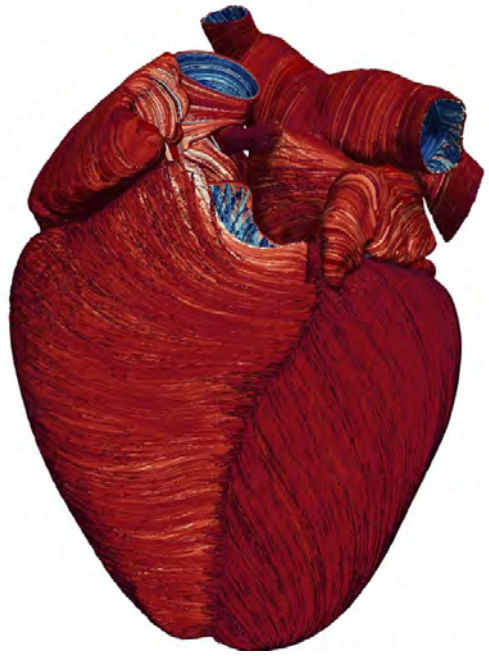

Fig. 1. Fiber generation, employing the full heart LDRBM, applied to the realistic Zygote Heart model.

distances, obtained by solving Laplace problems with specific Dirichlet boundary conditions on the heart boundaries. The inter-heart distances are used to define a transmural distance (from the endocardium to the epicardium), to discriminate the left from the right heart and the atria from the ventricles. Meanwhile, the intra-heart distances are computed to represent different atrial and ventricular distances, characteristic of the four chambers.

Afterwards, the heart LDRBM first sorts the atria from the ventricles. Then, it suitably combines the gradients of the inter-heart and intra-heart distances with the aim of defining an orthonormal local coordinate axial system in each nodal point of the heart computational domain. Finally, the reference frame is rotated with the purpose of defining the myofiber orientations.

3. RESULTS

The heart LDRBM has been applied to prescribe the whole heart muscular fiber architecture on the realistic 3D Zygote heart (see Figure 1), a CAD-model representing an average healthy human heart reconstructed from high-resolution Computed Tomography scan [Inc. (2014)]. As it is a very detailed geometry of the human heart, it demonstrates the applicability of the proposed methodology to arbitrary patient-specific scenarios.

ACKNOWLEDGEMENTS

This work has been supported by the ERC Advanced Grant iHEART, “An Integrated Heart Model for the simulation of the cardiac function”, 2017-2022, P.I. A. Quarteroni (ERC-2016-ADG, project ID: 740132).

REFERENCES

Fastl, T., Tobon-Gomez, C., Crozier, A., Whitaker, J., Rajani, R., McCarthy, K., Sanchez-Quintana, D., Ho, S., O’Neill, M., Plank, G., et al. (2018). Personalized computational modeling of left atrial geometry and transmural myofiber architecture. *Medical Image Analysis*.

Gerach, T., Schuler, S., Fröhlich, J., Lindner, L., Kovacheva, E., Moss, R., Wülfers, E.M., Seemann, G., Wieners, C., and Loewe, A. (2021). Electro-mechanical whole-heart digital twins: A fully coupled multi-physics approach. *Mathematics*, 9(11), 1247.

Gil, D., Aris, R., Borras, A., Ramírez, E., Sebastian, R., and Vázquez, M. (2019). Influence of fiber connectivity in simulations of cardiac biomechanics. *International Journal of Computer Assisted Radiology and Surgery*, 14(1), 63–72.

Inc., Z.M.G. (2014). Zygote solid 3d heart generation II developement report. *Technical report*.

Krueger, M., Rhode, K., Weber, F., Keller, D., Caulfield, D., Seemann, G., Knowles, B., Razavi, R., and Dössel, O. (2010). Patient-specific volumetric atrial models with electrophysiological components: a comparison of simulations and measurements. *Biomedizinische Technik/Biomedical Engineering*, 55.

Land, S. and Niederer, S. (2018). Influence of atrial contraction dynamics on cardiac function. *International Journal for Numerical Methods in Biomedical Engineering*, 34(3), e2931.

Piersanti, R., Africa, P., Fedele, M., Vergara, C., Dedè, L., Corno, A., and Quarteroni, A. (2021). Modeling cardiac muscle fibers in ventricular and atrial electrophysiology simulations. *Computer Methods in Applied Mechanics and Engineering*, 373, 113468.

Potse, M., Dubé, B., Richer, J., Vinet, A., and Gulrajani, R.M. (2006). A comparison of monodomain and bidomain reaction-diffusion models for action potential propagation in the human heart. *IEEE Transactions on Biomedical Engineering*, 53(12), 2425–2435.

Punske, B., Taccardi, B., Steadman, B., Ershler, P., England, A., Valencik, M., McDonald, J., and Litwin, S. (2005). Effect of fiber orientation on propagation: electrical mapping of genetically altered mouse hearts. *Journal of Electrocardiology*, 38(4), 40–44.

Roney, C., Bendikas, R., Pashakhanloo, F., Corrado, C., Vigmond, E., McVeigh, E., Trayanova, N., and Niederer, S. (2020). Constructing a human atrial fibre atlas. *Annals of Biomedical Engineering*.

Strocchi, M., Augustin, C., Gsell, M., Karabelas, E., Neic, A., Gillette, K., Razeghi, O., Prassl, A., Vigmond, E., Behar, J., et al. (2020). A publicly available virtual cohort of four-chamber heart meshes for cardiac electromechanics simulations. *PloS One*, 15, e0235145.

Toussaint, N., Stoeck, C., Schaeffter, T., Kozerke, S., Sermesant, M., and Batchelor, P. (2013). In vivo human cardiac fibre architecture estimation using shape-based diffusion tensor processing. *Medical Image Analysis*, 17(8), 1243–1255.

A large-strain poroelastic model for myocardial oedema formation

Nicolás Barnafi [*] **Bryan Gómez-Vargas** [**]
Wesley de Jesus Lourenço [***] **Ruy Freitas Reis** [***]
Bernardo Marcelo Rocha [***] **Marcelo Lobosco** [***]
Ricardo Ruiz-Baier [****] **Rodrigo Weber dos Santos** [***]

[*] *Department of Mathematics "Federigo Enriques", Università degli Studi di Milano, Via Saldini 50, 20133 Milano, Italy. nicolas.barnafi@unimi.it*
[**] *Sección de Matemática, Sede de Occidente, Universidad de Costa Rica, San Ramón de Alajuela, Costa Rica. bryan.gomezvargas@ucr.ac.cr.*
[***] *Graduate Program on Computational Modeling, Federal University of Juiz de Fora, José Lourenço Kelmer - Martelos, Juiz de Fora, Minas Gerais, Brazil. marcelo.lobosco@ice.ufjf.br, wesleydejesuspearl@ice.ufjf.br, ruyfreitas@ice.ufjf.br, bernardomartinsrocha@ice.ufjf.br, rodrigo.weber@ufjf.edu.br*
[****] *School of Mathematical Sciences, Monash University, 9 Rainforest Walk, Melbourne 3800 VIC, Australia; and Institute of Computer Science and Mathematical Modelling, Sechenov University, Moscow, Russian Federation; and Universidad Adventista de Chile, Casilla 7-D, Chillán, Chile. ricardo.ruizbaier@monash.edu.*

1. INTRODUCTION

Poroelastic structures can be found in many biological applications, such as the study of biofilm growth distribution near fluids, cardiac perfusion and myocarditis formation (see Showalter (2005); Barnafi et al. (2021); Freitas Reis et al. (2019a)). This work concerns the formation of oedema, a build up of excess of fluid content in the myocardial intercellular space, due to an inflammatory reaction driven by the immune system.

We extend the results from Freitas Reis et al. (2019a,b) and develop a phenomenological model for the dynamic interaction between poroelastic finite-strain deformations and the chemotaxis of leukocytes towards pathogens. We address the local solvability of such model by studying its linearization, and additionally include the applicability of this model for large scale simulations by devising a robust block preconditioner (White et al. (2016)).

The main advantages of the proposed mathematical model and the associated computational methods are:

(1) a framework valid for finite strains,
(2) the versatility of the formulation to accommodate 2D or 3D geometries,
(3) the accuracy and efficiency of the numerical scheme,
(4) the potential of replacing invasive methods for the detection of interstitial fibrosis and myocarditis (such as endomyocardial biopsy) by techniques hinging only on MRI data.

2. THE MODEL

We consider an open connected domain Ω representing the heart that is deformed by a deformation field $\boldsymbol{x}$. A reference point $\boldsymbol{X}$ is deformed into the point $\boldsymbol{x}(\boldsymbol{X}, t) = \boldsymbol{X} + \boldsymbol{u}(\boldsymbol{X}, t)$, where $\boldsymbol{u}$ is the displacement field and $\boldsymbol{F} := \nabla \boldsymbol{x}$. The domain represents a mixture of extracellular and intracellular space, distributed according to their porosity, i.e. the local percentage of such phase pulled-back to reference configuration (MacMinn et al. (2016)), given respectively by ϕ, and $\phi_{\mathrm{IC}} = \det(\boldsymbol{F}) - \phi$. In the extracellular space we consider the concentration of the leukocytes and a pathogen, given by c_l and c_p respectively. These concentrations, together with the porosity, the pressure p acting on the intracellular space and the displacement form the main (primary) variables of our model.

The conservation of linear momentum is given by (MacMinn et al. (2016)):

$$-\operatorname{div}\left(\boldsymbol{P} - \alpha p \det(\boldsymbol{F})\boldsymbol{F}^{-T}\right) = \boldsymbol{0} \quad \text{in } \Omega,$$

where $\boldsymbol{P}$ is the Piola stress tensor, and α is the Biot-Willis modulus. The Piola stess tensor $\boldsymbol{P}$ is related to the primary variables through a Helmholtz potential Ψ such that $\boldsymbol{P} = \frac{\partial \Psi}{\partial \boldsymbol{F}}$, in our case given by the Holzapfel-Ogden energy (Holzapfel and Ogden (2009)).

In the extracellular space we consider the mass conservation of the liquid it contains, given by the following equation (MacMinn et al. (2016)):

$$\frac{d\phi}{dt} + \operatorname{div}\left(\phi \boldsymbol{K}(\boldsymbol{F}, \phi)\, \nabla\, p\right) = \Theta(p, c_p) \quad \text{in } \Omega,$$

where $\boldsymbol{K}$ is modeled with an isotropic power law, and the immune response is modeled through Θ using a Starling-Hill function (Freitas Reis et al. (2019a)). The evolution of the immune system dynamics related to the concentrations c_p, c_l is dictated by the following mass conservation laws:

$$\frac{d(\phi c_p)}{dt} - \operatorname{div}\left(\phi \boldsymbol{D}_p(\boldsymbol{F}) \nabla c_p\right) = r_p(\phi, c_p, c_l), \quad \text{in } \Omega,$$

$$\frac{d(\phi c_l)}{dt} - \operatorname{div}\left(\phi \boldsymbol{D}_l(\boldsymbol{F}) \nabla c_l - \chi \phi c_l \nabla c_p\right) = r_l(\phi, c_p, c_l), \quad \text{in } \Omega.$$

both valid throughout Ω, where $\boldsymbol{D}_p, \boldsymbol{D}_l$ are the pulled-back diffusion tensors for the species in the extracellular space, χ is the leukocyte chemotactic rate and r_p, r_l are the reaction terms that yield the interaction between the pathogen and the leukocytes. The last equation is given by the incompressibility of the intracellular space:

$$\det(\boldsymbol{F}) - \phi = 1 - \phi_0, \quad \text{in } \Omega,$$

where ϕ_0 represents the initial (resting) porosity.

3. RESULTS

In Figure 1 we show the evolution of the chemotaxis variables c_p (first row) and c_l (second two), where it can be appreciated how leukocytes appear as a reaction to the passage of the pathogen.

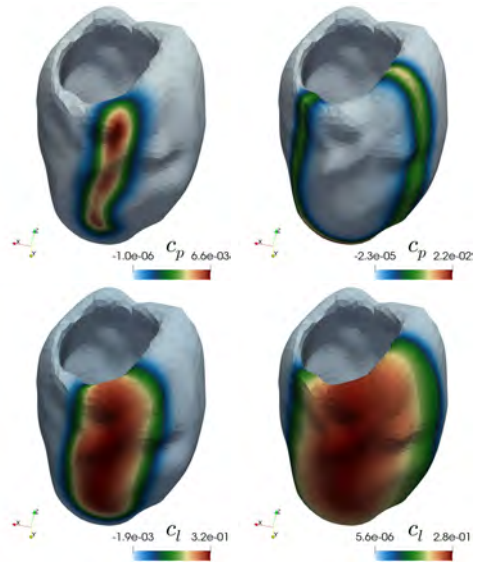

Fig. 1. Evolution of pathogens and leukocytes concentration (first and second row, respectively) at $t = 0$ minutes and $t = 15$ minutes.

In our work we report five different numerical tests: i) a sensitivity analysis, where pathogen concentration, pressure and displacement were studied for a wide range of different parameters; ii) an isolated poromechanics study, where compression and drainage responses of the tissue were verified; iii) a coupled chemotaxis study, where the entire model was tested with an initial concentration of pathogen in a 2D square domain; iv) a convergence study, to validate the approximability properties of our proposed numerical scheme; lastly, v) an integrated simulation in a real left ventricle geometry, together with a verification of the robustness of our preconditioner in such case.

4. CONCLUSIONS

We have proposed a general model capturing the phenomenological features of the interaction between chemotaxis of the immune system in saturated poroelastic media admitting large deformations. The problem exhibits a saddle-point structure that allowed us to devise an adequate approximation scheme, that we complemented with a block-partitioned preconditioner. The vast collection of numerical tests allow us to conclude that our model yields a physiologically accurate behavior, which together with our scalable solver results in a realistic model that can be efficiently approximated numerically in large scale simulations.

Further investigation is necessary, for instance, regarding the specific role of the anisotropic porous structure of the tissue, as well as in designing new coupling mechanisms that will contribute to a better understanding of the formation and termination of myocarditis and myocardial oedema. Another fundamental problem to address is that of a more thorough sensitivity analysis, in order to better understand the role of each of the many parameters involved in the model, so that they can be more easily adapted to patient-specific scenarios.

REFERENCES

Barnafi, N., Di Gregorio, S., Dede', L., Zunino, P., Vergara, C., and Quarteroni, A.M. (2021). A multiscale poromechanics model integrating myocardial perfusion and systemic circulation. *MOX Reports*, (39).

Freitas Reis, R., Fernandes, J.L., Schmal, T.R., Martins Rocha, B., Weber Dos Santos, R., and Lobosco, M. (2019a). A personalized computational model of edema formation in myocarditis based on long-axis biventricular MRI images. *BMC Bioinformatics*, 20(6), 532(11).

Freitas Reis, R., Weber Dos Santos, R., Martins Rocha, B., and Lobosco, M. (2019b). On the mathematical modeling of inflammatory edema formation. *Comput. Math. Appl.*, 78(9), 2994–3006.

Holzapfel, G.A. and Ogden, R.W. (2009). Constitutive modelling of passive myocardium: a structurally based framework for material characterization. *Phil. Trans. Royal Soc. Lond. A*, 367, 3445–3475.

MacMinn, C.W., Dufresne, E.R., and Wettlaufer, J.S. (2016). Large deformations of a soft porous material. *Phys. Rev. Appl.*, 5(4), 044020(30).

Showalter, R.E. (2005). Poroelastic filtration coupled to Stokes flow. In O. Imanuvilov, G. Leugering, R. Triggiani, and B.Y. Zhang (eds.), *Control Theory of Partial Differential Equations*, volume 242 of *Lecture Notes in Pure and Applied Mathematics*, 229–241. Chapman & Hall, Boca Raton.

White, J., Castelletto, N., and Tchelepi, H. (2016). Block-partitioned solvers for coupled poromechanics: A unified framework. *Computer Methods in Applied Mechanics and Engineering*, 303, 55–74. doi: 10.1016/j.cma.2016.01.008.

Optimization-Based Structured Reduced Order Modeling from Frequency Samples ⋆

Paul Schwerdtner * **Matthias Voigt** **

* *Technische Universität Berlin, Institut für Mathematik, Straße des 17. Juni 136, 10623 Berlin, Germany. E-Mail: schwerdt@math.tu-berlin.de*
** *UniDistance Suisse, Schinerstrasse 18, 3900 Brig, Switzerland. E-Mail: matthias.voigt@fernuni.ch*

Keywords: model reduction, H-infinity optimization, port-Hamiltonian systems

1. INTRODUCTION

We consider the computation of low-order *port-Hamiltonian* (pH) surrogate models of the form

$$\Sigma_{\mathrm{pH}} : \begin{cases} \dot{x}(t) = (J - R)Qx(t) + Bu(t), \\ y(t) = B^{\mathsf{T}}Qx(t), \end{cases}$$

where J, R, $Q \in \mathbb{R}^{r\times r}$ and $B \in \mathbb{R}^{r\times m}$ with $J = -J^{\mathsf{T}}$, $R \geq 0$, and $Q \geq 0$. We call $x : \mathbb{R} \to \mathbb{R}^r$, $u : \mathbb{R} \to \mathbb{R}^m$, and $y : \mathbb{R} \to \mathbb{R}^m$ the *state*, *input*, and *output* of the system, respectively. The state dimension r is also called the model order of the system. We compute surrogate models in the sense that Σ_{pH} is not derived by first-principle modeling but is instead obtained by approximating the input-to-output mapping of a given system.

For linear dynamical systems, the input-to-output mapping is characterized by the *transfer function* in the frequency domain. The transfer function of Σ_{pH} is given by

$$H_{\mathrm{pH}}(s) := B^{\mathsf{T}}Q(sI_r - (J - R)Q)^{-1}B.$$

In this work, we aim at determining matrices J, R, Q, and B such that H_{pH} approximates the transfer function H_{g} of a given (possibly unstructured) system Σ_{g} with respect to the $\mathcal{H}_\infty$ norm. Let $\mathcal{RH}_\infty^{m\times m}$ denote the normed space of all real-rational and proper $m \times m$ transfer functions that have no poles in the set $\overline{\mathbb{C}^+} := \{\lambda \in \mathbb{C} \mid \mathrm{Re}(\lambda) \geq 0\}$. Then the $\mathcal{H}_\infty$ norm of a function $H \in \mathcal{RH}_\infty^{m\times m}$ is given by

$$\|H\|_{\mathcal{H}_\infty} := \sup_{\lambda\in\mathbb{C}^+} \|H(\lambda)\|_2 = \sup_{\omega\in\mathbb{R}} \sigma_1(H(\mathrm{i}\omega)),$$

where $\sigma_1(\cdot)$ denotes the largest singular value of its matrix argument.

Two use cases for the construction of low-order surrogate models that approximate a given input-to-output mapping are *model order reduction* (MOR) and *system identification*. MOR is used when a given model has a high complexity (e. g., a large state-dimension), which makes its repeated simulation or model-based control computationally prohibitively expensive. Therefore, MOR is applied to construct a low-order surrogate model that is then used in place of the high-complexity model. On the other hand, system identification is applied when no mathematical model of a given system is available, and instead a model must be constructed from experimental data. Our method can be applied in both situations. However, in this note, we only explain our method in the context of MOR and refer to Schwerdtner (2021) for a related system identification algorithm.

The main features of our method are as follows:

- We construct surrogate models with pH structure, which are automatically passive. Passivity leads to several benefits for simulation and controller design.
- We only use transfer function evaluations to construct our low-order model. In this way, no particular model structure of the original model is required for our computation of a pH surrogate model. Therefore, our method can be applied to a wide range of dynamical systems.
- Our experiments show that our algorithm can determine pH surrogate models that are as accurate as models found by well-established (and unstructured) MOR routines such as *balanced truncation* (BT).

2. OUR METHOD

In Schwerdtner and Voigt (2020) we pose MOR as a parameter optimization problem. For that, we define a parametrized pH system as follows.

Lemma 1. (Schwerdtner and Voigt (2020)). Let $\theta \in \mathbb{R}^{n_\theta}$ be a vector with $n_\theta := r\left(\frac{3r+1}{2} + m\right)$. Furthermore, let θ be partitioned as $\theta := \left[\theta_J^{\mathsf{T}}, \theta_R^{\mathsf{T}}, \theta_Q^{\mathsf{T}}, \theta_B^{\mathsf{T}}\right]^{\mathsf{T}}$ with $\theta_J \in \mathbb{R}^{r(r-1)/2}$, $\theta_R \in \mathbb{R}^{r(r+1)/2}$, $\theta_Q \in \mathbb{R}^{r(r+1)/2}$, and $\theta_B \in \mathbb{R}^{rm}$. Further define the matrices

$$\begin{aligned} J(\theta) &= \mathrm{vtsu}(\theta_J)^{\mathsf{T}} - \mathrm{vtsu}(\theta_J), \\ R(\theta) &= \mathrm{vtu}(\theta_R)^{\mathsf{T}}\,\mathrm{vtu}(\theta_R), \\ Q(\theta) &= \mathrm{vtu}(\theta_Q)^{\mathsf{T}}\,\mathrm{vtu}(\theta_Q), \\ B(\theta) &= \mathrm{vtf}_{r,m}(\theta_B), \end{aligned}$$

where the function $\mathrm{vtu} : \mathbb{R}^{r(r+1)/2} \to \mathbb{R}^{r\times r}$ maps a vector of length $r(r+1)/2$ to an upper triangular matrix, the

⋆ This work is supported by the German Research Foundation (DFG) within the project VO2243/2-1: "Interpolationsbasierte numerische Algorithmen in der robusten Regelung" and the DFG Cluster of Excellence MATH+ within the project AA4-5: "Energy-based modeling, simulation, and optimization of power systems under uncertainty". This research has mainly been carried out while the second author was affiliated with Universität Hamburg and Technische Universität Berlin. Their support is gratefully acknowledged.

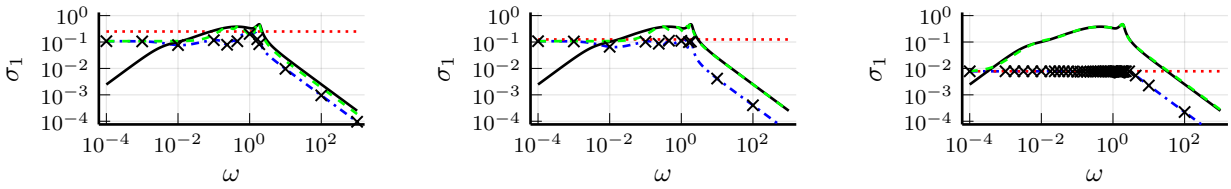

(a) $\gamma = 2.5 \cdot 10^{-1}$ (b) $\gamma = 1.25 \cdot 10^{-1}$ (c) $\gamma = 7.81 \cdot 10^{-3}$

Fig. 1. The progress of our method for reduced model order of $r = 8$ is depicted for decreasing levels γ. The given transfer function is illustrated as black solid line, the low-order surrogate transfer function is depicted as green dashed line, and the error is shown as blue dash-dotted line. The sample points are depicted as black crosses.

function vtsu : $\mathbb{R}^{r(r-1)/2} \to \mathbb{R}^{r\times r}$ maps a vector of length $r(r-1)/2$ to a strictly upper triangular matrix, and the function vtf$_{r,m} : \mathbb{R}^{rm} \to \mathbb{R}^{r\times m}$ reshapes a vector of length rm to an $r \times m$ matrix. Then, to each $\theta \in \mathbb{R}^{n_\theta}$ one can assign the pH system

$$\Sigma_{\mathrm{pH}}(\theta) : \begin{cases} \dot{x}(t) = (J(\theta) - R(\theta))\, Q(\theta)x(t) + B(\theta)u(t), \\ y(t) = B(\theta)^{\mathsf{T}} Q(\theta)x(t). \end{cases} \tag{1}$$

Conversely, to each pH system Σ_{pH} with r states and m inputs and outputs one can assign a vector $\theta \in \mathbb{R}^{n_\theta}$ such that $\Sigma_{\mathrm{pH}} = \Sigma_{\mathrm{pH}}(\theta)$ with $\Sigma_{\mathrm{pH}}(\theta)$ as in (1).

For details of the construction, we refer the reader to Schwerdtner and Voigt (2020). In the following, we denote the transfer function of $\Sigma_{\mathrm{pH}}(\theta)$ by $H_{\mathrm{pH}}(\cdot, \theta)$.

Using this parametrization, we minimize the objective function

$$\mathsf{L}\left(\gamma, H, H_{\mathrm{pH}}(\cdot,\theta), S\right) := \frac{1}{\gamma} \sum_{s_i \in S} \left(\left[\|H_{\mathrm{g}}(s_i) - H_{\mathrm{pH}}(s_i,\theta)\|_2 - \gamma \right]_+ \right)^2, \tag{2}$$

with respect to θ for decreasing values of $\gamma > 0$, where

$$[\cdot]_+ : \mathbb{R} \to [0,\infty), \quad x \mapsto \begin{cases} x & \text{if } x \geq 0, \\ 0 & \text{if } x < 0 \end{cases}$$

and $S \subset \mathrm{i}\mathbb{R} := \{\lambda \in \mathbb{C} \mid \mathrm{Re}(\lambda) = 0\}$. Minimizing this objective function for decreasing values of γ effectively reduces the $\mathcal{H}_\infty$ error between H_{g} and H_{pH}. Furthermore, using L comes with several benefits compared to a direct minimization of $\|H_{\mathrm{g}} - H_{\mathrm{pH}}\|_{\mathcal{H}_\infty}$. These are discussed in Schwerdtner and Voigt (2020).

To obtain a good approximation of H_{g} by minimizing L, the sample points $s_i \in S$ must capture the error transfer function $H_{\mathrm{g}} - H_{\mathrm{pH}}$ with sufficient accuracy, such that

$$\max_{s_i \in S} \|H_{\mathrm{g}}(s_i) - H_{\mathrm{pH}}(s_i)\|_2$$

is close to $\|H_{\mathrm{g}} - H_{\mathrm{pH}}\|_{\mathcal{H}_\infty}$. However, each new sample point also increases the computational demand of the optimization, since both the large-scale transfer function and our surrogate transfer function (and gradient of the their difference with respect to θ) must be evaluated at each sample point. This speed/accuracy trade-off is circumvented by a recently developed adaptive sampling strategy, which adds new sample points at those locations where the discrepancy between $H_{\mathrm{g}}(s)$ and $H_{\mathrm{pH}}(s)$ is larger than a tolerance which is automatically adjusted by the algorithm. For implementation details we refer to Schwerdtner and Voigt (2021).

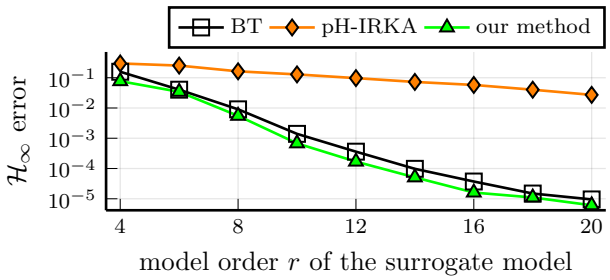

Fig. 2. $\mathcal{H}_\infty$ error comparison for different MOR methods

3. EXPERIMENTAL RESULTS

We assess the performance of our described optimization-based MOR by computing low-order approximations to a large-scale mass-spring-damper model from Gugercin et al. (2012). Fig. 1 illustrates how the minimization of L for decreasing values of γ leads to increasingly accurate surrogate models. Furthermore, it can be observed that the number of sample points is increased as γ is reduced to capture the error transfer function with sufficient accuracy.

In Fig. 2, we report the $\mathcal{H}_\infty$ errors that are obtained when using our method in comparison with another structure-preserving as well as an unstructured MOR method. The key observation is that using our method, we can obtain pH structured surrogate models that are as accurate as models obtained from unstructured MOR routines (such as BT), while other structured MOR methods (such as pH-IRKA developed in Gugercin et al. (2012)) typically lead to a decrease in accuracy. All reported results are obtained with the setup described in Schwerdtner and Voigt (2021).

REFERENCES

Gugercin, S., Polyuga, R.V., Beattie, C., and van der Schaft, A. (2012). Structure-preserving tangential interpolation for model reduction of port-Hamiltonian systems. *Automatica J. IFAC*, 48(9), 1963–1974.

Schwerdtner, P. (2021). Port-Hamiltonian system identification from noisy frequency response data. Preprint arXiv:2106.11355.

Schwerdtner, P. and Voigt, M. (2020). Structure preserving model order reduction by parameter optimization. Preprint arXiv:2011.07567.

Schwerdtner, P. and Voigt, M. (2021). Adaptive sampling for structure-preserving model order reduction of port-Hamiltonian systems. *IFAC-PapersOnline*, 54(19), 143–148.

Modelling Crop Rotations and Nutrient-Balances in Organic Farming Systems

Colja Krugmann[*] Jochen Wittmann[**] Johann Bachinger[***] Mosab Halwani[****]

[*]*Institute of Land Use Systems and Landscape Ecology, Leibniz-Centre for Agricultural Landscape Research (ZALF), Eberswalder Str. 84, 15374 Müncheberg, Germany*
[*]*(e-mail: colja.krugmann@zalf.de)*
[***]*(e-mail: jbachinger@zalf.de)*
[****]*(e-mail: mosab.halwani@zalf.de)*
[**]*HTW Berlin University of Applied Science (e-mail: jochen.wittmann@htw-berlin.de*

1. INTRODUCTION

ROTOR is an agronomic planning tool used by farmers and consultants to generate and evaluate crop rotations, which are crucial to organic farming systems in terms of their projected yields, humus-, nitrogen- (N), phosphorus- (P), and potassium- (K) balances, considering weed infestation risks and phytosanitary restrictions. ROTOR has been developed since 1997 at the Leibniz-Centre for Agricultural Landscape Research (ZALF). A rule-based static approach is used to determine crop sequences and to assess their yields (Bachinger and Zander 2007).

The fact that ROTOR 3.1 runs within the commercial software Microsoft (MS) Access and that the software's structure and database have grown over the years, becoming less maintainable, made a software re-engineering indispensable. The newly developed version 4.0 of ROTOR is an open-source standalone software written in Python with a PostgreSQL database. The graphical user interface (GUI) was created with Qt and PyQt. Although the core principles of the underlying models have remained, the calculations of nutrient-balances were refined, whereas the generation of crop rotations was comprehensively revised. The modular structure of the new software allows for easy scalability and better maintainability.

2. THE SOFTWARE RE-ENGINEERING OF ROTOR 4.0

2.1 ROTOR 4.0's functionalities

The site-specific parameters such as the soil rating index (SRI) and precipitation necessary for the generation and assessment of crop rotations are gathered from user input. Standard values for manure types and soil specifications are retrieved from the database but can all be modified by the user. The new database in ROTOR also contains user-related project data and all data used in the nutrient and humus calculations. The user input, as well as all results, are stored in a project file. Projects can be imported and exported as a JavaScript Object Notation (JSON) file with the extension '.rotor'.

In ROTOR 4.0, three use-cases for the generation and assessment of crop rotations are implemented. All three options rely on the 'key-and-lock principle' (chapter 2.2) and evaluate the crop rotations executing all nutrient and humus calculations, as well as the weed infestation risk assessment. The new software inhibits user inputs where not needed or not possible for the selected method of crop rotation generation or assessment.

i. The 'free generation' allows an unordered input of crops and available organic manure types. ROTOR then generates and - if necessary - extends and completes optimized crop rotations putting the crops in sensible orders. The result includes recommendations for manure use and amounts.
ii. The option 'assessment' allows any ordered selection of crops and cover crops, as well as manure types and amounts. This method is meant to evaluate existing crop rotations. Its criteria are the nutrient- and humus-balances, but also the rules of succession. The input crop rotation is checked for discrepancies from ROTOR's key-and-lock principle and phytosanitary restrictions.
iii. The 'guided generation' provides a context sensitive user input for the generation of new crop rotations. In the selection for each crop in a rotation, all impossible options are greyed out or not displayed according to the expert knowledge implemented in ROTOR, as these options are not only dependent on the currently selected crop, but also on the previous and following selections.

2.2 The models in ROTOR

Modelling in ROTOR consists of two parts: The model for the generation of crop rotations and the calculations of nutrient- and humus-balances. The latter remains unchanged in its principle in ROTOR 4.0 but is adapted to the changes in the model for the generation crop rotations.

Several rules apply in the generation of sensible crop rotations in organic farming:

i. The first crop should be legume-grass (Bachinger and Zander 2007).
ii. Leaf crops should not follow leaf crops.
iii. No wheat after cereals.
iv. Grain legumes should not follow grain legumes or legume grass (Stein-Bachinger and Reckling 2013).

v. Alternation between leaf crops and cereals.
vi. Alternation between winter and summer crops (Kolbe 2008).
vii. Summer crops after cover crops.
viii. Deep rooting crops to loosen the soil after shallow rooting crops (Stein-Bachinger and Reckling 2013)

Crop rotations should be composed of 30-50% legumes, 30-60% cereals, 5-25% leaf crops and 20-60% cover crops per area according to the farming type (dairy, stockless or stock farming) (Stein-Bachinger 2013). Phytosanitary restrictions limit the frequency and share of crops or crop types in a crop rotation according to their infestation risks in order to prevent pest and fungal infestations and plant diseases and therefore the use of pesticides (Stein-Bachinger and Reckling 2013). Since in organic farming no mineral fertilizers are applied, the nitrogen-balance must be regulated in part by using legumes, as they fix atmospheric nitrogen in the soil. They can be cultivated as main crops or as catch crops that are either undersown or sown after the main crop's harvest. This distinction is crucial to the model as it is based on the concept of 'crop production activities' (CPA), describing the variable time span starting after and ending with the harvests of the main crops and their cultivation methods (Bachinger and Zander 2007). The CPAs in the database have to be created manually for each crop according to expert knowledge.

A crop sequence is generated applying the key-and-lock principle by matching the properties of the preceding crop with the requirements of the current crop concerning crop type, N-delivery of the preceding CPA with the N-need of the current CPA and a matching catch crop (Bachinger and Zander 2007). Thus, a CPA with an undersown catch crop needs to be followed by a CPA with a catch crop. To make the rather complex calculations concerning the N levels required and output by each CPA applicable in the generation of crop rotations in a software, the N-delivery of each CPA to the following is classified as either high or low according to expert knowledge (Bachinger and Zander 2007).

The above-mentioned rules i. – v. are implemented by an entry for possible preceding crop types (cereal, leaf crop, grain legume and legume grass) in the CPA database table. The alternation of summer and winter crops (vi.) is ensured by the according SQL-queries in the crop rotation generation. Rule vii., cover crops should always be followed by summer crops, is implemented by restricting the availability of the option for cover crops in the GUI to summer crops. The last rule mentioned (viii.) is partially neglected in the software, as there is no clear definition of deep and shallow rooting plants. Root structure not only depends on the crop, but also on several surrounding factors such as the soil type and its density. With the previously mentioned preceding crop type defined in each CPA, this principle is only applied by a rule of thumb, since legumes are generally classified as deep rooting, whereas cereals tend to have shallower roots (Kutschera et al. 2018).

The new model reduces the possible number of CPAs per crop to 16, as only the four crop types, two levels of N delivery of the previous crop and a Boolean value for undersowing that can, but does not necessarily affect the N-delivery to the next crop. This reduction was achieved not only by removing all degrees of freedom introduced by parameters of the CPA that do not affect the N-delivery of a CPA such as manuring, but also by shifting the timespan describing a CPA. Although in agronomy, a cultivation period starts after the harvest of the main crop, the revised model applies a timespan starting with the sowing of a main crop, making it obsolete to include the type of catch crop (none, undersown, or sown after the main crop's harvest), reducing the maximum number of manually created CPAs by a factor of three.

After the generation of a crop rotation, the yields are calculated. These amounts can be modified by the user. Based on the yields, the humus balance is calculated according to Ebertseder et al. (2014). The P and K balances are assumed to be the difference of by manuring added and by the harvest removed P and K. The N-balance is obtained by a complex chain of calculations, not only determining the N removed by harvest and added by manuring, but also the amount of atmospheric N fixed by legumes, the amount of mineralised N that is available to the plants, the N lost through leaching, and volatilisation. The weed infestation risks are assessed by assigning values to relevant elements of the cultivation methods such as tillage (Bachinger and Zander 2007).

3. CONCLUSIONS

The new version 4.0 of ROTOR is a software for the generation and evaluation of crop rotations in organic farming systems. The new modular software build facilitates the introduction of new CPAs and functionalities. Currently, an economic assessment of crop rotations is implemented and the software's accessibility will be improved by the development of a web frontend.

REFERENCES

Bachinger, Johann/Zander, Peter (2007). ROTOR, a tool for generating and evaluating crop rotations for organic farming systems. European Journal of Agronomy of 2007, 130–143.

Ebertseder, T., Engels, C., Heyn, J., Hülsbergen, K.-J., Isermann, K., Kolbe, H., Leithold, G., Reinhold, J., Schmid, H., Schweitzer, K., Willms, M., Zimmer, J. (2014). Standpunkt. Humusbilanzierung - Eine Methode zur Analyse und Bewertung der Humusversorgung von Ackerland. VDLUFA. Speyer.

Kolbe, H. (2008). Fruchtfolgegrundsätze im ökologischen Landbau. Available online at http://orgprints.org/15100 (accessed 4/11/2021).

Kutschera, L., Lichtenegger, E., Sobotik, M. (2018). Wurzelatlas der Kulturpflanzen gemäßigter Gebiete mit Arten des Feldgemüsebaues. 2nd ed. Frankfurt am Main, DLG-Verlag.

Stein-Bachinger, K. (2013). Bodenfruchtbarkeit. In: Stein-Bachinger, K., Reckling, M., Granstedt, A. (Eds.). Pflanzenbau & Tierhaltung. Müncheberg/Järna, Sweden, Leibniz-Zentrum für Agrarlandschaftsforschung (ZALF); Kulturcentrum 13, 15–26.

Stein-Bachinger, K., Reckling, M. (2013). Fruchtfolge. In: Stein-Bachinger, K. Reckling, M., Granstedt, A. (Eds.). Pflanzenbau & Tierhaltung. Müncheberg/Järna, Sweden, Leibniz-Zentrum für Agrarlandschaftsforschung (ZALF); Kulturcentrum 13, 27–38.

Solving parametric PDEs with an enhanced model order reduction method based on Linear/Ridge expansions

Constantin Greif [*], **Philipp Junk** [**], **Karsten Urban** [*]

[*] *Ulm University, Institute for Numerical Mathematics, Helmholtzstr. 20, 89081 Ulm (Germany),*
{constantin.greif,karsten.urban}@uni-ulm.de
[**] *Justus-Liebig-University Giessen, Lehrstuhl Numerische Mathematik, Arndtstr. 2, 35392 Giessen (Germany),*
Philipp.Junk@math.uni-giessen.de

Abstract: Classical projection-based model order reduction methods, like the reduced basis method, are popular tools for getting efficiently solvable reduced order models for parametric PDEs. However, for some problems, the error-decay with respect to the dimension of the linear projection space is predetermined to be slow, e.g., for parameterized wave equations with jump discontinuities.
In order to cope with this issue, we consider approximations formed by a linear combination of given functions enhanced by ridge functions – a Linear/Ridge expansion. For an explicitly or implicitly solution of a parameter-dependent problem, we reformulate finding a best Linear/Ridge expansion in terms of an optimization problem that we solve with a particle grid algorithm.
The linear functions as well as the ridge profiles are built offline with a greedy-type algorithm. By training the directions offline, we can achieve an efficient online evaluation to solve the projected parametric PDE.

Keywords: Model reduction of distributed parameter systems, Subspace methods, Particle filtering/Monte Carlo methods, Parametric optimization, Evolutionary algorithms, Control of partial differential equations

1. MOTIVATION

As a motivating example for the developed method, we recall the parametric linear wave equation.

Parametric wave Consider the linear wave equation $\partial_{tt}^2 u - \mu^2 \partial_{yy}^2 u = 0$ for $t > 0$ and $y \in \mathbb{R}$ with initial conditions $u(0) = u_0$ and $\dot{u}(0) = 0$. The parameter-dependent solution is given by the famous d'Alembert formula as $u(t, y; \mu) = \frac{1}{2}(u_0(y - \mu t) + u_0(y + \mu t))$. Hence, choosing $v_1 = v_2 = u_0$, $c_1 = c_2 = \frac{1}{2}$, $b_1 = b_2 = 0$ as well as $a_1 = (-\mu, 1)^\top, a_2 = (\mu, 1)^\top$ and $x = (t, y)^\top$ yields a representation of the solution $u(t, y; \mu) = c_1 v_1(a_1^\top x + b_1) + c_2 v_2(a_2^\top x + b_2)$ as a sum of two ridge functions. Besides, also for $\dot{u}(0) \neq 0$, the wave equation is a sum of two, but then different, ridge functions.

This problem is particularly interesting since it is known that projection-based (i.e., linear) model order reduction techniques do not work in the sense that the decay of the Kolmogorov N-width is at most $\mathcal{O}(N^{-1/2})$, Greif and Urban (2019). Nevertheless, the use of ridge functions can enhance such error reduction and is in fact convenient to use here since we only need two appropriate ridge profiles.

2. LINEAR/RIDGE EXPANSIONS

We consider a given function $u : \Omega \to \mathbb{R}$, where $\Omega \subset \mathbb{R}^d$ is an open bounded domain and $u \in L_2(\Omega)$. In order to formulate the approximation problem under consideration, let $X_N := \operatorname{span}(\Phi_N) \subset L_2(\Omega)$, $\Phi_N := \{\varphi_1, ..., \varphi_N\}$ be a given linear space of dimension $N \in \mathbb{N}$ with φ_i, $i = 1, ..., N$, being given functions.

In addition to Φ_N, we assume that we are given a finite number $M \in \mathbb{N}$ of (ridge) profiles $\mathcal{V}_M := \{v_1, ..., v_M\} \subset L_2(\mathbb{R})$ and consider the approximation problem for $x \in \Omega$

$$u(x) \approx \sum_{i=1}^{N} \alpha_i \varphi_i(x) + \sum_{j=1}^{M} c_j v_j(a_j^\top x + b_j) =: u_\delta(x) \in U_{N,M},$$

where $U_{N,M}$ is the nonlinear space built with Φ_N and $\mathcal{V}_M$. The objective is to minimize the residual of the PDE, where $u = u(\cdot; \mu)$ is the implicit solution.

Given directions and offsets For fixed directions $a_j \in \mathbb{R}^d$ and offsets $b_j \in \mathbb{R}$, the coefficients $\alpha_i \in \mathbb{R}$ and $c_j \in \mathbb{R}$ are just given as the solution of a linear system of equations (Lemma 2.5 in Greif et al. (2022)). Therefore we reformulate the approximation to just search for the optimal $(a_j, b_j) \in \mathbb{R}^{d+1}$.

2.1 A particle grid algorithm

Since the determination of directions and offsets amounts to solving a complex optimization problem, we aim at using a well-known heuristic method, the particle swarm algorithm. In order to reduce computational complexity, we arrange our particles (which are associated to the collection of all directions $a_j \in \mathbb{R}^d$ and offsets $b_j \in \mathbb{R}$, $j = 1, ..., M$) in a dynamic grid. For each profile, we collect the direction and the offset in one vector $d_j := (a_j, b_j) \in \mathbb{R}^{d+1}$. These vectors are then associated to some component $p_j \in (-1, 1)^D =: \mathbb{S}^D$. The vector $(d_j)_{j=1,...,M} \in \mathbb{R}^{DM}$ of all directions and offsets is then associated to one particle $\mathbf{p} \in (-1, 1)^{DM} = \mathbb{S}^P$.

The algorithm produces a sequence of particle grids, where each grid (i.e., a swarm in form of a grid) $\mathbf{P}^{(k)}$ consists of m_{par} particles in $\mathbb{S}^P$. We choose n_{par} nodes in each dimension, i.e., $m_{\text{par}} = n_{\text{par}}^P$ for $n_{\text{par}} \in \mathbb{N}$. Then, we initialize the initial particle grid $\mathbf{P}^{(0)}$ by taking the tensor product, yielding a regular grid. Each particle has uniquely defined next neighbors in each diagonal direction. This next neighbor relation does not change in the course of the iteration. This means that each swarm is a grid whose internal geometry does not change even if the position of each particle may vary. We may associate each particle grid $\mathbf{P}^{(k)}$ with a tensor of dimension P (e.g., a matrix for $P = 2$).

Solve parametric PDEs We used the method with the particle grid algorithm to solve two different PDEs, the already introduced wave equation as well as the thermal block, that is a classical problem for model reduction, Haasdonk (2017). (For the thermal block, we used the domains $\Omega = (0, 1)^2, \overline{\Omega}_i := [0, 1] \times [\frac{i-1}{4}, \frac{i}{4}]$, $i = 1, ..., 4$). We fed the method with $\Phi_N = \{\varphi_1, \varphi_2, \varphi_3, \varphi_4\}$ and $\mathcal{V}_M = \{v_1, v_2\}$ and the algorithm was able, for a new parameter μ, to choose the appropriate functions and discard the remaining functions by setting the coefficients to zero. The results can be seen in Table 1. Obviously there are more iterations needed for the case of the wave equation.

PPDE	parameter μ	no. iterat. K	L_2-error
Thermal block	$(0.1, 10, 1, 0.6)$	1	$5.1019e-15$
Thermal block	$(10, 2, 0.1, 0.5)$	1	$1.4446e-14$
Thermal block	$(0.4, 2, 0.3, 5)$	1	$6.0861e-15$
Wave	1/4	20	$7.6682e-05$
Wave	1/4	83	$8.9850e-16$
Wave	1	21	$8.2400e-05$
Wave	1	86	$3.1765e-16$
Wave	4	28	$4.3012e-05$
Wave	4	83	$8.9850e-16$

Table 1. Errors and iterations for both parametric PDEs and different parameter values.

3. COMPLETE MODEL REDUCTION METHOD

Generation of basis functions Until now, we considered Φ_N and $\mathcal{V}_M$ as given. However, we need to extract them from the problem. (Due to page limitation we can just sketch the idea here.) Using a greedy-type algorithm, we build a linear basis from snapshots and successively add ridge functions attained by integration along directions according to Pinkus (2015).

Efficient online computation By assuming certain affine parameter dependence, we can get an efficient online computation that is faster than the classical particle grid algorithm. Therefore we offline train the parameter-dependence on the directions using the particle grid algorithm and online use this as an initial guess to just evaluate a very local optimization.

3.1 Full model reduction method

- Offline: Build basis functions $X_N = \{\varphi_1, \ldots, \varphi_N\}$ and profiles $V_M = \{v_1, \ldots, v_M\}$.
- We first build X_N by a greedy method minimizing an residual error.
- If the error decay is not "fast" any more, we switch and add profiles to V_M to further reduce the error.
- With the obtained space $U_{N,M}$, we train the parameter-dependence of the directions using a training set of snapshots.
- Online: For a parameter μ find directions with a local optimization method by solving the PDE on the projected space $U_{N,M}$.

3.2 Conclusion

We introduced a model order reduction method that is able to solve a broader class of problems than classical projection-based methods. Unfortunately, the method also has some drawbacks, like the harder to reach online efficiency. Computing the optimal ridge directions is more costly than just solving a linear system of equation.
Furthermore, the Linear/Ridge expansions are still a restricted approximation type. One can easily think of function classes that are still hard to solve with approaches like this, like PDEs with nonlinear characteristics. But unlike in the linear case, there won't be a nonlinear method that fits all problems. Related approaches are an active field of research, c.f. Black et al. (2020).

REFERENCES

Black, F., Schulze, P., and Unger, B. (2020). Projection-based model reduction with dynamically transformed modes. *ESAIM: Math. Model. Numer. Anal.*, 54(6), 2011–2043.

Buhmann, M.D. and Pinkus, A. (1999). Identifying linear combinations of ridge functions. *Adv. Appl. Math.*, 22(1), 103–118.

Greif, C., Junk, P., and Urban, K. (2022). Linear/ridge expansions: Enhancing linear approximations by ridge functions. *Advances in Computational Mathematics*, 48, 15.

Greif, C. and Urban, K. (2019). Decay of the kolmogorov n-width for wave problems. *Appl. Math. Letters*, 96, 216 – 222.

Haasdonk, B. (2017). Reduced Basis Methods for Parametrized PDEs — A Tutorial. In P. Benner, A. Cohen, M. Ohlberger, and K. Willcox (eds.), *Model Reduction and Approximation*, chapter 2, 65–136. SIAM, Philadelphia.

Ohlberger, M. and Rave, S. (2016). Reduced basis methods: Success, limitations and future challenges. *Proceedings of the Conference Algoritmy*, 1–12.

Pinkus, A. (2015). *Ridge Functions*. Cambridge University Press.

Stacked Models for Earthworks Logistics: A field-tested Optimization and Simulation Workflow

Stefan Brunner * **Gerhard Höfinger** **

* *SID, STRABAG AG, 1220 Vienna, Austria (e-mail: stefan.brunner@strabag.com)*
** *SID, STRABAG AG, 1220 Vienna, Austria (e-mail: gerhard.hoefinger@strabag.com)*

1. INTRODUCTION

Earthworks in infrastructure construction are dominated by extensive logistics operations. They have to be planned thoroughly, even in a very early phase of a project. Herein, the authors report the practical use of optimisation models and simulation to achieve an optimal allocation of transports.

Despite its commonly acknowledged usefulness in other industries, simulation of logistics systems is not yet commonplace in the construction industry. Clients usually ask for a variety of documents and calculations, ensuring a timely and highly qualitative execution of the owed work. These include construction schedules and site layouts, but hardly ever simulation models (with one of the rare exceptions being Deutsche Bahn in the project Rastatt tunnel in Germany). Occasional collaborations of academic institutions with companies in the field look promising yet still have to prove usefulness in a large scale of application (see Gschwendtner (2021) for a recent example). In general, the application of simulation appeared to be restricted to simplified cases or very special processes (Höfinger and Brunner (2016)). An interesting example of simulation is a marketing tool by an equipment vendor, allowing to select the transportation equipment suited best for the given task (Volvo Construction Equipment (2021))

Earthworks, the field of application considered herein, is typically a part of road construction, and includes all activites necessary to create a plane surface carrying the asphalt or concrete top layer of a road. Especially for green-field projects, activities are dominated by moving massive amounts of earth materials within the project area.

A logistics concept is understood here as a list of transports necessary to complete the project. A transport is defined by start and end point, transport mean, material quantity and type, and time of execution. A good or even optimal logistics concept considers re-use of materials within the site, storing and production capacities, availability and performance of machinery, road connections including temporary roads, temporal constraints, etc.

Even before actual operation, a logistics concept is used to derive schedules, estimate costs, and procure logistics ressources. Especially when working in the tender phase of a project, frequent updates to input data are made, and scenarios have to be compared. This calls for an efficient tool, allowing the creator of the concept to finish optimization cycles in the range of a few hours, which means a practically useful optimisation model has to be executed in several minutes (considering manual updates of input data, and necessary pre- and post-processing).

2. MODELS FOR THE EARTHWORKS PROCESS

With the given challenges, a workflow with three steps was designed, which can provide insights after every step. The first two steps consist of solving a linear program (LP) , while the third step is the execution of a generic simulation model, using the result of the LP model.

2.1 LP model

A detailed description of the linear programs used as first and second step is given in Dell'Amico et al. (2019). These models were first applied in 2012 for the highway project Pedemontana Lombarda in Italy (see Dell'Amico et al. (2016)) and since then used regularly for major projects tendered or executed by STRABAG AG all over the world. It has to be noted, that in pratical use cases, optimality is defined by a minimal transport effort, measured in $m^3 \cdot km$. The total flow of material is determined as a result of the first model, with the other models splitting the material flow into transports and allocating ressources to the transports, respectively. Thus, the actual optimization part is completed after the first step, allowing to stop the process of optimization, if results are undesirable or non-consistent inputs were given (infeasible model). In addition, a mathematically optimal solution is guaranteed, because LP solvers find global optima and the transport effort is not changed in the second and third step.

With demand for material (filling process, e.g. construction a road dam), supply of material (cutting process, e.g. preparing a trench) and a connection road network, in principle, a simple minimum-cost flow problem has to be solved. Adding construction related constraints (e.g. limit supply by excavating equipment), and a time dimension, the problem becomes increasingly complex. In contrast to warehouse location problems, demand and supply locations tend to be located along longitudinal axes (string of pearls), and typically a main axis dominates the topology

of the network. This special structure is used to split the problem into two models. In the first phase, an optimal material flow is determined, that uniquely defines for each network edge and time step which material is transported there, where material is procured and where it is disposed. Only relations between neighbouring nodes in the network are considered, with material allowed to pass through nodes. This reduces the number of relations, and with the given structure they are in a nearly linear relation with the number of nodes instead of a quadratic one. In the second phase, transports over the network are combined in a way that the solution from the first phase is represented as transport relations, i.e. transports from a source location (e.g. a cutting location or a quarry) to a sink location (e.g. a filling location, disposal site, temporary storage) The two-phase LP model therefore creates transport relations which are connected with an arbitrary small or big quantity, which later has to be translated to single hauls by actual trucks. It provides added value, as it already solves, how demands can be fulfilled, which parts of the road network will be (over-)used, which procurement locations will be used (an important information for negotiating contracts) and what the overall haul effort, expressed in $m^3 \cdot km$ will be.

2.2 Simulation model

An important limiting factor in construction performance is the availability of haulage equipment that is often not provided by the main construction contractor but by subcontractors. Therefore, it is of importance to have knowledge about the haulage equipment at an early stage to be able to make appropriate contracts. In the LP model described above, no statements are made on individual trucks, loading and placing equipment. The intention of the simulation model is to close this information gap. The simulation model is implemented as an agent-based model in AnyLogic, using a straight-forward approach with machinery represented as agents on a network with exactly the same nodes and relations as in the LP model. The target performance of the construction equipment in combination with the distance to the optimal source/sink for each working location and assumed loading capacities and driving speeds of the haulage equipment is sufficient to trivially calculate round times and thus required truck numbers for each task. These calculations are automatically done by the simulation model.

Additionally, a schematic visualization of the process is generated as a by-product. This can be useful as a means of communication towards the client. For this standardized simulation, a 3D-representation is omitted, as 3D-data of the project is not always available, even less 3D-models for all the surrounding area relevant for logistics (quarries and dump sites typically are in radius up to 50km around a construction site).

The filling and cutting tasks are located on certain nodes of this network. The quantities for each location are stored within a so-called workstation agent. Once all workstations have reached the "done" state (i.e.: all quantities have reached 0), the simulation is finished. The actual performance of the machine is depending on the availability of a sufficient number of trucks - material can only be cut when there is a truck to load it on and only material that has already been delivered to the machine can be filled.

The present simulation model can be used on any project where an optimization with the LP model is done. The project specific need for adaption is limited to adjusting the background map and start date of the simulation model to the actual project. Unfortunately, this cannot yet be automatized due to technical reasons. Apart from that the simulation model is entirely dynamically built on data that is generated during the LP optimization process anyway. There is an analysis view within the simulation model, where real time data is visualized, e.g. number of trucks used, transport distances, processed quantities etc.

3. CONCLUSION

With our three-model approach, we are in a position to quickly evaluate major earthworks projects with respect to minimal (optimal) transport effort, usage of ressources, optimal locations for procurement etc. The workhorse of the approach is the first LP model, where the flow of material over the network is determined. Nevertheless, the following stages are necessary to create the required input for cost estimators, project technicians and procurement. The graphical capabilities of the simulation model can be used in an educational way to explain our method to teams who never worked with us (as opposed to the LP model, where only macro code can be shown). Models of this kind need comprehensive input information, available only in projects with well-designed processes, especially in the case of time-critical tender phases. The introduction of BIM is therefore a facilitator for simulation as well as many other downstream processes. With BIM becoming a standard, more and more often required by clients, together with our model, the way is pathed for a standard application of simulation in major projects in infrastructure construction.

REFERENCES

Dell'Amico, M., Fuellerer, G., Hoefinger, G., Iori, M., and Novellani, S. (2016). A decision support system for highway construction: The autostrada pedemontana lombarda. *Interfaces*, 46. doi:10.1287/inte.2016.0847.

Dell'Amico, M., Fuellerer, G., Hoefinger, G., and Novellani, S. (2019). *A View of Operations Research Applications in Italy*, chapter A Decision Support System for Earthwork Activities in Construction Logistics, 167–178. Springer International Publishing.

Gschwendtner, C. (2021). *Development and Analysis of Process Simulation in Building Construction*. Master's thesis, Technical University Munich.

Höfinger, G. and Brunner, S. (2016). Network-based Simulation in Water Construction – a Flexible Tool for Equipment Selection. *Simulation Notes Europe*, 26(1), 55–58. doi:10.11128/sne.26.sn.10329.

Volvo Construction Equipment (2021). URL `https://www.volvoce.com/deutschland/de-de/services/volvo-services/ fuel-efficiency-services/volvo-site-simulation/`.

Planar Bipedal Walking Robot with Differentially Flat Dynamics

Akshay Kumar * **Vivek Sangwan** **

* *Indian Institute of Technology Bombay, Mumbai,India (e-mail: akshayk1741@iitb.ac.in).*
** *Indian Institute of Technology Bombay, Mumbai,India (e-mail: vivek.sangwan@iitb.ac.in).*

Abstract: Under-actuated bipedal walking robots are an active area of research. Previously, Sangwan and Agrawal (2007) have presented a mechanical design methodology for under-actuated bipeds based on placing center-of-mass of the legs at the hip joint that renders dynamics of a class of planar bipedal walking robots differentially flat. Once this class of under-actuated bipeds is proven to be differentially flat, one can analytically write down a feasible parametrized family of trajectories. Proving flatness results for an n-dof bipedal robot does not guarantee the existence of reasonable walking solutions satisfying the motion constraints. This work demonstrates planning and tracking control of feasible walking trajectories satisfying motion constraints for a higher degree-of-freedom four-link biped with a knee joint in each leg.

Keywords: Robotics, Algebraic methods, Optimization, Under-actuated Biped, Differential flatness.

1. INTRODUCTION

In case of walking robots, under-actuation makes the robot motion more human like since human walking does have phases of under-actuation McGeer (1990); Collins et al. (2001). One approach of planning and controlling trajectories is based on mechanically redesigning the biped, with center of mass at the hip for each leg, such that the continuous component of its overall hybrid dynamics becomes differentially flat Sangwan and Agrawal (2007). Once this class of under-actuated bipeds is proven to be differentially flat, a family of feasible parameterized trajectories can be written down analytically and then can be numerically optimized to satisfy additional motion constraints. Although the previous flatness result was proven for an n-dof bipedal robot with potentially multiple joints in each leg but it was numerically demonstrated with a simple biped with only two links without a knee joint. For bipeds with more joints, it does not directly imply that reasonable walking solutions will always exist because differential flatness only guarantees existence of dynamically feasible periodic trajectories but not necessarily trajectories feasible w.r.t additional motion constraints such as ground clearance, positive ground normal reaction etc. The key contribution in this note is, planning and tracking control of feasible walking trajectories based on the property of differential flatness combined with numerical optimization for a higher degree-of-freedom (DoF) biped having four links with a knee joint in each leg. A full-state feedback controller based on the differentially flat structure of the dynamics is also shown to track the planned trajectories in presence of initial errors.

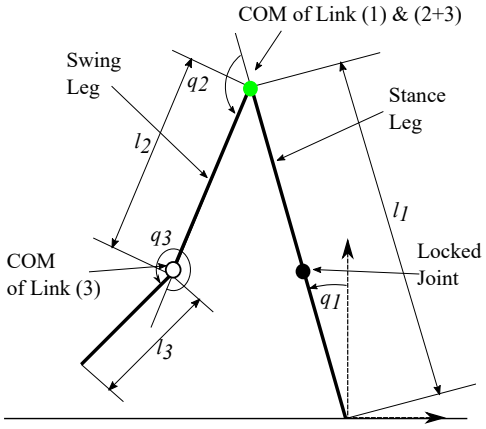

Fig. 1. A four-link planar bipedal robot with a knee joint in each leg.

2. FOUR-LINK BIPED

In this section, the flatness based design methodology is applied to a more complicated biped with knees shown in Fig. 1. The knee and hip joints are actuated whereas the ankle joints are unactuated. Besides actuators, knee joints also have a solenoid actuated latch that is used to lock these joints. At any given instant one of the legs (stance leg) is in contact with ground and the other leg (swing leg) is swinging freely in air. Although the biped has four joints but the knee joint of the stance leg is always locked and hence at any given instant the biped has a maximum of three degrees-of-freedom. The swing and stance legs interchange roles instantaneously when the swing leg hits the ground at ground impact as shown in 2. Following the design methodology presented in Sangwan and Agrawal

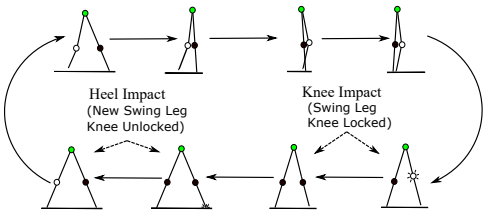

Fig. 2. A four-link planar bipedal robot with a knee joint in each leg.

(2007), COM of both legs is at the hip joint. This COM placement is achieved by first placing the COM of shank segment at the knee joint followed by the placement of combined COM of shank and thigh at the hip joint by means of counter-masses. A complete dynamic model of the biped consists of four separate models (i) 3-DoF phase (ii) 2-DoF phase (iii) the impact model for heel impact and (iv) impact model for knee impact. All of these are derived using energy method.

3. DIFFERENTIAL FLATNESS BASED TRAJECTORY PLANNING

The dynamics for both continuous phases of this system is such that flat outputs with total relative degree equal to the number of states exist. There also exists difeomorphism between state space and flat output space. Outputs for 3-DoF phase are as follows

$$y_1 = q_1 + \bar{m}_{22}q_2 + \bar{m}_{33}q_3, \qquad y_2 = \bar{m}_{33}(q_1 + q_2 + q_3). \quad (1)$$

Parameters $\bar{m}_{22}$ and $\bar{m}_{22}$ are non-dimensionalized inertia parameters appearing in the dynamic model. y_1 with relative degree four and y_2 with relative degree two makes the total relative degree of outputs equal to six i.e. equal to number of states. Similarly, for the 2-DoF phase, flat output is given by:

$$y_1 = q_1 + \bar{m}_{22}q_2, \quad (2)$$

with relative degree four. To satisfy the dynamic feasibility and periodicity requirements, flatness framework is used to generate a family of cyclic dynamically feasible trajectories having a set of free parameters. Then an SQP based optimization routine is used to modulate those free parameters such that the motion constraints mentioned previously are also satisfied. The planning has to be done for two distinct phases the 3-DOF phase from heel impact to knee impact and the 2-DOF phase from knee impact to next heel impact as shown in Fig.2. Critical instances like pre-heel and knee impact states, and post-heel and knee impact states, were made the anchor points during the numerical optimization. Then output's collocation function of time were chosen such that one part of the collocation function is used to satisfy the anchor states and other is used in modulating the trajectories to satisfy the constraints.

4. RESULTS AND CONCLUSIONS

Feasible walking trajectories shown in Fig. 3 are obtained using SQP based numerical optimization over a family of dynamically feasible periodic trajectories, with motion constraints such as positive ground normal reaction, positive heal height. Solid blue lines in this figure are planned

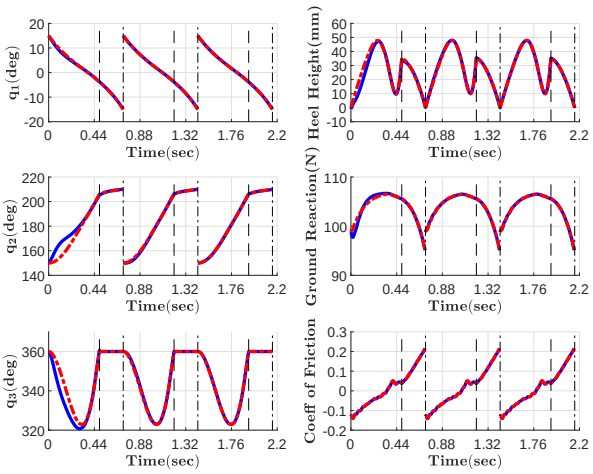

Fig. 3. [Left] Joint angle trajectories, [Right] various constraints imposed during optimization, (dash line - planned trajectory, solid line - actual trajectory).

trajectories and dashed lines are trajectories of the system with the full state feedback controller having some initial errors. Clearly, trajectories converge to the planned even in presence of initial errors and joint angles stay within reasonable range. Also Heel height and normal reaction stay positive and coefficient of friction is within acceptable range.

In conclusion, this work demonstrated construction of feasible walking trajectories based on the property of differential flatness for a biped with higher degrees-of-freedom with a knee joint in each leg. These trajectories were constructed using numerical optimization over a family of dynamically feasible trajectories.The optimizer only had to satisfy the motion constraints such as positive ground normal reaction and ground clearance due to guaranteed periodicity because of flatness and collocation function. Simulations with a linear full-state feedback controller is also shown to eliminate initial errors in the trajectories.

REFERENCES

Collins, S.H., Wisse, M., and Ruina, A. (2001). A three-dimensional passive dynamic walking robot with two legs and knees. *International Journal of Robotics Research*, 20(7), 607–615.

McGeer, T. (1990). Passive dynamic walking. *The International Journal of Robotics Research*, 9(2), 62–82.

Sangwan, V. and Agrawal, S.K. (2007). Differentially flat design of bipeds ensuring limit-cycles. In *Proceedings IEEE International Conference on Robotics and Automation (ICRA'07)*. Rome, Italy.

Effect of left atrial appendage occlusion for patients with atrial fibrillation during mechanical circulatory support: in-silico study

M. Ghodrati[1,2], T. Schlöglhofer[1,2,3], C. Gross[3], D. Zimpfer[3], D. Beitzke, F. Zonta[5], F. Moscato[1,2], H. Schima[1,2,3], P. Aigner[1,2]

[1]*Center for Medical Physics and Biomedical Engineering, Medical University of Vienna, Austria,*

[2]*Ludwig Boltzmann Institute for Cardiovascular Research, Vienna, Austria,*

[3]*Department for Cardiac Surgery, Medical University of Vienna, Austria,*

[4]*Department of Biomedical Imaging and Image guided Therapy, Medical University of Vienna, Austria,*

[5]*Institute of Fluid Dynamics and Heat Transfer, Technical University of Vienna, Austria,*

1. INTRODUCTION

Atrial fibrillation (AF) is a common comorbidity in left ventricular assist device (LVAD) patients and has been identified as a risk factor for stroke. (Deshmukh *et al.*, 2018). Clinical studies in heart failure patients have shown reduced thromboembolic risk after occlusion of the left atrial appendage (LAA) (Deshmukh *et al.*, 2019). However potential benefits in LVAD patients are not yet fully understood. This study aims to investigate the effect of left atrial appendage occlusion (LAAO) on thrombosis-related parameters using LVAD patient-specific hemodynamic simulations.

2. MATERIAL AND METHOD

2.1 Patient Model

Left ventricular (LV) and left atrial (LA) models of an LVAD patient were obtained from computed tomography images using Mimics Research 20.0 and 3-matics Research 13.0 (Materialise, Belgium NV) (Fig. 1).

2.2 Boundary Conditions

Hemodynamics for LVAD patient were generated by lumped parameter model for AF patients and was applied for two CFD simulations with passive atrial contraction and active ventricular contraction for 8 cardiac cycles.

The Navier-Stokes equations were solved with a finite volume approach and an Arbitrary Lagrangian-Eulerian formulation in the CFD solver (FLUENT, Ansys 19.3, Pennsylvania, USA). Blood flow was modelled using the Laminar method and considered to be a Newtonian fluid with a density of 1060 kg/m3 and a dynamic viscosity of 0.0035 Pa s. The velocity and pressure boundary conditions were imposed at the inlet and outlet.

2.3 Flow Parameter Evaluation

Stasis volume (SV) was defined to highlight regions with a time-averaged velocity of less than 10 mm/s (Rayz *et al.*, 2008).

Atrial and ventricular blood washout was quantified using a virtual ink technique (Rayz *et al.*, 2010). The virtual ink was transported by the resultant flow. All fluid domains were initialized with an ink concentration of 0, with the value of 1 at inlets, representing a flow of fresh blood. The rate of LA washout was calculated by the percentage of old blood in the LA, normalized by the LA volume.

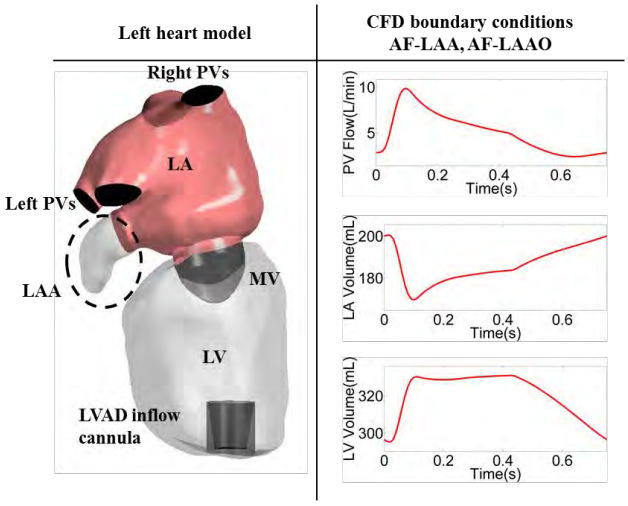

Fig. 1. Patient-specific left heart model (red geometry shows the atrium with LAAO) and CFD boundary conditions; PV: pulmonary vein, LA: left atrium, LV: left ventricle, MV: mitral valve, LAA: left atrial appendage, LAAO: left atrial appendage occlusion, AF: atrial fibrillation, LVAD: left ventricular assist device.

3. RESULTS

Occlusion of the appendage increased the overall average velocity within the LA, while comparable values were observed within the LV pre and post-LAAO. A recirculation zone with low blood velocity was observed within the LAA (Figure 2 A) and therefore after occlusion average blood velocity increased by +5%.

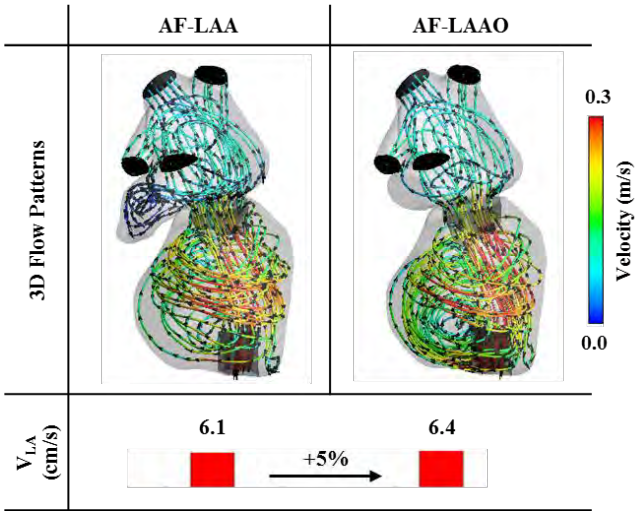

Fig. 2. Time-averaged flow streamline colored by mean velocity (V).

Appendage occlusion results in significant reduction of the stagnation volume which mainly was observed within the LAA. The reduction of 64% in stasis volume (from 6.5 to 2.3 cm^3) was observed post-LAAO.

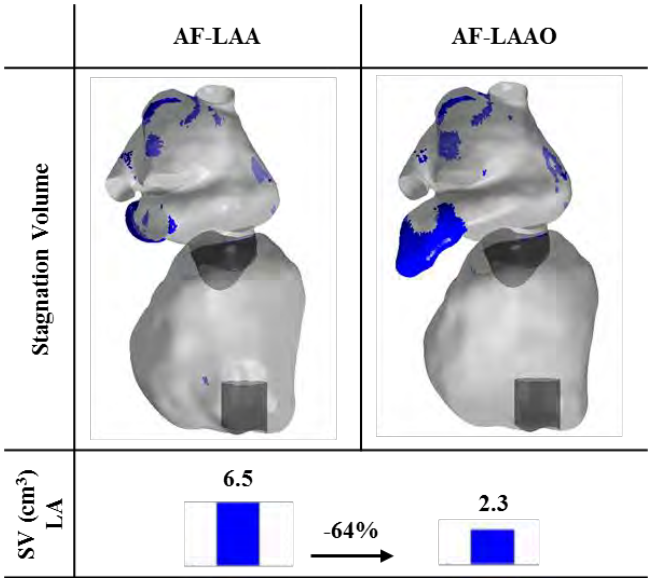

Fig. 3. Time-averaged stagnation volume (SV).

Occlusion of the appendage significantly accelerates the replacement of the old blood with the new blood within the LA. After 3 cardiac cycles the entire old blood within the LA was replaced with new blood for LAAO simulation (Fig. A and B), while without occlusion of the appendage 4.3% of the old blood remained in the atrial appendage for more than 8 cardiac cycles.

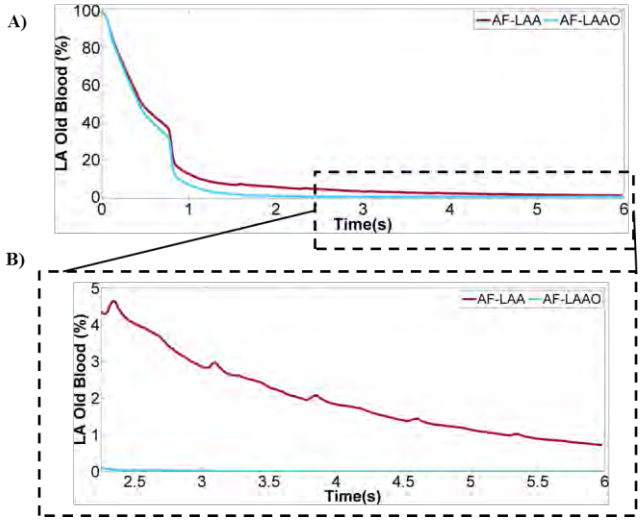

Fig. 4. Atrial blood washout A) over 8 cardiac cycles, and B) after third cardiac cycle

4. CONCLUSIONS

The results of this study showed a significant stasis volume within the left atrial appendage. These regions are known as potential sources for thrombus formation. Therefore, to reduce the stasis zones for LVAD patients with atrial fibrillation, occlusion of the appendage could be considered.

REFERENCES

Deshmukh, A. *et al.* (2018) 'Incidence and Outcomes of Postoperative Atrial Fibrillation After Left Ventricular Assist Device', *ASAIO Journal*, 64(5), pp. 581–585. doi:10.1097/MAT.0000000000000763.

Deshmukh, A. *et al.* (2019) 'Left Atrial Appendage Occlusion With Left Ventricular Assist Device Decreases Thromboembolic Events', *The Annals of Thoracic Surgery*, 107(4), pp. 1181–1186. doi:10.1016/j.athoracsur.2018.09.004.

Rayz, V.L. *et al.* (2008) 'Numerical Modeling of the Flow in Intracranial Aneurysms: Prediction of Regions Prone to Thrombus Formation', *Annals of Biomedical Engineering*, 36(11), pp. 1793–1804. doi:10.1007/s10439-008-9561-5.

Rayz, V.L. *et al.* (2010) 'Flow Residence Time and Regions of Intraluminal Thrombus Deposition in Intracranial Aneurysms', *Annals of Biomedical Engineering*, 38(10), pp. 3058–3069. doi:10.1007/s10439-010-0065-8.

Stabilization of the wave equation in port-Hamiltonian modelling ⋆

Birgit Jacob * **Nathanael Skrepek** **

* *Department of Mathematics and Science, IMACM, University of Wuppertal, Germany, (e-mail: bjacob@uni-wuppertal.de)*
** *Department of Mathematics and Science, IMACM, University of Wuppertal, Germany, (e-mail: skrepek@uni-wuppertal.de)*

Abstract: We investigate the stability of the wave equation with spatial dependent coefficients on a bounded multidimensional domain. The system is stabilized via a scattering passive feedback law. We formulate the wave equation in a port-Hamiltonian fashion and show that the system is semi-uniformly stable.

1. INTRODUCTION

In this paper we investigate the boundary control system

$$\begin{aligned} u(t,\zeta) &= \frac{\partial w}{\partial T\nu}(t,\zeta), && \zeta\in\Gamma_1,\\ \frac{\partial^2 w}{\partial t^2}(t,\zeta) &= \frac{1}{\rho(\zeta)}\operatorname{div}\left(T(\zeta)\nabla w(t,\zeta)\right), && \zeta\in\Omega,\\ w(t,\zeta) &= h(\zeta), && \zeta\in\Gamma_0,\\ w(0,\zeta) &= w_0(\zeta), && \zeta\in\Omega,\\ \frac{\partial w}{\partial t}(0,\zeta) &= w_1(\zeta), && \zeta\in\Omega,\\ y(t,\zeta) &= \frac{\partial w}{\partial t}(t,\zeta), && \zeta\in\Gamma_1, \end{aligned} \tag{1a}$$

with feedback law

$$u(t,\zeta) = -k(\zeta)y(t,\zeta), \qquad \zeta\in\Gamma_1, \tag{1b}$$

where $t\geq 0$, $\Omega\subseteq\mathbb{R}^n$ is a bounded domain with Lipschitz boundary $\partial\Omega=\overline{\Gamma_0}\cup\overline{\Gamma_1}$ with $\Gamma_0\cap\Gamma_1=\emptyset$, Γ_0 and Γ_1 are open in the relative topology of $\partial\Omega$ and the boundaries of Γ_0 and Γ_1 have surface measure zero. Furthermore, $w(\zeta,t)$ is the deflection at point $\zeta\in\Omega$ and $t\geq 0$, and profile h is given on Γ_0, where the wave is fixed. Let Young's elasticity modulus $T\colon\Omega\to\mathbb{C}^{n\times n}$ be a Lipschitz continuous matrix-valued function such that $T(\zeta)$ is a positive and invertible matrix (a.e.) and $T(\cdot)^{-1}\in\mathsf{L}^\infty(\Omega)^{n\times n}$. The vector ν denotes the outward normal at the boundary and $\frac{\partial}{\partial T\nu}w(t,\zeta)=T\nu\cdot\nabla w(t,\zeta)=\nu\cdot T\nabla w(t,\zeta)$ is the conormal derivative. The Lipschitz continuous mass density $\rho\colon\Omega\to\mathbb{R}_+$ satisfies $\rho,\frac{1}{\rho}\in\mathsf{L}^\infty(\Omega)$. Further, $k\colon\Gamma_1\to\mathbb{R}$ is a measurable positive and bounded function such that also its pointwise inverse is bounded, i.e. $k,\frac{1}{k}\in\mathsf{L}^\infty(\Gamma_1)$. Finally, w_0 and w_1 are the initial conditions.

Strong stability of (1) has been investigated in Quinn and Russell (1977). In Humaloja et al. (2019) this system also appears in port-Hamiltonian formulation, but with constant T and ρ and C^2 boundary. Under these restrictions, they show that this system is exponentially stable. However, semi-uniform stability, a notion which is stronger than strong stability and weaker than exponential stability, of (1) with spatial dependent functions ρ and T on quite general domains has not been studied so far.

We aim to show semi-uniform stability of (1) using a port-Hamiltonian formulation. Semi-uniform stability implies strong stability, and thus we extend the results obtained in Quinn and Russell (1977). To prove our main result we use the fact that semi-uniform stability is satisfied if the port-Hamiltonian operator generates a contraction semigroup and possesses no spectrum in the closed right half plane. Port-Hamiltonian systems encode the underlying physical principles such as conservation laws directly into the structure of the system structure. For finite-dimensional systems there is by now a well-established theory Maschke and van der Schaft (1992); Duindam et al. (2009). The port-Hamiltonian approach has been further extended to the infinite-dimensional situation, see e.g. Villegas (2007); Jacob and Zwart (2012); Kurula and Zwart (2015). In Kurula and Zwart (2015) the authors showed that the port-Hamiltonian formulation of the wave equation (1) possess unique mild and classical solutions.

2. PORT-HAMILTONIAN FORMULATION OF THE SYSTEM

We split the system (1) into a time independent system

$$\begin{aligned} \operatorname{div} T(\zeta)\nabla w_{\mathrm{e}}(\zeta) &= 0, && \zeta\in\Omega,\\ w_{\mathrm{e}}(\zeta) &= h(\zeta), && \zeta\in\Gamma_0,\\ \frac{\partial w_{\mathrm{e}}}{\partial T\nu}(\zeta) &= 0, && \zeta\in\Gamma_1, \end{aligned} \tag{2}$$

and a dynamical system

$$\begin{aligned} \frac{\partial^2 w_{\mathrm{d}}}{\partial t^2}(t,\zeta) &= \frac{1}{\rho(\zeta)}\operatorname{div}(T(\zeta)\nabla w_{\mathrm{d}}(t,\zeta)), && \zeta\in\Omega,\\ w_{\mathrm{d}}(t,\zeta) &= 0, && \zeta\in\Gamma_0,\\ w_{\mathrm{d}}(0,\zeta) &= w_0(\zeta)-w_{\mathrm{e}}(\zeta), && \zeta\in\Omega,\\ \frac{\partial w_{\mathrm{d}}}{\partial t}(0,\zeta) &= w_1(\zeta), && \zeta\in\Omega,\\ \frac{\partial w_{\mathrm{d}}}{\partial T\nu}(t,\zeta) &= -k\frac{\partial w_{\mathrm{d}}}{\partial t}(t,\zeta), && \zeta\in\Gamma_1 \end{aligned} \tag{3}$$

⋆ The authors are working in the ITN network ConFlex. This project is funded by the European Union's Horizon 2020 research and innovation programme under the Marie Sklodowska-Curie grant agreement No 765579.

where $t \geq 0$. The original system is solved by $w(t,\zeta) = w_{\mathrm{e}}(t,\zeta)+w_{\mathrm{d}}(\zeta)$. As in Kurula and Zwart (2015) the system in (3) can be described in a port-Hamiltonian manner by choosing the state $x(t,\zeta) = \begin{bmatrix} \rho(\zeta)\frac{\partial}{\partial t} w_{\mathrm{d}}(t,\zeta) \\ \nabla w_{\mathrm{d}}(t,\zeta) \end{bmatrix}$. By using the convention

$$\begin{bmatrix} x_1(t) \\ x_2(t) \end{bmatrix} := x(t) := x(t,\cdot)$$

we can write the system (3) as

$$\begin{aligned} \frac{\mathrm{d}}{\mathrm{d}t} x(t) &= \begin{bmatrix} 0 & \operatorname{div} \\ \nabla & 0 \end{bmatrix} \begin{bmatrix} \frac{1}{\rho} & 0 \\ 0 & T \end{bmatrix} x(t), \\ x(0) &= \begin{bmatrix} \rho w_1 \\ \nabla(w_0 - w_{\mathrm{e}}) \end{bmatrix}, \\ \gamma_0 \tfrac{1}{\rho} x_1(t)\big|_{\Gamma_0} &= 0, \\ \gamma_\nu T x_2(t)\big|_{\Gamma_1} &= -k\gamma_0 \tfrac{1}{\rho} x_1(t)\big|_{\Gamma_1} \end{aligned}$$

By γ_0 and γ_ν we denote the boundary trace (extension of $f \mapsto f\big|_{\partial\Omega}$) and the normal trace (extension of $f \mapsto \nu \cdot f\big|_{\partial\Omega}$), respectively. Kurula and Zwart (2015) choose the state space $\mathsf{L}^2(\Omega)^{n+1}$ equipped with the energy inner product

$$\langle x, y\rangle := \left\langle x, \begin{bmatrix} \frac{1}{\rho} & 0 \\ 0 & T \end{bmatrix} y \right\rangle_{\mathsf{L}^2(\Omega)^{n+1}},$$

which is equivalent to the standard inner product of $\mathsf{L}^2(\Omega)^{n+1}$ thanks to the assumptions on T and ρ. They then show the existence of mild and classical solution via semigroup methods. For well-posedness this is a suitable state space, but when it comes to stability this state space is too large as it does not reflect the fact that the second component of the state variable x_2 is of the form ∇v, for some function v in the Sobolev space $\mathsf{H}^1_{\Gamma_0}(\Omega)$. Thus, we choose the state space $\mathcal{X}_{\mathcal{H}}$ as $\mathsf{L}^2(\Omega) \times \nabla\mathsf{H}^1_{\Gamma_0}(\Omega)$, instead of $\mathsf{L}^2(\Omega)^{n+1}$. Note that $\nabla\mathsf{H}^1_{\Gamma_0}(\Omega)$ is closed in $\mathsf{L}^2(\Omega)^n$ by Poincaré's inequality. Hence, $\mathcal{X}_{\mathcal{H}}$ is also a Hilbert space with the L^2-inner product. Nevertheless, we also use the equivalent energy inner product on $\mathcal{X}_{\mathcal{H}}$, that is

$$\langle x, y\rangle_{\mathcal{X}_{\mathcal{H}}} := \left\langle x, \begin{bmatrix} \frac{1}{\rho} & 0 \\ 0 & T \end{bmatrix} y \right\rangle_{\mathsf{L}^2(\Omega)^{n+1}}.$$

Furthermore, we define

$$\begin{aligned} \mathfrak{A} &:= \begin{bmatrix} 0 & \operatorname{div} \\ \nabla & 0 \end{bmatrix} \begin{bmatrix} \frac{1}{\rho} & 0 \\ 0 & T \end{bmatrix} \\ \text{with} \quad \mathcal{D}(\mathfrak{A}) &:= \begin{bmatrix} \frac{1}{\rho} & 0 \\ 0 & T \end{bmatrix}^{-1} \left(\mathsf{H}^1_{\Gamma_0}(\Omega) \times \mathsf{H}(\operatorname{div},\Omega)\right) \end{aligned}$$

as densely defined operator on $\mathsf{L}^2(\Omega)^{n+1}$. Note that we have already packed the boundary condition $\gamma_0 \frac{1}{\rho} x_1 = 0$ on Γ_0 into the domain of $\mathfrak{A}$. Moreover, by construction $\operatorname{ran}\mathfrak{A} = \mathcal{X}_{\mathcal{H}}$. Taking the state space and the remaining boundary conditions (feedback) into account gives

$$\begin{aligned} A &:= \mathfrak{A}\big|_{\mathcal{D}(A)}, \qquad \text{where} \\ \mathcal{D}(A) &:= \left\{ x \in \mathcal{D}(\mathfrak{A}) \;\middle|\; \gamma_\nu T x_2 = -k\gamma_0 \tfrac{1}{\rho} x_1 \text{ on } \Gamma_1 \right\} \cap \mathcal{X}_{\mathcal{H}} \end{aligned} \tag{4}$$

as an operator on $\mathcal{X}_{\mathcal{H}}$.

Proposition 1. The operator A given by (4) is a generator of contraction semigroup.

3. STABILITY RESULTS

Definition 2. We say a strongly continuous semigroup $(T(t))_{t\geq 0}$ on a Hilbert space X is *strongly stable*, if for every $x \in X$ we have $\lim_{t\to\infty}\|T(t)x\|_X = 0$.

We say a continuous semigroup $(T(t))_{t\geq 0}$ on a Hilbert space X is *semi-uniformly stable*, if there exists a continuous monotone decreasing function $f\colon [0,\infty) \to [0,\infty)$ with $\lim_{t\to\infty} f(t) = 0$ and

$$\|T(t)x\|_X \leq f(t)\|x\|_{\mathcal{D}(A)}, \qquad x \in \mathcal{D}(A).$$

Note that semi-uniform stability is also defined by $\|T(t)A^{-1}\| \to 0$ or $\|T(t)(1+A)^{-k}\| \to 0$ as in Batty and Duyckaerts (2008). However, this is equivalent to our definition. Semi-uniform stability implies strong stability.

We denote by A the operator given by (4) which is associated to the port-Hamiltonian formulation of (1). Our main result is the following theorem.

Theorem 3. The semigroup generated by A is semi-uniformly stable.

For the original system (1) strong stability of A translates to: There is a $w_{\mathrm{e}} \in \mathsf{H}^1(\Omega)$ such that for every initial values $w_0 \in \mathsf{H}^1(\Omega)$, $w_1 \in \mathsf{L}^2(\Omega)$ the solution w satisfies

$$\lim_{t\to\infty} \|w(t,\cdot) - w_{\mathrm{e}}(\cdot)\|_{\mathsf{H}^1(\Omega)} = 0.$$

4. CONCLUSION

In this paper we showed semi-uniform stability of the multidimensional wave equation equipped with a scattering passive feedback law.

REFERENCES

Batty, C.J.K. and Duyckaerts, T. (2008). Non-uniform stability for bounded semi-groups on Banach spaces. *J. Evol. Equ.*, 8(4), 765–780.

Duindam, V., Macchelli, A., Stramigioli, S., and Bruyninckx, H. (eds.) (2009). *Modeling and Control of Complex Physical Systems*. Springer, Germany.

Humaloja, J.P., Kurula, M., and Paunonen, L. (2019). Approximate robust output regulation of boundary control systems. *IEEE Trans. Automat. Control*, 64(6), 2210–2223. doi:10.1109/tac.2018.2884676.

Jacob, B. and Zwart, H. (2012). *Linear Port-Hamiltonian Systems on Infinite-dimensional Spaces*. Number 223 in Operator Theory: Advances and Applications. Springer, Germany.

Kurula, M. and Zwart, H. (2015). Linear wave systems on n-D spatial domains. *Internat. J. Control*, 88(5), 1063–1077. doi:10.1080/00207179.2014.993337.

Maschke, B. and van der Schaft, A. (1992). Port-controlled Hamiltonian systems: Modelling origins and system theoretic properties. *IFAC Proceedings Volumes*, 25(13), 359–365.

Quinn, J.P. and Russell, D.L. (1977). Asymptotic stability and energy decay rates for solutions of hyperbolic equations with boundary damping. *Proc. Roy. Soc. Edinburgh Sect. A*, 77(1-2), 97–127. doi:10.1017/S0308210500018072.

Villegas, J. (2007). *A Port-Hamiltonian Approach to Distributed Parameter Systems*. Ph.D. thesis, University of Twente, Netherlands.

Boundary control of infinite dimensional irreversible port-Hamiltonian systems: the heat equation.

Yann Le Gorrec * **Luis A. Mora** * **Hector Ramirez** **

* *FEMTO-ST Institute, AS2M department ,Univ. Bourgogne Franche-Comté, Univ. de Franche-Comté/ENSMM, 24 rue Savary, F-25000 Besançon, France (e-mail: yann.legorrec@femto-st.fr)*
** *AC3E, Universidad Técnica Federico Santa María, Av. España 1680, Valparaiso, Chile (e-mail: hector.ramireze@usm.cl)*

1. INTRODUCTION

In this discussion paper we consider the (boundary) control of irreversible thermodynamic systems using the irreversible port Hamiltonian framework. We first show how infinite dimensional port-Hamiltonian formulations initially derived for reversible systems (Le Gorrec et al., 2005) have been extended to the modelling of irreversible thermodynamic systems controlled at the boundaries of their spatial domains (Ramírez et al., 2022). In a second instance we show, on the heat equation example, how to adapt the well known control by interconnection and damping injection method to the boundary control of this particular class of systems.

2. IRREVERSIBLE PORT HAMILTONIAN SYSTEMS

Thermodynamic systems are systems for which the thermal domain plays a central role and the energy goes from one physical domain to the thermal domain in an irreversible way. It is the case for example of chemical reactors, diffusion systems, smart materials, and all temperature dependent systems. This class of irreversible systems does not fit in the port Hamiltonian framework. In order to overcome this issue, and nevertheless exploit as far as possible the physical properties of the system, many alternative approaches such as contact formulations, pseudo port Hamiltonian formulations and GENERICs (Grmela and Öttinger, 1997) have been proposed in the litterature. Among them the irreversible port Hamiltonian (IPH) formulations (Ramírez et al., 2013) have shown to be very useful for analysis and control design (Ramírez et al., 2016) in the finite dimensional case. These formulations have been recently extended to the modelling of infinite dimensional irreversible thermodynamic systems controlled at the boundaries of their spatial domains, leading to the following definition (Ramírez et al., 2022).

Definition 1. A boundary controller irreversible port Hamiltonian system is a system defined by the following set of PDEs:

$$\frac{\partial}{\partial t}\begin{bmatrix}x(t,z)\\ s(t,z)\end{bmatrix} = \begin{bmatrix}P_0 & G_0\mathbf{R_0}(\mathbf{x})\\ -\mathbf{R_0}(\mathbf{x})^\top G_0^\top & 0\end{bmatrix}\begin{bmatrix}\frac{\delta H}{\delta x}(t,z)\\ \frac{\delta H}{\delta s}(t,z)\end{bmatrix} + \begin{bmatrix}P_1\frac{\partial(.)}{\partial z} & \frac{\partial\left(G_1\mathbf{R_1}(\mathbf{x}).\right)}{\partial z}\\ \mathbf{R_1}(\mathbf{x})^\top G_1^\top\frac{\partial(.)}{\partial z} & g_s\mathbf{r_s}(\mathbf{x})\frac{\partial(.)}{\partial z}+\frac{\partial\left(g_s\mathbf{r_s}(\mathbf{x}).\right)}{\partial z}\end{bmatrix}\begin{bmatrix}\frac{\delta H}{\delta x}(t,z)\\ \frac{\delta H}{\delta s}(t,z)\end{bmatrix} \tag{1}$$

with $z\in[a,\,b]$, $x\in\mathbb{R}^n$ the set of energy variables, $s\in\mathbb{R}$ the entropy, $H(x,s)$ the total energy. $P_0=-P_0^\top\in\mathbb{R}^{n\times n}$, $P_1=P_1^\top\in\mathbb{R}^{n\times n}$, $g_s\in\mathbb{R}$, $G_0\in\mathbb{R}^{n\times m}$, $G_1\in\mathbb{R}^{n\times m}$ with m the number of states involved in the entropy production. $\mathbf{R_0}\in\mathbb{R}^{m\times 1}$, $\mathbf{R_1}\in\mathbb{R}^{m\times 1}$ and $r_s\in\mathbb{R}$ stand for the vectors of modulated driving forces with [1] $R_{k,i}=\gamma_{k,i}\left(x,z,\frac{\delta H}{\delta x}\right)\{S|G_k(:,i)|H\}$, $k\in\{0,1\}$ and $r_s=\gamma_s\left(x,z,\frac{\delta H}{\delta x}\right)\{S|H\}$ with $\gamma_{k,i}\left(x,z,\frac{\delta H}{\delta x}\right),\gamma_s\left(x,z,\frac{\delta H}{\delta x}\right):\mathbb{R}^n\to\mathbb{R}$, $\gamma_{k,i},\gamma_s\geq 0$, non-linear positive functions. The input/output are given by

$$u(t)=W_B\begin{bmatrix}e_e(t,b)\\ e_e(t,a)\end{bmatrix}\quad,\quad y(t)=W_C\begin{bmatrix}e_e(t,b)\\ e_e(t,a)\end{bmatrix} \tag{3}$$

where

$$e_e(t,z)=\begin{bmatrix}\frac{\delta H}{\delta x}(t,z)\\ \mathbf{R}(\mathbf{x})\frac{\delta H}{\delta s}(t,z)\end{bmatrix}\text{ with }\mathbf{R}(\mathbf{x})=\begin{bmatrix}1\\ \mathbf{R_1}(\mathbf{x})\\ \mathbf{r_s}(\mathbf{x})\end{bmatrix} \tag{4}$$

and

$$W_B=\left[\frac{1}{\sqrt{2}}\left(\Xi_2+\Xi_1P_{ep}\right)M_p\;\;\frac{1}{\sqrt{2}}\left(\Xi_2-\Xi_1P_{ep}\right)M_p\right],$$
$$W_C=\left[\frac{1}{\sqrt{2}}\left(\Xi_1+\Xi_2P_{ep}\right)M_p\;\;\frac{1}{\sqrt{2}}\left(\Xi_1-\Xi_2P_{ep}\right)M_p\right],$$

where $M_p=\left(M^\top M\right)^{-1}M^\top$, $P_{ep}=M^\top P_eM$ and M is spanning the columns of P_e, defined by [2] $P_e=$

[1] The following pseudo (locally defined) brackets are used to define the thermodynamic driving forces of the system

$$\{\Gamma|\mathcal{G}|\Omega\}=\begin{bmatrix}\frac{\delta\Gamma}{\delta x}&\frac{\delta\Gamma}{\delta s}\end{bmatrix}\begin{bmatrix}0&\mathcal{G}\\ -\mathcal{G}^*&0\end{bmatrix}\begin{bmatrix}\frac{\delta\Omega}{\delta x}\\ \frac{\delta\Omega}{\delta s}\end{bmatrix},$$
$$\{\Gamma|\Omega\}=\frac{\delta\Gamma}{\delta s}^\top\left(\frac{\partial}{\partial z}\frac{\delta\Omega}{\delta s}\right) \tag{2}$$

for some smooth functions Γ, Ω and $\mathcal{G}$.

[2] 0 has to be understood as the zero matrix of proper dimensions.

$\begin{bmatrix} P_1 & 0 & G_1 & 0 \\ 0 & 0 & 0 & g_s \\ G_1^\top & 0 & 0 & 0 \\ 0 & g_s & 0 & 0 \end{bmatrix}$ and where Ξ_1 and Ξ_2 satisfy $\Xi_2^\top \Xi_1 + \Xi_1^\top \Xi_2 = 0$ and $\Xi_2^\top \Xi_2 + \Xi_1^\top \Xi_1 = I$.

As an example the heat equation defined on a one dimensional spatial domaine ($z \in [0, L]$) can be formulated as an irreversible port Hamiltonian system choosing the entropy $s(z,t)$ as state variable and the total internal energy $U(t) = \int_0^1 u(z,t)dz$ where $u(z,t)$ is the internal energy density as Hamiltonian. From the balance equation on the internal energy and Gibb's equation one can write the IPH formulation

$$\frac{\partial s}{\partial t} = \frac{\partial}{\partial z}\left(\frac{\lambda}{T}\frac{\partial T}{\partial z}\right) + \frac{\lambda}{T^2}\left(\frac{\partial T}{\partial z}\right)^2 \tag{5}$$

where λ denotes the heat conduction coefficient. From (3) the boundary inputs and outputs of the system are

$$v(t) = \begin{bmatrix} \left(\frac{\lambda}{T}\frac{\partial T}{\partial z}\right)(t, L) \\ -\left(\frac{\lambda}{T}\frac{\partial T}{\partial z}\right)(t, 0) \end{bmatrix}, \quad y(t) = \begin{bmatrix} T(t, L) \\ T(t, 0) \end{bmatrix}, \tag{6}$$

respectively the entropy flux and the temperature at each boundary.

3. BOUNDARY CONTROL OF THE HEAT EQUATION

We consider now the boundary control of the 1D heat equation. The idea is to use the Thermodynamic availability function $\mathcal{A} = \int_0^1 a(z,t)dz$, defining the distance between the energy and the tangent plane at the desired equilibrium point as shown in Figure 1 as closed loop Lyapunov function (Availability Based Interconnection (ABI)) and to use Entropy Assignment (EA) to guarantee the convergence of trajectories to the desired equilibrium.

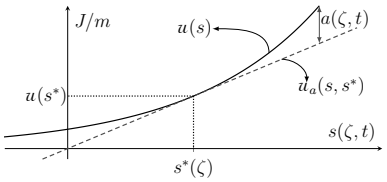

Fig. 1. Thermodynamic availability function.

In this respect the boundary control feedback $v = \beta(\mathbf{y}) + v'$, with v' an auxiliary boundary input, is chosen to map (6), (7) into the target system

$$\partial_t s = \bar{r}_s \partial_\zeta (\delta_s \mathcal{H}) + \partial_\zeta (\bar{r}_s \delta_s \mathcal{H}) \tag{7}$$

$$\tilde{\mathbf{u}} = \Xi v' \tag{8}$$

where $\mathcal{H} = U$ and

$$\Xi = \begin{bmatrix} \left.\frac{\delta_s \mathcal{A}}{T}\right|_L & 0 \\ 0 & \left.\frac{\delta_s \mathcal{A}}{T}\right|_0 \end{bmatrix} \text{ and } v' = \begin{bmatrix} \left.\lambda\left(\frac{\partial_\zeta (\delta_s \mathcal{A})}{T}\right)\right|_L \\ \left.\lambda\left(\frac{\partial_\zeta (\delta_s \mathcal{A})}{T}\right)\right|_0 \end{bmatrix} \tag{9}$$

and $\bar{r}_s = \gamma_s\{\mathcal{S}|\mathcal{A}\}$. It is the case if the following matching conditions are satisfied

$$\gamma_s\{\mathcal{S}|\mathcal{H}_a\}\partial_\zeta (\delta_s \mathcal{H}) + \partial_\zeta (\gamma_s\{\mathcal{S}|\mathcal{H}_a\}\delta_s \mathcal{H}) = 0 \tag{10}$$

$$\beta(\mathbf{y}) + \begin{bmatrix} \left.\lambda\left(\frac{\partial_\zeta (\delta_s \mathcal{H}_a)}{T}\right)\right|_L \\ \left.\lambda\left(\frac{\partial_\zeta (\delta_s \mathcal{H}_a)}{T}\right)\right|_0 \end{bmatrix} = 0 \tag{11}$$

A target temperature profile of the form $T_e^* = m^*\zeta + b^*, \forall \zeta \in [0, L]$ leads to the solution $\beta(\mathbf{y}) = \begin{bmatrix} \frac{km^*}{T|_L} & \frac{km^*}{T|_0} \end{bmatrix}^T$.

We consider now the additional feedback on (8)-(9)

$$\tilde{\mathbf{u}} = -\Gamma \mathbf{y} \tag{12}$$

with $\Gamma = \Xi \Phi \Xi^\top$, and $\Phi = \Phi^\top > 0$, then the system is asymptotically stable. If Φ is defined by $\Phi = diag\left(\frac{\phi_L}{T|_L}, \frac{\phi_0}{T|_0}\right)$ where ϕ_L and ϕ_0 are strictly positive, the target temperature profile is achievable from any initial condition T_0. At the end the control is

$$\mathbf{u} = \beta(\mathbf{y}) - \Phi \Xi^\top \mathbf{y} \tag{13}$$

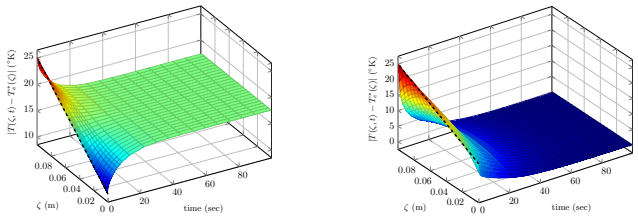

Fig. 2. Behavior of the absolute error of temperature response with respect to desired equilibrium profile, using ABI (left) control and ABI-EA (right) control.

As numerical application let's consider the heat equation with initial condition $T_0 = 303.15, \forall \zeta \in [0, 0.1]$ and target profile $T_e^* = 150\zeta + 313.15, \quad \zeta \in [0, 0.1]$. The closed loop performances using Availability based interconnection with or without Entropy assignment are given in Figure 2. It shows that the use of the availability based interconnection allows to reach an equilibrium but that EA is necessary to avoid bias.

REFERENCES

Grmela, M. and Öttinger, H.C. (1997). Dynamics and thermodynamics of complex fluids. I. Development of a general formalism. *Phys. Rev. E*, 56(6), 6620–6632. doi:10.1103/PhysRevE.56.6620.

Le Gorrec, Y., Zwart, H., and Maschke, B. (2005). Dirac structures and Boundary Control Systems associated with Skew-Symmetric Differential Operators. *SIAM Journal on Control and Optimization*, 44(5), 1864–1892. doi:10.1137/040611677.

Ramírez, H., Le Gorrec, Y., and Maschke, B. (2022). Boundary controlled irreversible port-Hamiltonian systems. *Chemical Engineering Science*, 248 part A, 117107.

Ramírez, H., Le Gorrec, Y., Maschke, B., and Couenne, F. (2016). On the passivity based control of irreversible processes: A port-Hamiltonian approach. *Automatica*, 64, 105–111.

Ramírez, H., Maschke, B., and Sbarbaro, D. (2013). Irreversible port-Hamiltonian systems: A general formulation of irreversible processes with application to the CSTR. *Chemical Engineering Science*, 89, 223–234.

Computing Truncated Joint Approximate Eigenbases for Model Order Reduction

Terry Loring * **Fredy Vides** **

* *Department of Mathematics and Statistics, University of New Mexico, Albuquerque, (e-mail: loring@math.unm.edu).*
** *Scientific Computing Innovation Center, School of Mathematics and Computer Science, Universidad Nacional Autónoma de Honduras, Tegucigalpa (e-mail: fredy.vides@unah.edu.hn)*

1. INTRODUCTION

Consider a collection of d Hermitian matrices $X_1, \ldots, X_d$ in $\mathbb{R}^{n\times n}$ and a d-tuple $\boldsymbol{\lambda} = (\lambda_1, \ldots, \lambda_d) \in \mathbb{R}^d$. Let us consider the problem determined by the computation of a collection of joint approximate eigenvectors that can be represented as a rectangular matrix $W \in \mathbb{C}^{n\times r}$ with orthonormal columns such that

$$W = \arg \min_{\hat{W}\in\mathbb{R}^{n\times r}} \sum_{j=1}^{d} \left\| X_j \hat{W} - \hat{W}\Lambda_j \right\|_F^2 . \tag{1}$$

Solutions to problem (1) can be used for model order reduction as will be illustrated in §4.

Given one Hermitian matrix X we are only interested in the real part of the pseudospectrum. By the usual definition, real λ is in the ϵ-pseudospectrum of X if

$$\left\| (X-\lambda)^{-1} \right\|^{-1} \leq \epsilon.$$

One can easily see this is equivalent to the condition

$$\exists \boldsymbol{v} \text{ such that } \|\boldsymbol{v}\| = 1 \text{ and } \|X\boldsymbol{v} - \lambda\boldsymbol{v}\| \leq \epsilon.$$

We will call $\|X\boldsymbol{v} - \lambda\boldsymbol{v}\|$ the *eigen-error*. This comes up all the time in applications, and the less matrices commute the more it must be considered.

For Hermitian matrices $X_1, X_2, \ldots, X_d$ we often want a unit vector with the various eigen-errors small. There are many ways to combine d errors, such as their sum or maximum. Not surprisingly, a clean theory arises when we consider the quadratic mean of the eigen-errors.

Here then is a definition of a pseudospectrum. In the noncommutative setting, there are several notions of joint spectrum and joint pseudospectrum that compete for our attention, such as one using Clifford algebras (Loring, 2015). None is best is all settings.

Definition 1. Suppose we have finitely many Hermitian matrices $X_1, X_2, \ldots, X_d$. Suppose $\epsilon > 0$. A d-tuple $\boldsymbol{\lambda}$ is an element of the quadratic ϵ-pseudospectrum of $(X_1, X_2, \ldots, X_d)$ if there exists as unit vector $\boldsymbol{v}$ so that

$$\sqrt{\sum_{j=1}^{d} \|X_j\boldsymbol{v} - \lambda_j\boldsymbol{v}\|^2} \leq \epsilon. \tag{2}$$

If (2) is true for $\epsilon = 0$ then we say $\boldsymbol{\lambda}$ is an element of the quadratic spectrum of $(X_1, X_2, \ldots, X_d)$. The notation for the quadratic ϵ-pseudospectrum of $(X_1, X_2, \ldots, X_d)$ is $Q\Lambda_\epsilon(X_1, X_2, \ldots, X_d)$.

Remark 2. Very simple examples show that the quadratic spectrum can often be empty.

It should be said that the more interesting examples of this tend to require calculation, or at least approximation, by numerical methods. Often the best way to display the data is via images of 2D slices through the function

$$\boldsymbol{\lambda} \mapsto \mu^Q_{\boldsymbol{\lambda}}(X_1, \ldots, X_d)$$

where we define

$$\mu^Q_{\boldsymbol{\lambda}}(X_1, \ldots, X_d) = \min_{\|\boldsymbol{v}\|=1} \sqrt{\sum_{j=1}^{d} \|X_j\boldsymbol{v} - \lambda_j\boldsymbol{v}\|^2}. \tag{3}$$

That is, we have a measure of how good of a joint approximate eigenvector we can find at $\boldsymbol{\lambda}$. Then, of course, the more traditional interpretation of $Q\Lambda_\epsilon(X_1, X_2, \ldots, X_d)$ as the sublevel sets of this function.

Remark 3. We will make frequent use of the following notation:

$$Q_{\boldsymbol{\lambda}}(X_1, \ldots, X_d) = \sum_{j=1}^{d} (X_j - \lambda_j)^2 ,$$

$$M_{\boldsymbol{\lambda}}(X_1, \ldots, X_d) = \begin{bmatrix} X_1 - \lambda_1 \\ \vdots \\ X_d - \lambda_d \end{bmatrix}$$

Finally we use $\sigma_{\min}$ to indicate the smallest singular value of a matrix.

As a particular application of quadratic pseudospectrum based techniques, for the computation of truncated joint approximate eigenbases, in section §4 we will present an application of these quadratic pseudospectral based methods to the computation of a reduced order model for a discrete-time system related to least squares realization of linear time invariant models (De Moor, 2019).

2. MAIN RESULTS

We now list the main results that corresponding to some important properties of the quadratic pseudospectrum.

⋆ Loring acknowledges partial support from the National Science Foundation #2110398. Vides acknowledges partial support from the Scientific Computing Innovation Center of UNAH under project PI-174-DICIHT.

Proposition 4. Suppose that $X_1, X_2, \ldots, X_d$ are Hermitian matrices, that $\epsilon > 0$ and $\boldsymbol{\lambda}$ is in $\mathbb{R}^d$. The following are equivalent.

(1) $\boldsymbol{\lambda}$ is an element of the quadratic ϵ-pseudospectrum of $(X_1, X_2, \ldots, X_d)$;
(2) $\sigma_{\min}\left(M_{\boldsymbol{\lambda}}(X_1, \ldots, X_d)\right) \leq \epsilon$;
(3) $\sigma_{\min}\left(Q_{\boldsymbol{\lambda}}(X_1, \ldots, X_d)\right) \leq \epsilon^2$.

The following technical result is very helpful for numerical calculations. Assuming that one does not care about the exact value of $\mu^Q_{\boldsymbol{\lambda}}(X_1, \ldots, X_d)$ once this value is above some cutoff, then knowing Lipschitz continuity allows one to skip calculating this values at many points near where a high value has been found.

Proposition 5. Suppose that $X_1, X_2, \ldots, X_d$ are Hermitian matrices. The function

$$\boldsymbol{\lambda} \mapsto \mu^Q_{\boldsymbol{\lambda}}(X_1, \ldots, X_d),$$

with domain $\mathbb{R}^d$, is Lipschitz with Lipschitz constant 1.

For details on the proofs of Propositions 4 and 5, the reader is kindly referred to (Cerjan et al., 2022).

3. ALGORITHM

Combining the ideas and methods presented in (Eynard et al., 2015) and (Cardoso and Souloumiac, 1996), with the ideas and results presented in §2, we obtained Algorithm 1.

Algorithm 1: Approximate Joint Eigenvectors Computation

Data: HERMITIAN MATRICES: $X_1, \ldots, X_d \in \mathbb{R}^{n\times n}$, d-TUPLE $\lambda \in \mathbb{C}^d$, INTEGER: $1 \leq k \leq n$, THRESHOLD: $\delta > 0$, SELECTOR: ϕ
Result: PARTIAL ISOMETRY $V \in \mathbb{O}(n, k)$

0: Set the choice indicator value ϕ: $\phi = 0$ for smallest eigenvalues or $\phi = 1$ for largest eigenvales;
1: Set $L := \sum_{j=1}^{N}(X_j - \lambda_j I_n)^2$;
2: Approximately solve $LV = V\Lambda$ for $V \in \mathbb{C}^{n\times k}, \Lambda \in \mathbb{C}^{k\times k}$ according to the flag value ϕ;
for $j \leftarrow 1$ **to** d **do**
  3.0: Set $Y_j := V^\top(X_j - \lambda_j I_n)V$;
  3.1: Set $Y_j := (Y_j + Y_j^\top)/2$;
end
4: Solve $W = \arg\min_{U\in\mathbb{O}(n)} \sum_{k=1}^{d} \operatorname{off}(U^\top Y_k U)$ using complex valued Jacobi-like techniques as in Cardoso and Souloumiac (1996) with threshold= δ.;
5: Set $V := VW$;
return V

In this document, the operation $A^\top$ represents the transpose of some given matrix A.

4. EXAMPLE

Consider the discrete-time system with states $x_1(t)$ and $x_2(t)$ in $\mathbb{R}^{400}$:

$$x_1(t+1) = A_1 x_1(t),\ x_2(t+1) = A_2 x_1(t+1), \quad (4)$$
$$y_1(t) = \hat{e}_{1,400}^\top x_1(t),\ y_2(t) = \hat{e}_{2,400}^\top x_2(t),$$

for some given matrices $A_1, A_2 \in \mathbb{R}^{400\times 400}$ such that $A_1 A_2 = A_2 A_1$ that are generated with the program

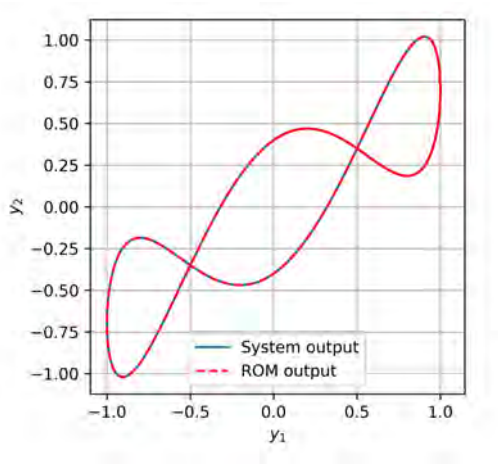

Fig. 1. Original system and ROM outputs.

`QLMORDemo.py` available at (Vides, 2021)., here $\hat{e}_{1,400}$ and $\hat{e}_{2,400}$ denote the first and second columns of the identity matrix in $\mathbb{R}^{400\times 400}$, respectively. Let us consider the matrices

$$H_1 = A_1^\top A_1,$$
$$H_2 = A_2^\top A_2,$$
$$H_3 = A_1^\top A_2 + A_2^\top A_1$$

We can apply Algorithm 1 to H_1, H_2, H_3 with $\delta = 10^{-5}$ obtaining the matrix $V \in \mathbb{R}^{400\times 6}$ with orthonormal columns, that can be used to compute a model order reduction for (4), determined by the following equations.

$$\hat{x}_1(t+1) = V^\top A_1 V \hat{x}_1(t),\ \hat{x}_2(t+1) = V^\top A_2 V \hat{x}_1(t+1),$$
$$\hat{y}_1(t) = \hat{e}_{1,400}^\top V \hat{x}_1(t),\ \hat{y}_2(t) = \hat{e}_{2,400}^\top V \hat{x}_2(t).$$

The outputs corresponding to the original and reduced order models are plotted in Figure 1.

REFERENCES

Cardoso, J.F. and Souloumiac, A. (1996). Jacobi angles for simultaneous diagonalization. *SIAM J. Mat. Anal. Appl.*, 17(1), 161–164.

Cerjan, A., Loring, T.A., and Vides, F. (2022). Quadratic pseudospectrum for identifying localized states. doi:10.48550/ARXIV.2204.10450. URL `https://arxiv.org/abs/2204.10450`.

De Moor, B. (2019). Least squares realization of lti models is an eigenvalue problem. In *2019 18th European Control Conference (ECC)*, 2270–2275. doi:10.23919/ECC.2019.8795987.

Eynard, D., Kovnatsky, A., Bronstein, M.M., Glashoff, K., and Bronstein, A.M. (2015). Multimodal manifold analysis by simultaneous diagonalization of laplacians. *IEEE Transactions on Pattern Analysis and Machine Intelligence*, 37(12), 2505–2517. doi:10.1109/TPAMI.2015.2408348.

Loring, T.A. (2015). K-theory and pseudospectra for topological insulators. *Ann. Physics*, 356, 383–416. doi:10.1016/j.aop.2015.02.031. URL `http://dx.doi.org/10.1016/j.aop.2015.02.031`.

Vides, F. (2021). Pytjae: A python toolset for truncated joint approximate eigenbases computation and reduced order modeling. URL `https://github.com/FredyVides/PyTJAE`.

A three-state hyperthermic cell death model for the prediction of myocardial lesion ⋆

Stefan Lämmermann [*] **Argyrios Petras** [**]
Massimiliano Leoni [**] **Jose M. Guerra** [***]
Luca Gerardo-Giorda [**,*]

[*] *Johannes Kepler University, Linz, 4020 Austria*
[**] *RICAM - Johann Radon Institute for Computational and Applied Mathematics, Linz, 4020 Austria (e-mail: argyrios.petras@ricam.oeaw.ac.at).*
[***] *Hospital de la Santa Creu i San Pau, IIB Sant Pau, Universitat Autónoma de Barcelona, Barcelona, 08025 Spain*

1. INTRODUCTION

Radiofrequency (RF) catheter ablation is a minimally invasive procedure commonly used for the treatment of cardiac arrhythmias. Though it has been effectively practiced for many years, this procedure is not exempt from complications, including charring formation due to blood overheating at temperatures higher than 80^oC and the occurrence of steam pops for tissue temperatures around 100^oC. Several models have been introduced to simulate the RF ablation procedure, which provide lesion size estimations at the end of the ablation. Typically, either the 50^oC isotherm is considered as an estimation for the lesion, or an Arrhenius type model, which accounts for the time at which the tissue is at an altered state. In this work a three-state cell death model is considered for the estimation of the lesion, which captures the shrinkage of the damage region after the completion of the ablation.

2. METHODS

2.1 Three-state cell death model

The model introduced in Park et al. (2016) considers three states for the proteins within the cell: Native (N), Unfolded (U) and Denaturated (D). The dynamics are described as follows:

$$\mathrm{N} \underset{k_3}{\overset{k_1}{\rightleftharpoons}} \mathrm{U} \xrightarrow{k_2} \mathrm{D},$$

$$\begin{aligned} \frac{dN}{dt} &= -k_1 N + k_3 U, \\ \frac{dU}{dt} &= k_1 N - k_3 U - k_2 U, \\ \frac{dD}{dt} &= k_2 U, \end{aligned} \tag{1}$$

where k_1, k_2 and k_3 follow the Arrhenius model

$$k_i = A_i e^{-\Delta E_i/(RT)}, \quad i = 1, 2, 3,$$

with A_i being the frequency factor, ΔE_i the activation energy, R the universal gas constant and T the temperature. Note that at all times $N + U + D = 1$. The system (1) is solved numerically using the Runge-Kutta third-order method and $\Delta t = 0.01$. This scheme allows for the conservation the quantity $N + U + D$ at all times.

2.2 Slow cell death dynamics

While for fast cell death dynamics equation (1) is capable of capturing the denaturation behavior for the rapid changes that occur during thermal ablation treatments, experimental data show that the cell viability decreases at a much slower pace in comparison to the duration of the procedure. In particular, experimental evidence on human liver hepatocellular carcinoma cells and human lung fibroblasts show that once cells receive thermal damage beyond some given threshold (i.e. the native proteins are below a threshold N_{thr}), they progressively reach a denaturated state. Following ONeill et al. (2011), we consider a threshold value of $N_{thr} = 80\%$.

3. RESULTS

3.1 Calibration

While experimental results exist for different types of cells, including bovine chordae tendineae (Park et al. (2016)), human liver hepatocellular carcinoma and human lung fibroblasts (ONeill et al. (2011)), no data are available for the estimation of the 6 parameters for the hyperthermic death of cardiac myocytes. To tune the parameters for such cells, we consider that thermal damage occurs at temperatures higher than 43^oC, however the tissue damage is reversible for heating up to 48^oC and exposure time of $60s$ (Zaltieri et al. (2021)). Additionally, the mean frequency A and activation energy ΔE defined as

$$\Delta E = \Delta E_1 + \Delta E_2 - \Delta E_3 \qquad \text{and} \qquad A = \frac{A_1 A_2}{A_3},$$

⋆ AP, ML and LGG were partially supported by the State of Upper Austria.

should lie within the physiological ranges of $100 - 800\,kJ/mol$ and $10^9 - 10^{129} s^{-1}$ found in the literature and the values given in Park et al. (2016) for proteins.

3.2 Application to RF ablation

Next, we apply the computational model to the simulated results obtained in Petras et al. (2019) using a 3D computational framework. The simulation protocol employs $30s$ of ablation followed by $30s$ of relaxation, where no ablation is performed and the saline irrigation rate drops to standby mode of $2mL/min$. We consider the three ablation protocols that have been used for validation, namely $(10g, 20W)$, $(10g, 35W)$ and $(20g, 20W)$, indicating the contact force in g and the applied power in W. The results after the completion of $60s$ appear in Figure 1 for the parameter set in Table 1 (A_i in s^{-1} and ΔE_i in kJ/mol, $i = 1, 2, 3$).

Table 1. The parameter set chosen for the three-state model.

A_1	ΔE_1	A_2	ΔE_2	A_3	ΔE_3
3.68×10^{30}	200.1	5.68×10^{3}	40.6	2.85×10^{5}	43

We get a good agreement with the experimental data shown in Petras et al. (2019) for the depth (D) and the depth at the maximum width (DW), while the simulated lesion underestimates the width (W), which is consistent with the observations in Petras et al. (2019) for the ablation protocols $(10g, 20W)$ and $(20g, 20W)$ using the 50^oC isotherm. On the other hand, the D and DW are slightly outside the experimental ranges in the case of $(10g, 35W)$. This is consistent with the 50^oC isotherm lesion estimation, since the measurements were close to the limits of the range of the observed experimental data. This might possibly happen due to the underestimation of the thermal conductivity of the tissue for large temperature values (maximum tissue temperature $T = 87^oC$), due to the lack of data available in the literature (available data appear only for temperatures lower than 76^oC).

4. CONCLUSION

The calibrated three-state hyperthermic cell death model is capable of capturing the shrinkage of the damaged tissue area after the ablation, simulating the reversible damage that occurs, while accounting for the slow cell death. Additionally, our results indicate that the 50^oC isotherm is overestimating the lesion size.

5. LIMITATIONS

Limitations of this study include the lack of experimental data for the validation of the thermal cell death for cardiac myocytes. While other parameters might satisfy the model calibration, we considered a parameter set that is producing lesions that are within the experimental measurements provided by Petras et al. (2019).

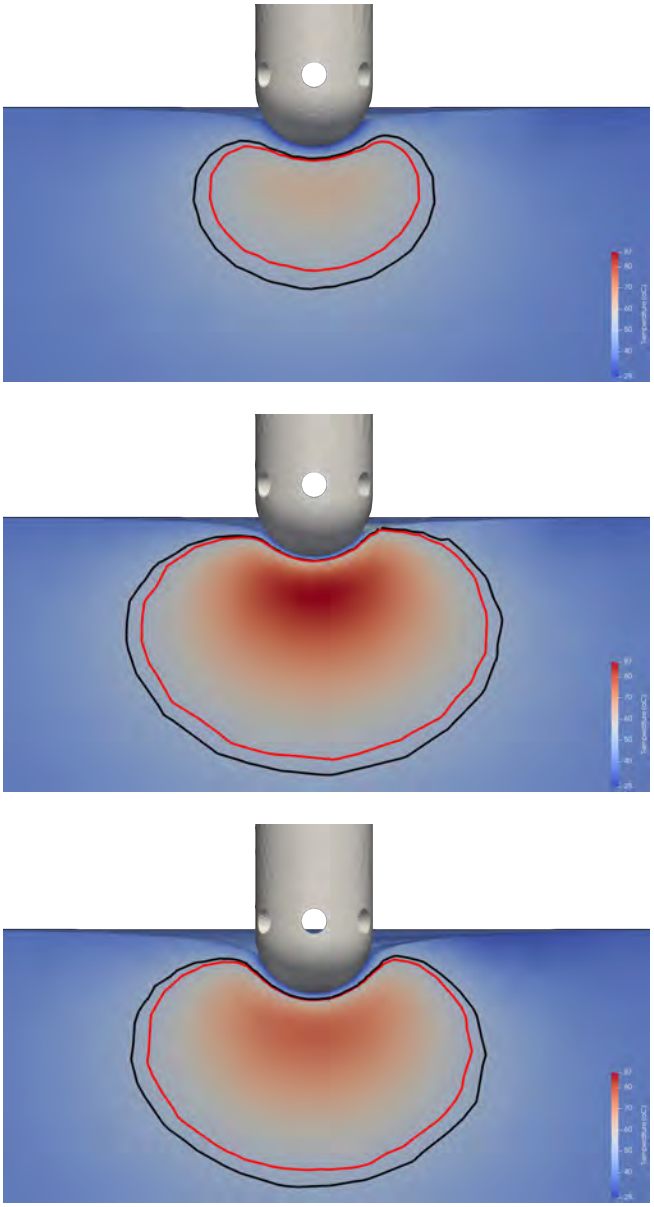

Fig. 1. The lesion size estimation using the 50^oC isotherm (black line) versus the $N_{thr} = 80\%$ contour from the three-state model (red line) for the cases of $(10g, 20W)$ (top), $(10g, 35W)$ (middle) and $(20g, 20W)$ (bottom).

REFERENCES

ONeill, D.P., Peng, T., Stiegler, P., Mayrhauser, U., Koestenbauer, S., Tscheliessnigg, K., and Payne, S.J. (2011). A three-state mathematical model of hyperthermic cell death. *Annals of biomedical engineering*, 39(1), 570–579.

Park, C.S., Hall, S.K., Liu, C., and Payne, S.J. (2016). A model of tissue contraction during thermal ablation. *Physiological measurement*, 37(9), 1474.

Petras, A., Leoni, M., Guerra, J.M., Jansson, J., and Gerardo-Giorda, L. (2019). A computational model of open-irrigated radiofrequency catheter ablation accounting for mechanical properties of the cardiac tissue. *International Journal for Numerical Methods in Biomedical Engineering*, 35(11), e3232.

Zaltieri, M., Massaroni, C., Cauti, F.M., and Schena, E. (2021). Techniques for temperature monitoring of myocardial tissue undergoing radiofrequency ablation treatments: An overview. *Sensors*, 21(4), 1453.

Towards Model Predictive Control for Maintaining a Hard Infection Cap during an Outbreak of Dengue Fever

Philipp Sauerteig * **Karl Worthmann** * **Kurt Chudej** **

* *Institute of Mathematics, Technische Universität Ilmenau, Germany (e-mail: philipp.sauerteig@tu-ilmenau.de)*
** *Forschungszentrum MODUS, Universität Bayreuth, Germany*

Abstract: A dynamical model for an outbreak of dengue fever with countermeasures as control inputs is considered. We formulate an optimal control problem (OCP) for maintaining a hard infection cap with preferably low control effort and study different scenarios numerically. To this end, we solve the OCP in both open and closed loop using model predictive control (MPC).

Keywords: epidemiology, hard infection cap, dynamic models, optimal control, model predictive control, numerical optimisation

1. INTRODUCTION

Mathematical models have been used to model epidemics since decades. For instance, compartmental models, where people are characterised by their state of infection, are used to describe the spread of the disease, see, e.g., Hethcote (2000). Due to the ongoing COVID-19 pandemic researchers proposed a variety of compartmental models tailored to model particular characteristics of the disease, see e.g. Grundel et al. (2022). Here, optimal control problems (OCPs) are formulated with countermeasures as control inputs and solved to determine a reasonable (theoretically optimal) strategy. Here, the main goal is to maintain a hard infection cap while keeping drawbacks resulting from the enforced countermeasures as low as possible. However, besides COVID-19, a couple of vector-borne diseases seriously endangering public health are re-emerging in Europe. Hence, we aim at transferring recently proposed methods, see e.g. Grundel et al. (2021), to determine (near) optimal intervention strategies to a dengue fever model, see e.g. Fischer et al. (2019). In particular, we propose an MPC scheme to solve the problem and study the impact of the choice of the prediction horizon length and weights in the objective function on the total number of infections.

2. MODEL AND PROBLEM FORMULATION

We consider the model studied in Fischer et al. (2019) consisting of two species: humans and mosquitos (vectors). Transmission may occur if a susceptible mosquito bites an infectious human or if an infectious mosquito bites a susceptible human.

2.1 System dynamics

Let S_h, V_h, I_h, and R_h denote the total number of susceptible, vaccinated, infected, and recovered people and A_m, S_m, and I_m denote the aquatic (larves), susceptible, and infected mosquitos, respectively. Then, the dynamics for the humans and mosquitos are given by

$$\begin{aligned}
\dot{S}_h &= \mu_h N_h + \theta V_h - \left(\frac{B\beta_{mh}}{N_h} I_m + \psi + \mu_h\right) S_h \\
\dot{V}_h &= \psi S_h - \left(\theta + \sigma\frac{B\beta_{mh}}{N_h} I_m + \mu_h\right) V_h \\
\dot{I}_h &= \frac{B\beta_{mh}}{N_h} I_m \left(S_h + \sigma V_h\right) - (\eta_h + \mu_h) I_h \\
\dot{R}_h &= \eta_h I_h - \mu_h R_h \\
\dot{A}_m &= \varphi\left(1 - \frac{A_m}{3N_h}\right)(S_m + I_m) - (\eta_A + \mu_a + c_a) A_m \\
\dot{S}_m &= \eta_a A_m - \left(\frac{B\beta_{hm}}{N_h} I_h + \mu_m + c_m\right) S_m \\
\dot{I}_m &= \frac{B\beta_{hm}}{N_h} I_h S_m - (\mu_m + c_m) I_m.
\end{aligned}$$

The control $u = (\psi, c_a, c_m) \in L^\infty_{\mathrm{loc}}([0,\infty), [0,1]^m)$, $m = 3$, consists of the vaccination rate ψ as well as the rates of larvicide c_a and adulticide c_m, respectively. In the remainder, we collect all states in $x(t) \in \mathbb{R}^n$, $n = 7$, and write $\dot{x}(t) = f(x(t), u(t))$.

2.2 Optimal control problem

Our goal is to maintain a hard infection cap, i.e.,

$$I_h(t) \;\leq\; I_{\max} \qquad \forall\, t \geq 0,$$

with as little control effort as possible. This motivates the following OCP

$$\min_u \quad J(x_0, u) = \int_0^{t_f} \ell(x(t; x_0, u), u(t))\,\mathrm{d}t \tag{1a}$$

$$\text{s.t.} \quad \dot{x}(t) = f(x(t), u(t)), \quad x(0) = x^0 \tag{1b}$$

$$I_h(t) \leq I_{\max} \quad \forall\, t \geq 0 \tag{1c}$$

with stage costs $\ell : \mathbb{R}^n \times \mathbb{R}^m \to \mathbb{R}$,

$$\ell(x, u) \;:=\; \omega\left(\frac{I_h}{I_{\max}}\right)^2 + \frac{1-\omega}{m}\,\|u\|_2^2$$

and non-negative weights $\omega \in [0, 1]$.

We enforce the controls to be constant over one week reflecting the fact that it takes time to implement the countermeasures. Moreover, we use model predictive control (MPC) to mimic real-life decision making by updating the control variables when novel data is available. Given step size $\Delta t > 0$, prediction horizon length $N \in \mathbb{N}_{\geq 2}$, and the current time instant $k \in \mathbb{N}_0$, the three main steps of MPC are

(1) measure current state $\hat{x} = x(k\Delta t)$,
(2) solve the OCP (1) on $[k\Delta t, (k + N - 1)\Delta t)$ to get optimal control $u_k : [k\Delta t, (k + N - 1)\Delta t)$,
(3) implement solution $\mu(k) = u_k(k\Delta t)$ and increment $k \leftarrow k + 1$.

3. NUMERICAL RESULTS

In our simulations we set $N_h = 100,000$ as well as

$$S_h^0 = 99,990, V_h^0 = 0, I_h^0 = 10, R_h^0 = 0,$$
$$A_m^0 = 300,000, S_m^0 = 300,000, I_m^0 = 0.$$

The values of the system parameters are listed in Table 1. We solve the OCP (1) both in open and closed loop over a time window of one year.

Table 1. Overview of all parameters

symbol	description	value
N_h	total human population	100,000
B	average biting rate	0.8
β_{mh}	infection rate from vector to human	0.375
β_{hm}	infection rate from human to vector	0.375
μ_h^{-1}	average life expectancy of humans	$80 \cdot 365$
η_h^{-1}	average infectious time of humans	3
μ_m^{-1}	average life expectancy of mosquitoes	10
η_a	maturation rate of larvae	0.08
φ	amount of eggs per breeding place	6
μ_a	natural death rate of larvae	0.25
σ	efficacy of the vaccine	0.2
θ	waning immunity	0.05

We study the impact of the different choices of the weighting parameter $\omega \in [0, 1]$ and the prediction horizon length $N \in \mathbb{N}_{\geq 2}$ on the total nunber of infections within one year. Results can be found in Figure 1. Note that in all scenarios the hard infection cap is maintained. If we do not penalise the number of infections ($\omega = 0$) the infection cap is reached and the outbreak evolves faster. The higher the weight on penalising infections, the more people are vaccinated (top to bottom). Moreover, the total number of infections for different combinations of ω and N is listed in Table 2. Both, in open and closed loop, increasing

Table 2. Total number of infections within one year depending on weighting ω and horizon N.

N \ ω	0	0.001	0.005	0.01	0.5
2	95422	91194	87334	77446	10036
4	95359	89693	58552	41937	4389
6	95313	87914	43004	29524	2959
8	95382	87769	36919	24284	2311
12	95318	89256	35951	20859	1681
open loop	95296	89715	76131	50060	1552
$\|u\|_\infty$	0.0557	0.0626	0.0738	0.0771	0.1116

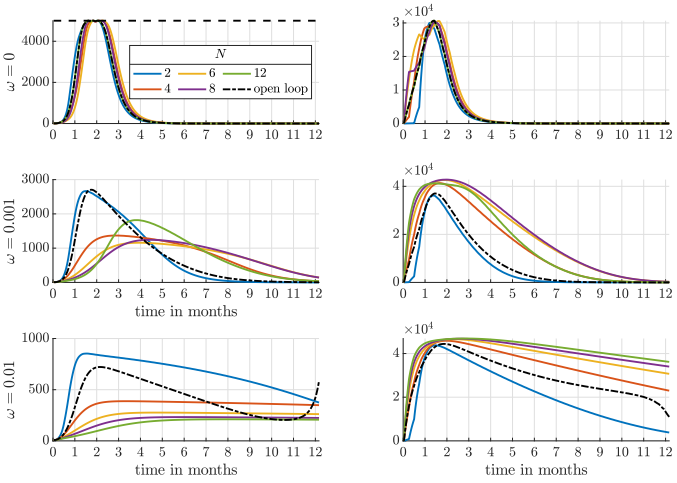

Fig. 1. Results with cap $I_{\max} = 5,000$ for increasing weight ω from top to bottom: I_h (left), V_h (right).

the weight ω yields a reduction of the total number of infections for a fixed prediction horizon length N (left to right).

For fixed weight ω, we observe that in most cases, increasing the horizon length N also results in lower case numbers. However, there is an exception for $\omega = 0.001$: If we increase the prediction horizon from $N = 8$ to $N = 12$, the total number of infections slightly increases. However, the weight $\omega = 0.001$ for penalising the number of infections is very small. Thus, it is cheaper to accept more infections for the trade-off of less control effort. This becomes particularly prominent in open loop with $\omega = 0.01$. In Figure 1 (bottom left), the infection numbers rise towards the end of the prediction horizon since we cannot reduce the control effortwithout causing the number of infections to explode within the considered time window.

4. CONCLUSIONS AND OUTLOOK

We studied an OCP for maintaining a hard infection cap in case of an outbreak of dengue fever. We found that the choice of both the weights in the objective function and the prediction horizon length are crucial to reduce the total number of infections. Future research will consider several serotypes to model vaccination more accurately.

REFERENCES

Fischer, A., Chudej, K., and Pesch, H.J. (2019). Optimal vaccination and control strategies against dengue. *Math. Meth. Appl. Sci.*, 42, 3496–3507.

Grundel, S., Heyder, S., Hotz, T., Ritschel, T.K.S., Sauerteig, P., and Worthmann, K. (2021). How to Coordinate Vaccination and Social Distancing to Mitigate SARS-CoV-2 Outbreaks. *SIAM J. Appl. Dyn. Syst.*, 20(2), 1135–1157.

Grundel, S., Heyder, S., Hotz, T., Ritschel, T.K.S., Sauerteig, P., and Worthmann, K. (2022). How Much Testing and Social Distancing is Required to Control COVID-19? Some Insight Based on an Age-Differentiated Compartmental Model. *SIAM J. Control Optim.*, S145–S169.

Hethcote, H.W. (2000). The mathematics of infectious diseases. *SIAM Rev.*, 42(4), 599–653.

Real-Time Forecasting of Seasonal Influenza in South Korea with Compartment model and Assimilation Filtering

Minhye Kim [*] **Kyeongah Nah** [**] **Masud M A** [***]
Sangil Kim [****] **Yongkuk Kim** [*]

[*] *Department of Mathematics, Kyungpook National University, Daegu, Korea*
[**] *Busan Center for Medical Mathematics, National Institute for Mathematical Sciences, Busan, Korea (e-mail: knah@nims.re.kr)*
[***] *Natural Product Informatics Research Center, Korea Institute of Science and Technology, Gangneung, Korea*
[****] *Department of Mathematics, Pusan National University, Busan, Korea*

Abstract: Seasonal influenza is an acute respiratory infection caused by several types of influenza viruses worldwide. Its outbreak exhibits a seasonal cycle in temperate climates. For public health decision-making and medical resource management during the time course of seasonal epidemics, a reliable real-time forecasting system is necessary. In this study, we introduce a novel approach combining two different data assimilation techniques to produce a real-time prediction of seasonal influenza governed by the standard SIR model. When applying our developed approach to Influenza-Like-Illness(ILI) data collected in Korea for 2016–2021, it successfully near-casted the upcoming week's flu incidence.

Keywords: Variational data assimilation, Particle filtering/Monte Carlo methods, Modeling and identification, Epidemic modeling.

1. INTRODUCTION

Influenza-like-illness is an acute respiratory infection appearing with cough and fever. As it shows up in seasonal cycles in South Korea, supporting the infected individuals with proper treatment and care using the existing medical resources becomes a challenge during the outbreak.

Data fitting techniques along with cutting edge machine learning algorithms are commonly used to forecast epidemic trend of an outbreak. During Covid-19 pandemic, several machine learning techniques approaches are raised and provided fairly accurate prediction of the epidemic trends [Wang et al. (2020); Tuli et al. (2020)]. In general, the machine learning models are not interpretable from public health perspective and hence comes with limitation in applicability. Instead, SIR-type of compartment models which incorporates the mechanisms of disease transmission and controls are often used in analyses which requires specific interpretation, such as in scenario analysis [Osthus et al. (2017); Law et al. (2021); Bjørnstad et al. (2002); Law et al. (2020)]. Although SIR-type of models resolve the issue of interpretablity, it is often studies with constant values of the parameters over the whole period of interest which however changes with time due to many associated factors like environmental conditions, public health measures, etc. Markov Chain Monte Carlo derived techniques though produce time dependent estimates, its accuracy is low in the beginning. To address this issue, we use variational data assimilation technique to predict the initial states of SIR model and then use Bayesian filtering to forecast the flu incidence of the upcoming weeks.

2. METHODS

We assume the following simple SIR model with constant population $N = S(t) + I(t) + R(t)$.

$$\begin{aligned} \frac{dS(t)}{dt} &= -\beta S(t)\frac{I(t)}{N} \\ \frac{dI(t)}{dt} &= \beta S(t)\frac{I(t)}{N} - \sigma I \\ \frac{dR(t)}{dt} &= \sigma I \end{aligned} \tag{1}$$

where, β is the transmission rate and σ is the recovery rate. Firstly, we estimate β and initial states using ICC curves and data assimilation techniques. As introduced in Lega (2021), for a total susceptible population of size N and each initial condition $k = \frac{S(0)}{N} = 1 - \frac{C(0)}{N}$, the ICC curve of the model (1) is given by,

$$G_{k,N} = \beta\left(C + \frac{N}{R_0}\ln\left(1 - \frac{C}{N}\right) - \frac{N}{R_0}\ln(k)\right)\left(1 - \frac{C}{N}\right) \tag{2}$$

where, $C = I + R \in [0, C_\infty]$ and C_∞ the final number of cases is the positive solution of the transcendental equation

$$C_\infty + \frac{N}{R_0}\ln\left(1 - \frac{C_\infty}{N}\right) - \frac{N}{R_0}\ln(k) = 0 \tag{3}$$

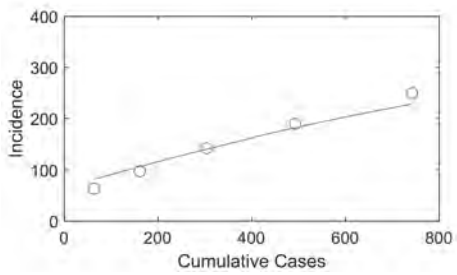

Fig. 1. Blue circles represent the pairs of cumulative cases and incidences of ILI data. Red curve is SIR model-derived ICC curve with parameters that best fits the cumulative cases – incidence data.

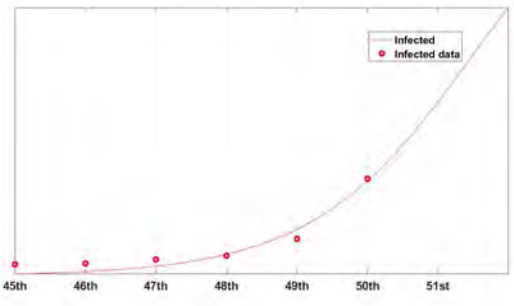

Fig. 2. Predicted numbers of weekly ILI cases using VDA method based on SIR model.

where R_0 is the basic reproduction number, which is one of the important quantities in dynamics, and is obtained as $R_0 = \beta/\sigma$. It is the expected number of secondary cases generated by one case in a population where no other individuals are infected or immunized.

We estimate the values of $C(0)$ and σ using cumulative incidence data of the first week and empirically observed duration of infectiousness, respectively. Then, the unknown value of the transmission rate β is determined to be the one which best-fit ICC to the observed incidence data, see Fig. 1.

Next, using the Variational data assimilation(VDA) introduced by Rhodes and Hollingsworth (2009), we find the initial states of SIR model which yield the best-fit of the model to the observed data. Fig. 2 shows that the number of ILI patients at 51 weeks can be predicted through initial state estimates. In the numerical optimization process, we used the adjoint method to compute gradients of the predefined cost function. In order to forecast the flu incidence in real-time, we adapt the technique of Bayesian filtering. Starting with the estimated initial states, we use Particle filtering in each time step to forecast the states in the next time step. Upon receiving the observed data in the next time step the forecast is updated to produce the estimate, which is further used to forecast in the next time step. And the cycle goes on until the end.

3. RESULTS

We implement the above mentioned approach to weekly incidence ILI data of South Korea over the period 2016-2021. The Fig. 3 shows good agreement of forecast with the trend observed in the data for two consecutive peaks

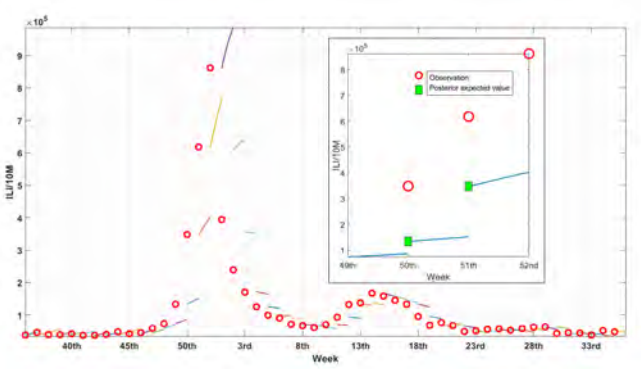

Fig. 3. Weekly forecasting of ILI cases. The red circles represent the weekly data and the solid lines shows weekly forecast.

during 2016-2017. A limitation of the suggested technique is that there is no established method in determining the time of season onset and it has to be changed each year for the accurate prediction of the epidemic curve. As a future work, we aim to develop a method which determines the time of season onset using Markov Switching.

REFERENCES

Bjørnstad, O.N., Finkenstädt, B.F., and Grenfell, B.T. (2002). Dynamics of measles epidemics: estimating scaling of transmission rates using a time series SIR model. *Ecological monographs*, 72(2), 169–184.

Law, K.B., M Peariasamy, K., Mohd Ibrahim, H., and Abdullah, N.H. (2021). Modelling infectious diseases with herd immunity in a randomly mixed population. *Scientific Reports*, 11(1), 1–12.

Law, K.B., Peariasamy, K.M., Gill, B.S., Singh, S., Sundram, B.M., Rajendran, K., Dass, S.C., Lee, Y.L., Goh, P.P., Ibrahim, H., et al. (2020). Tracking the early depleting transmission dynamics of covid-19 with a time-varying SIR model. *Scientific reports*, 10(1), 1–11.

Lega, J. (2021). Parameter estimation from ICC curves. *Journal of Biological Dynamics*, 15(1), 195–212.

Osthus, D., Hickmann, K.S., Caragea, P.C., Higdon, D., and Del Valle, S.Y. (2017). Forecasting seasonal influenza with a state-space SIR model. *The annals of applied statistics*, 11(1), 202.

Rhodes, C. and Hollingsworth, T. (2009). Variational data assimilation with epidemic models. *Journal of Theoretical Biology*, 258(4), 591–602.

Tuli, S., Tuli, S., Tuli, R., and Gill, S.S. (2020). Predicting the growth and trend of covid-19 pandemic using machine learning and cloud computing. *Internet of Things*, 11, 100222.

Wang, P., Zheng, X., Li, J., and Zhu, B. (2020). Prediction of epidemic trends in covid-19 with logistic model and machine learning technics. *Chaos, Solitons & Fractals*, 139, 110058.

SNE SIMULATION NOTES EUROPE

Simulation Notes Europe (**SNE**) provides an international, high-quality forum for presentation of new ideas and approaches in simulation - from modelling to experiment analysis, from implementation to verification, from validation to identification, from numerics to visualisation - in context of the simulation process.

SNE seeks to serve scientists, researchers, developers and users of the simulation process across a variety of theoretical and applied fields in pursuit of novel ideas in simulation and to enable the exchange of experience and knowledge through descriptions of specific applications. **SNE** puts special emphasis on the overall view in simulation, and on comparative investigations, as benchmarks and comparisons in methodology and application. Additionally, **SNE** welcomes also contributions in education in / for / with simulation.

SNE is the official membership journal of EUROSIM, the federation of European simulation societies and simulation groups, so **SNE** is open for postconference publication of contributions to conferences of the EUROSIM societies, and fo special issues organized by EUROSIM societies.

SNE, primarily an electronic journal, follows an open access strategy, with free download in basic layout. Members of EUROSIM societies are entitled to download SNE in an elaborate and extended layout. Print **SNE** is available for specific groups of EUROSIM societies, and as print-on-demand from TU Verlag, TU Wien (www.tuverlag.at).

www.sne-journal.org

MATHMOD 2022

TU Wien, Vienna, July 27-29, 2022

---- a conference as it used to be ----

ALGORITHMIC ART BY VLATKO CERIC VCERIC.NET

ARGESIM Publisher, Vienna, www.argesim.org
ARGESIM Report no. 17, ISBN: 978-3-901608-95-7 (ebook)
DOI: 10.11128/arep.17